NUMERICAL MODELLING OF TUNNELLING PROCESSES FOR ASSESSMENT OF DAMAGE TO BUILDINGS

by

Charles Edward Augarde

Keble College

Michaelmas Term 1997

A thesis submitted for the degree of Doctor of Philosophy at the
University of Oxford

NUMERICAL MODELLING OF TUNNELLING PROCESSES FOR ASSESSMENT OF DAMAGE TO BUILDINGS

by

Charles Edward Augarde

Keble College
Michaelmas Term 1997

A thesis submitted for the degree of Doctor of Philosophy at the
University of Oxford

ABSTRACT

The development and implementation of a complex numerical model for the determination of the damage to masonry buildings resulting from tunnelling settlements is described in this thesis. The current methods of damage prediction do not, in general, take into account the stiffness and weight of the surface structure. The model addresses this deficiency by explicit inclusion of the structure. Three-dimensional finite elements are used to model the ground with a non-linear, elasto-plastic soil model based on kinematic hardening. Tunnel linings are modelled using a novel overlapping elastic shell element; volume loss being simulated by shrinkage of linings coincidentally with excavation. Structures are modelled as collections of facades comprised of plane stress elements using a non-linear material model for masonry, similar to elastic-no tension. In developing the three-dimensional model, its two-dimensional counterpart is also studied. While the beam and shell elements used for linings (in two- and three-dimensions respectively) have the advantage of no rotational degrees of freedom the need to model boundary conditions at the element stiffness level complicates implementation. Tests using the shell elements show them to be satisfactory for the purpose of modelling tunnel linings. Results from a small number of analyses are given for construction of a straight tunnel beneath simple masonry structures. It is shown that the effect of the building on settlements depends heavily on its location in plan with respect to the tunnel axis. Predictions of crack patterns using the model for these analyses show that facades which the tunnel passes under first are less damaged than those later in the excavation sequence. Both of these conclusions serve to demonstrate that the problem can only be realistically modelled using three-dimensional methods. At present, however, the computer resources required to run the three-dimensional model are considerable.

Acknowledgements

Firstly, I would like to thank my supervisor, Dr. Harvey Burd, for his encouragement, accuracy, enthusiasm and good-naturedness throughout the period of research which has led to this thesis. Harvey has shown patience in dealing with my queries and has always made himself available.

Secondly, I would like to thank Professor Guy Houlsby for asking searching questions and for showing how neat and highly efficient Fortran can be written. The software used throughout this thesis is based on programs developed by Guy, Harvey and others over many years. Thanks are due to them for providing this valuable resource and permitting it to be savaged.

Many other members of the Civil Engineering Research Group need thanking. In particular the small sub-group with whom I worked at the early stages of the project, namely, Liu Gang (my above ground counterpart on this project), Luan Ngo Tran, and Jian Qian Zhou. Liu Gang deserves some sort of award for having to work closely with me throughout this project. Other people I would like to mention are Brendan Ruck (for help with Unix), Ken Dunford (for the solution of hardware problems) and Nicola Houliston (for the use of her printer).

Much needed financial and moral support has come from my parents. They have maintained a high level of interest in my work and have been positive throughout, helping me to appreciate the achievements rather than dwell upon shortcomings.

Finally, I could never have stayed the course were it not for the love and encouragement of my partner, Cathy who has put up with writing-up. It is to her, and to my daughters Elizabeth and Ruth, that I dedicate this thesis.

Contents

1. INTRODUCTION

2. PREVIOUS STUDIES OF TUNNELLING SETTLEMENTS AND BUILDING DAMAGE

3. COMPOSITION OF NUMERICAL MODEL

4. EXCAVATION MODELLING

5. MODELLING LINING INSTALLATION IN TWO-DIMENSIONS

6. MODELLING LINING INSTALLATION IN THREE-DIMENSIONS

7. ANALYSIS PROCEDURE

8. EXAMPLE ANALYSES

9. INTERPRETATION OF NUMERICAL RESULTS

10. CONCLUDING REMARKS

List of Symbols

c	von Mises failure stress
c_α	intermediate shear strength (nested yield material model)
c'_α	hardening parameter per unit c
$\boldsymbol{d}$	vector of displacements at degrees of freedom
$\boldsymbol{d}_{be}$	local displacement vector (expanded plate element)
$\boldsymbol{d}_{end}$	final displacements
$\boldsymbol{d}_{exc}$	displacements arising from excavation
$\boldsymbol{d}_p$	local displacment vector (plate element)
$\boldsymbol{f}$	vector of forces at degrees of freedom
h_α	hardening parameter
h'_α	hardening parameter per unit G
i	trough width parameter
s_u	undrained shear strength of soil
t	lining thickness
u, v, w	local displacements
$\bar{\mathrm{x}}$	generalised local co-ordinate
$\boldsymbol{B}$	strain-displacement matrix
$\boldsymbol{C}$	(Chp. 5) constraint equation matrix
$\boldsymbol{C}$	Chp. 6 matrix of curvature components
D	tunnel diameter
D_p	plate stiffness
$\boldsymbol{D}$	material stiffness matrix
$\boldsymbol{D}'$	material stiffness matrix (shell element)
E	elastic modulus
$\mathrm{E_t}$	tensile modulus for masonry
$\mathrm{E_v}$	vertical elastic modulus
$\boldsymbol{F}_g$	nodal force vector for self-weight
G	shear modulus

$\mathrm{G_{hv}}$	independent shear modulus
$\mathrm{G_0}$	shear modulus at surface
$\boldsymbol{G}$	matrix of hinge angles (shell element)
H	building depth
I	2nd moment of area of section
$\boldsymbol{I}$	Identity matrix
$\boldsymbol{J}$	Jacobian matrix of shape functions
K	bulk modulus
K_0	coefficient of earth pressure at rest
K^*	trough width parameter linking i and Z
$\boldsymbol{K}$	stiffness matrix
$\boldsymbol{K}_{be}$	local stiffness matrix (kinked plate element)
$\boldsymbol{K}_{beg}$	global stiffness matrix (kinked plate element)
$\boldsymbol{K}_{bg}$	global stiffness matrix
L	building length or span
$\boldsymbol{L}$	kinematic matrix for shell element formulation
L_a	element - d.o.f. connectivity list
$\mathrm{L_i}$	element order list for frontal solver
$L_i(\bar{x})$	Lagrange polynomial
$\boldsymbol{M}_f$	front matrix
$\boldsymbol{N}$	shape function matrix
N^*	stability ratio
R	tunnel radius
S	vertical settlement
$\boldsymbol{T}$	Transformation matrix
U, V	two-dimensional global displacements
U_e	eliminated freedoms
U_r	retained freedoms
$\mathrm{V_1}$	parent element volume

V_L	percentage volume loss
V_L^t	percentage volume loss measured at the tunnel
V_0	volume required to construct tunnel
V_S	volume per unit length of the settlement trough
V_{tun}	volume change at tunnel
X, Y	two-dimensional global axes
Z	depth to tunnel axis
α	mesh refinement parameter
β	angular distortion
γ	unit weight
δ	radial movement in Mair & Taylor (1993)
Δ	deflection (of building)
ϵ_b	maximum bending strain
ϵ_{crit}	critical tensile strain
ϵ_d	maximum diagonal strain due to shear
$\boldsymbol{\epsilon}_l$	volume loss strain vector
ϵ_{lt}	strain at change of moduli (masonry model)
κ	curvature
$\boldsymbol{\kappa}$	curvature vector
μ	variation of s_u
ν	Poisson's ratio
ϕ'	effective friction angle
$\boldsymbol{\sigma}$	stress matrix
σ_h	total horizontal stress
σ_{lt}	limiting tensile stress (masonry model)
σ_r	radial stress
σ_v	total vertical stress
$\sigma_1, \sigma_2, \sigma_3$	principal stresses
τ	shear stress

ω	variation of shear modulus with depth

Subscripts

cv	refers to expanded overlapping beam element
i	internal
l	lining
max	maximum
g	ground
v	vertical

CHAPTER ONE

INTRODUCTION

Placing transport infrastructure underground, in tunnels, is increasingly popular in the world's cities since above ground road or rail links need land which is either unavailable or prohibitively expensive. In London, 13 kilometres of tunnels for the Jubilee Line Extension were recently completed and other projects, such as CrossRail, are planned. The construction of a tunnel usually leads to some surface disturbance, particularly settlement. These effects are often of little importance to greenfield sites, but where structures are present, significant damage can result. The acceptance of a tunnelling project in an urban area, by building owners and the public, depends on the availability of reliable predictions of the potential harmful effects.

Tunnels can be constructed through virtually any type of ground. While tunnelling in rock can lead to surface disturbance and damage, this is usually the result of a collapse rather than from continuous deformation as witnessed in soft ground, such as sand and clay. This chapter contains descriptions of tunnelling methods in soft ground and the procedures most commonly adopted in practice for the determination of settlements and damage to buildings.

1.1 Tunnelling Methods

All methods of tunnel construction in soft ground, except NATM (see below), use some form of temporary ground support to protect workers or machinery removing the ground at the tunnel face. This support is usually in the form of a shield which may have an open or closed face. As the name suggests, an open face shield provides no support to the face of the tunnel. Tunnelling using an open shield is therefore only satisfactory in ground with a reasonable degree of self-support, such as a stiff clay.

Where ground conditions become too unstable to use an open shield then a *closed shield* method must be employed where devices to provide face support during tunnelling are included. *Compressed air working* uses a modified shield with a pressurised chamber behind the face and *slurry shields* (Stack, 1985; Sterling, 1992; Flint and Foreman, 1992) provide support to the face through a liquid pumped into the chamber. *Earth pressure balance* (EPB) machines (Barrett, 1993), aim to improve on the support supplied by a slurry shield by matching the earth pressure exerted by the exposed face. An EPB shield consists of a rotating cutter with slots through which excavated spoil passes into a closed chamber. This chamber is kept full throughout tunnelling providing an earth pressure in balance with that from the face.

The New Austrian Tunnelling Method (NATM) is a shieldless tunnel construction method only recently applied to soft ground conditions. The method aims to use the minimum required support for the ground around the tunnel by permitting deformations after excavation and before application of a support lining. The stresses in the ground are redistributed as the ground attempts to support itself. Careful monitoring of soil movements are necessary to determine when to apply a temporary lining.

Once constructed, tunnels are permanently lined with one of the following:

- Temporary steel arches (or ribs) and walings (or timber lagging) followed by insitu concrete,
- Lining segments, either reinforced concrete, cast iron or steel, with grouting between excavated soil face and the outside of the segment. Some designs of concrete segment can be expanded to reduce the annular void between lining and soil face.
- Insitu reinforced concrete constructed sequentially as the shield progresses. This is often automated.
- Shotcrete over steel mesh with rock anchors (NATM).

1.2 Settlement prediction

In practice, the prediction of surface settlements arising from tunnelling and the resulting damage to structures are usually treated as separate procedures. Firstly, the settlements predicted for the tunnel under a greenfield site (i.e. one without surface structures) are calculated. These settlements are then applied to a model of the building, or buildings, affected. The details of these procedures have been reviewed many times over the years (e.g. Attewell (1978), Rankin (1988), Institution of Structural Engineers (1989), New and O'Reilly (1992), Mair et al. (1996)) and they are widely used in industry.

Immediate settlements arise from two sources:

- Movement of material into an annular void around the tunnel formed from the difference between the excavated volume and the overall volume of the lining, often termed *tail loss*.
- Movement of material into the face of excavation, termed *face loss*.

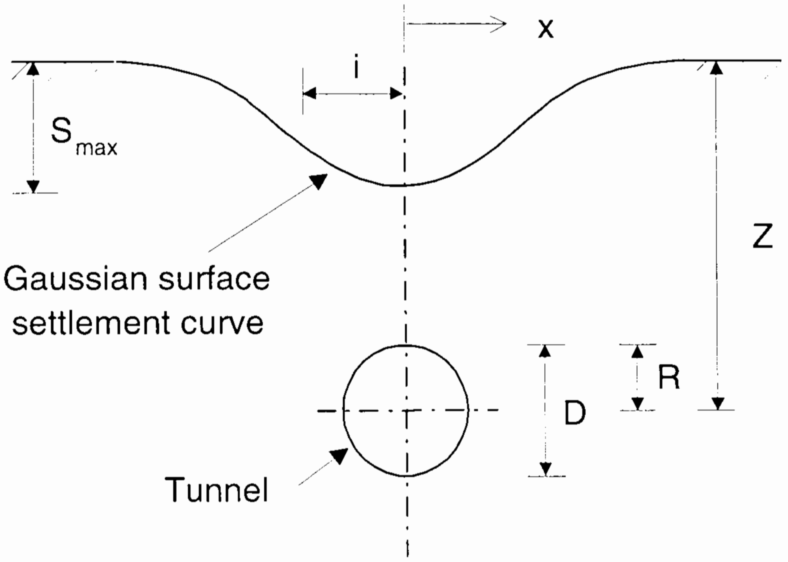

Figure 1.1: **Section through a tunnel showing trough parameters**

Once the tunnel is constructed, settlements continue as the ground consolidates. However, settlements from consolidation are usually ignored in assessments of likely damage from tunnelling (Ward and Pender, 1981).

The most commonly adopted method used to determine greenfield site settlements from tunnelling in soft ground presumes the transverse profile of vertical displacements, after the tunnel has passed, to follow a Gaussian (or Normal) distribution curve, as shown in Figure 1.1. This curve was proposed by Peck who compared it with many sets of field data from tunnelling in his state-of-the-art paper to the 7th International Conference on Soil Mechanics and Foundation Engineering (Peck, 1969). Others (Rankin, 1988) have since backed up Peck's assertion by examination of subsequent field data. The transverse settlement curve is represented by the symmetrical formula,

$$S = S_{max}\ e^{\frac{-x^2}{2i^2}} \tag{1.1}$$

where S_{max} is the maximum vertical settlement over the axis of the tunnel and x is the transverse distance from the axis to the point of interest (see Figure 1.1). The width of the settlement trough, is defined by the parameter i, which is the distance to the point of inflexion of the curve (corresponding to one standard deviation of the Normal distribution curve). S_{max} and i fully define the curve. The trough width parameter, i is determined by the ground conditions and is not linked to the tunnelling method used (Mair et al., 1993; Mair et al., 1996). Various expressions have been proposed for i (New and O'Reilly, 1992; Gunn, 1993) but in practice the relation,

$$i = K^* Z \tag{1.2}$$

is used, with $K^* = 0.5$ for clays and $K^* = 0.25$ for cohesionless soils (Rankin, 1988).

The volume per unit length of tunnel of the surface settlement trough can be obtained by integrating Equation 1.1 to give,

$$V_s = \sqrt{2\pi} i S_{max}. \tag{1.3}$$

If it is assumed that the soil deforms under constant volume (i.e. undrained) then V_s can be equated to the extra amount of soil removed in excavation over that required for the tunnel lining. This is usually expressed as a percentage volume loss, V_L in the following form,

$$V_L = \frac{V_s}{V_0} \times 100\% \tag{1.4}$$

where V_0 is the volume required to construct the tunnel. Using Equations 1.3 and 1.4 the following expression for S_{max} can be obtained,

$$S_{max} = \frac{V_L \pi D^2}{400\sqrt{2\pi} i} \approx \frac{V_L D^2}{319 i}. \tag{1.5}$$

The value of volume loss depends on the ground conditions and the tunnelling method. Losses are usually greater in cohesionless soils than in clays. For a stiff overconsolidated soil such as London Clay, volume loss is usually below 2% (Attewell et al., 1986; Mair et al., 1996). Given a value of V_l and the tunnel dimensions, Equations 1.2 to 1.4 determine the transverse settlement profile.

The longitudinal profile of settlements along the axis is often assumed to take the form of a cumulative probability curve (Attewell and Yeates, 1984; New and O'Reilly, 1992) which moves with the tunnel excavation. This assumption is tested against field data by Attewell and Woodman (1982) who derive expressions for the displacements and ground strains at any point ahead of the tunnel. Contours of settlements can then be determined for intermediate stages of excavation.

Tunnelling methods which provide external face pressure sometimes produce a more complex set of ground movements and heaves are occasionally induced from poor control or abrupt changes in ground conditions (de Moor and Taylor, 1991; New and O'Reilly, 1992). Apart from these situations, it is generally accepted that different tunnelling methods or cross-sectional shapes do not affect the shape of the settlement profile and the above procedure may be used (New and Bowers, 1994; Zawadzki, 1994). Examples are to be found in investigations of the ground response to tunnelling using earth pressure balance machines by Fang et al. (1993) and Clough et al. (1983). These works also indicate the relative importance of tail loss over face loss which, in EPB tunnelling, is more tightly suppressed (Inokuma and Fujimoto, 1996). Farmer (1978) found that deviations from the predicted settlements were affected as much by the care with which excavation was undertaken as by the method itself.

1.3 Damage prediction

Once settlements have been determined, they are usually applied directly to an idealisation of a structure. This study is confined to masonry structures (i.e. brick or stone) although other forms of construction are also sensitive to tunnelling settlements. The inability of masonry to withstand even moderate tensile stresses leads to cracking which

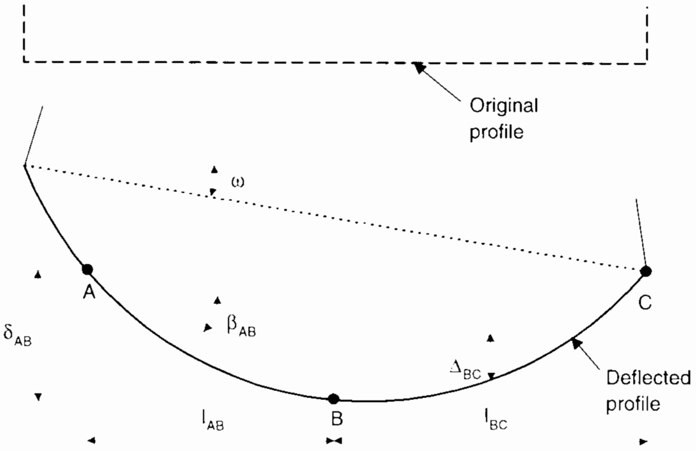

Figure 1.2: **Measurements to assess damage in buildings**

can be unsightly or lead to structural instability. Prediction of damage, in these structures, consists of linking the induced deformations to the expected onset and degree of cracking. Damage is difficult to quantify; the most successful attempts to classify damage use a mixture of measurable quantities (e.g. crack width) and visual assessment.

Past research into settlement related damage does not generally distinguish between different sources of settlements which could be long-term in nature, arising from consolidation under self-weight, or short term from tunnelling. In the 1950's, Skempton and MacDonald (1956) and Polshin and Tolkar (1957) examined existing buildings affected by settlements and proposed limits on some measurable physical distortions to prevent damage. Skempton and MacDonald (1956) used *angular distortion*, β which they defined as the rotation of the straight line joining any two points on the structure, less any rigid-body rotation of the structure (see Figure 1.2). Polshin and Tolkar (1957) proposed similar rules and, importantly, introduced the concept of a limiting tensile strain, ϵ_{crit} signalling the onset of cracking.

The important work of Burland and Wroth (1975) gives an analytical explanation for damage to buildings which is compared to the earlier empirical studies. A building

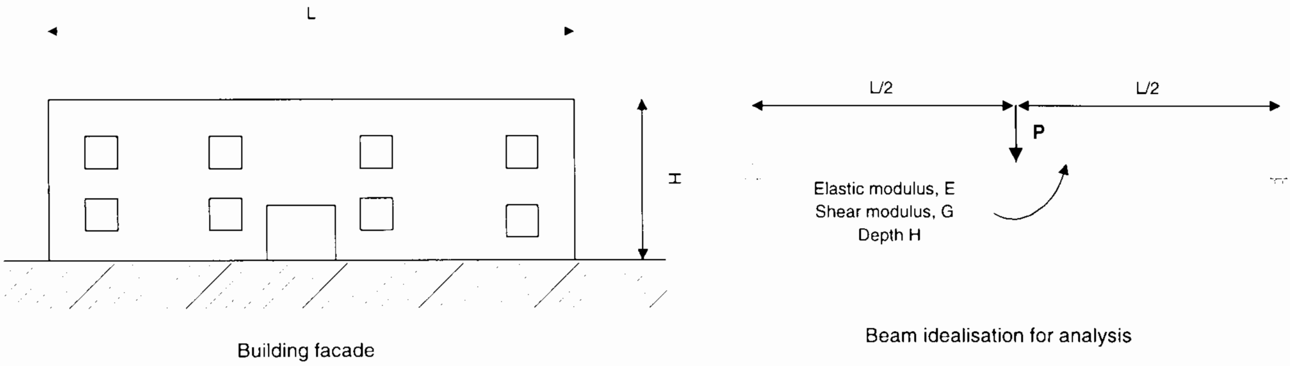

Building facade

Beam idealisation for analysis

Figure 1.3: **Idealisation of a building after Burland and Wroth (1975)**

is idealised as a deep, elastic, simply-supported beam (Figure 1.3) and a kinematic relation is derived between a measurable quantity, the *deflection ratio* (Δ/l, see Figure 1.2), and the maximum tensile strain in the beam. The method is developed from the solution for the central deflection Δ of a deep elastic beam of depth H, span L and second moment of area I under a central point load, P (Timoshenko, 1957)

$$\Delta = \frac{PL^3}{48EI}\left[1 + \frac{18EI}{L^2HG}\right]. \tag{1.6}$$

G and E are the shear and Young's moduli which are assumed constant throughout the beam. If bending and shear deformation are each considered on their own to lead to the deflection Δ, the load P in Equation 1.6 can be replaced by an expression containing the maximum bending strain ϵ_b or maximum direct strain arising from shear deformation (diagonal strain) ϵ_d in the beam (Burland et al., 1977). After rearrangement this gives,

$$\frac{\Delta}{L} = \epsilon_b \frac{L}{12}\left[1 + \frac{18EI}{L^2HG}\right] \tag{1.7}$$

$$\frac{\Delta}{L} = \epsilon_d \left[1 + \frac{L^2HG}{18EI}\right]. \tag{1.8}$$

In Equations 1.7 and 1.8 it is assumed that the neutral axis is located at the mid-height of the beam. In practice, the foundations tend to restrain a building making it more realistic to assume the neutral axis at the base. The equations can be easily reformulated for this case. Often a building will experience both hogging and sagging deformation. In this case, the affected parts are treated separately with L taken as the length of building to the point of inflexion. The predicted maximum strain in the building is usually taken as the largest of ϵ_b and ϵ_d. This is compared to a critical tensile strain ϵ_{crit} which signals the start of visible cracking, usually taken as 500 microstrain (0.05%) (Boscardin and Cording, 1989; Mair et al., 1996).

The approach of Burland & Wroth is widely used in practice despite the simple model used for the building both in terms of geometry and of material properties. Kerisel (1975) highlights the heterogeneous rigidity of older masonry buildings caused by features such as large windows and staircases that often have significance for damage prediction and which are difficult to incorporate into an analytical model like that of Burland & Wroth.

Boscardin and Cording (1989) extend Burland & Wroth's approach to include horizontal strain and compare the resulting method with field measurements of settlement damage to structures. The maximum tensile strain becomes the sum of the strain from bending or shear deformation together with a component of horizontal strain. One conclusion from this study is that, for masonry buildings, shear deformations will be dominant leading to the appearance of diagonal cracking first, before vertical cracking due to bending. A figure is given (Figure 1.4) which brings together the recommendations of Burland & Wroth, the earlier empirical works on angular distortion, β, the effect of horizontal strain and the subjective classification system for damage of Burland et al. (1977). Boscardin's approach was used in the recent assessment of potential damage to structures at Waterloo Station, London (Harris et al., 1993) from tunnelling. The results of the study prompted the use of compensation grouting to limit settlements.

Geddes (1992) criticises the direct inclusion of the horizontal strain from the ground

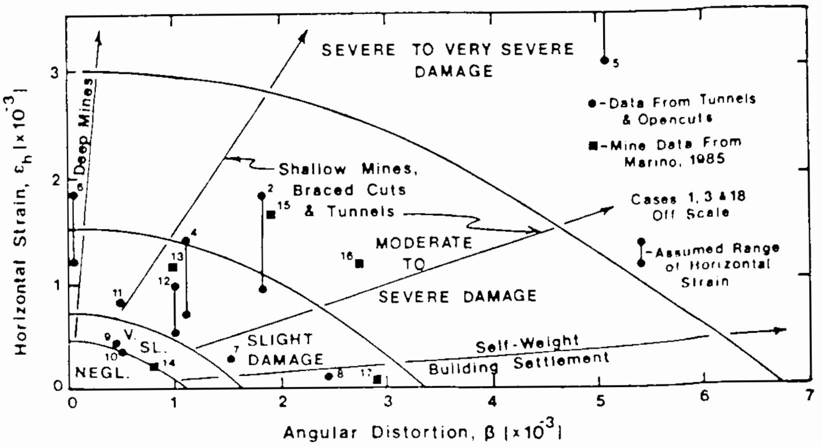

Figure 1.4: **Calculation of damage to buildings from Boscardin & Cording (1989)**

into Boscardin's calculations for damage to the building on the basis that it is likely that slippage will occur between the ground and the base of the building. This is one of the few references which raises the question of interaction between the ground and the building.

1.4 Combined settlement and damage prediction

An obvious criticism of the procedure detailed above, is that the stiffness and self-weight of the building is neglected in the assessment of the settlement profiles. This deficiency in current practice was recognised nearly 20 years ago by Burland et al. (1977) who stated that the inclusion of the effects of the building is vital to the correct determination of the settlement profile.

Later works, (Attewell and Yeates, 1984; Dulacska, 1992) refer indirectly to the deficiency by saying the shape of the greenfield settlement profile has little relevance to the type or degree of damage caused. Mair (1993) argues that the extent of building damage is probably overestimated in practice due to the neglect of the building stiffness and states that three-dimensional non-linear finite element analyses are required to model the situation correctly. Such an approach is also recommended by Gunn (1993).

There are very few examples of case studies from industry where interaction between the building and the ground has been considered when predicting damage. Papers by Hellings (1994) and Frischmann et al. (1994) describe tunnelling works adjacent to the Mansion House in London where building and ground movements were closely monitored. The first phase of the works consisted of a tunnel driven directly beneath the building. Severe levels of damage to the building were predicted, assuming a greenfield settlement trough, and the tunnel diameter was reduced to limit damage to acceptable levels. Monitoring of the building and ground in the following two years, prior to the second phase of tunnelling, revealed the shape of the settlement troughs not to follow the original predictions but to be much wider and flatter due to the presence of the building. An improved assessment procedure was therefore adopted for the second phase of tunnelling for this scheme using the measurements taken after the first tunnel was constructed. A numerical model was devised, including the ground and the first tunnel, and parameters controlling the response of the model, both for the building and for the ground, were tuned until the settlements predicted from the model matched those measured at the site. The second phase of tunnelling was then simulated to identify critical areas of the building which were analysed in greater detail. While this was an improvement over the assessment for the first phase, the tuning of the numerical model appears to have ignored the real properties of the ground and building. The procedure also assumes a uniform structural response to tunnelling which is difficult to justify, given the complex layout of the building. The numerical modelling aspects of these papers are discussed further in Chapter 2.

In summary, the damage expected from a given tunnelling scheme is generally determined in practice using a semi-empirical, two-stage procedure. Interaction between the ground and the building is often ignored and a highly simplistic model of the building is usually employed. In industry it is recognised that soil-structure interaction effects are important but the lack of any suitable design rules forces the use of the simple procedures described above.

1.5 Research objectives

New methods are needed to predict tunnelling settlements and damage which include the effects of buildings on the surface. While there is interest in physical modelling of this problem, using centrifuge testing, for example, more versatility can be gained from numerical modelling. As Chapter 2 demonstrates, there is considerable interest in solving this problem using these techniques.

The objective of the research at Oxford University is to produce a three-dimensional numerical model of the construction of a tunnel with a surface structure present. The study is confined to tunnelling in clay with a structure constructed of masonry. This combination matches conditions found for tunnelling schemes in London. Additionally, investigation is confined to the immediate settlements following tunnelling so that undrained soil behaviour is assumed throughout. The production of the model is a joint effort with work split roughly into above and below ground components. The former work is described in a separate thesis (Liu, 1997) and comprises the development of a constitutive model for masonry, modelling of building facades and the tying of the facades to the ground. This thesis describes the development of the below ground aspects of the modelling of tunnelling.

The model is based on the finite element program OXFEM (Burd, 1986) and incorporates various features which are described in Chapter 3. A necessary stage in the development of the three-dimensional model is development of a two-dimensional model of tunnelling. This has allowed testing and validation of some ideas later used in the three-dimensional model and comparisons of results to be made.

Chapters 4 to 6 of this thesis describe in detail two particularly complex parts of the model: excavation and lining installation. Three-dimensional modelling also requires a complicated analysis procedure to be followed because of difficulties in checking input data and in visualising results. To explain some of these problems, Chapter 7 describes the analysis procedure.

Demonstration analyses using the models are described in Chapter 8 with typical tunnelling configurations for both two- and three-dimensional cases. The results of these analyses are discussed in Chapter 9. Comparisons are made between the different versions of the model, between greenfield and urban sites and against solutions derived from the conventional approaches to settlement and damage prediction discussed in Sections 1.2 and 1.3.

CHAPTER TWO

PREVIOUS STUDIES OF TUNNELLING SETTLEMENTS AND BUILDING DAMAGE

2.1 Introduction

This review covers work which has employed either exact (closed form) analytical methods or approximate numerical analysis techniques to predict settlements and damage resulting from tunnelling. In light of the specification for the current research set out in Chapter 1, the review concentrates on studies generally concerned with tunnelling in clay, rather than in non-cohesive soils.

A complete closed form solution for the deformations arising from the installation of a tunnel in soft ground, taking account of soil material non-linearity is, not surprisingly, unavailable at present. The solutions discussed below model some aspects of tunnelling behaviour and provide useful approximations relatively easily. Numerical methods are more successfully applied to the problem and in recent years there has been considerable work in this area. The main advantage of analytical methods, and small scale numerical modelling, is that parametric tests are simple. The main disadvantage is the need for calibration against data from field observations.

2.2 Closed form solutions

2.2.1 Tunnelling settlements

In the methods which follow, the nomenclature of Figure 1.1 (Chapter 1) is used. The first method (Chow, 1994) to be examined here uses the solution for vertical displacements at a distance from a point load in an elastic half space (Poulos and Davis, 1980). The unloading of the soil mass, due to excavation, is modelled as a line load along the tunnel axis. Unfortunately it is not possible to obtain, analytically, the integral of the point load solution (i.e. the solution for a line load) so relative differences in vertical displacements are derived which cancel the insoluble part of the integral. The surface settlement over the tunnel, S is then calculated as the settlement relative to some distant point on the surface which will, in practice, experience negligible settlement:

$$S = \frac{\gamma D^2 Z^2}{8G(x^2 + Z^2)} \tag{2.1}$$

where γ is the unit weight of the soil and G its shear modulus. The method accounts for unloading only, neglecting movement due to volume loss which dominates in reality. For this reason heaves rather than settlements are predicted.

The second of the closed form methods is described in Chow (1994) and is attributed to Sagaseta (1987). It is a purely kinematic approach to the problem given that the boundary conditions of the tunnelling settlement problem are displacements, and only displacements (i.e. surface settlements) are required as output. Sagaseta uses an analogy with fluid mechanics (sinks and sources) to model the displacement field in an incompressible soil. Chow uses this approach to derive the solution for vertical displacements at the soil surface as,

$$S = -\frac{\gamma D^2 Z^2}{4G(x^2 + Z^2)} \tag{2.2}$$

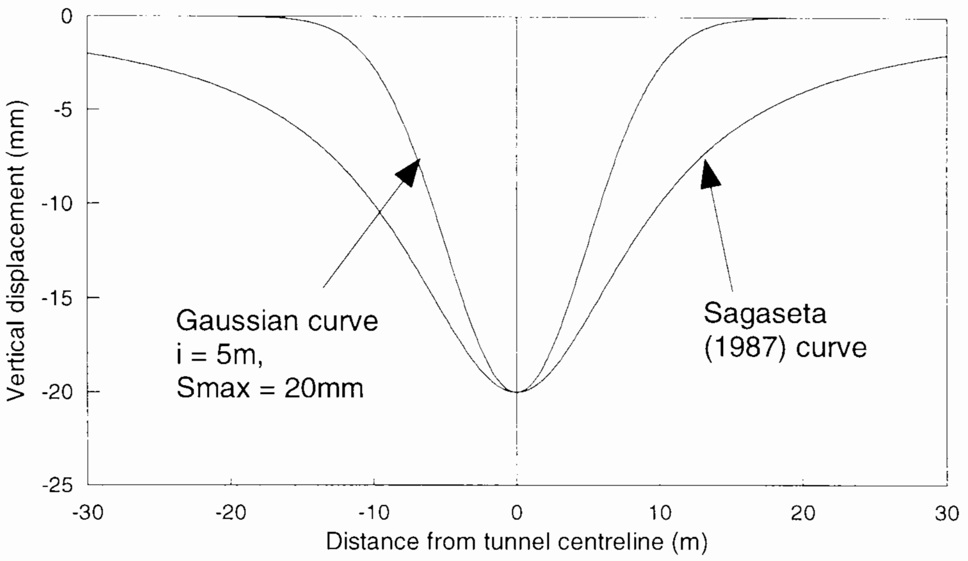

Figure 2.1: **Settlement profiles**

A comparison of the predicted transverse profile from Equation 2.2 with that using a Gaussian curve having the same S_{max} and $i = 0.5Z$, is given in Figure 2.1. This demonstrates the wider trough predicted by this method which is further highlighted in Sagaseta's paper where he relates his closed form solution to measurements from the Caracas Metro (Sagaseta, 1987).

More advanced elastic approaches to the analysis of tunnelling are given in Einstein and Schwartz (1979) and Pender (1980). They assume the tunnel to be located at depth, so there are no conclusions for surface settlements however they are useful for comparison purposes. These studies idealise tunnels as cavities which appear suddenly in a prestressed medium, in this case the ground. If the tunnel is unlined there is a relief of radial and shear stresses at the tunnel periphery in the prestressed medium. Assuming linear elasticity and plane strain the stress changes arising from the removal of a circular disc, representing the tunnel, can be determined. Boundary conditions at the tunnel face are imposed depending on the amount of slippage between liner and ground. The stiffness of the liner is accounted for by including Flügge's stress displacement relations for a circular elastic shell (Flügge, 1966).

An approach which includes soil plasticity is described by Mair and Taylor (1993) who compare subsurface ground movements around tunnels in London Clay with the closed form solutions for contracting spherical and cylindrical cavities in a linear elastic - perfectly plastic medium. Respectively these are,

$$\frac{\delta}{D} = \frac{s_u}{3G}\left(\frac{D}{r}\right)^2 e^{(0.75N^*-1)} \tag{2.3}$$

and,

$$\frac{\delta}{D} = \frac{s_u}{2G}\left(\frac{D}{r}\right) e^{(N^*-1)} \tag{2.4}$$

where δ is the radial movement at radius r from the tunnel centreline, s_u is the undrained shear strength of the soil, $N^* = \sigma_v/s_u$, is the stability ratio and σ_v is the overburden stress at the tunnel centreline before excavation starts. Measurements of axial displacements ahead of monitored tunnels are shown to vary with $(D/r)^2$ (i.e. the spherical cavity solution) while radial movements around tunnels appear to follow variation in (D/r) (i.e. the cylindrical cavity solution).

Mair and Taylor (1993) extend the analysis to include a permanent tunnel lining which prevents the cavity from fully unloading to zero stress modifying Equation 2.4 to,

$$\frac{\delta}{D} = \frac{s_u}{2G}\left(\frac{D}{r}\right) e^{[N^*(1-n)-1]} \tag{2.5}$$

where n is the proportion of the overburden pressure taken by the lining. This plasticity approach is useful for gaining approximate solutions for the subsurface settlement profiles. The overall stability of a tunnel, with and without an internal support pressure is also examined, using the cavity contraction solutions, in Davis et al. (1980) and Sloan and Assadi (1992).

Probabilistic methods for predicting subsidence have received attention in studies of large scale mining works but appear not to have been applied to tunnelling. Attewell (1978) describes how soil may be modelled as a collection of particles, each assumed to be a disc, configured in a regular grid. A void is developed at the origin into which either of the two adjacent particles moves, each having an equal probability of doing so. The void moves upwards through the grid until it reaches the free surface where it manifests as a depression. The process is repeated with other voids from the origin to create a surface settlement profile. The mathematical formulation for this stochastic model is developed in two-dimensions by Sweet and Bogdanoff (1965) who show, for small-scale subsidence, that the trough formed at the surface follows a Gaussian distribution, thereby agreeing with the semi-empirical prediction method for greenfield sites. The formulation is restated in a paper by Litwiniszyn (1994) who links the trough shape to the thermodynamic principle of entropy. Whilst of interest, this approach is limited by the particulate model adopted for the soil with no cohesion between particles, neglecting an important property of clays.

2.2.2 Building damage

The approach of Burland and Wroth (1975) and its extension by Boscardin and Cording (1989) represents the most significant attempt to date to predict damage in buildings subjected to tunnelling settlements using an analytical method. This approach has already received attention in Section 1.3.

2.3 Numerical methods

2.3.1 Tunnelling settlements

The finite element method has proved the most popular numerical technique to be applied to the tunnelling settlement prediction problem. This is not to underplay the difficulties involved which are emphasised in the following quote taken from New and O'Reilly (1992),

> *The soil tunnelling problem has proved resistant to finite element modelling because it is complex, often involves parameters which are not well-defined and is unforgiving if the analyst does not properly model both the soil and tunnel supports as well as the construction process.*

Descriptions of the finite element method, applied to solid mechanics, are to be found in many references (Cook, 1981; Astley, 1992) and no attempt is made here to restate the fundamentals of the technique.

Two-dimensional, plane strain modelling is chosen by most researchers because of the considerable resources required for a satisfactory three-dimensional model. An early example is found in Gioda and De Donato (1979). A linear elastic-plastic model with a Mohr-Coulomb failure surface is used for the soil. The tunnel lining is simulated using thin elements whose properties are changed during the analysis. This models the imposition of a sprayed concrete lining which subsequently gains strength and stiffness over time. The surface settlement profiles predicted by this model are wider than expected in practice.

Oteo and Sagaseta (1982) use a simpler elastic model for the soil and find that the results become dependent on the size of the finite element mesh. This is due to the heave which occurs from unloading through excavation. This problem can be solved by increasing the soil stiffness with depth and reasonable troughs are obtained as in the study by Chow (1994).

Elastic soil is also used in the model of Ghaboussi et al. (1983) for the analysis of the effects of construction of a new sewer tunnel over two existing subway tunnels. Two dimensional analyses are carried out for a plane normal to the subways and for a plane normal to the new tunnel. No allowance is made in this model for any ground loss during construction of the new tunnel but linings are included using beam elements. Major changes to the actual sequence of construction were made following these analyses so it is not possible to compare to field data.

Romo and Resendez (1982) also use pairs of orthogonal two-dimensional analyses in an attempt to capture the three-dimensional effects of tunnelling. In one of the analyses, the mesh covers a slice transverse to the tunnel and the ground loss is modelled by relieving radial stress uniformly around the tunnel to give transverse settlements. Longitudinal settlements are found from the other analysis where the mesh consists of a slot (i.e. a section along the tunnel axis) subject to similar stress relief. Throughout, a non-linear (hyperbolic) elastic model is used for the ground. Wider troughs are predicted from these analyses than would arise from the semi-empirical approach described in Section 1.2 which the authors blame on the elasticity of the ground.

In Mair et al. (1981), the soil is modelled using Modified Cam clay and the results are compared to earlier centrifuge tests (Mair, 1979). The surface settlement profiles predicted are wider and flatter than the centrifuge results but the prediction of ground loss, measured by the volume change of the tunnel, is in good agreement. The explanation given is that around the tunnel, plasticity is mobilised which is modelled well by Modified Cam clay. In contrast the isotropic elasticity of the soil model dominates the response at the surface.

An attempt to improve the predicted shape of transverse settlement profiles is made in Lee and Rowe (1989) where analyses using a cross-anisotropic, elastic-perfectly plastic soil model are described. No lining is included since the analyses are linked to centrifuge tests of unlined tunnels (Mair, 1979). The findings indicate that variation of the anisotropic ratio of independent shear modulus G_{hv} to vertical modulus E_v has a marked effect on the shape of the settlement curve. This is attributed to the large shear strains developed in the soil at 45° to the vertical as the soil arches around the excavation. A more recent study related to London Clay also stresses the importance of anisotropy on profile shape (Simpson et al., 1996).

Criticism of the use of linear elasticity to model the ground in the tunnelling problem occurs quite far back in the literature. Ward and Pender (1981) survey the work to 1981 and conclude that experimental and field work shows there to be a contained region of yielding ground around a freshly excavated tunnel. Another conclusion arising from this paper is that immediate effects dominate surface settlements. Unless there are changes subsequent to excavation and lining, such as drainage into the tunnel from the surrounding ground, deformation of the surface is usually negligible following passage of the tunnel shield. This implies that modelling should concentrate on undrained behaviour.

More recently, accurate laboratory testing has verified that shear modulus in overconsolidated clays decreases rapidly with strain, from a high initial level, for small strain values (Atkinson and Stallebrass, 1991). With correct modelling of this property, deformations may be more localised over and around the tunnel leading to narrower, and hence more realistic, settlement profiles (Lee and Rowe, 1989). The soil model adopted by Gunn (1993) goes some way to represent this behaviour. Non-linear elasticity with stiffness related to strain level is used together with yielding following a Tresca failure surface. This model, and linear elasticity, are employed in unlined analyses. Comparison is made to equivalent Gaussian curve predictions having calculated ground losses from analysis results. Some improvement is made to the predicted shapes of settlement profiles but they are still wider than expected in practice.

Modelling of the small strain stiffness behaviour is better achieved using kinematic nested surfaces in the pre-failure region (Atkinson and Stallebrass, 1991). Chow (1994) and Stallebrass et al. (1996) use these type of soil models: Chow carries out unlined analyses and achieves some good settlement profiles. Stallebrass et al. (1996) do the same for the analysis of centrifuge tests of tunnels.

As will be clear from the above, a tunnel lining is modelled explicitly in relatively few two-dimensional analyses. Beam finite elements of quite high complexity (including shear deformation effects) are used by Bakker et al. (1996), El-Nahhas et al. (1992) and Addenbrooke and Potts (1996). In the first two papers, the beams are attached to the soil and shrunk to model ground loss. In the third, the soil is allowed to deform until the point where it would come into contact with a lining. The lining elements are then activated.

The true three-dimensional effects of tunnelling include changes ahead of the tunnel face (Ward and Pender, 1981; Lee et al., 1992) which alter the insitu stress regime from that assumed in all two-dimensional analyses. The estimation of the disturbance ahead of the tunnel is incorporated into two-dimensional analyses by Lee et al. (1992) using their *Gap* parameter. This is defined as the vertical distance over the tunnel crown of the annular ground loss void. A component of this parameter is attributed to three-dimensional disturbance effects ahead of the face. This component is itself derived from the results of three-dimensional finite element analyses reported elsewhere (Lee and Rowe, 1990a; Lee and Rowe, 1990b). An accompanying paper demonstrates the effectiveness of this method against field studies (Rowe and Lee, 1992).

The relatively few previous studies using three-dimensional analysis tend to employ simple soil models, to reduce the computer time required to obtain solutions. Lee and Rowe (1990a) use a cross-anisotropic elastic-perfectly plastic soil model with a rounded off Mohr-Coulomb failure surface, similar to that described in their earlier two-dimensional work (Lee and Rowe, 1989). Two cases are examined:

(a) unlined analysis of a three-dimensional block from which a length of tunnel is removed.

(b) the same analysis with a rigid lining where movement of the soil is permitted at the tunnel face.

These two analyses are thought to bracket the real situation. The study (Lee and Rowe, 1990b) concludes that the two-dimensional transverse settlement profile may occur a significant distance back from the tunnel face. The distance appears dependent upon the plasticity mobilised in the soil around the tunnel. Before the plane strain state is reached, the surface will have undergone horizontal and axial deformation not predictable with a two-dimensional analysis.

In the work of Akagi and Komiya (1996) tunnelling is modelled in three-dimensions by changing the properties of elements within and ahead of the tunnel. Incremental excavation is carried out with the activation of stiffer continuum elements representing a lining. Reasonable agreement with Gaussian type profiles is reported but no allowance is made for volume loss in the analyses.

Swoboda et al. (1989) reduce the computer resources required for their three-dimensional analyses by coupling finite elements in and adjacent to the area of tunnel construction to boundary elements representing the soil in the far field. This is similar to the use of *infinite elements* in Beer (1983) and the boundary element method in Ito and Hisatake (1982). Swoboda et al. (1989) model excavation and lining with layers of shotcrete (as in NATM), which gains strength as the analysis proceeds.

2.3.2 Combined analyses including buildings

In the work examined in the previous section, and in common with most numerical modelling of the tunnelling settlement problem, neither the self-weight nor the stiffness of a surface structure have been included in the numerical model.

Simple studies, using elastic models for the soil and building are given in Parry-Jones and Cline (1993) and Hirst (1994). The latter work uses three-dimensional modelling and shows the dramatic way that stiff elastic elements on the soil surface flatten out the settlement profile.

A two-dimensional finite element model, including a building, is used in the prediction of settlement damage to the Mansion House (Hellings, 1994; Frischmann et al., 1994) as described in Section 1.4. Single facades of the building are modelled with linear elastic beam elements. Material properties are determined from modelling the construction of an earlier tunnel and adjusting parameters until a close fit is achieved with actual measured settlements. Cracking of the masonry is dealt with by reducing the effective section thickness of elements in areas expected to be cracked. It is notable that satisfactory agreement with the data from the first tunnel can only be achieved when the boundary conditions are also adjusted, to model the support of another facade. It is also interesting that in the prediction of the effects from the second phase of tunnelling, a factor of safety of two is applied, without explanation, to a predicted volume loss of 2.5% which is already conservative for London Clay.

The assessment of the effect of a tunnel for the CrossRail project on Britannic House in London, (Simpson, 1994) uses two-dimensional finite elements. Three linked facades of the building are modelled with a single two-dimensional mesh. The facades are assumed to act like deep, many-flanged beams. Each flange represents a horizontal strip of facade between windows and they are linked by more flexible webs representing strips containing windows. In recognising that the building changes the settlement profile from that expected for the tunnel construction, the greenfield settlement profile is not applied directly to the base of the facade model. Instead, it is applied at the base of a strip of elements representing the ground beneath the facades. The material model for the building is linear elastic with a low limiting tensile strength, to model masonry.

The results presented by Simpson (1994) show flattened settlement profiles and highlight critical areas of the building for cracking. An interesting observation is made in analyses where the settlements are applied incrementally. Initially, vertical cracking is indicated, starting at the base of the building. This continues with cracks lengthening up the building until suddenly, major cracking occurs from the top of the building to divide the building into separate structures. The practical significance of this is that there may be little warning, from site measurements, of major damage by this mechanism. The different parts of the structure are modelled well in this study but the settlement profile is still imposed on the model, albeit in an attenuated form, through the cushion of soil below the building.

Potts and Addenbrooke (1996) describe a procedure for modifying greenfield values of horizontal strain and deflection ratio to include the effect of a surface structure. The work is based on a parametric study using two-dimensional finite elements. The soil is modelled with non-linear elasto-plastic behaviour and undrained conditions are assumed. The building is modelled with linear elastic beam elements rigidly attached to the ground surface. In the study, the axial and bending stiffness of the beam were varied. Increasing either stiffness were seen to flatten the trough immediately beneath the building, producing similar profiles to other recent work (Frischmann et al., 1994; Simpson, 1994). Manipulation of the study data provides modification factors to be applied to the horizontal strains and deflection ratios calculated assuming greenfield site conditions. The factors depend on the relative stiffnesses (axial and bending) of the building compared to the ground. While there may be difficulties in deciding on suitable values for the two moduli required. the procedure appears to be first (and only) simple design method for this problem.

Despite the large amount of literature on the subject of modelling masonry using finite elements (Liu. 1997) there are few references where an entire building is modelled using a complex model for masonry. Mensah-Dwumah (1984) describes a finite element model of a full-size building subjected to the surface settlement profile predicted for a tunnel using the semi-empirical method. The material model used for masonry is an elasto-plastic one with a tension cut-off. calibrated against a set of laboratory tests on small panels of brickwork. The main finding of the study is that existing methods of damage prediction overestimate the ability of the building to sustain damage. This is ascribed to the insufficient attention paid to the effect of lateral strains. The same conclusion is reached by Boscardin (1980) without using a complex model for masonry.

2.4 Summary

No closed form methods exist which adequately model tunnelling. In contrast. numerical techniques have achieved some success despite some difficulties with material models although little work exists which either attempts to model three-dimensional effects or the presence of a building. The major deficiency in the closed form approaches and many of the numerical ones. is that they account only for the components of settlement arising from stress relaxation and unloading. They neglect the more important component arising from the volume loss over the tunnelling shield (tail loss).

While there are few studies which attempt to include surface structures in the analysis of this problem, the importance of doing so is clearly recognised. The studies which do exist mainly relate to particular schemes and buildings and provide little guidance for other site layouts.

CHAPTER THREE

COMPOSITION OF NUMERICAL MODEL

3.1 Introduction

The numerical model developed and demonstrated in this thesis uses the finite element method. Special techniques are employed to simulate processes such as excavation, lining installation and volume loss. In developing the model it is necessary to ensure that each technique used is correct and that they are mutually compatible. This is achieved by testing and validation using existing solutions, some of which is described in later chapters. Previous research using numerical modelling, as described in Chapter 2, has provided guidance in the choices outlined below.

The general arrangement of the numerical model is shown in Figure 3.1 for two- and three-dimensional cases. Analyses with or without a surface structure are possible, both to demonstrate the validity of the model against greenfield site predictions and to show the effects of the structure. Excavation, lining installation and volume loss are simulated coincidentally. The model allows the user to control the sequence of excavation, the amount of volume loss and the properties of the materials used for the ground, structure and tunnel lining.

As already stated, the development of the entire model, including a building, is a joint effort. In particular, the masonry material model, used in the building, is the subject

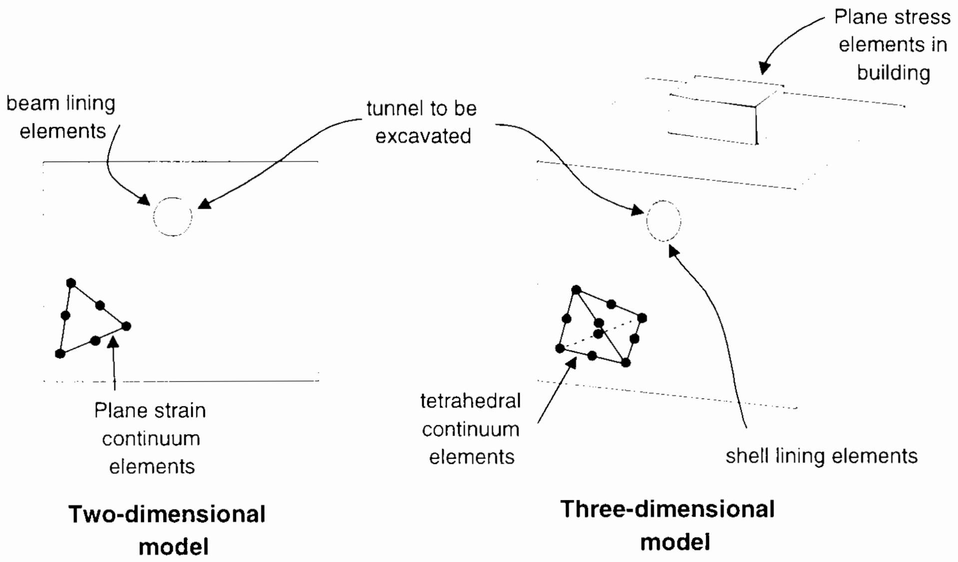

Figure 3.1: **General arrangement of numerical model**

of a contemporary thesis (Liu, 1997) and is not described here in detail. The features chosen for the model are now described and explained.

3.2 The choice of numerical technique

As demonstrated in Chapter 2, previous work using numerical models has almost wholly used the finite element method and it is adopted here. Other possible numerical methods are finite difference and boundary element techniques. The finite difference method is similar to the finite element method, indeed it can be shown that the two methods are the same in some situations (Zienkiewicz and Morgan, 1983), but it is best suited for problems where the domain consists of a single material, such as in fluid flow problems. The boundary element method involves approximation of behaviour using trial functions at the boundaries of the problem domain only.

Both techniques are inferior to the finite element method for this problem. Finite difference techniques cannot easily model structures comprised of parts with different properties, which is the case with the tunnelling model. The boundary element method requires development of analytical solutions linking stresses inside the domain to the displacements on the boundary. In the model, this would require solutions accounting for interaction between ground and lining, and between ground and building and would clearly be mathematically complex. Boundary elements have been employed in the numerical modelling of tunnelling but no published work exists, to the author's knowledge, where a surface structure is included. Another, more practical reason for the choice of the finite element method is the availability of an existing finite element program (*OXFEM*), which could be developed to fulfill the needs of the tunnelling model.

The main computational task in the finite element method is the solution for the displacements $\boldsymbol{d}$ at nodal degrees of freedom of,

$$\boldsymbol{K}\boldsymbol{d} = \boldsymbol{f} \tag{3.1}$$

where $\boldsymbol{K}$ is the structure stiffness matrix and $\boldsymbol{f}$ the force vector. A frontal solver (Irons and Ahmad, 1980) is used in *OXFEM* to obtain this solution. This is a form of Gaussian elimination with additional procedures to reduce the number of arithmetic operations and the storage requirements. The solver loops over all the elements in the order defined in a list L_i. For each element, the terms of the stiffness matrix are calculated and added to a front matrix $\boldsymbol{M}_f$ of terms for the active degrees of freedom. That is, degrees of freedom which have appeared in previous elements but which are still not complete; terms are still required from elements appearing later in L_i. When all terms for a degree of freedom have been collected, the terms are stored separately for later back-substitution. The location of these terms in $\boldsymbol{M}_f$ is then overwritten by terms for the next degree of freedom which becomes active, thus optimising storage for $\boldsymbol{M}_f$. The maximum size the front matrix, $\boldsymbol{M}_f$ reaches during an analysis can be minimised by reordering of L_i using, for example, the algorithm devised by Sloan and Randolph (1983). The optimisation also reduces the number of mathematical operations to reach the solution. The former effect is important for the three-dimensional model where storage during solution of Equation 3.1 is the main influence on analysis time. Optimisation using Sloan's algorithm is available using either an in-house package or the commercial package *I-DEAS*.

For non-linear materials, $\boldsymbol{K}$ becomes dependent on the current stresses. Solution in *OXFEM* uses the Modified Euler Scheme (Burd, 1986) where the loading is applied over a number of small steps. In this respect it is an incremental solution scheme as opposed to an iterative one, such as the Newton-Raphson Method. At each step, Equation 3.1 is solved using $\boldsymbol{K}$, based on the current stresses. The nodal forces which are in equilibrium with the current stresses can then be determined. The forces are then subtracted from the original force vector to give a residual which is applied as a correction in the next load step.

3.3 Element formulations

The elements chosen here for the ground are the six-noded triangle and the ten-noded tetrahedron for the two- and the three-dimensional cases respectively. Isoparametric formulations are used to permit curved element edges in the model. The most important reason for this choice, rather than quadrilateral and cube elements, lies in the need to model incompressible material behaviour. Additional kinematic constraints are imposed by incompressibility which can cause the mesh to lock, or give an over-stiff response. The number of constraints per element depends on the shape functions used to interpolate displacement in the element and on the numerical integration rule used

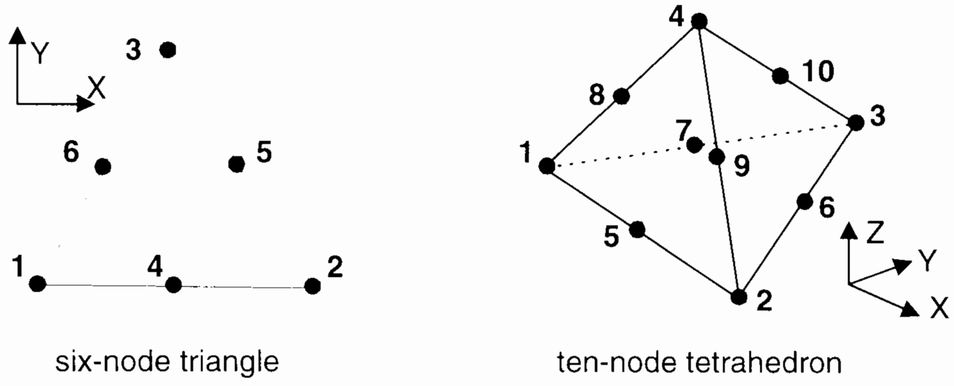

Figure 3.2: **Continuum elements used to model the ground**

to solve the finite element equations (Sloan and Randolph, 1982). The type of element and the mesh topology determine whether mesh locking will affect the solution. Previous studies (Sloan and Randolph, 1982; Bell et al., 1993) of idealised refined meshes and numerical test problems have shown that some two-dimensional elements (notably quadrilaterals) are unsuitable for plane strain analyses using incompressible material where exact integration is used. In three-dimensions, under similar conditions, the ten-noded tetrahedron is found to be just suitable whereas cube elements of comparable order are not. The problem of locking can also be dealt with by other techniques such as reduced integration and mixed formulations (Cook, 1981).

A second reason for the choice of elements is linked to mesh refinement. One way of reducing solution time is to reduce the number of elements in the mesh by refinement and extensive use of this technique is made for the three-dimensional models demonstrated in this thesis. It is also generally accepted that less element distortion is needed in meshes of triangular elements than in a mesh of the same number of quadrilateral elements, unless a regular domain is being modelled. Less distortion then leads to greater accuracy in the finite element solution. The same can be said of the three-dimensional choice.

A final consideration is efficiency: will solution times using the elements be reasonable? Solution time for a mesh depends partly on the number of elements present and partly on the individual element complexity. In the models described in this thesis, the elements chosen have been of the lowest order suitable to model incompressible material. Mesh generation has been constrained to produce elements with as little distortion as possible leading to meshes with many, low order elements. An alternative would be to adopt high order elements and produce low density meshes of distorted elements, to follow the required geometry. As elements for the linings and building are included in the model, it is also preferable to adopt simple elements for the ground to make joining different element types easier.

The tunnel lining is a shell, i.e. a thin three-dimensional structure with membrane and bending stiffness. Various approaches exist to model shells using finite elements. In this work, a novel shell element having only translational degrees of freedom is used. An alternative is to use thin continuum elements. More discussion of this topic is given in Chapters 5 and 6.

3.4 Material models for the ground

As highlighted in the review of previous work in Chapter 2, the choice of the material model for the ground is of considerable importance in the success of any numerical model of tunnelling. As specified in the research objectives in Chapter 1, this study is limited to the modelling of tunnel construction in clay, assuming undrained behaviour. Two material models are employed in the analyses described in Chapter 8. Both models represent a normally consolidated clay soil but the second models the rapid decrease in stiffness at very small strain levels, known to be an important feature of

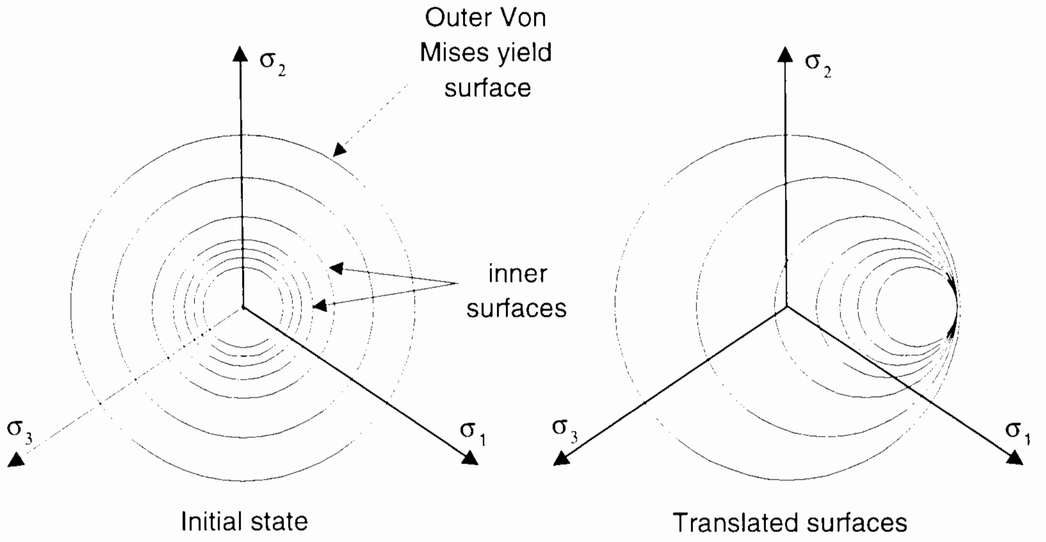

Figure 3.3: **Nested yield surfaces material model**

overconsolidated clay behaviour, as discussed in Section 2.3.1.

The first model is linear elasticity with increasing stiffness with depth from the ground surface. Shear modulus G at depth z is

$$G = G_0 + \omega z \tag{3.2}$$

where G_0 is the shear modulus at the surface and ω is a positive constant. Chow (1994) shows this model to produce reasonable results for two-dimensional unlined tunnelling analyses. It is accepted that this material model cannot represent the soil behaviour around the tunnel, for the reasons discussed in Section 2.3.1. However, its value is that results can be obtained quickly with which to compare to the more complex second material model.

The second material model is an elasto-plastic formulation which uses kinematic hardening to model rapidly decreasing stiffness, from a high initial level, over a small range of strain at low strain levels (Houlsby, 1994). Non-linearity of the small-strain response is achieved using a number of nested surfaces of the same shape as the von Mises failure criterion which translate as the stress state changes. An outer von Mises failure surface surrounds these surfaces to model perfect plastic behaviour with no work hardening. Figure 3.3 shows the initial arrangement of these surfaces, plotted in principal stress space and their re-arrangement following changes in stress. The configuration of the inner surfaces can be different for a given state of stress, representing the stress history of the material. The material is defined with the following properties,

- shear modulus, G at very small strain; when operating inside the first nested surface,
- bulk modulus, K where, from elasticity,

  $$K = \frac{G(1+\nu)}{3(1-2\nu)} \tag{3.3}$$

  (taking Poisson's ratio, $\nu = 0.49$, for incompressible material, gives $K \approx 50G$)
- undrained shear strength, s_u.

The nested surfaces are defined with two non-dimensional parameters each,

- a hardening parameter, $h'_\alpha = h_\alpha / G$ representing the change in stiffness as the yield surface is mobilised and
- an intermediate yield strength $c'_\alpha = c_\alpha / c$ representing the radius of the yield surface where

  $$c = \frac{2}{\sqrt{3}} s_u \tag{3.4}$$

  from the von Mises failure criterion.

These parameters are easier to understand if the stress-strain behaviour is plotted, as shown in Figure 3.4. In the first subfigure, the shear stiffness progressively reduces as each surface is activated. The second subfigure shows the characteristic S-shaped

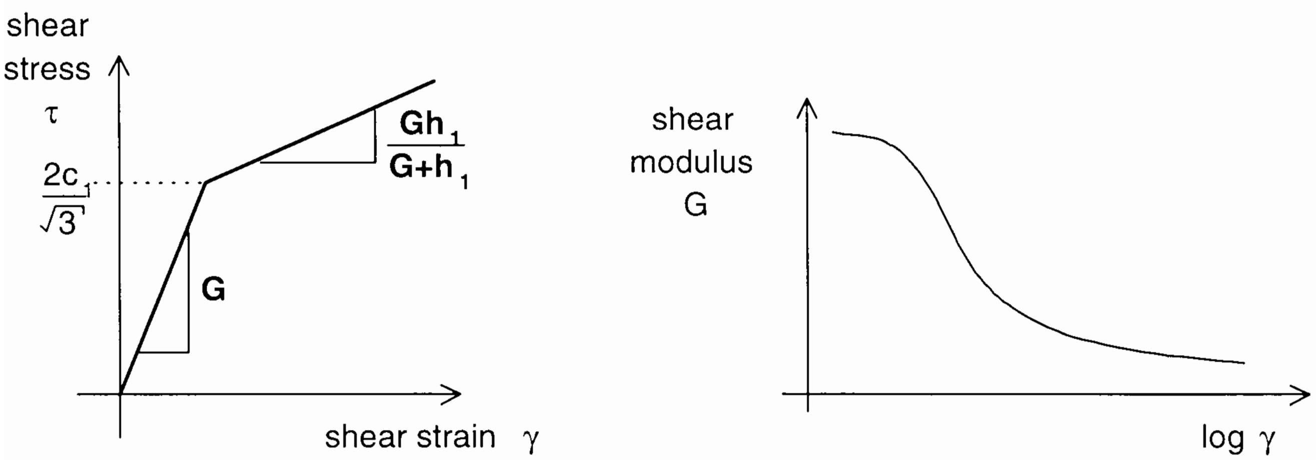

Figure 3.4: **Variations in shear modulus, G in the nested yield surface model**

curve as shear modulus decreases sharply from a high level at low strain. In addition both the base stiffness and undrained strength increase with depth from the ground surface. A full validation of the implementation of this model in *OXFEM* is described in Chow (1994).

3.5 Mesh generation

Mesh refinement is mentioned above (Section 3.3) in the discussion of element choices. Consideration is now given to how suitable refined meshes may be generated for the model. Creation of a mesh consists of defining node locations and then associating nodes with elements. Meshes for finite element analyses may be divided into two classes: structured and unstructured. In the former, the positions of all element nodes can be described by a simple mathematical relation. A uniform mesh (Figure 3.5(a)), where all elements are the same size and nodes lie on a uniform grid, is the simplest type of structured mesh. Refinement is possible with structured meshes, as Figure 3.5(b) shows but unstructured meshing usually permits more versatile refinement, as indicated in Figure 3.5(c). Generation of structured meshes is straightforward once a

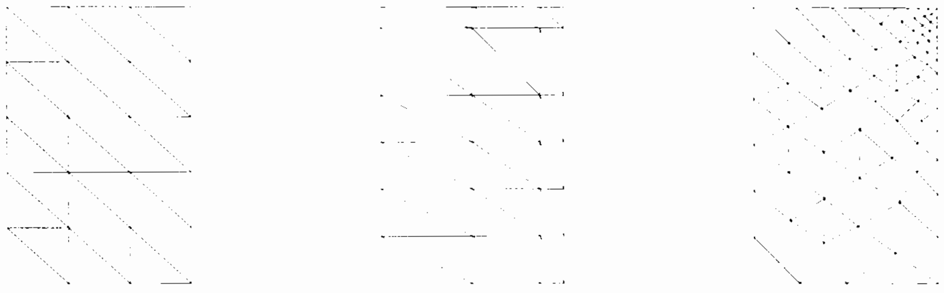

(a) Uniform mesh (b) Structured mesh (c) Unstructured mesh

Figure 3.5: **Types of meshes**

basic pattern has been defined. Unstructured meshing is usually much more difficult and in three-dimensions is a major computational task. Considerable research effort has been expended in recent years on algorithms for three-dimensional mesh generation as indicated by Augarde (1993). Since the objective of the project is the development of a three-dimensional model, it is important that unstructured mesh generation be used as this will give better refinement for a given number of elements than possible using structured meshing. This will lead to efficient meshes and reduced solution times. The development of software to accomplish this task would, in itself, form another research project so a commercial package (*I-DEAS*) and a package developed in-house (*OXMESH*) are used. Previous examples of the use of *I-DEAS* to generate efficient meshes for similar geotechnical problems are given in Grabinsky and Curran (1993).

I-DEAS is a solid modelling package with excellent graphics facilities and some finite element analysis capabilities. Most importantly, it provides three-dimensional meshing using a range of solid elements, both tetrahedral and cuboid. In *I-DEAS*, meshes are defined with a parameter α for the domain representing a desired element side length. Refinement can be achieved either by splitting the domain into regions and assigning each a different value of α or by the definition of values of α at particular points in the domain. Figure 3.6 shows stages of mesh refinement for a three-dimensional domain

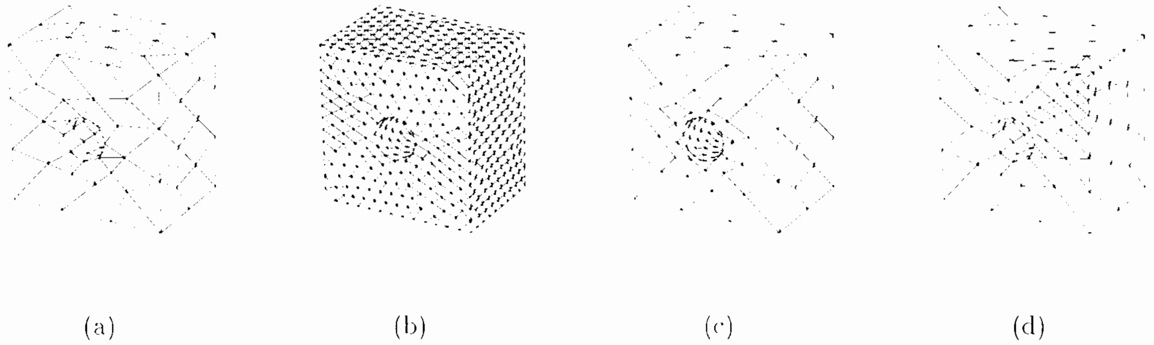

Figure 3.6: **Stages of mesh refinement**

(10m wide by 10m high by 5m deep) with a central hole of diameter 2.5m. A mesh of 669 elements, generated using $\alpha = 3.0m$, is shown in Figure 3.6(a). A much denser mesh, of 12561 elements, is obtained by setting $\alpha = 0.75m$ (Figure 3.6(b)). In Figures 3.6(c) and 3.6(d), α for the domain reverts to $3.0m$ but values of α of $0.75m$ are specified around the hole and at one corner respectively leading to meshes with 1462 and 1028 elements. Further discussion of the role of *I-DEAS* in the analysis procedure for this numerical model is made in Section 7.2.2 but it should be noted that none of the finite element analysis capabilities of this package are used in the model.

3.6 Tunnel installation

Previous research has recognised that the most important processes in tunnelling, when considering surface settlements, are the volume loss and the lining installation. All of the other processes involved in constructing a tunnel, which vary according to the method adopted, usually have little influence. The same philosophy is adopted in this model.

The model most closely matches tunnelling using an open face shield with a segmental precast concrete lining. The procedure of operations to construct a tunnel under these

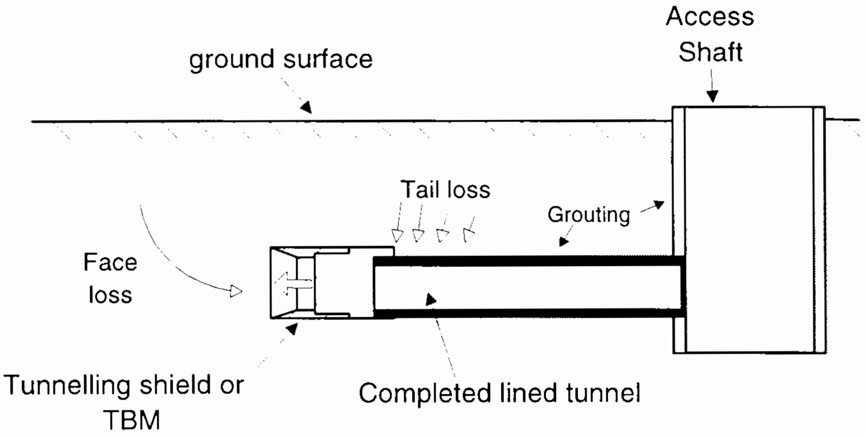

Figure 3.7: **Real tunnelling processes simulated in the model**

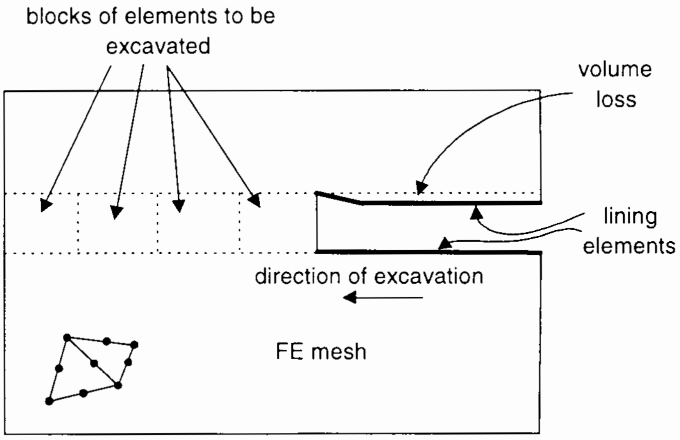

Figure 3.8: **Numerical modelling of tunnel installation**

conditions is shown in Figure 3.7. The ground ahead of the shield is excavated allowing the shield to be jacked forwards off the completed lining. A ring of tunnel lining is then constructed inside the tail of the shield. Grout is pumped into the void behind the lining, either immediately or after a set number of rings have been finished. Tail loss occurs in the period from excavation to hardening of the grout.

In the numerical model the procedure described above is idealised, as shown in Figure 3.8. Elements modelling a thin tunnel lining are activated at the same time that excavation is simulated of a block of elements inside the tunnel volume. The lining elements are then shrunk uniformly to model the tail loss. No restraint to the tunnel face is provided, allowing face loss to occur. Excavation is modelled by the application of loads to the mesh and the removal of the stiffness of elements within a predefined tunnel outline. The loads are calculated using a procedure given by Brown and Booker (1985). Full details are given in Chapter 4 which is devoted to excavation.

As mentioned above, shell elements are used for the tunnel lining in the three-dimensional model. When activated they are fixed to the surrounding ground. Shrinking is achieved by the application of loads as described in Section 6.4. Modelling the volume loss in this way may be regarded as somewhat crude. However, the global displacements of the liner element nodes are not determined and the liner is not fixed in space. The method only defines a change in the enclosed volume of the liner. The procedure is simple to implement in two- and three-dimensions and does not require the use of complex interface elements.

One technique which is a reasonable alternative to the method proposed to model volume loss is that used in Potts and Addenbrooke (1996) where lining elements are activated once the excavated ground has converged to a pre-defined point where it comes into contact with the lining.

It is demonstrated, in the first closed form solution in Section 2.2.1, that the unloading of the ground due to excavation is of secondary importance to the tail loss in surface settlements. For this reason, the weight of the tunnel lining and the shield are ignored. Both are small in comparison to the weight of soil excavated. The forces generated in the ground from the jacking forwards of the shield are likely to be confined to a small area around the shield and will be greatest along the tunnel axis. In practice they will also be reduced due to lubrication of the outer surface of the shield. They are therefore not likely to influence the settlement response and are ignored here.

Another simplification of the installation process is the absence, in the model, of vertical

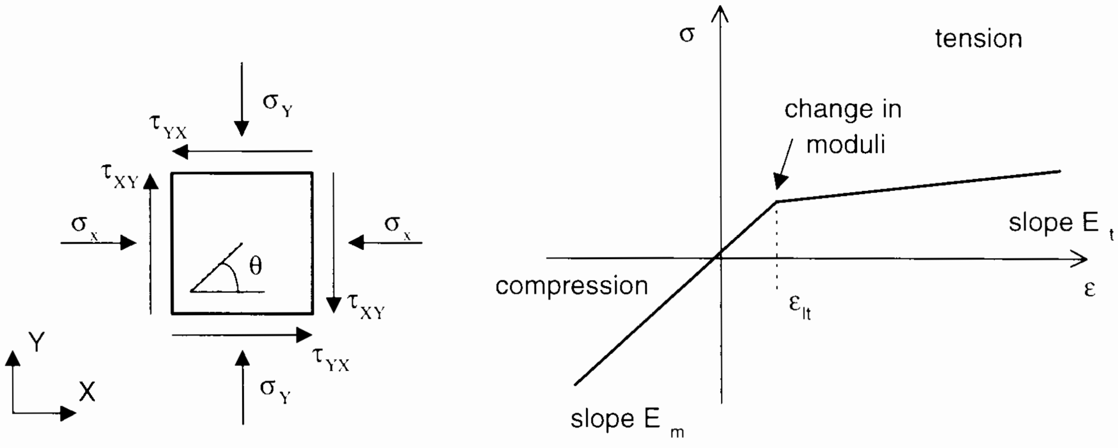

(a) cracked masonry material (after Burd et al., (1994))

(b) simplified stress-strain relation for masonry material

Figure 3.9: **Cracked masonry material (after Burd et al. (1994))**

shafts providing access to the tunnel. It is clear that the presence of vertical excavations would change the settlement profiles resulting from the tunnel construction. The model developed here can therefore be considered representative of tunnels away from shafts.

The procedure to model excavation is described in detail in Chapter 4 while Chapters 5 and 6 describe elements to represent tunnel linings.

3.7 Masonry modelling

The structures of interest in this study are existing masonry (i.e. stone or brick) buildings. Masonry is characterised by its high compressive strength and its propensity to crack under low tensile stress. The material model adopted here for masonry elements is linear elasticity with infinite strength in compression. This is reasonable since compressive failure (i.e. crushing) is rarely a problem when considering the effects of tunnelling settlements. In tension the material is assumed to have a very low limiting strength at which cracks form. Figure 3.9(a) shows an element of this material subjected to normal and shear stresses under plane stress conditions. Once one principal stress becomes greater than the limiting tensile stress σ_{lt}, cracking is simulated at an angle θ, perpendicular to the direction of this stress, by amending the material stiffness matrix, $\boldsymbol{D}$ to remove any resistance normal to the crack direction. The model is close to "elastic no-tension" but, for numerical stability, the material has a small tensile strength and tensile stiffness. The change in stiffness as stress moves from compressive to tensile is not abrupt, again for reasons of numerical stability. The reduction of Young's moduli is shown in Figure 3.9(b); the tensile modulus, E_t is not attained until the limiting tensile direct strain ϵ_{lt} is reached. The detailed formulation and verification of this material model is given by Liu (1997).

3.8 Summary

A complex numerical model is required to simulate the construction of a tunnel in the presence of a surface structure. A balance must be drawn between accuracy and practicality in all decisions relating to components of this model . The model developed is comprised of components which are of complementary complexity: overemphasis on detail for one part of the model has been avoided. It can be criticised as being too simplistic in places but the need to model in three-dimensions and obtain results in a reasonable amount of time has motivated the development and justifies this approach.

CHAPTER FOUR

EXCAVATION MODELLING

4.1 Introduction

The first component of the numerical model to be examined in detail is excavation. When a tunnel is excavated, unloading and stiffness reduction occur simultaneously. The first results from removal of material having self-weight. The second occurs because the ground structure is altered. The processes are coupled, with the effects of unloading dictated in part by the change in stiffness of the ground. To model the first of these processes, loads are applied to the mesh remaining after excavation. The second process is modelled by excluding the stiffness of each element excavated from the calculation of structure stiffness.

A formulation for excavation loading was selected from the literature and implemented into the analysis program *OXFEM*. The amendments required to the structure stiffness were devised for the particular analysis procedure and then added to *OXFEM*. To validate the formulation, a number of test problems were modelled and the results compared to analytical solutions.

4.2 Formulation for excavation

Ideally, excavation in the model should be a continuous process, to match excavation of a real tunnel. Aubry and Modaressi (1989) develop a general analytical basis for solution of problems where the domain is continuously changing size over time, as in excavation, although it is rather complex and its numerical implementation is unclear. Since the finite element technique discretises the problem domain into individual elements, it is reasonable to simulate excavation in a number of discrete steps involving the removal of groups of elements. The accuracy of the simulation then depends on the number of separate steps used to excavate a given length of tunnel.

The first component of excavation requires the calculation of nodal loads equivalent to the self-weight, or body force, associated with the volume of material represented by each element. In calculating these loads in finite element problems the unit weight γ is usually assumed constant although the components in different coordinate directions may differ so that,

$$\gamma^T = \{\gamma_x, \gamma_y, \gamma_z\} \tag{4.1}$$

The nodal forces $\boldsymbol{F}_g$ due to self-weight are calculated from,

$$\boldsymbol{F}_g = \int_V \boldsymbol{N}^T \gamma \, dV \tag{4.2}$$

where $\boldsymbol{N}$ is the matrix of element shape functions. In the isoparametric formulation integrals over the element volume are calculated for the parent element defined in local coordinates (ξ, η, ζ). The body force equation then becomes,

$$\boldsymbol{F}_g = \int_{V_l} \boldsymbol{N}^T \gamma \det \boldsymbol{J} \, dV_l \tag{4.3}$$

where V_l is the volume of the parent element. The Jacobian $\det \boldsymbol{J}$ in Equation 4.3 accounts for the scaling of the integration to the local coordinates and is a matrix of products of nodal coordinates and shape function derivatives (Cook, 1981).

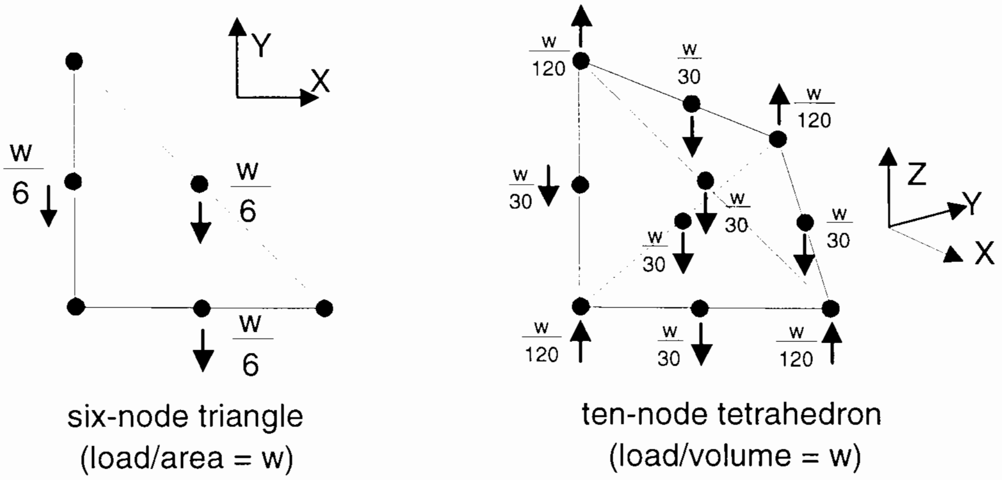

Figure 4.1: **Nodal loads equivalent to body forces**

In this numerical model, γ_z is the only non-zero component of $\boldsymbol{\gamma}$. The nodal forces calculated from Equation 4.2 for the undistorted forms of the elements (i.e. with unit length sides along axes) used to model the ground in this thesis are shown in Figure 4.1.

An additional complication arises because plane stress elements are included to model building facades. These elements are defined in local two-dimensional coordinate systems referring to each facade separately. The facades of elements are tied to each other and to the (three-dimensional) ground using special tie elements (Liu, 1997). Although parts of the building were not excavated in the analyses described in this thesis, their body force is included and was calculated using the area integral form of Equation 4.2.

The above deals with the calculation of body forces in finite elements. The forces to be applied to the mesh to model excavation are now discussed. In the past, various methods have been used to calculate the applied nodal forces which are equivalent to excavation (Chandrasekaran and King, 1974; Gioda and De Donato, 1979; Medeiros et al., 1982; Swoboda et al., 1989; Chow, 1994). Firstly, the loads $\boldsymbol{f}_i$ associated with nodes on the tunnel periphery, equivalent to the internal stresses $\boldsymbol{\sigma}_i$ are calculated using

$$\boldsymbol{f}_i = \int_V \boldsymbol{B}^T \boldsymbol{\sigma}_i dV \tag{4.4}$$

where V is the volume of the complete, unexcavated mesh and $\boldsymbol{B}$ is the strain-displacement matrix. The excavation loading is then taken to be $\boldsymbol{f}_i$ applied in reverse setting the nodal forces on the tunnel periphery to zero. This method overestimates the excavation load as it neglects the body forces and surface tractions associated with the remaining elements, i.e. those still present after excavation has taken place. Although it is correct to say that an excavated unlined (i.e. unsupported) face or edge in a finite element mesh is free of surface tractions, where self-weight is present there will be nodal loads representing the body forces of unexcavated ground.

The following procedure, derived from Brown and Booker (1985), gives the correct nodal loads and ensures equilibrium at each stage of excavation. An initial mesh volume, V_0 of linear elastic soil is considered. Excavation reduces this to a new volume, V_1. No loading other than that arising from the material self-weight is considered. For the initial volume V_0 , displacements $\boldsymbol{d}_0$ can be obtained from the standard finite element equation:

$$\boldsymbol{K}_0\boldsymbol{d}_0 - \boldsymbol{f}_0 = 0 \tag{4.5}$$

where is $\boldsymbol{K}_0$ the structure stiffness matrix and $\boldsymbol{f}_0$ is the applied force vector. For the case of body forces only, the force vector is calculated from Equation 4.2 above.

The stresses $\boldsymbol{\sigma}_0$ resulting from the effects of these body forces can be calculated from

$$\boldsymbol{\sigma}_0 = \boldsymbol{D}\boldsymbol{B}\boldsymbol{d}_0 \tag{4.6}$$

where $\boldsymbol{D}$ is the material stiffness matrix (linking stresses to strains) in standard finite element notation. Now consider the excavation to volume V_1 : the final displacement vector $\boldsymbol{d}_{end}$ of the nodes in the mesh volume is,

$$\boldsymbol{d}_{end} = \boldsymbol{d}_0 + \boldsymbol{d}_{exc} \tag{4.7}$$

where $\boldsymbol{d}_{exc}$ is the vector of incremental displacements occurring during the excavation. The finite element method leads to the solution of.

$$\boldsymbol{K}_1\left(\boldsymbol{d}_0+\boldsymbol{d}_{exc}\right)=\int_{V_1}\boldsymbol{N}^T\gamma dV \tag{4.8}$$

where $\boldsymbol{K}_1$ is the structure stiffness matrix for the new volume (i.e. neglecting the elements removed in the excavation). Then.

$$\begin{aligned}
\boldsymbol{K}_1\boldsymbol{d}_{exc} &= \int_{V_1}\boldsymbol{N}^T\gamma dV-\boldsymbol{K}_1\boldsymbol{d}_0 && (4.9)\\
&= \int_{V_1}\boldsymbol{N}^T\gamma dV-\int_{V_1}\boldsymbol{B}^T\boldsymbol{D}\boldsymbol{B}\boldsymbol{d}_0 dV && (4.10)\\
&= \int_{V_1}\boldsymbol{N}^T\gamma dV-\int_{V_1}\boldsymbol{B}^T\boldsymbol{\sigma}_0 dV && (4.11)
\end{aligned}$$

Therefore, the correct incremental displacements are found by applying loading comprising one term representing the body forces on the new volume less an internal loading term associated with the stresses obtained for the unexcavated mesh. Adjacent to the excavation the incremental loads are non-zero while away from the excavation the internal and external load terms cancel. This derivation assumes linear elasticity in the use of Equation 4.6 but the result is also applicable to non-linear materials. If the two terms in Equation 4.11 are considered, it can be seen that the first is the current loading due to self-weight in the mesh which is calculated in the same way for all materials. The second term is the nodal force vector equivalent to the current stresses which have been calculated for the non-linear material model in particular. The difference between the two terms is an out-of-balance force remaining at the start of the new load step equivalent to the loading effect of excavation.

4.3 Amendment of structure stiffness

The second of the two processes noted in Section 4.1 is the alteration of the structure stiffness during excavation. The element order list L_i required by the frontal solution method (see Section 3.2) is used to indicate elements that have been excavated. As L_i is traversed, another list L_a is consulted to determine when all terms have been collected for a given degree of freedom. List L_a gives, for each node in the mesh, the location in L_i when all stiffness terms for the degrees of freedom at that node have been obtained.

At each stage of excavation, lists L_i and L_a are revised. Entries in the first list for elements excavated that stage are turned negative. This avoids changing the size of the list and makes it easier to reintroduce those elements at a later stage, if required. The second list is fully revised using the updated L_i, stepping over any elements found to have negative entries. The element stiffness matrices are not stored but are calculated at each load step. Therefore, excavated elements do not disappear but are just ignored. Stresses and strains calculated in previous steps for excavated elements are zeroed to avoid confusion in intermediate output data.

Instead of ignoring the stiffness of excavated elements their stiffness and strength can be revised to very low values as is the case in the study by Comodromos et al. (1990). Desai (1977) claims this may cause problems with large deflections for the nodes in the excavated area and the mesh should really be reformed without the excavated elements. This approach appears to add unnecessary complication and is not adopted here.

During excavation, some nodes may become disconnected from any active element. It is necessary to identify these *dead* nodes so that their associated degrees of freedom are also excluded from the frontal solution procedure. Back-substitution of the coefficients stored in the solver is then carried out for a reduced number of degrees of freedom. The dead nodes can be identified by the following procedure:

1. Assemble the list A of all nodes on excavated elements,
2. Assemble the list, B of all elements remaining in the mesh after excavation (i.e. the non-negative entries in list L_i)
3. For each node in A, loop over elements in B.
    - If the node is found in an element in B, remove node from A and go to next unexcavated element
4. The remaining nodes in A are connected only to excavated elements and so form the dead nodes for that stage of excavation.

4.4 Validation and examples

The procedures described above were added to the existing program *OXFEM* and then tested with the problems which follow. All meshes used in the test problems are comprised of ten-noded tetrahedral elements. This reflects the main aim of the project, the development of a three-dimensional model. Similar testing for the two-dimensional case was also carried out but is not described here.

4.4.1 Test problem 1

The first test problem tests the accuracy with which body forces are calculated and consists of a cylindrical block of isotropic linear elastic material, 20m high and 10m in diameter loaded only by its self-weight. The base of the block is free to translate in

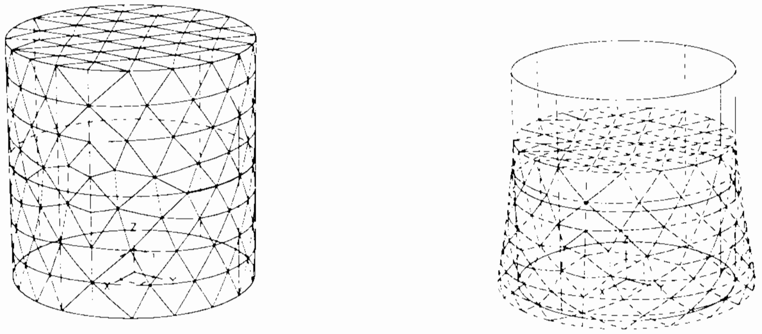

(a) Finite element mesh (b) Deformed shape for $\nu = 0.3$

Figure 4.2: **Test problem 1**

the horizontal plane but is fully fixed at its centre. All other surfaces are free. The values of Poisson's ratio ν taken for the block material are 0.0 and 0.3. An analytical solution exists for the former but for $\nu \neq 0.0$, lateral displacements will occur and the vertical displacement varies in the x, y (horizontal) plane. The analytical solution to this problem is not known and so the results are compared to those obtained from the analysis of the same mesh of identical elements in the commercial package *I-DEAS*.

The analytical solution for vertical displacement w of any point in the block at an elevation z above the base for Poisson's ratio $\nu = 0.0$ can be obtained from simple statics as,

$$w = \frac{\gamma l^2}{2E}\left(2\left(\frac{z}{l}\right) - \left(\frac{z}{l}\right)^2\right) \tag{4.12}$$

where γ is the unit weight of the material and l is the height of the block. The finite element mesh is shown in Figure 4.2(a) and consists of 1653 elements and 2693 nodes. The shear modulus assigned to the material is 400 kPa and its unit weight is 10 kN/m^3. Displacements for all nodes in the mesh for the first case, with $\nu = 0.0$, are plotted in Figure 4.3. The error, e in the finite element solution, calculated from the analytical solution δ_a and numerical results δ_f as,

$$e = \frac{\|\delta_a\|\|\delta_f\|}{\|\delta_{max}\|} \times 100\% \tag{4.13}$$

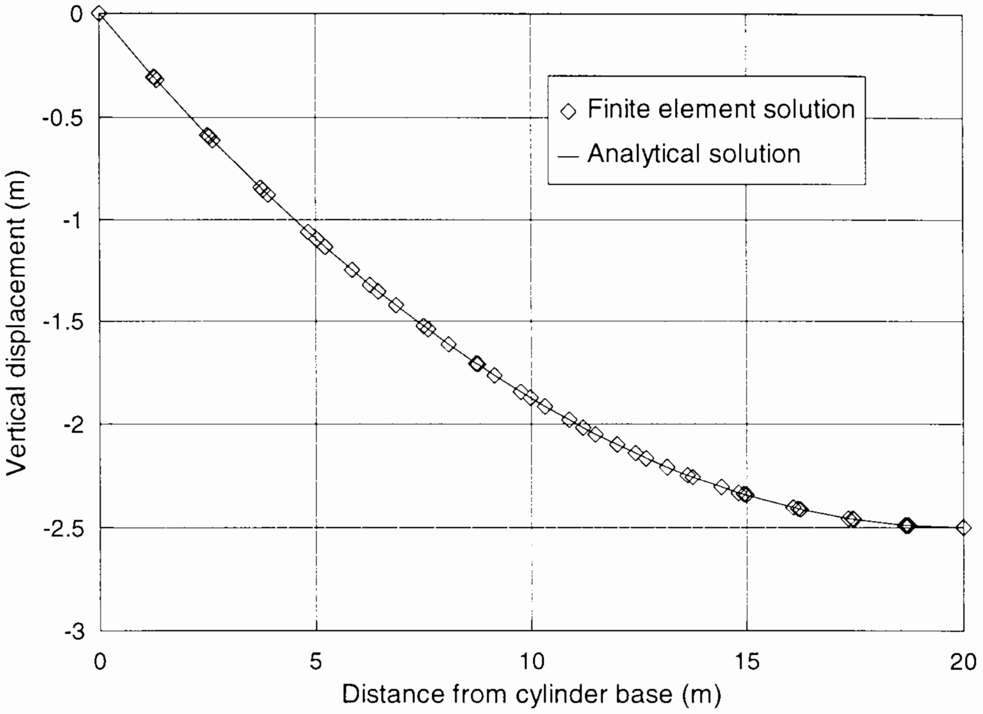

Figure 4.3: **Results for test problem 1:** $\nu = 0.0$

where δ_{max} is the maximum analytical result (at the top), was found to be less than 0.01% and the analytical solution is not shown for clarity.

With $\nu = 0.3$ the block distorts laterally as shown in Figure 4.2(b). Displacements for a central vertical plane in the block are plotted in Figure 4.4 for the analysis using *OXFEM*. Results for the same analysis carried out with *I-DEAS* are virtually identical and are not plotted for clarity. The maximum difference between the two is less than 0.01% of the largest displacement in the *I-DEAS* solution.

4.4.2 Test problem 2

This problem consists of a rectangular block of overall initial height, 20m resting on a level surface with its top face unconstrained and its base on rollers, permitting movement in the horizontal plane. Rigid body movement is prevented by additional con-

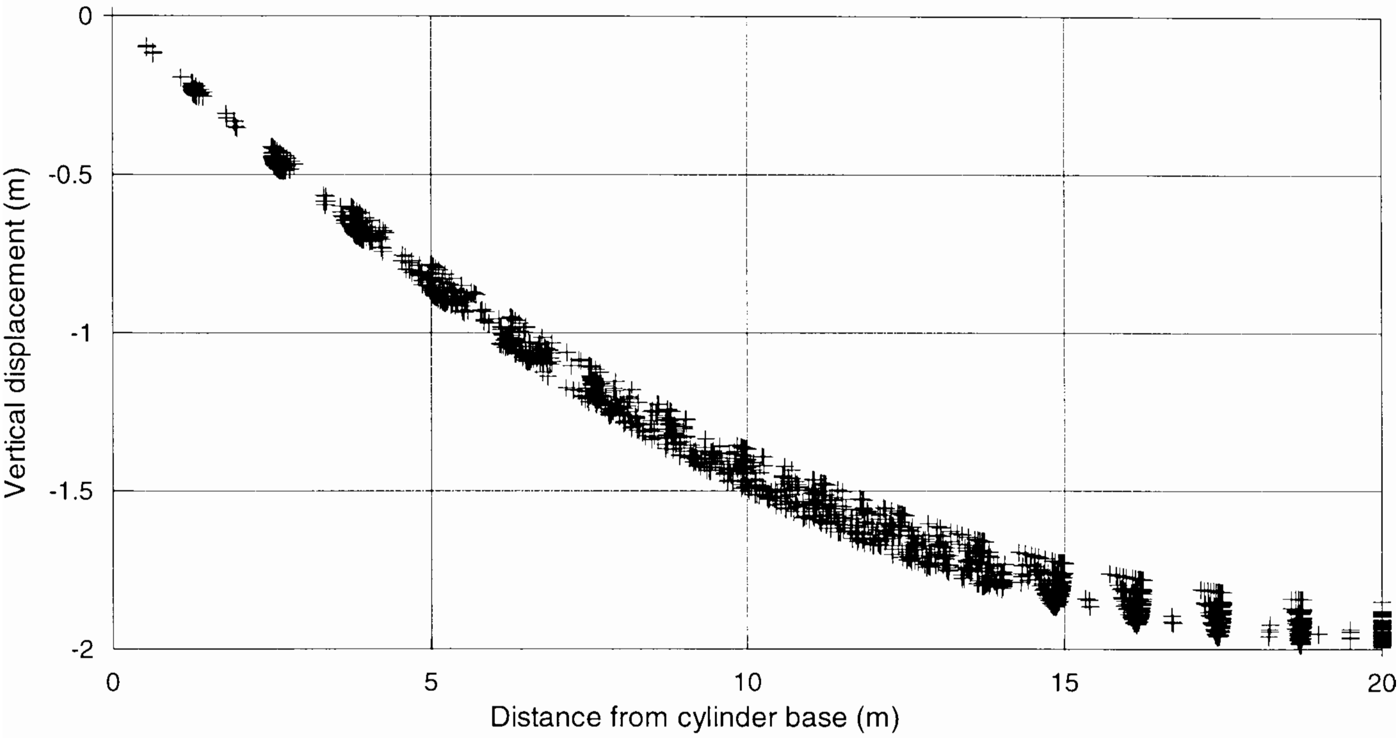

Figure 4.4: **Results for test problem 1:** $\nu = 0.3$

straints on particular base nodes. The problem models the removal of layers of material from the top of the block and thus tests unloading. Two meshes are used: a structured mesh and one with an irregular pattern of meshing in the top layers of the block. The block material in this problem has a shear modulus of 400 kPa and a unit weight of $10\,\mathrm{kN/m^3}$.

In Figure 4.5, vertical displacements of a point at the initial centroid of the block (i.e. at an elevation of 10m) are plotted for for both meshes and values of ν of 0.0 and 0.49. The first mesh is excavated in four equal stages where each layer is 2.5m thick. The second mesh is excavated to the same final level over sixteen stages in an irregular pattern. The plots are compared against the analytical solution for the displacement for each value of ν. For the removal of a layer of thickness t, simple elasticity theory gives the displacement of a point at elevation l as,

$$w = \frac{\gamma l t}{4G(1+\nu)} \tag{4.14}$$

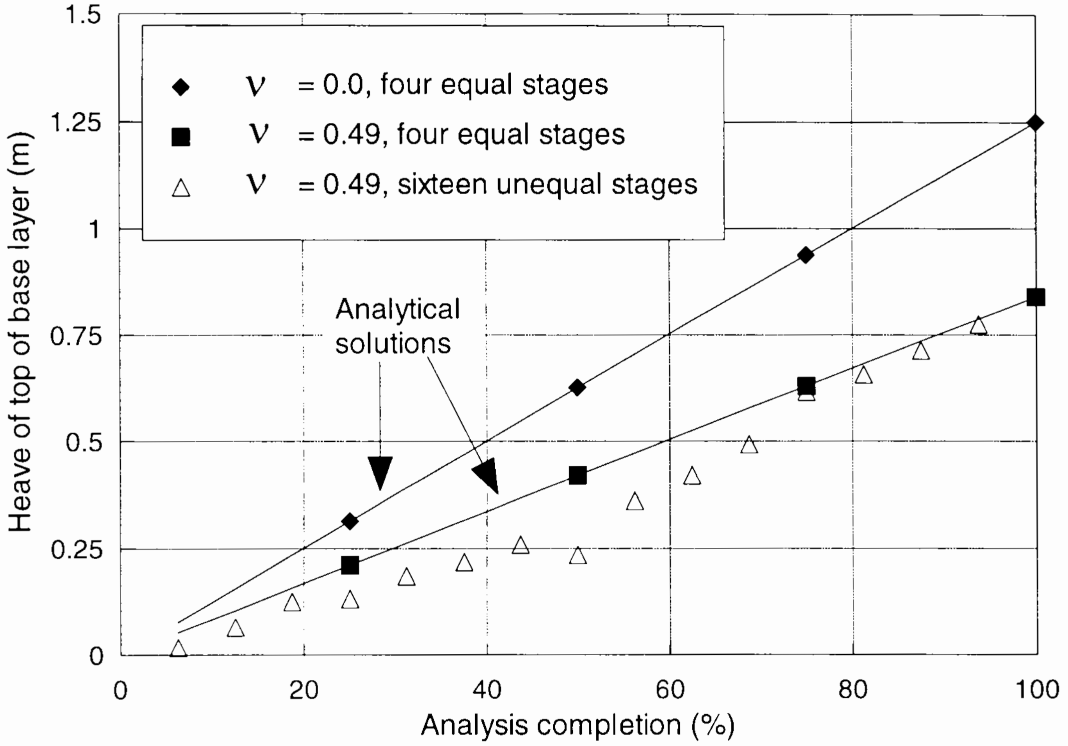

Figure 4.5: **Displacements for test problem 2**

The results show the final solution to be path independent as expected for linear elasticity. Figure 4.6 shows the deformation of the lower half of the block at each stage of excavation for the case when $\nu = 0.49$, showing the lateral deformations expected. The direct vertical stresses at integration points in the remaining elements, for each stage of excavation are plotted in Figure 4.7. The plots indicate that at each stage, the vertical stress profile is linear and increasing down the block, as expected from the remaining body forces.

4.4.3 Test problem 3

This problem involves the removal of a cylindrical volume from a prestressed cube of weightless elastic material. The cube has side lengths of 100m and the cylinder removed is full length and 5m in diameter. The finite element mesh for this problem

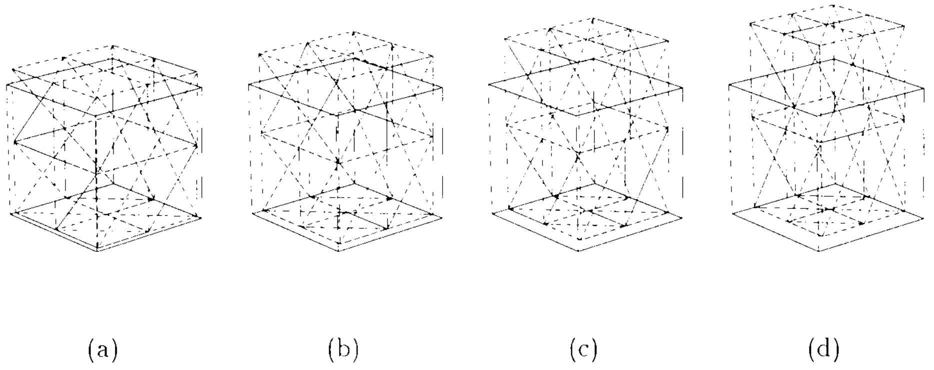
(a) (b) (c) (d)

Figure 4.6: **Test problem 2: deformation of lower half of block**

contains 3995 nodes and 2762 elements and is shown in Figure 4.8 which also shows the boundary conditions. Even with this high number of elements, it is evident that refinement around the cylinder is fairly poor. The Poisson's ratio ν for the material is 0.25. Prior to excavation, an isotropic compressive stress state is imposed of 500 kPa. in the x and z (horizontal and vertical) directions. As the material has zero unit weight the test checks the ability of the implemented excavation procedure to predict incremental stresses following the change in stiffness.

The analytical solution for the stresses in the ground following excavation is given by Pender (1980) for plane strain conditions. The incremental radial stress $\Delta\sigma_r$ due to excavation at radius r from the tunnel axis and at angle θ from the horizontal is,

$$\Delta\sigma_r = -\frac{1}{2}(\sigma_v - \sigma_h)\left(\frac{R^2}{r^2}\right) - \frac{1}{2}(\sigma_v - \sigma_h)\left(\frac{3R^4}{r^4} - \frac{4R^2}{r^2}\right)\cos 2\theta \tag{4.15}$$

where σ_v and σ_h are the vertical and horizontal stresses and R is the tunnel radius. The radial stress prior to excavation is,

$$\sigma_r = \frac{1}{2}(\sigma_v + \sigma_h) - \frac{1}{2}(\sigma_v - \sigma_h)\cos 2\theta \tag{4.16}$$

For compressive isotropic initial stresses,

$$\sigma_h = \sigma_v = -\sigma_0 \tag{4.17}$$

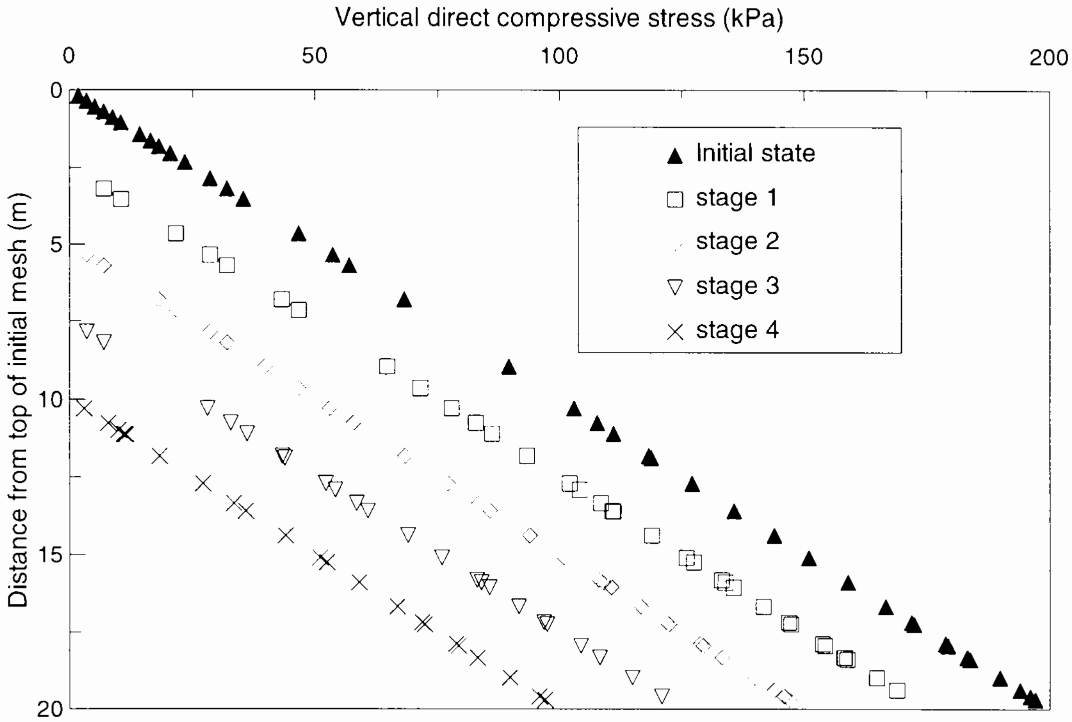

Figure 4.7: **Stress results for test problem 2**

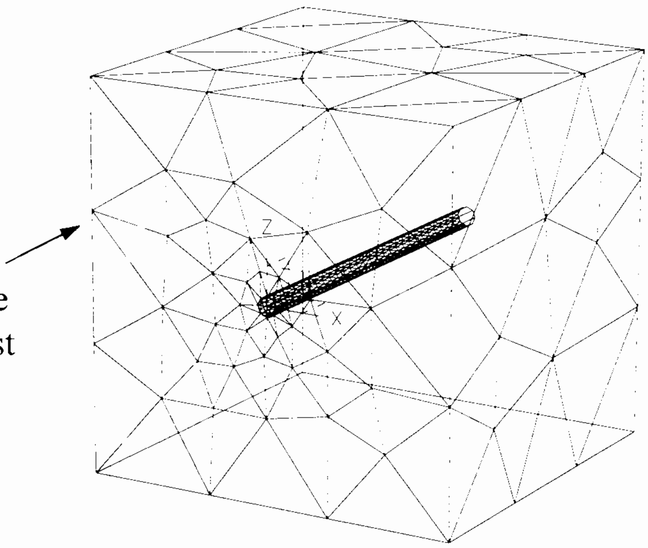

Boundary conditions:
All faces free to translate
in-plane but fixed against
normal translation

Figure 4.8: **Mesh for test problem 3**

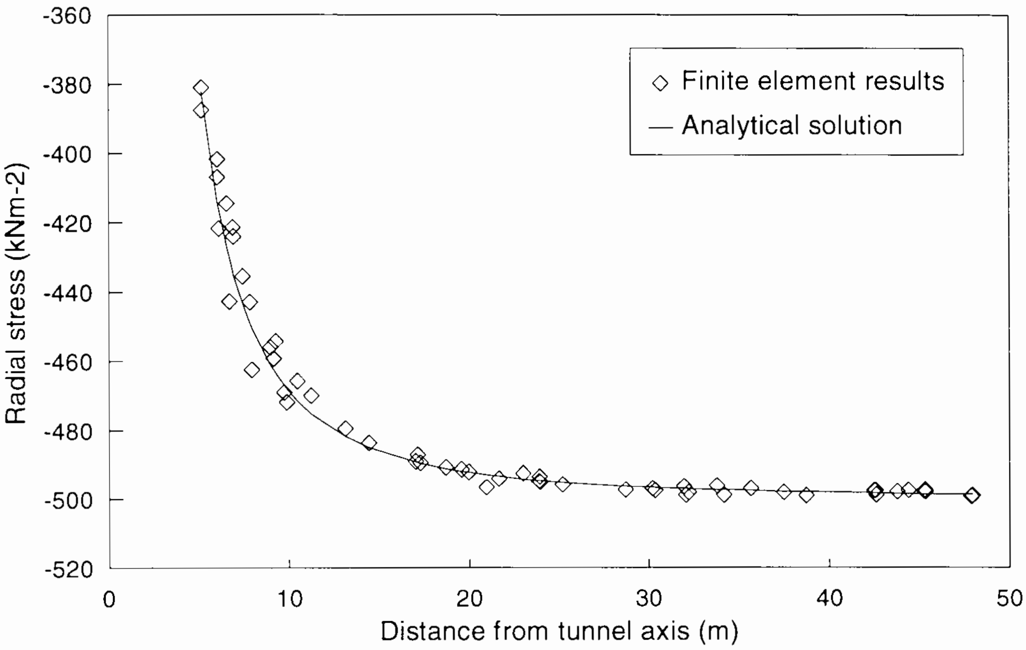

Figure 4.9: **Test problem 3: Predictions of radial stress**

therefore the radial stress after excavation is,

$$\sigma_r^e = \sigma_r + \Delta\sigma_r = -\sigma_0\left(1 - \frac{R^2}{r^2}\right) \tag{4.18}$$

Under plane strain conditions the only stress components which need be considered in the calculation of σ_r from the analysis results are $\tau_{xz}(=\tau_{hv})$, $\sigma_x(=\sigma_h)$ and $\sigma_z(=\sigma_v)$.

Figure 4.9 shows the radial stresses obtained by the above procedure from the *OXFEM* analysis for a section through the centre of the mesh, transverse to the tunnel. Comparison to the analytical solution shows that the numerical model gives a reasonable prediction of the radial stress.

CHAPTER FIVE

MODELLING LINING INSTALLATION IN TWO-DIMENSIONS

5.1 Introduction

This chapter describes the finite elements which model the tunnel lining in the two-dimensional model and how they are used to simulate volume loss. Chapter 6 repeats the process for the three-dimensional case.

A tunnel lining resists the pressure from the surrounding ground usually by a combination of membrane (i.e. stretching) and flexural (i.e. bending) stiffness. As circular tunnels are to be modelled it is natural to seek curved finite element formulations to model these effects. Continuously curved elements in two- and three-dimensions are highly complex since the membrane and flexural effects are coupled continuously throughout elements. In the models developed in this thesis, these complexities are avoided by using faceted element formulations (i.e. formulations where curved geometries are approximated using a mesh of flat elements). Membrane stiffness is provided by simple continuum elements which are overlaid by more complicated flexural elements. Coupling of membrane and flexural effects is confined to the element nodes. This approach is less accurate than the use of curved elements, due to the geometrical approximation made and to the neglect of coupling effects. The advantage is that simple element formulations are possible which give satisfactory results.

Two formulations for beam elements have been implemented: the first is formulated in the usual framework adopted for beam elements although it is unusual in that it has three, rather than two nodes. The second element is a novel overlapping formulation which has no rotational degrees of freedom.

The two-dimensional model was developed partly to validate ideas and techniques later adopted for the three-dimensional model. In particular, the unusual overlapping shell element formulation adopted to model the flexural response of the lining in the three-dimensional model was investigated using its two-dimensional counterpart, the overlapping beam element. Consequently, significant emphasis is placed in this chapter on an explanation of the overlapping formulation, on its advantages and its difficulties. Linear elastic material behaviour and small displacement theory are assumed throughout for all lining elements.

5.2 Finite elements for linings

The constituent parts of the two-dimensional lining elements are shown in Figure 5.1 for two types of beam formulation. In both, the membrane stiffness is provided by two, one-dimensional rod elements having a single axial degree of freedom at each of their two nodes. The contribution to the element stiffness matrix is calculated for the two elements in turn and combined into a single global stiffness matrix to add to the stiffness contribution from the beam elements. The derivation of the membrane stiffness follows a conventional procedure (Astley, 1992) and is given in Appendix A.

Both beam element formulations assume Bernoulli-Euler bending theory where the deformations arising from shearing are assumed to be zero. This is a reasonable as-

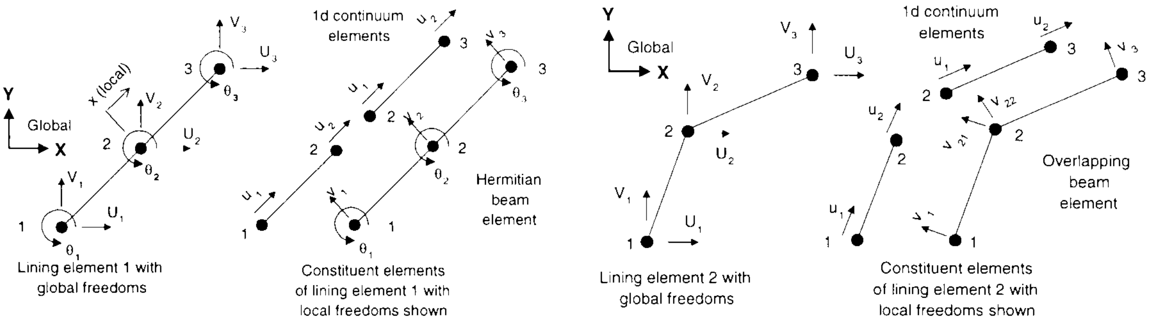

(a) Element 1 (b) Element 2

Figure 5.1: **Lining elements used in two-dimensional analyses**

sumption since the structures the elements represent are long and thin rather than deep, where shear effects may be important. Both beam elements are three-noded to match the number of elements along the edge of a six-noded triangular continuum element, as used for the ground. It is shown below that the displacements interpolated between the nodes for the first beam element is of a higher order than that on the edge of the continuum element. The elements are therefore incompatible away from nodes but this does not lead to deficiencies in the solutions obtained.

5.2.1 Beam elements based on Hermitian interpolation

5.2.1.1 Shape functions

The first beam element shown in Figure 5.1 is straight and has two degrees of freedom at each node; one lateral translation and one rotation. A common convention, and that adopted here, is to derive the shape functions in terms of a non-dimensional variable $\bar{x}$ defining any point in the beam

$$\text{i.e.} \qquad \bar{x} = \frac{x}{l} \tag{5.1}$$

so that the beam element, of overall length $2l$, has nodes at $\bar{x} = -1, 0, +1$. Using shape functions, the lateral displacement $v(\bar{x})$ is

$$v(\bar{x}) = \boldsymbol{N}\boldsymbol{d} \tag{5.2}$$

where

$$\boldsymbol{N} = \{\ N_1 \quad N_2 \quad N_3 \quad N_4 \quad N_5 \quad N_6\ \} \qquad \& \qquad \boldsymbol{d}^T = \{\ v_1 \quad \theta_1 \quad v_2 \quad \theta_2 \quad v_3 \quad \theta_3\ \} \tag{5.3}$$

$N_j, (j = 1, 6)$ are the shape functions and $v_i, \theta_i, (i = 1, 3)$ are the normal displacements and rotations at the nodes.

The shape functions are Hermite interpolation polynomials since the lateral displacements at nodes and their first derivatives are used to interpolate the displacement $v(\bar{x})$ throughout the beam. The rotations can be considered as the first derivatives of the lateral displacements providing small displacement theory is used. The required Hermite polynomials can be obtained directly from Lagrangian interpolation polynomials (Spanier and Oldham, 1987), which provide shape functions for continuum elements, as

$$\begin{aligned} N_i, (i = 1, 3, 5) &= [1 - 2l(\bar{x} - \bar{x}_i)L_i'(\bar{x}_i)][L_i(\bar{x})]^2 && (5.4) \\ N_i(i = 2, 4, 6) &= l(\bar{x} - \bar{x}_i)[L_i(x)]^2 && (5.5) \end{aligned}$$

where $L_i(\bar{x})$ is the one-dimensional Lagrangian polynomial of degree $(nnod - 1)$ calculated at node i given by

$$L_i(\bar{x}) = \prod_{j=1, j \neq i}^{nnod} \frac{\bar{x} - \bar{x}_j}{\bar{x}_i - \bar{x}_j} \tag{5.6}$$

and $L_i'(\bar{x})$ is its first derivative with respect to $\bar{x}$ and $nnod$ is the total number of nodes on the element. The advantage of this derivation, which is not given in the majority of finite element texts, is that the Lagrangian polynomials are already present in the analysis program code. The former are required for continuum elements and the derivatives are required for isoparametric elements. The derivation of the particular shape functions for the three-node beam element used here is given in Appendix B.

5.2.1.2 Formation of the element stiffness matrix

The stiffness matrix formation for this beam element is structured in a similar way to that for a continuum element. In this case, matrix $\boldsymbol{B}$ links the curvature κ in the beam, rather than strains, to displacements

$$\kappa = \boldsymbol{B}\boldsymbol{d} \tag{5.7}$$

and the generalised stress-strain relationship links the bending moment to the curvature. Having obtained the shape functions, $\boldsymbol{B}$ can be derived from Equations 5.1 and 5.2 as

$$\boldsymbol{B} = \frac{1}{l^2}\{\ N_1'' \quad N_2'' \quad N_3'' \quad N_4'' \quad N_5'' \quad N_6''\ \} \tag{5.8}$$

where a prime indicates differentiation with respect to the axial coordinate, $\bar{x}$. The material stiffness matrix is

$$\boldsymbol{D} = [EI] \tag{5.9}$$

where E is Young's modulus and I is the second moment of area of the beam cross-section. The local flexural stiffness matrix $\boldsymbol{K}_b$ is formed in the usual manner from

$$\boldsymbol{K}_b = l\int_{-1}^{1} \boldsymbol{B}^T\boldsymbol{D}\boldsymbol{B}\,d\bar{x} \tag{5.10}$$

It is possible to derive $\boldsymbol{K}_b$ analytically from Equation 5.10 but the implementation in *OXFEM* of this element uses one-dimensional Gaussian quadrature to evaluate this equation since this is the procedure adopted for all other elements. The element is effectively assumed to be an undistorted isoparametric element (i.e. $\det \boldsymbol{J} = l$). Since the shape functions include terms of order five and below, $\boldsymbol{B}$ contains functions of order three and below. Therefore the integral in Equation 5.10 will be solved exactly using four-point Gaussian quadrature which is exact for order seven and below.

$\boldsymbol{K}_b$ is a 6×6 matrix related to the local degrees of freedom (two per node) and is transformed into global coordinates and added to the terms arising from the membrane elements. Following solution for the global displacements, the stress resultant (moment) is calculated using Gaussian quadrature to give four results per element

5.2.1.3 Validation

Many analytical solutions exist for beam bending problems under Bernoulli-Euler conditions with linear elastic material behaviour. Four problems were used to test the implementation of the first beam formulation in the two-dimensional lining element. Displacements associated with membrane effects were minimised by increasing the membrane stiffness to a high level relative to the flexural stiffness (EI). The first three problems were analysed using successively finer meshes to demonstrate convergence to the analytical solutions and were:

- a single span, straight beam with a central point load,
- a two-pin arch with a central point load,
- a ring with point loads applied across its diameter.

The general arrangements of each are shown in Figure 5.2. In problem 3, symmetry was exploited and only a semi-circular mesh was analysed, with appropriate boundary conditions. The analytical solutions for central deflection for these statically indeterminate problems can be found using virtual work (an example, for the third of the problems, is given in Todd (1974)).

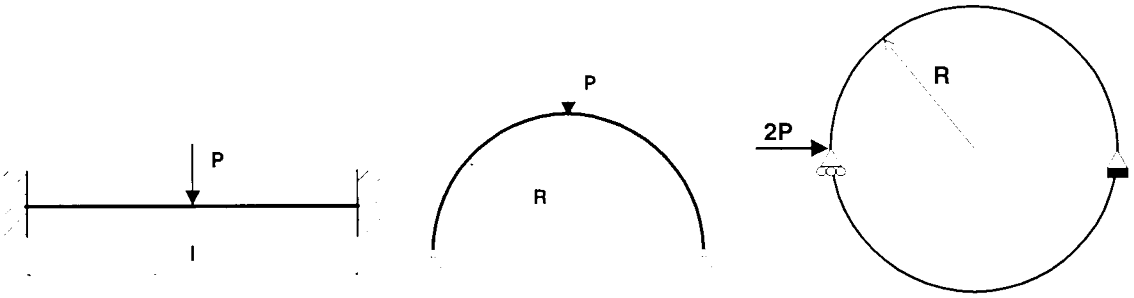

(a) Problem 1 (b) Problem 2 (c) Problem 3

Figure 5.2: **Two-dimensional validation problems**

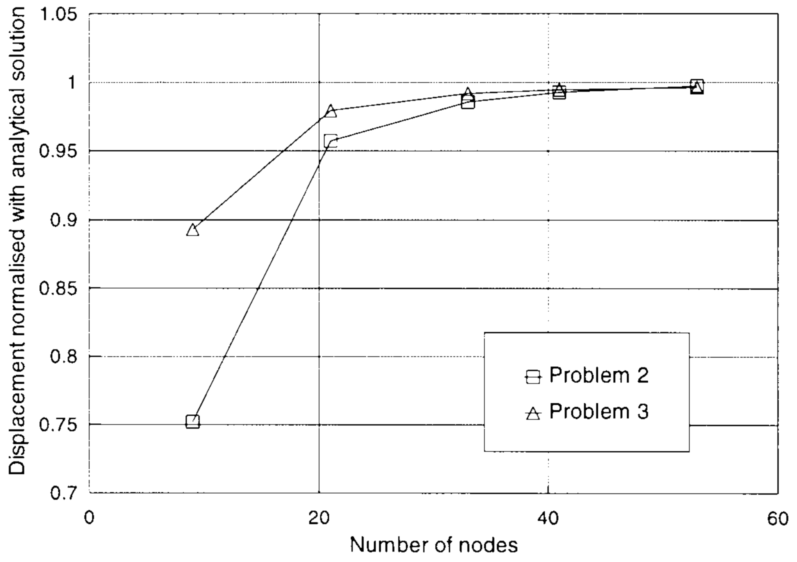

Figure 5.3: **Displacement results for problems 2 & 3**

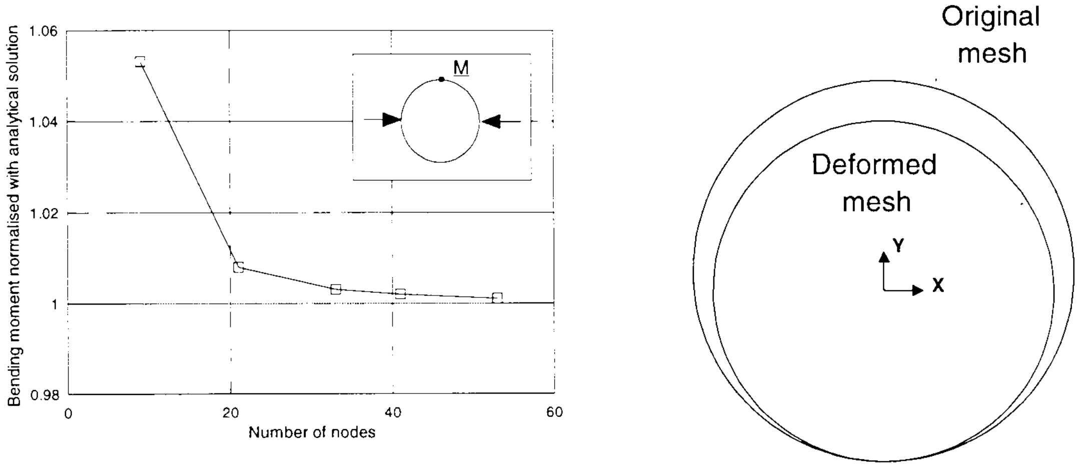

(a) Bending moment result for problem 3

(b) Uniform shrinkage in problem 4

Figure 5.4:

The exact analytical solution for displacement was predicted by the finite element analysis for the first problem using a single element. This result was unsurprising since the element interpolates displacements with a polynomial of higher order than the cubic required for the exact displacement field (due to bending) of the first problem. Figure 5.3 shows the convergence of the finite element results towards the analytical solutions for particular displacements in the second two problems. For problem 2, the displacement under the load is plotted while for problem 3 it is the displacement across the diameter of the ring normal to that loaded. The finite element results converge to within 2% of the analytical solution for meshes with 40 nodes and above

Figure 5.4(a) shows the convergence of the bending moment result at the same location in the ring (opposite the load) in problem 3. Once again, convergence is quick but interestingly, the results converge from above the analytical solution rather than from below as shown in Figure 5.3 for the displacements. This implies that the curvatures are greater at the point of interest for the coarser meshes than for the finer meshes. This can be explained by considering the difference between the element length and the length of the curve between the element end nodes. As refinement proceeds, this difference reduces and since curvature is effectively the first derivative of displacement divided by the element length, it is directly affected by this geometrical error. For the first problem, bending moments are very close to the analytical solution.

The final problem used to test the implementation of this element examined the loads required to shrink uniformly a circular ring of lining elements, as required to model volume loss in the tunnelling model. The mesh was subjected to the same boundary conditions as used in problem 3 so that shrinkage occurred with the ring fixed at its invert. Initially this test was carried out using nodal loads equivalent to uniformly distributed loads normal to the element length. This appeared to be appropriate loading to obtain a uniform shrinkage of the circular mesh. However under these loads, small bending moments were generated within each element. These arose from the components of the loading at the central node of each element. The application of radial loads at the end nodes only produced uniform shrinkage as shown in Figure 5.4(b) and negligible bending moments. A procedure to calculate loads corresponding to a given degree of shrinkage is described in Section 5.3.

5.2.2 Elements based on overlapping interpolation fields

The second beam element formulation implemented into *OXFEM* is that given in Phaal and Calladine (1992). A mesh of these elements is shown in Figure 5.5. Each node in the mesh, apart from those at boundaries, is the centre node of one element and the end node of two other elements. Figure 5.5 demonstrates the most unusual feature of this formulation in that each element overlaps two others. This ensures C^1 continuity, i.e. of slope, without the need to interpolate using rotations at nodes and hence no rotational degrees of freedom are needed, unlike conventional beam formulations.

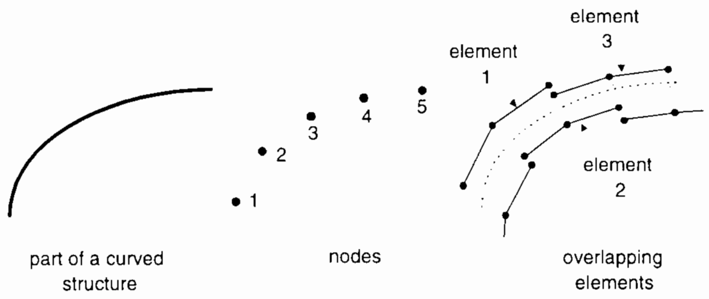

Figure 5.5: **A mesh of overlapping beam elements**

Another important difference is that this element can be curved.

In developing the finite element equations for an overlapping curved beam element, the stiffness matrix for a straight three-noded overlapping element is derived first, using shape functions. This element has one lateral displacement degree of freedom at each node (Figure 5.6). The same stiffness matrix is then found using an unconventional approach where the element is considered to be formed from two rigid links joined with a rotational spring (Figure 5.7). This mechanical analogy then permits the formulation to be extended to the kinked element of Figure 5.8(a) which has four lateral displacement local degrees of freedom. The global stiffness matrix is then obtained using a transformation matrix.

The lack of any rotational degrees of freedom in these elements is of relatively low significance in two-dimensional analyses. It does, however, lead to the possibility of developing shell elements for use in three-dimensional analyses in which rotational degrees of freedom are not required. This avoids several complications inherent in many conventional shell element formulations which will be discussed in Chapter 6.

5.2.2.1 Formation of the element stiffness matrix

In the description which follows, the same nomenclature is used, where possible, as for the derivation of the Hermite beam element. Initially, the straight element of Figure 5.6 is considered which has three lateral displacement degrees of freedom; one at each node. The formulation permits unequal leg lengths (i.e. $h_1 \neq h_2$, see Figure 5.6). However, the element implemented into *OXFEM* had equal length legs (i.e. $h_1 = h_2$) and this fact is used to simplify some of the derivations which follow.

A : Straight three-noded element with three degrees of freedom from shape functions

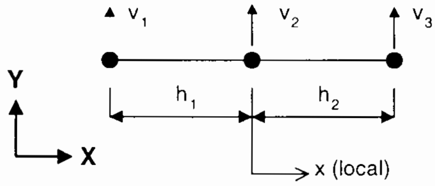

Figure 5.6: **Straight three-noded, overlapping beam element**

Lateral displacement $v(x)$ is interpolated with a complete quadratic polynomial in x, the local axial coordinate measured from the centre of the beam

$$v(x) = c_1 + c_2 x + c_3 x^2 . \tag{5.11}$$

Expressed in terms of shape functions

$$v(x) = N_1 v_1 + N_2 v_2 + N_3 v_3 \tag{5.12}$$

where $\{v_1, v_2, v_3\} = \boldsymbol{d}^T$ is the vector of local lateral displacements at nodes 1, 2, 3 and the shape functions are the Lagrange polynomials of order 2, found from Equation 5.6

$$N_1 = \left(\frac{-h_2}{h_1(h_1+h_2)}\right) x + \left(\frac{1}{h_1(h_1+h_2)}\right) x^2 \tag{5.13}$$

$$N_2 = 1 + \left(\frac{1}{h_1} - \frac{1}{h_2}\right) x + \left(\frac{-1}{h_1 h_2}\right) x^2 \tag{5.14}$$

$$N_3 = \left(\frac{h_1}{h_2\left(h_1+h_2\right)}\right)x + \left(\frac{1}{h_2\left(h_1+h_2\right)}\right)x^2 \qquad (5.15)$$

In the above, h_1 and h_2 are the lengths of each "leg" of the element as shown in Figure 5.6. The next step in the formulation is the derivation of the generalised strain-displacement relationship. The curvature κ of the element is constant since the interpolation polynomial in Equation 5.11 is quadratic and

$$\kappa = \boldsymbol{B} \;\; \boldsymbol{d} \qquad (5.16)$$

$$\boldsymbol{B} = \frac{d^2}{dx^2}\boldsymbol{N} \qquad (5.17)$$

$$= \left(\frac{2}{h_1+h_2}\right)\left[\begin{array}{ccc} \frac{1}{h_1} & \frac{-(h_1+h_2)}{h_1 h_2} & \frac{1}{h_2} \end{array}\right] \qquad (5.18)$$

The material stiffness matrix $\boldsymbol{D} = [EI]$ is the same as the Hermite beam element and the local element stiffness matrix $\boldsymbol{K}_b$ is formulated in the standard way using

$$\boldsymbol{K}_b = \int_{-h_1/2}^{h_2/2} \boldsymbol{B}^T \boldsymbol{D} \boldsymbol{B}\, dx \qquad (5.19)$$

The limits in Equation 5.19 cover the central half of the element reflecting the overlapping nature of this formulation. To illustrate this formulation, $\boldsymbol{K}_b$ is now formed for a straight element with equal length legs ($h_1 = h_2 = a$). The resulting matrix will be used later (in Appendix C) for the paper analysis of a simple beam problem. From Equation 5.18 the strain-displacement matrix is

$$\boldsymbol{B} = \frac{1}{a^2}\left[\begin{array}{ccc} 1 & -2 & 1 \end{array}\right] \qquad (5.20)$$

and the local stiffness matrix follows from Equation 5.19 as

$$\boldsymbol{K}_b = \frac{EI}{a^3}\left[\begin{array}{ccc} 1 & -2 & 1 \\ -2 & 4 & -2 \\ 1 & -2 & 1 \end{array}\right] \qquad (5.21)$$

B: Straight three-noded element with three degrees of freedom from mechanical analogy

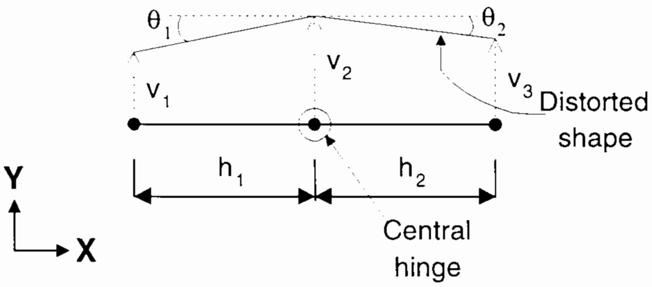

Figure 5.7: **Mechanical analogue of the straight three-noded beam element**

The stiffness matrix for the straight, three-noded, overlapping beam element is now obtained via a different route, similar to that employed by Phaal and Calladine (1992). The element is considered to be two rigid links connected together at a central hinge (see Figure 5.7). Once again, the local displacements at the three nodes are

$$\boldsymbol{d} = \{\ v_1 \quad v_2 \quad v_3\ \}^T \tag{5.22}$$

The change $\theta = \theta_1 + \theta_2$ in the angle between the rigid links is

$$\begin{aligned} \theta &= \frac{v_1 - v_2}{h_1} + \frac{v_3 - v_2}{h_2} = \boldsymbol{Ld} && (5.23) \\ \text{where} \quad \boldsymbol{L} &= \begin{bmatrix} \frac{1}{h_1} & \frac{-(h_1+h_2)}{h_1 h_2} & \frac{1}{h_2} \end{bmatrix} && (5.24) \end{aligned}$$

For a state of unit curvature in the element $\kappa = 1$, equivalent nodal displacements can be found from Equation 5.11,

$$\kappa = \frac{d^2 v}{dx^2} = 2c_3 \tag{5.25}$$

$$c_3 = \frac{1}{2} \quad \text{and} \quad v_1 = \frac{x_1^2}{2} \tag{5.26}$$

where v_1 is the component of displacement at node 1 for unit curvature κ. Repeating for each node, a vector of displacements can be formed,

$$\boldsymbol{C} = \{\ \tfrac{x_1^2}{2} \quad \tfrac{x_2^2}{2} \quad \tfrac{x_3^2}{2}\ \}^T \tag{5.27}$$

Then the nodal displacement vector for any curvature κ is

$$\boldsymbol{d} = \boldsymbol{C}\kappa \tag{5.28}$$

and change in hinge angle, θ from Equation 5.23 is

$$\theta = \boldsymbol{L}\boldsymbol{C}\kappa = \boldsymbol{G}\kappa \tag{5.29}$$

From Equations 5.23 and 5.29, a strain-displacement relation can be obtained and hence an expression for the matrix $\boldsymbol{B}$:

$$\begin{aligned} \boldsymbol{L}\boldsymbol{d} &= \boldsymbol{G}\kappa & (5.30)\\ \kappa &= \boldsymbol{G}^{-1}\boldsymbol{L}\boldsymbol{d} & (5.31)\\ \text{hence} \quad \boldsymbol{B} &= \boldsymbol{G}^{-1}\boldsymbol{L} & (5.32) \end{aligned}$$

$\boldsymbol{K}_b$ is then derived using the standard finite element approach (Equation 5.19).

As an example, considering an element with equal length legs ($h_1 = h_2 = a$) (for which $\boldsymbol{K}_b$ was derived in Section 5.2.2.1A)

$$\begin{aligned} \boldsymbol{L} &= \frac{1}{a}\begin{bmatrix} 1 & -2 & 1 \end{bmatrix} & (5.33)\\ \boldsymbol{C} &= \{\ \tfrac{a^2}{2} \quad 0 \quad \tfrac{a^2}{2}\ \}^T & (5.34)\\ \boldsymbol{G} &= \boldsymbol{L}\boldsymbol{C} = a & (5.35)\\ \boldsymbol{B} &= \boldsymbol{G}^{-1}\boldsymbol{L} = \frac{1}{a^2}\begin{bmatrix} 1 & -2 & 1 \end{bmatrix} & (5.36) \end{aligned}$$

which agrees with the earlier derivation (Equation 5.20).

C: Kinked three-noded element from mechanical analogy

The third step in the derivation of the stiffness matrix for the curved beam element is now possible. Using the mechanical analogue, the element is kinked at the hinge, so that the nodes lie on a curve (Figure 5.8(a)). The local degrees of freedom remain

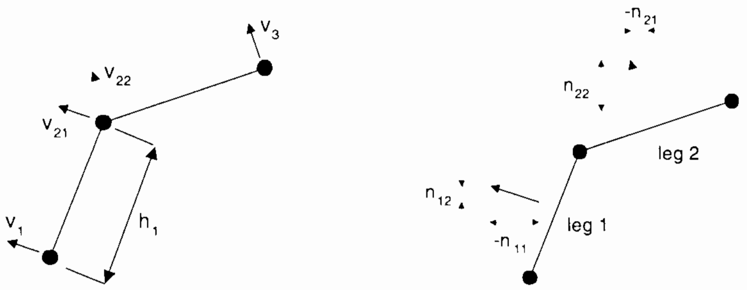

(a) Kinked element (b) Leg normals

Figure 5.8: **Kinked three-noded overlapping beam element**

lateral displacements: those at the end nodes (v_1 and v_3) are therefore rotated to remain normal to their individual element "legs". At the central node, the local degree of freedom is split into two (v_{21} and v_{22}), one normal to each leg. The vector of local degrees of freedom becomes

$$\boldsymbol{d}_{cv} = \{\ v_1 \quad v_{21} \quad v_{22} \quad v_3\ \}^T \tag{5.37}$$

and by inspection the change in the angle at the hinge, θ is

$$\theta = \frac{v_1 - v_{21}}{h_1} + \frac{v_3 - v_{22}}{h_2} = \boldsymbol{L}_{cv}\boldsymbol{d}_{cv} \tag{5.38}$$

$$\text{where} \quad \boldsymbol{L}_{cv} = \left(\frac{2}{h_1 + h_2}\right)\left[\begin{array}{cccc} \frac{1}{h_1} & \frac{-1}{h_1} & \frac{-1}{h_2} & \frac{1}{h_2} \end{array}\right] \tag{5.39}$$

As for the straight beam, a vector of displacements $\boldsymbol{C}_{cv}$ at degrees of freedom is formed which are equivalent to a unit curvature κ.

$$\boldsymbol{C}_{cv} = \{\ \tfrac{x_1^2}{2} \quad \tfrac{x_2^2}{2} \quad \tfrac{x_2^2}{2} \quad \tfrac{x_3^2}{2}\ \}^T = \boldsymbol{X}\boldsymbol{C} \tag{5.40}$$

$$\text{where} \qquad \boldsymbol{X} = \begin{bmatrix} 1 & 0 & 0 & 0 \\ 0 & 1 & 1 & 0 \\ 0 & 0 & 0 & 1 \end{bmatrix}^T \tag{5.41}$$

Then the displacement vector $\boldsymbol{d}_{cv}$ for any curvature κ is

$$\boldsymbol{d}_{cv} = \boldsymbol{C}_{cv}\kappa \tag{5.42}$$

and the change in hinge angle θ

$$\begin{aligned}\theta &= \boldsymbol{L}\boldsymbol{C}_{cv}\kappa && (5.43)\\ &= \boldsymbol{L}\boldsymbol{X}\boldsymbol{C}\kappa && (5.44)\\ &= \boldsymbol{G}_{cv}\kappa && (5.45)\end{aligned}$$

In combination with Equation 5.38 the strain-displacement matrix is found as

$$\boldsymbol{B}_{cv} = \boldsymbol{G}_{cv}^{-1}\boldsymbol{L}_{cv} \qquad (5.46)$$

The local stiffness matrix $\boldsymbol{K}_{cv}$ is found from Equation 5.19

$$\boldsymbol{K}_{cv} = \left(\frac{h_1 + h_2}{2}\right)\boldsymbol{B}_{cv}^T\boldsymbol{D}\boldsymbol{B}_{cv} \qquad (5.47)$$

The final step is the transformation of $\boldsymbol{K}_{cv}$ to global axes. The 4 × 6 transformation matrix, $\boldsymbol{T}_{cv}$ converts the vector of the six global displacements (see Figure 5.1(b))

$$\boldsymbol{U} = \{\ U_1 \quad V_1 \quad U_2 \quad V_2 \quad U_3 \quad V_3\ \}^T \qquad (5.48)$$

to local ones as

$$\boldsymbol{d}_{cv} = \boldsymbol{T}_{cv}\boldsymbol{U} \quad \text{where} \quad \boldsymbol{T}_{cv} = \begin{bmatrix} n_{11} & n_{12} & 0 & 0 & 0 & 0\\ 0 & 0 & n_{11} & n_{12} & 0 & 0\\ 0 & 0 & n_{21} & n_{22} & 0 & 0\\ 0 & 0 & 0 & 0 & n_{21} & n_{22}\end{bmatrix} \qquad (5.49)$$

n_{ij} are components of the unit normal vectors to each leg of the element, as shown in Figure 5.8(b). The strain energy U^e of the element in terms of its local stiffness matrix is

$$U^e = \frac{1}{2}\boldsymbol{d}_{cv}^T\boldsymbol{K}_{cv}\boldsymbol{d}_{cv} \qquad (5.50)$$

In terms of the global element stiffness matrix $\boldsymbol{K}_g$

$$U^e = \frac{1}{2}\boldsymbol{U}^T\boldsymbol{K}_g\boldsymbol{U} \qquad (5.51)$$

so substituting the expression for $\boldsymbol{U}$ in Equation 5.49 into Equation 5.50 gives

$$U^e = \frac{1}{2}\boldsymbol{U}^T\boldsymbol{T}_{cv}^T\boldsymbol{K}_{cv}\boldsymbol{T}_{cv}\boldsymbol{U} \quad (5.52)$$

$$\text{therefore} \quad \boldsymbol{K}_g = \boldsymbol{T}_{cv}^T\boldsymbol{K}_{cv}\boldsymbol{T}_{cv} \quad (5.53)$$

This completes the derivation of the global stiffness matrix for the curved overlapping beam element.

5.2.2.2 Boundary conditions

A major problem in the implementation of this beam element comes in applying boundary conditions. A node attached to a boundary is the end node of one element only. The structure's flexural stiffness adjacent to the boundary will be calculated incorrectly if taken as the contribution from this element alone. An element spanning the boundary is necessary, with the node on the boundary as its centre node and an imaginary leg beyond. In the implementation of this formulation, an imaginary node is created beyond the boundary and the global stiffness matrix $\boldsymbol{K}_g$ for a complete edge element is formed. The location of the imaginary node is found from reflecting the position of the real end node across the boundary. The degrees of freedom associated with the imaginary node are eliminated using constraint equations which describe the nature of the boundary. This approach is necessary both because of the overlapping nature of the elements and because there are no rotational degrees of freedom to fix.

In determining how to account for different types of boundary, it is simplest to consider each type and then imagine its physical effect on a complete element spanning that boundary. It is also easier to understand the procedure if the straight element (with three degrees of freedom) is examined, as in the initial derivation of $\boldsymbol{K}_b$. Figure 5.9 shows an element of this type spanning a boundary where V_1, V_2, V_3 are the global lateral displacements at nodes. For a simply-supported edge, the element rotates rigidly about

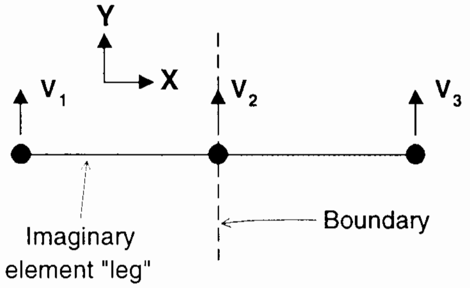

Figure 5.9: **An overlapping element spanning a boundary**

the boundary node. For a fully fixed (i.e. clamped) edge, the node beyond the boundary moves mirror-image displacements to the other end node to ensure zero rotation at the boundary. For a symmetrical boundary, the effect is the same as for the fixed case although one translational degree of freedom is released. The translational fixities are dealt with at the solution stage, as with conventional elements. The rotational effects can be numerically modelled by writing them in the form of constraint equations. Taken with the element stiffness matrix, the constraint equations allow the degree of freedom beyond the boundary to be eliminated leaving a reduced $\boldsymbol{K}_g$ which accounts for the nature of the boundary. For the displacements indicated in Figure 5.9, a single constraint equation is required to eliminate the single degree of freedom beyond the boundary. In this example, there is only one global degree of freedom per node since the element is straight and lies with its local x−axis parallel to the global X−axis. For a simply-supported boundary the constraint equation is

$$V_1 + V_3 = 0 \tag{5.54}$$

and for a fixed (or symmetrical) boundary,

$$V_1 - V_3 = 0 \tag{5.55}$$

Elimination of the unwanted degree of freedom is accomplished using the following method (Cook, 1981) which is illustrated at each stage for the element in Figure 5.9 spanning a fixed boundary.

- The matrix of global displacements at nodes $\boldsymbol{U}$ is partitioned into freedoms to be retained ($\boldsymbol{U}_r$) and freedoms to be eliminated ($\boldsymbol{U}_\epsilon$).

$$\boldsymbol{U} = \{\boldsymbol{U}_\epsilon \boldsymbol{U}_r\}^T \tag{5.56}$$

$$\text{in the example,} \quad \boldsymbol{U}_\epsilon = \{V_1\} \qquad \boldsymbol{U}_r = \{V_2 V_3\}^T \tag{5.57}$$

- A matrix $\boldsymbol{T}_c$ is derived where

$$\boldsymbol{U} = \{\boldsymbol{U}_\epsilon \boldsymbol{U}_r\}^T = \boldsymbol{T}_c \boldsymbol{U}_r \tag{5.58}$$

  This is similar to transformation matrices which convert global degrees of freedom to local ones (as used in Appendix A) or matrix $\boldsymbol{T}_{cv}$ in Equation 5.49. $\boldsymbol{T}_c$ is applied to the global stiffness matrix $\boldsymbol{K}_g$ in the same way to obtain the reduced stiffness matrix $\boldsymbol{K}_{g(red)}$ for the retained degrees of freedom i.e.

$$\boldsymbol{K}_{g(red)} = \boldsymbol{T}_c^T \boldsymbol{K}_{bg} \boldsymbol{T}_c \tag{5.59}$$

  The final stiffness matrix is one-half of $\boldsymbol{K}_{g(red)}$ to remove stiffness attributable to the imaginary leg.

- Derivation of $\boldsymbol{T}_c$ begins by rewriting the constraint equations in matrix form as

$$\boldsymbol{C}\boldsymbol{U} = 0 \tag{5.60}$$

$$\text{in the example,} \quad \boldsymbol{C} = \begin{bmatrix} 1 & 0 & -1 \end{bmatrix} \tag{5.61}$$

- Equation 5.60 is rewritten in partitioned format,

$$[\boldsymbol{C}_\epsilon \boldsymbol{C}_r]\{\boldsymbol{U}_\epsilon \boldsymbol{U}_r\}^T = 0 \tag{5.62}$$

$$\text{in the example,} \quad \boldsymbol{C}_\epsilon = [1] \qquad \boldsymbol{C}_r = [0 \; -1] \tag{5.63}$$

- Equation 5.62 is rearranged to solve for $\boldsymbol{U}_\epsilon$

$$\boldsymbol{U}_\epsilon = [\boldsymbol{C}_{er}]\{\boldsymbol{U}_r\}^T \tag{5.64}$$

$$\text{where} \quad [\boldsymbol{C}_{er}] = -[\boldsymbol{C}_\epsilon]^{-1}[\boldsymbol{C}_r] \tag{5.65}$$

$$\text{and in the example,} \qquad [\boldsymbol{C}_{er}] = \begin{bmatrix} 0 & 1 \end{bmatrix} \tag{5.66}$$

- Substitution for $\boldsymbol{U}_c$ in Equation 5.58 gives

$$\boldsymbol{T}_c = \begin{bmatrix} \boldsymbol{C}_{er} \\ \boldsymbol{I} \end{bmatrix} \tag{5.67}$$

where $\boldsymbol{I}$ is the identity matrix of the same dimension as $\boldsymbol{U}_r$.

In the example,

$$\boldsymbol{T}_c = \begin{bmatrix} 0 & 1 \\ 1 & 0 \\ 0 & 1 \end{bmatrix} \tag{5.68}$$

The reduced global stiffness matrix for the example element then follows from Equations 5.21, 5.59 and 5.68 as

$$\boldsymbol{K}_{g(red)} = \frac{EI}{a^3} \begin{bmatrix} 2 & -2 \\ -2 & 2 \end{bmatrix} \tag{5.69}$$

This procedure is simple to extend to the kinked element with four degrees of freedom. In this case, each boundary condition is represented by two constraint equations (as for a straight element not aligned to the global axes), and two degrees of freedom are eliminated beyond the boundary.

Appendix C contains a paper analysis of a straight fixed end beam formed of the straight overlapping beam elements (with three degrees of freedom) which demonstrates the assembly of individual element stiffnesses and the imposition of boundary conditions.

5.2.2.3 Stress updating

Calculation of the bending stress resultants (moments) in elements generally follows the procedure used for conventional elements but, once again, the applied boundary conditions require extra treatment. A single value of curvature is calculated for each element and is assigned to the centre node. For the simply-supported boundary, the rotation of the node at the boundary is unrestrained and the effect of the rotation is excluded from the curvature calculation. This is simply dealt with in this implementation by assigning zero curvature to the edge element (i.e. one having an imaginary leg). For fixed and symmetrical boundaries, the curvature in the edge element is calculated assuming that the fictitious leg of the element moves by the same angle as the real leg, with respect to the boundary, to produce mirror-image local displacements. This completes the displacement vector $\boldsymbol{d}_{cv}$ for the edge element to which $\boldsymbol{B}_{cv}$ is applied to give the curvature. The single moment M associated with the single curvature is obtained from

$$M = EI\kappa \tag{5.70}$$

To complete the updating procedure, nodal forces $\boldsymbol{f}_{int}$ equivalent to the stresses are calculated using

$$\boldsymbol{f}_{int} = \int_{-h_1}^{h_2} \boldsymbol{B}_{cv}^T \boldsymbol{M}\, dx \tag{5.71}$$

Therefore, there is no contribution from the edge element at a simply supported boundary but there will be a contribution from the bending of the first complete element. For a fixed or symmetrical edge, M will already account for its effect and $\boldsymbol{B}_{cv}$ for the entire element, including the fictitious leg, is used in Equation 5.71.

5.2.2.4 Validation

The implementation of this beam element was tested on the same problems as were adopted for the first element (Figure 5.2). Generally the results were slightly poorer than with the first element but this was expected since the displacement uses interpolation functions of lower order than the Hermite beam element. Figure 5.10 shows the displacement results for this element taken at the same locations as plotted in Figure

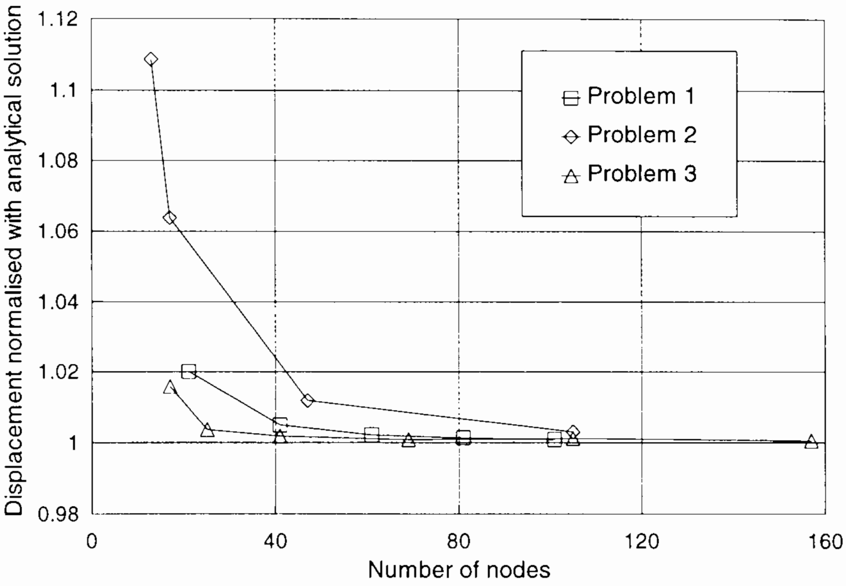

Figure 5.10: **Displacement results for the overlapping beam element**

5.3 for the first beam element. What is most noticeable is the difference in convergence characteristics for the three problems. This is probably attributable to the different boundary conditions (simple supports) leading to slower convergence although it is unclear as to the cause of this effect.

The overlapping element solutions predicted bending moments more accurately than they did displacements. Agreement was obtained with the analytical solution for problem 1 while Figure 5.11 shows the convergence of results for bending moment for problem 3. The plot is equivalent to Figure 5.4(a) for the Hermite beam element. Like the first element, convergence is from above but unlike the first element, this convergence is from the same side as the displacements. This can be explained by the element nodes all lying on the curve for the overlapping element.

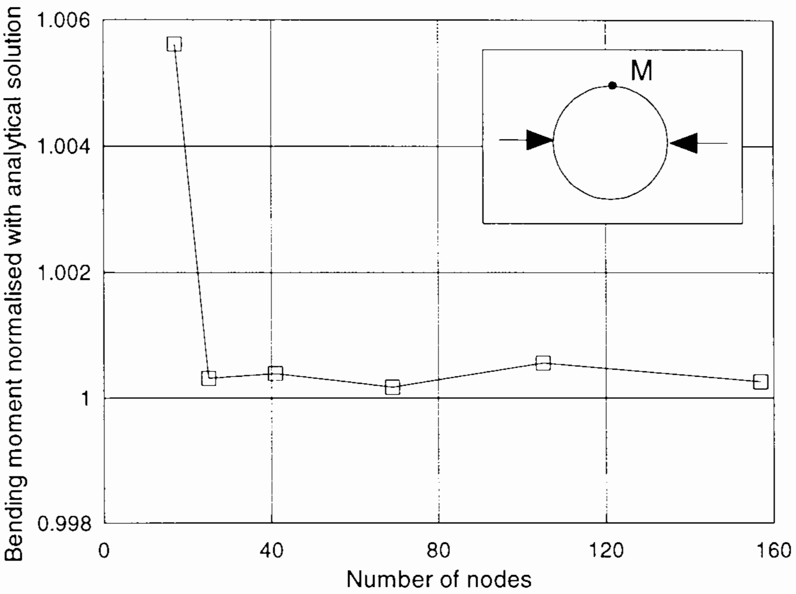

Figure 5.11: **Bending moment results for the overlapping beam element**

5.2.3 Comparison of the approaches

The first noticeable difference in the results for the two beam formulations is that they converge to the analytical solutions for displacements from opposite sides. The Hermitian beam element initially gives an overstiff response while the overlapping formulation stiffens up as the mesh is improved. The behaviour of the first element follows that expected from the finite element method since fewer degrees of freedom are used in the model than are present in a real beam. The finite element beam is over-constrained and therefore stiffer but this effect reduces as the over-constraint is reduced as more degrees of freedom are added. Phaal and Calladine (1992) have shown the overlapping formulation to be the same as a finite difference solution for the element stiffness and therefore a lower bound on the structural stiffness should be expected with these elements.

The displacement results for both elements are replotted in Figure 5.12 against total number of degrees of freedom in the problem rather than number of nodes. This shows

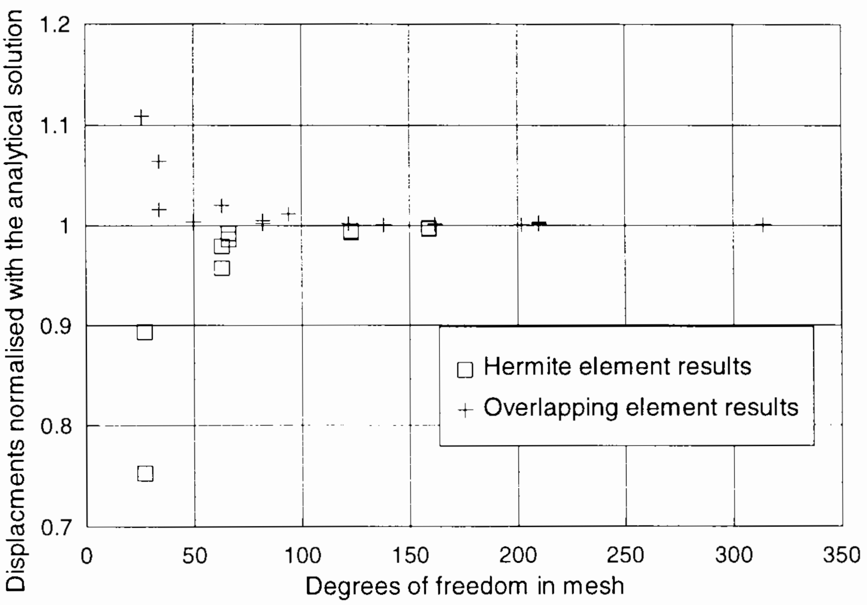

Figure 5.12: **Comparison of displacement results**

the overlapping beam to give adequate accuracy for approximately the same number of global degrees-of-freedom as the Hermite element in these test problems.

Table 5.1 gives storage and memory statistics for the first of the test problems meshed with 101 nodes, using both element formulations. Statistics for single step and 100 step runs are given. The overlapping elements require marginally less CPU time than the Hermite elements and use considerably smaller memory during solution. However, the real time to complete the overlapping element analysis exceeds that for the Hermite element mesh once the time spent in initial input data reading and final output becomes less significant, in the 100 step runs. This reflects the greater number of elements in the overlapping mesh (twice that in the Hermite element mesh). These statistics are of little significance in themselves since the memory and time required to complete these simple analyses are very small. The difference in memory requirements would only begin to affect the timing for very large meshes of these elements.

To summarise, it can be concluded that

Table 5.1: Memory and timing comparison

Element type	*Solution steps*	*Nodes*	*Elements*	*d.o.f.*	*Buffer*	*Front*	*CPU time (s)*	*Real time (s)*
Hermite	1	101	50	303	3637	9	12.6	20.0
	100						205.5	225.0
Overlap	1	101	100	202	1819	6	11.2	15.0
	100						200.5	241.0

Notes: *buffer* is the maximum matrix dimension required to store stiffness coefficients during solution, *front* is the maximum front width during solution.

- The element formulations give comparable levels of accuracy for both displacements and bending moments and,
- there does not appear to be any major reduction in processing time for the overlapping elements, despite the reduced number of global degrees of freedom which they offer.

5.3 Modelling volume loss

As described in Section 3.6, volume loss is modelled by uniformly shrinking the lining elements. Loads are applied to the lining elements which reduce the enclosed area (or volume, in the three-dimensional case) by a specified amount assuming the elements to be unconnected to the ground. Therefore, while the shape of the lining is determined by the shrinkage forces applied, its global location, in the mesh including elements representing the ground, is undetermined. A displacement controlled approach would allow complete control over the shape and the location of the liner but would impose an undesirable level of constraint on the movement of the ground around the tunnel

In Section 1.2 volume loss, V_L was defined in Equation 1.4 as

$$V_L = \frac{V_s}{V_0} \times 100\% \tag{5.72}$$

where V_s is the volume of the surface settlement trough and V_0 is the volume required to construct the tunnel. In all meshes, to a greater or lesser degree, the circular tunnel cross-section is approximated by a sequence of straight edges. Since volume loss is modelled entirely by changing the size of the tunnel lining then in the two-dimensional model, considering a triangular area formed by one edge and the tunnel centre,

$$V_L = \left[1 - \frac{A_1}{A_0}\right] \times 100\% \tag{5.73}$$

where A_0 is the original area of the triangular sector and A_1 is its area following shrinkage. It is simple to show that

$$A_0 = \frac{l_0^2}{4\tan(\theta/2)} \tag{5.74}$$

where l_0 is the original length of the edge and θ the apex angle of the triangle. Then Equation 5.73 can be written

$$V_l = \left[1 - \left(\frac{l_1}{l_0}\right)^2\right] \times 100\% \tag{5.75}$$

where l_1 is the length of the edge after shrinkage since θ remains the same during shrinkage. The change in edge length, defined by the axial strain ϵ_{ax} along the edge, is

$$l_1 = l_0(1 - \epsilon_{ax}) \tag{5.76}$$

so that

$$V_l = (2\epsilon_{ax} - \epsilon_{ax}^2) \times 100\% \tag{5.77}$$

Therefore, the volume loss required can be obtained by applying the forces to each element which give an axial strain of ϵ_{ax}. The direction of the forces is known, from the orientation of the element and their magnitude can be found from simple elastic theory. In fact, the nodal loads calculated from separate element contributions are radial, as expected. Test problem 4 has already demonstrated that both lining element formulations can model pure membrane loading.

The calculation of the required loads was implemented into the analysis program *OXFEM* using the procedure above so that the user has only to provide an input value of volume loss. The procedure assumes that the element nodes are connected only to the lining element and there is no other component of axial stiffness. Clearly this neglects any stiffness contribution from continuum elements representing the ground which are attached to a lining in the tunnelling model. This assumption will be shown (in the demonstration analyses of Chapter 8) to be quite adequate and lead to only minor differences between in measured and required volume losses.

5.4 Summary

In this chapter, two different two-dimensional lining elements have been described, each using a different beam element formulation. The formulations have been implemented in the analysis program *OXFEM* and tested, both against analytical solutions for beam problems and to check that the proposed method of modelling volume loss is feasible. In developing the second of the beam formulations, the difficulties associated with an overlapping finite element have been demonstrated and solutions proposed, implemented and tested. This work is useful for the understanding of the overlapping shell element which is described in Chapter 6.

APPENDIX A

Derivation of axial stiffness contribution

The stiffness matrix $\boldsymbol{K_l}$ for a single rod element, with respect to its local degrees of freedom is,

$$\boldsymbol{K_l} = \frac{EA}{l}\begin{bmatrix} 1 & -1 \\ -1 & 1 \end{bmatrix} \tag{5.78}$$

where E is the Young's modulus of the rod material, A the cross-sectional area and l the element length. $\boldsymbol{K_l}$ is transformed into the stiffness matrix with respect to the global (two-dimensional) coordinate system, $\boldsymbol{K_g}$ by,

$$\boldsymbol{K_g} = \boldsymbol{T}^T \boldsymbol{K_l} \boldsymbol{T} \tag{5.79}$$

$$\text{where} \quad \boldsymbol{T} = \begin{bmatrix} \cos\theta & \sin\theta & 0 & 0 \\ 0 & 0 & \cos\theta & \sin\theta \end{bmatrix} \tag{5.80}$$

and θ is the anticlockwise angle made by the element with the global x-axis. Note that the matrix $\boldsymbol{T}$ relates only to the global translational degrees of freedom. Combining the stiffness matrices of two rod elements which share a node gives a global membrane stiffness contribution for the lining element of,

$$\begin{bmatrix} (c_1)^2 & c_1s_1 & -(c_1)^2 & -c_1s_1 & 0 & 0 \\ & (s_1)^2 & -c_1s_1 & -(s_1)^2 & 0 & 0 \\ & & (c_1)^2+(s_1)^2 & c_1s_1+c_2s_2 & -(c_2)^2 & -c_2s_2 \\ & & & (s_1)^2+(s_2)^2 & -c_2s_2 & -(s_2)^2 \\ & & & & (c_2)^2 & c_2s_2 \\ & & & & & (s_2)^2 \end{bmatrix} \tag{5.81}$$

$$\text{where}\, c_1 = \cos\theta_1,\ s_1 = \sin\theta_1 c_2 = \cos\theta_2,\ s_2 = \sin\theta_2 \tag{5.82}$$

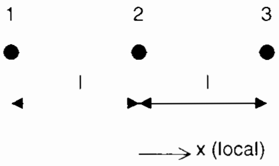

Figure 5.13: **Three-noded Hermitian element**

APPENDIX B

Derivation of shape functions for a three-noded beam element using Hermite polynomials

Shape functions are derived for the straight element with a single local coordinate x as shown in Figure 5.13. The derivation commences with the Lagrangian polynomials of order 2.

$$L_1(x) = \frac{(x-x_2)(x-x_3)}{(x_1-x_2)(x_1-x_3)} \tag{5.83}$$

$$L_2(x) = \frac{(x-x_1)(x-x_2)}{(x_2-x_3)(x_2-x_1)} \tag{5.84}$$

$$L_3(x) = \frac{(x-x_1)(x-x_2)}{(x_3-x_1)(x_3-x_2)} \tag{5.85}$$

where x_i is the *ith* nodal coordinate. Rewriting in terms of the non-dimensional locator $\bar{x}$ and substituting for values of $\bar{x}$ at nodes gives.

$$L_1(x) = \frac{\bar{x}}{2}(\bar{x}-1) \tag{5.86}$$

$$L_2(x) = -\bar{x}(\bar{x}+1) \tag{5.87}$$

$$L_3(x) = \frac{\bar{x}}{2}(\bar{x}+1) \tag{5.88}$$

The derivatives are.

$$L_1'(x) = \frac{1}{2l}(2\bar{x}-1) \tag{5.89}$$

$$L_2'(x) = -\frac{1}{l}(2\bar{x}+1) \tag{5.90}$$

$$L_3'(x) = \frac{1}{2l}(2\bar{x}+1) \tag{5.91}$$

From Equations 5.4, 5.86 and 5.89 with substitution for $\bar{x}_1$ the first shape function is

$$N_1 = \left[1 - 2l(\bar{x}+1)\left(-\frac{3}{2l}\right)\right]\left[\frac{\bar{x}}{2}(\bar{x}-1)\right]^2 = \bar{x}^2 - \frac{5}{4}\bar{x}^3 - \frac{1}{2}\bar{x}^4 + \frac{3}{4}\bar{x}^5 \qquad (5.92)$$

Similarly,

$$\begin{aligned}
N_2 &= l(\bar{x}+1)\left[\frac{\bar{x}}{2}(\bar{x}-1)\right]^2 &&= \frac{l}{4}\left[\bar{x}^2 - \bar{x}^3 - \bar{x}^4 + \bar{x}^5\right] && (5.93)\\
N_3 &= \left[1 - 2l\bar{x}\left(-\frac{1}{l}\right)\right]\left[-\bar{x}(\bar{x}+1)\right]^2 &&= 1 - 2\bar{x}^2 + \bar{x}^4 && (5.94)\\
N_4 &= l\bar{x}\left[-\bar{x}(\bar{x}+1)\right]^2 &&= l\left[\bar{x} - 2\bar{x}^3 + \bar{x}^5\right] && (5.95)\\
N_5 &= \left[1 - 2l(\bar{x}-1)\left(\frac{3}{2l}\right)\right]\left[\frac{\bar{x}}{2}(\bar{x}+1)\right]^2 &&= \bar{x}^2 + \frac{5}{4}\bar{x}^3 - \frac{1}{2}\bar{x}^4 - \frac{3}{4}\bar{x}^5 && (5.96)\\
N_6 &= l(\bar{x}-1)\left[\frac{\bar{x}}{2}(\bar{x}+1)\right]^2 &&= \frac{l}{4}\left[-\bar{x}^2 - \bar{x}^3 + \bar{x}^4 + \bar{x}^5\right] && (5.97)
\end{aligned}$$

The suitability of the above as shape functions can be demonstrated by plotting each polynomial (Figure 5.14). The polynomials related to displacements have value 1 at the associated node and zero elsewhere. Those related to derivatives have slopes of 1 at the associated node.

APPENDIX C

Example analysis using overlapping straight beam elements

A fixed end beam, as shown in Figure 5.15(a), subject to a central point load, P is modelled using a mesh of five overlapping straight beam elements (Figure 5.15(c)). Each element is of the form shown in Figure 5.15(b) with three local degrees of freedom and equal leg lengths. Elements 1 and 5 span the boundaries while elements 2,3 & 4 lie completely within the structure. The global stiffness matrix for this structure $\boldsymbol{K}_{struct}$ can be formed directly from the local element stiffness matrices, $\boldsymbol{K}_b$ since the local and global axes coincide, in this example.

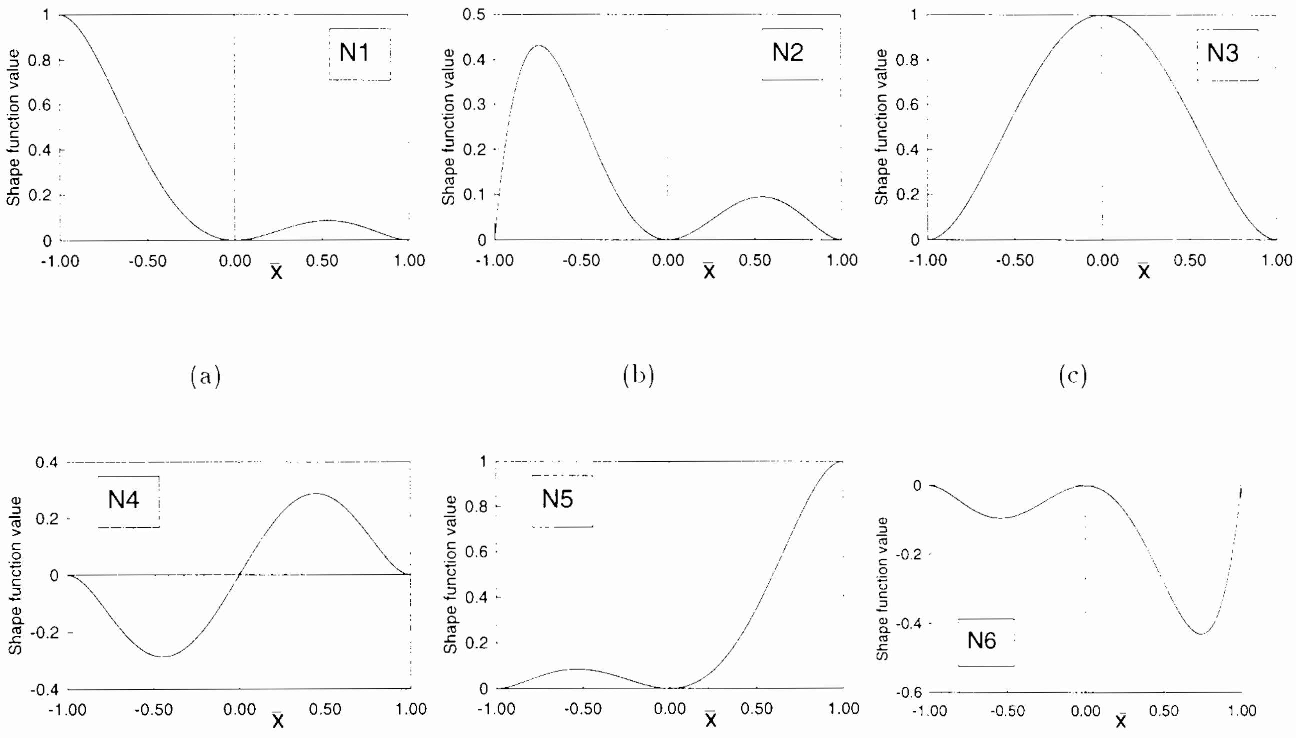

(a) (b) (c)

(d) (e) (f)

Figure 5.14: **Hermite polynomial shape functions for 3-node beam element**

The structure stiffness matrix $\boldsymbol{K}_{struct}$ relates only to the (five) real degrees of freedom i.e.

$$\boldsymbol{K}_{struct}\boldsymbol{U} = \boldsymbol{F} \tag{5.98}$$

$$\text{where} \quad \boldsymbol{U} = \{\, V_2 \quad V_3 \quad V_4 \quad V_5 \quad V_6 \,\}^T \tag{5.99}$$

and $\boldsymbol{F}$ is the vector of global forces at the real degrees of freedom. The stiffness contribution from each complete element consists of $\boldsymbol{K}_b$ in Equation 5.21 related to

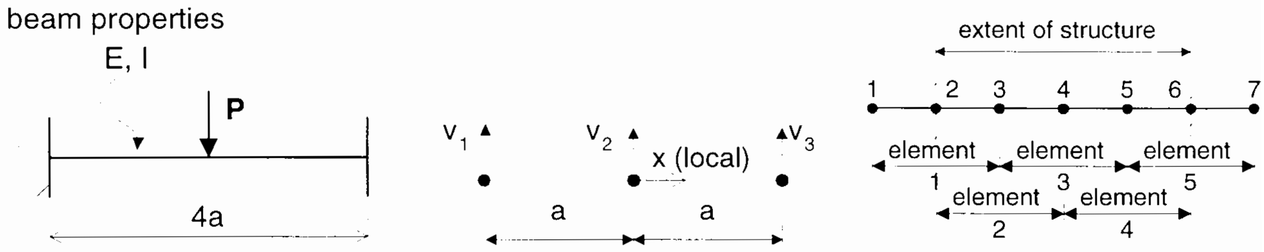

(a) (b) (c)

Figure 5.15: **Appendix C example**

the three degrees of freedom in the element. They give

$$\boldsymbol{K}_{struct} = \frac{EI}{a^3}\begin{bmatrix} 1 & -2 & 1 & 0 & 0 \\ -2 & 5 & -4 & 1 & 0 \\ 1 & -4 & 6 & -4 & 1 \\ 0 & 1 & -4 & 5 & -2 \\ 0 & 0 & 1 & -2 & 1 \end{bmatrix} . \tag{5.100}$$

The next step is to add reduced stiffness matrices for the elements which span the boundaries. These are given by Equation 5.69 and when added to $\boldsymbol{K}_{struct}$ above give

$$\boldsymbol{K}_{struct} = \frac{EI}{a^3}\begin{bmatrix} 3 & -4 & 1 & 0 & 0 \\ -4 & 7 & -4 & 1 & 0 \\ 1 & -4 & 6 & -4 & 1 \\ 0 & 1 & -4 & 7 & -4 \\ 0 & 0 & 1 & -4 & 3 \end{bmatrix} . \tag{5.101}$$

This accounts for the rotational boundary conditions. The translational boundary conditions are zero displacements for V_2 and V_6. Solution of the finite element Equation 5.98 with a force vector F including the applied load $-P$ at degree of freedom 4 gives

$$V_4 = \frac{-Pa^3}{2EI} \tag{5.102}$$

which compares reasonably well with the analytical solution ($= \frac{-Pa^3}{3EI}$), given the coarseness of the mesh.

CHAPTER SIX

MODELLING LINING INSTALLATION IN THREE-DIMENSIONS

6.1 Introduction

This chapter describes the element choices available for the three-dimensional modelling of a tunnel lining. Shell elements are required which have both flexural and membrane stiffness. As for the two-dimensional case, described in Chapter 5, a faceted approach is chosen where the membrane stiffness is provided by one element and the flexural stiffness by another. The two separate element formulations are overlaid to provide the faceted shell element.

In determining a suitable formulation for a shell element for the numerical model of tunnelling, it was important to remember that the main aim of this research was modelling the effects of tunnelling at the soil surface. The behaviour of the liner itself was of interest but of secondary importance. The formulation had to be suitable for connection to the continuum elements modelling the ground and economical, to minimise computer resource requirements. A shell element, rather than a thin continuum element was chosen since it was thought easier to control volume loss with the former. As will be demonstrated over subsequent chapters, the shell elements chosen were found to be satisfactory for the tunnelling model but were less satisfactory for modelling true shell behaviour. A detailed survey of existing shell element formulations is beyond the scope of this thesis, as is the implementation of more than one type of element (which was feasible in the two-dimensional case). The first part of this chapter is therefore not intended as a detailed examination of the various shell element formulations available but justification for the choice of a faceted approach.

6.2 Formulations for shell elements

Existing shell element formulations are generally based on one of two approaches:

- true curved elements either based directly on classical shell theory or derived from degeneration of a solid continuum element.
- faceted elements, where bending stiffness is attributed to a plate element and membrane stiffness to a plane stress, continuum element.

The first of these approaches remains the subject of considerable active research for the reason that no firm consensus has arisen for the best formulation. Indeed, many are highly complex and have received little validation. Formulations derived analytically from classical shell theory vary in the relationship adopted linking strains to displacements. The complexity lies in the need to model C^1 continuity in three-dimensions. This is the Poisson-Kirchoff requirement for plates applied to shells and is the same as the Bernoulli-Euler requirement for beams. These formulations often require many degrees of freedom at nodes, some of which are high-order derivative terms which can lead to problems from their dependence on other lower-order terms which are also degrees of freedom (Phaal and Calladine, 1992a).

Shell elements derived from a degenerated solid continuum element are more popular. The formulation of these elements usually accommodates transverse shear deformation to remove the need for C^1 continuity. However this often leads to locking problems since the solution becomes dominated by the shear deformation. The remedy is to employ reduced integration, but this can then lead to unwanted zero-energy modes (Hughes, 1987) which must be suppressed.

A review of over 280 publications is given in Yang et al. (1990) where shell element formulations (mainly of the curved variety) are described. The large number of different formulations demonstrates the lack of agreement in the research community in this area. There is also little guidance on potential difficulties in joining shell elements, possibly having many higher derivative degrees of freedom, to simple continuum elements. These difficulties prompted the investigation of simpler faceted formulations for this model. The two-dimensional faceted formulations described in Chapter 5 were found to be adequate to model the two-dimensional curved beam so it appeared reasonable that the same approach could be adopted in the three-dimensional case.

6.2.1 Faceted shell formulations

Opinion appears divided on the utility of faceted shell elements: some authors criticise the approach as being highly inaccurate (Cook, 1981) while others (Huang, 1989) praise their efficiency in providing adequate solutions for many problems. In adopting a faceted approach, further choices of element formulations are necessary for the separate flexural and membrane stiffnesses. In the two-dimensional case, beam elements and one-dimensional continuum elements, respectively, provided these stiffnesses. For three-dimensions, the obvious choice for the membrane component of the shell stiffness is a standard plane stress continuum element based on Lagrangian polynomial inter-

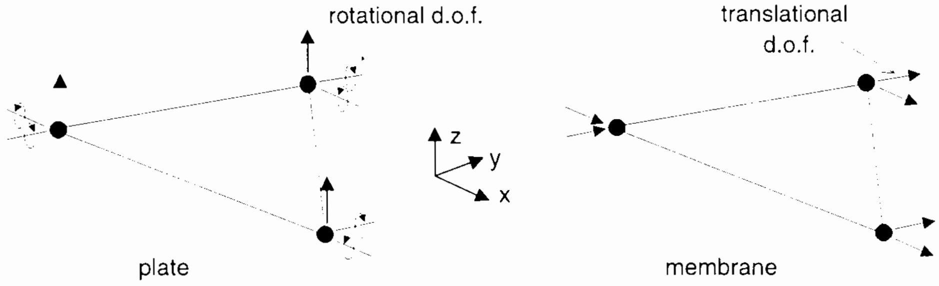

Figure 6.1: **Plate and membrane elements**

polation. The remaining choice, that of the appropriate bending element, is further complicated by the need to consider the in-plane bending stiffness (often referred to as the *drilling* degree of freedom stiffness). This is a difficulty specific to shells and does not appear in the two-dimensional case.

Simple formulations for flat bending elements (i.e. plates) include three degrees of freedom at each node: one out-of-plane displacement and two rotations as shown in Figure 6.1. The two degrees of freedom per node provided by a standard membrane element gives a total of five degrees of freedom at each node of the shell element. Since a three-dimensional element is required to model a curved shell, six degrees of freedom are required at each node (three translations and three rotations). An in-plane rotation is therefore omitted by this approach; this is commonly referred to as the *drilling* degree of freedom (by reference to the physical analogy of drilling into the shell). This degree of freedom is related to the membrane action of the shell and is not linked to the plate degrees of freedom, even though it is rotational. A problem therefore arises in deciding where or how to incorporate this stiffness into the formulation for a shell element.

The problem can be dealt with at the element stiffness formation level or at assembly of elements' stiffnesses. There are formulations for membrane elements which include this degree of freedom (Allman, 1984; Bergen and Felippa, 1985; Hughes et al., 1995)

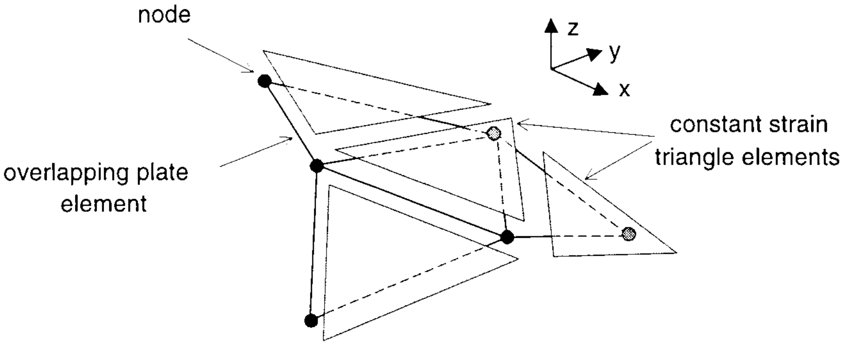

Figure 6.2: **Three-dimensional lining element used in the model**

although these elements were developed to model beam bending more accurately with plane stress elements rather than to alleviate the problem outlined above. Alternatively, a fictitious stiffness can be placed in the element stiffness matrix at the location of the missing degree of freedom following determination of the other terms from the overlaid plate and membrane elements. If no stiffness is provided and the structure is nearly flat then the structure stiffness matrix becomes poorly conditioned, leading to inaccuracies.

An alternative element, which avoids any difficulties with the drilling degree of freedom is described in Phaal and Calladine (1992b). This element has a major advantage over other faceted formulations since it has no rotational degrees of freedom and hence there is no *drilling* degree of freedom to account for in the stiffness formulation. The flexural component of the shell element is provided by an overlapping curved plate element which is an extension of the two-dimensional overlapping beam element described in Section 5.2.2. Figure 6.2 shows the constituent parts of this shell element; a six-noded, overlapping plate element and four constant strain triangle elements. The latter account for the membrane stiffness of the shell while the former models the bending stiffness.

The final element described above was chosen to model the three-dimensional tunnel lining since

- It is a faceted element and, as such, avoids the complexities of coupled membrane and bending actions inside elements.
- The element is especially appropriate for the tunnelling model where shell elements are connected to continuum elements having no rotational degrees of freedom themselves.
- There is no drilling degree of freedom problem.
- The lack of rotational degrees of freedom make it economical

The following section describes the formation of the stiffness matrix for this element and how specified boundary conditions are dealt with.

6.3 Formation of the element stiffness matrix for the overlapping shell element

The formulation for the constant strain triangle elements, which provide the membrane stiffness, is trivial and available in a number of references (Astley, 1992). Care is needed to factor terms of membrane stiffness if calculated for all facets of an overlapping element and this is discussed later in the chapter.

The bending component of the shell element is provided by the overlapping plate element shown in Figure 6.3(b). This element has six nodes and the element is divided into four regions (called facets, for reasons which will become clear later in this section). The facets attached to the three sides of the centre facet overlap centre facets of adjacent elements. Each triangle in the mesh of Figure 6.3(a) therefore represents the central facet of one element overlapped by three outer facets from adjacent elements, unless the element is adjacent to a boundary.

Calculation of the global stiffness contribution of this element mirrors the development of the overlapping beam element in Section 5.2.2. Firstly, a six-node overlapping flat plate element is considered. Its local stiffness matrix is developed using a standard finite element approach. Secondly, the derivation is repeated considering the element facets to be rigid and connected to adjoining facets with rotational springs. This mechanical analogue allows the formulation to be extended to an initially curved element. The stiffness matrix of this element is derived in terms of its local degrees of freedom which are lateral displacements with respect to each facet. Finally, the local stiffness matrix is transformed to global axes. Much of this development is based upon the work of Phaal and Calladine (1992b).

Throughout the derivations which follow, linear elastic, small displacement theory is assumed. Poisson-Kirchoff thin plate theory is also assumed, where normals to the neutral axis in a plate subjected to bending remain normal after deformation. This is also a definition of C^1 continuity and is adopted for conventional plate element formulations. One method of ensuring this in an element formulation is to include rotational degrees of freedom at nodes and this is done with conventional plate elements. The overlapping plate element does not have any rotational degrees of freedom and C^1 continuity is met by the overlapping nature of the elements.

A: Six-noded flat plate element with six local degrees of freedom

Lateral displacement $w(x,y)$ with reference to the local co-ordinate system (x,y), is interpolated with a complete quadratic polynomial.

$$w(x,y) = c_1 + c_2x + c_3y + c_4x^2 + c_5xy + c_6y^2 \tag{6.1}$$

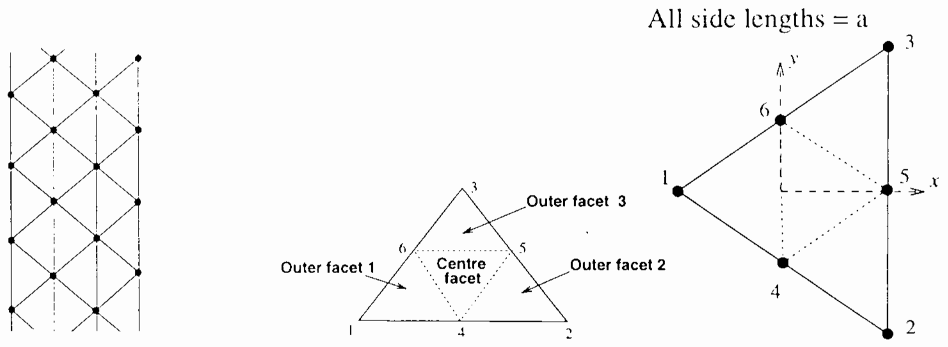

(a) Mesh

(b) element showing facets

(c) Equilateral element

Figure 6.3: **Overlapping plate elements**

where $c_1 \ldots c_6$ are real constants. This can be re-written as

$$w(x, y) = \boldsymbol{W}\boldsymbol{c} \tag{6.2}$$

where

$$\boldsymbol{W} = \{\ 1 \quad x \quad y \quad x^2 \quad xy \quad y^2\ \} \quad \text{and} \quad \boldsymbol{c} = \{\ c_1 \quad c_2 \quad c_3 \quad c_4 \quad c_5 \quad c_6\ \}^T \tag{6.3}$$

The vector of nodal displacements $\boldsymbol{d}_p$ is,

$$\boldsymbol{d}_p = \{\ w_1 \quad w_2 \quad w_3 \quad w_4 \quad w_5 \quad w_6\ \}^T \tag{6.4}$$

then rewriting Equation 6.1 for each nodal displacement gives,

$$\boldsymbol{d}_p = \boldsymbol{A}\boldsymbol{c} \tag{6.5}$$

where,

$$\boldsymbol{A} = \begin{bmatrix} 1 & x_1 & y_1 & x_1^2 & x_1y_1 & y_1^2 \\ 1 & x_2 & y_2 & x_2^2 & x_2y_2 & y_2^2 \\ 1 & x_3 & y_3 & x_3^2 & x_3y_3 & y_3^2 \\ 1 & x_4 & y_4 & x_4^2 & x_4y_4 & y_4^2 \\ 1 & x_5 & y_5 & x_5^2 & x_5y_5 & y_5^2 \\ 1 & x_6 & y_6 & x_6^2 & x_6y_6 & y_6^2 \end{bmatrix} \tag{6.6}$$

In terms of shape functions $\boldsymbol{N}$, the lateral displacement can be expressed as,

$$w(x, y) = \boldsymbol{N}\boldsymbol{d}_p \tag{6.7}$$

where,

$$\boldsymbol{N} = \{\ N_1 \quad N_2 \quad N_3 \quad N_4 \quad N_5 \quad N_6\ \}^T \tag{6.8}$$

From Equation 6.5,

$$\boldsymbol{c} = \boldsymbol{A}^{-1}\boldsymbol{d}_p \tag{6.9}$$

Substituting into Equation 6.2 gives,

$$\begin{aligned} w(x, y) &= \boldsymbol{W}\boldsymbol{A}^{-1}\boldsymbol{d}_p && (6.10) \\ \text{i.e.}\quad \boldsymbol{N} &= \boldsymbol{W}\boldsymbol{A}^{-1} && (6.11) \end{aligned}$$

thus determining the shape functions from the local nodal coordinates. For the equilateral element of Figure 6.3(c), where all side lengths are equal to a,

$$\boldsymbol{A} = \frac{a}{4}\begin{bmatrix} \frac{4}{a} & -2\sqrt{3} & 0 & 3a & 0 & 0 \\ \frac{4}{a} & 2\sqrt{3} & -4 & 3a & -2a\sqrt{3} & 4a \\ \frac{4}{a} & 2\sqrt{3} & 4 & 3a & 2a\sqrt{3} & 4a \\ \frac{4}{a} & 0 & -2 & 0 & 0 & a \\ \frac{4}{a} & 2\sqrt{3} & 0 & 3a & 0 & 0 \\ \frac{4}{a} & 0 & 2 & 0 & 0 & a \end{bmatrix} \tag{6.12}$$

and

$$\boldsymbol{A}^{-1} = \frac{4}{a}\begin{bmatrix} 0 & -\frac{a}{32} & -\frac{a}{32} & \frac{a}{8} & \frac{a}{16} & \frac{a}{8} \\ -\frac{a}{4\sqrt{3}} & 0 & 0 & 0 & \frac{a}{4\sqrt{3}} & 0 \\ 0 & 0 & 0 & -\frac{1}{4} & 0 & \frac{1}{4} \\ \frac{1}{6a} & \frac{1}{24a} & \frac{1}{24a} & -\frac{1}{6a} & \frac{1}{12a} & -\frac{1}{6a} \\ 0 & \frac{1}{4a\sqrt{3}} & \frac{1}{4a\sqrt{3}} & \frac{1}{2a\sqrt{3}} & 0 & -\frac{1}{2a\sqrt{3}} \\ 0 & \frac{1}{8a} & \frac{1}{8a} & 0 & -\frac{1}{4a} & 0 \end{bmatrix} \tag{6.13}$$

so for example,

$$N_1 = \frac{4}{a}\left(-.144x + \frac{.167}{a}x^2\right) \tag{6.14}$$

The generalised strain-displacement relationship for a flat plate element links curvatures to local lateral displacements, $\boldsymbol{d}_p$.

$$\boldsymbol{\kappa} = \boldsymbol{B}\boldsymbol{d}_p \tag{6.15}$$

where

$$\boldsymbol{\kappa} = \left\{ \begin{array}{ccc} \frac{\partial^2 w}{\partial x^2} & \frac{\partial^2 w}{\partial y^2} & \frac{\partial^2 w}{\partial x \partial y} \end{array} \right\}^T = \left\{ \begin{array}{ccc} \kappa_x & \kappa_y & \kappa_{xy} \end{array} \right\}^T \tag{6.16}$$

From Equation 6.7,

$$\boldsymbol{B} = \boldsymbol{\partial}^2 \boldsymbol{N}^T \tag{6.17}$$

where,

$$\boldsymbol{\partial}^2 = \left\{ \begin{array}{ccc} \partial^2/\partial x^2 & \partial^2/\partial y^2 & \partial^2/\partial x \partial y \end{array} \right\}^T \tag{6.18}$$

For the equilateral element of Figure 6.3(c),

$$\boldsymbol{B} = \frac{1}{3a^2} \begin{bmatrix} 4 & 1 & 1 & -4 & 2 & -4 \\ 0 & 3 & 3 & 0 & -6 & 0 \\ 0 & -\sqrt{3} & \sqrt{3} & 2\sqrt{3} & 0 & -2\sqrt{3} \end{bmatrix} \tag{6.19}$$

The generalised stress-strain relationship for a plate links moments $\boldsymbol{M}$ to curvatures $\boldsymbol{\kappa}$

$$\boldsymbol{M} = \boldsymbol{D}\boldsymbol{\kappa} \tag{6.20}$$

$$\text{where} \quad \boldsymbol{M} = \left\{ \begin{array}{ccc} M_x & M_y & M_{xy} \end{array} \right\}^T \qquad \boldsymbol{D} = \begin{bmatrix} D_p & \nu D_p & 0 \\ \nu D_p & D_p & 0 \\ 0 & 0 & (1-\nu) D_p \end{bmatrix} \tag{6.21}$$

$$\text{and the plate bending stiffness,} \quad D_p = \frac{Et^3}{12(1-\nu^2)} \tag{6.22}$$

In the above, M_x and M_y are direct moments in the plate and M_{xy} is a twisting moment. The plate bending stiffness, D_p is formed from the Young's modulus, E, the plate thickness, t and Poisson's ratio, ν and is analogous to the quantity EI in beam bending. To ensure that element bending strain energy, for an element under pure bending, derived from the stiffness matrix agrees with the analytical solution for strain energy (Phaal and Calladine, 1992a), the moment-curvature matrix used is

$$\boldsymbol{D}' = \boldsymbol{I}_d \boldsymbol{D} \tag{6.23}$$

$$\text{where} \quad \boldsymbol{I}_d = \begin{bmatrix} 1 & 0 & 0 \\ 0 & 1 & 0 \\ 0 & 0 & 2 \end{bmatrix} \tag{6.24}$$

The element stiffness matrix $\boldsymbol{K}_b$ related to local axes then follows from

$$\boldsymbol{K}_b = \int_A \boldsymbol{B}^T \boldsymbol{D}' \boldsymbol{B} \, dA \tag{6.25}$$

The integration in Equation 6.25 can be computed analytically. The area A of the mesh associated with this element is not that of the entire six-noded, four-faceted element but the area of the centre facet alone. This takes account of the overlapping nature of these elements since each facet is overlapped by three others. This derivation of $\boldsymbol{K}_b$ can be easily adapted for elements of any geometry; the element in Figure 6.3(c) is used an example only. The similarities with the overlapping beam element described in Section 5.2.2 are now evident. The "legs" of the beam element are replaced here with four facets. Each beam "leg" is overlapped by one other element; each facet is overlapped by three other facets because of the use of triangular facets.

B: Flat six-noded plate element from mechanical analogy

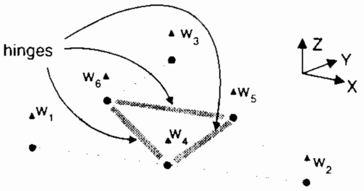

Figure 6.4: **Mechanical analogue of element**

The same stiffness matrix can be obtained by a slightly different route (Phaal and Calladine, 1992a) considering the element to be formed from three rigid facet plates joined by hinges to a central facet plate (see Figure 6.4). The hinges lie between node pairs 4/5, 5/6 and 6/4. Given nodal displacements, the angles across the hinges consistent with this mechanical analogy can be determined from kinematics;

$$\boldsymbol{\alpha} = \boldsymbol{L}\boldsymbol{d}_p \tag{6.26}$$

where $\boldsymbol{\alpha} = \{\ \alpha_1 \quad \alpha_2 \quad \alpha_3\ \}^T$ is the vector of angles at hinges 1,2 & 3. The matrix $\boldsymbol{L}$ comprises terms calculated from the flattened dimensions of each facet. The full matrix is given in Phaal and Calladine (1992a). For a state of unit curvature in the element,

$$\text{i.e.} \quad \boldsymbol{\kappa} = \{\ 1 \quad 1 \quad 1\ \}^T \tag{6.27}$$

equivalent nodal displacements can be obtained from Equation 6.1,

$$\text{e.g. given} \qquad \kappa_x = 1 \quad = \quad \frac{\partial^2 w}{\partial x^2} = 2c_4 \tag{6.28}$$

$$\text{then} \quad c_4 = \frac{1}{2} \qquad w_{1x} = \frac{x_1^2}{2} \tag{6.29}$$

where x_1 is the local x co-ordinate of node 1 and w_{1x} is the component of displacement at node 1 due to a unit curvature κ_x. Repeating for each combination of curvature and nodal degree of freedom yields a 6 × 3 matrix $\boldsymbol{C}$,

$$\boldsymbol{C} = \begin{bmatrix} x_1^2/2 & y_1^2/2 & x_1y_1 \\ x_2^2/2 & y_2^2/2 & x_2y_2 \\ x_3^2/2 & y_3^2/2 & x_3y_3 \\ x_4^2/2 & y_4^2/2 & x_4y_4 \\ x_5^2/2 & y_5^2/2 & x_5y_5 \\ x_6^2/2 & y_6^2/2 & x_6y_6 \end{bmatrix} \tag{6.30}$$

A matrix, $\boldsymbol{G}$, of the components of hinge rotation for each unit curvature, $\kappa_x, \kappa_y, \kappa_{xy}$, is obtained using the transformation matrix $\boldsymbol{L}$,

$$\text{i.e.} \quad \boldsymbol{G} = \boldsymbol{L}\boldsymbol{C} \tag{6.31}$$

so that G_{ij} is the angle at hinge i due to unit curvature in direction j, ($j = 1$, direction $= x$ etc.). For any curvature vector, $\boldsymbol{\kappa}$, the hinge angles are given by,

$$\boldsymbol{\alpha} = \boldsymbol{G}\boldsymbol{\kappa} \tag{6.32}$$

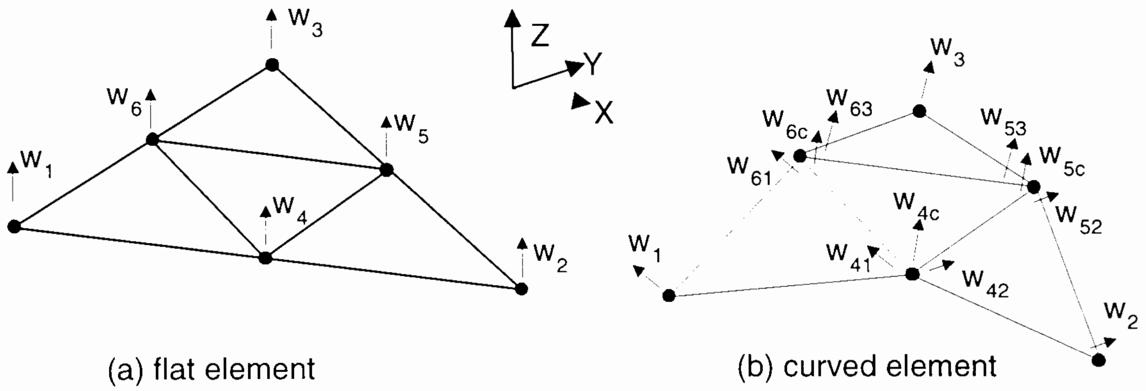

(a) flat element local freedoms

(b) curved element local freedoms

Figure 6.5: **Degrees of freedom on flat and curved elements**

then from Equation 6.26,

$$\boldsymbol{L}\boldsymbol{d}_p = \boldsymbol{G}\boldsymbol{\kappa} \tag{6.33}$$

$$\boldsymbol{\kappa} = \boldsymbol{G}^{-1}\boldsymbol{L}\boldsymbol{d}_p \tag{6.34}$$

Comparison with Equation 6.15 gives the strain-displacement matrix $\boldsymbol{B}$ as,

$$\boldsymbol{B} = \boldsymbol{G}^{-1}\boldsymbol{L} \tag{6.35}$$

The stiffness matrix, $\boldsymbol{K}_b$ follows by the same procedure adopted in Section 6.3A. This derivation introduces the mechanical analogy of rigid facets and hinges as carried out for the overlapping beam element of Section 5.2.2.1B.

C: Curved six noded plate element from mechanical analogy

The derivation above permits the formulation of the plate element to be extended to an initially curved element where the hinges between facets are imagined to have initial rotations. Local degrees of freedom remain lateral displacements since the formulation is still effectively that of a plate (i.e. a bending) element. However, the lateral displacements are now set with respect to the rotated facets. At corner nodes (1,2,3) the direction of the new degrees of freedom is straightforward (see Figure 6.5). At nodes lying on hinge lines, the degrees of freedom are expanded to give one lateral freedom to each of the three facets meeting at the node. The "expanded" element therefore possesses twelve local degrees of freedom,

$$\boldsymbol{d}_{be} = \{\ w_1 \quad w_2 \quad w_3 \quad w_{41} \quad w_{4c} \quad w_{42} \quad w_{53} \quad w_{5c} \quad w_{52} \quad w_{61} \quad w_{6c} \quad w_{63}\ \}^T \tag{6.36}$$

Following the convention in Phaal and Calladine (1992b), these degrees of freedom are numbered according to the node and facet to which they relate. Considering a flattened element, the degrees of freedom on the flat plate (of A and B above) can be linked to the expanded element displacements $\boldsymbol{d}_{be}$ by,

$$\boldsymbol{d}_{be} = \boldsymbol{X}\boldsymbol{d}_p \quad \text{where} \boldsymbol{X} = \begin{bmatrix} 1 & 0 & 0 & 0 & 0 & 0 & 0 & 0 & 0 & 0 & 0 & 0 \\ 0 & 1 & 0 & 0 & 0 & 0 & 0 & 0 & 0 & 0 & 0 & 0 \\ 0 & 0 & 1 & 0 & 0 & 0 & 0 & 0 & 0 & 0 & 0 & 0 \\ 0 & 0 & 0 & 1 & 1 & 1 & 0 & 0 & 0 & 0 & 0 & 0 \\ 0 & 0 & 0 & 0 & 0 & 0 & 1 & 1 & 1 & 0 & 0 & 0 \\ 0 & 0 & 0 & 0 & 0 & 0 & 0 & 0 & 0 & 1 & 1 & 1 \end{bmatrix}^T \tag{6.37}$$

An equivalent relation to Equation 6.26 can be written for the hinge angles on the expanded element,

$$\boldsymbol{\alpha} = \boldsymbol{L}^e \boldsymbol{d}_{be} \tag{6.38}$$

Similarly, the matrix of components of nodal displacement due to unit curvatures (Equation 6.30) can be written for the expanded element as ,

$$\boldsymbol{C}^e = \boldsymbol{X}\boldsymbol{C} \tag{6.39}$$

since the displacements at degrees of freedom $\boldsymbol{d}_{be}$ and $\boldsymbol{d}_p$ are equivalent. By similar reasoning to the derivation in B above, the strain-displacement matrix for the expanded element is,

$$\boldsymbol{B}^e = \boldsymbol{G}^{-1}\boldsymbol{L}^e \tag{6.40}$$

$$\text{where} \quad \boldsymbol{G} = \boldsymbol{L}^e \boldsymbol{X}\boldsymbol{C} \tag{6.41}$$

and the local stiffness matrix for the expanded element, $\boldsymbol{K}_{b\epsilon}$ follows from $\boldsymbol{B}^e$ by the standard procedure. Now, the formulation can accommodate an initial curvature through the splitting of the midside node degrees of freedom. The procedure outlined above can be viewed as the splitting of the assumed interpolation field into separate fields over each facet with a discontinuity along hinges.

The global stiffness matrix, $\boldsymbol{K}_{b\epsilon g}$ of the overlapping plate element is obtained using a transformation matrix, $\boldsymbol{T}_\epsilon$ as described for the two-dimensional, overlapping beam element in Section 5.2.2.1. Here the components of $\boldsymbol{T}_\epsilon$ (a 12×18 matrix) are the unit normal vectors to each facet, considered flat between defining nodes.

$$\boldsymbol{K}_{b\epsilon g} = \boldsymbol{T}_\epsilon^T \boldsymbol{K}_{b\epsilon} \boldsymbol{T}_\epsilon \tag{6.42}$$

The above deals with the calculation of bending terms. To the global matrix $\boldsymbol{K}_{b\epsilon g}$, in-plane, membrane stiffness terms must be added from the overlain constant strain triangles. One approach is to overlay only the membrane stiffness relating to the centre facet of the element. Another is to add terms for membrane stiffness for all four facets on an element, factoring each to account for the number of overlaps. The second approach is adopted here since it results in element stiffness matrices with fully populated leading diagonals. This then removes any problems, with pivoting for example, at the solution stage.

For each element, the stiffness matrix of a constant strain triangle element, of equivalent dimensions to each flattened facet on the element, is formed. This results in some duplication of effort unless the individual membrane element matrices are saved and reused in subsequent elements. However, the formation of one of these element matrices is a minor computational operation since the terms are fully determined without recourse to numerical integration. The factor applied to the membrane stiffness terms is found from a record of the number of overlaps to each outer facet of an element.

which is made immediately after the data input stage of the analysis and is described in more detail in Section 7.3.2.

6.3.1 Boundary conditions

Similar problems are met accommodating specified boundary conditions with this overlapping formulation as described for the two-dimensional overlapping element (see Section 5.2.2.2). Since the elements have no rotational degrees of freedom at nodes, it is not possible to fix or free rotations at the solution stage as would be possible with conventional shell elements. Instead, amendments are made to the element stiffness matrices themselves to account for rotational freedoms. Translational fixities are included at the solution stage in common with conventional elements. The membrane stiffness of an element requires no alteration at boundaries.

Figure 6.6(a) shows part of a mesh of shell elements adjacent to a domain boundary. The elements shown hatched are complete since their outer facets are all within the domain. The other elements are incomplete since one or two edges of the central facet lie on the domain boundary. The formulation requires that, for these incomplete elements, an imaginary outer facet is generated beyond the domain boundary. For elements having two edges on a boundary (such as element A in Figure 6.6(a)) two imaginary outer facets are required. These imaginary facets complete the elements and allow their stiffness matrices to be derived in the same manner as for the originally complete elements. Alterations or omissions are made to the resulting stiffness matrices depending on the nature of the boundary condition.

Unlike the overlapping beam element, rotational boundary conditions are accounted for here by direct modelling of the physical effect of the different boundaries. Where

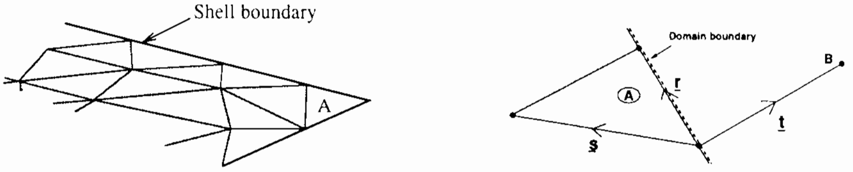

(a) (b)

Figure 6.6: **Overlapping elements at boundaries**

constraint equations are formed they are not used to form transformation matrices to apply to the global element stiffness of an element adjacent to a boundary. This is a result of the particular development history of this project. Transformation matrices could be used here to give the same results.

6.3.2 Simple supports and free edges

A simply-supported boundary is one where displacements are fixed but rotations are free. Free and simply-supported edges are accounted for in a similar manner with the overlapping shell element. The local element stiffness matrix, $\boldsymbol{K}_{be}$ is formed having determined the location of a *fictitious* node beyond the boundary. This is found by reflection of an existing centre facet side across the boundary as shown in Figure 6.6(b). If $\underline{\hat{r}}$ is a unit position vector along the boundary and $\underline{s}$ is a position vector along the centre facet edge to be reflected, then fictitious node B is located with the position vector, $\underline{t}$ where,

$$\underline{t} = [R] \quad \underline{s} \tag{6.43}$$

and,

$$[R] = \begin{bmatrix} 2r_x^2 - 1 & 2r_x r_y & 2r_x r_z \\ 2r_x r_y & 2r_y^2 - 1 & 2r_y r_z \\ 2r_x r_z & 2r_y r_z & 2r_z^2 - 1 \end{bmatrix} \tag{6.44}$$

where subscripts refer to components of $\underline{\hat{r}}$ in the global X, Y, Z directions. The fictitious node location is generated solely for the derivation of $\boldsymbol{K}_{be}$ and has no analysis results associated with it. Transformation to global co-ordinates is also carried out for the full matrix; it is after this stage that the unwanted terms are removed from the matrix. These are the terms related to global degrees of freedom on *fictitious* nodes. The terms also include the effects of the outer facet to which they are attached, through the transformation procedure, so that the final stiffness contains no contribution from the *fictitious* facets. An alternative approach is to formulate only those members of the element stiffness matrix which will be assembled before solution. This would remove the benefit of having element stiffness matrices of the same dimensions which simplifies considerably the coding for variable passing between subroutines.

The condition that the rotations are free at a simply supported edge implies that those rotations do not contribute to the element curvature for the purposes of calculating stress resultants. To understand this with the shell elements we again use the hinged facet idealisation. To remove the effect of a rotation on the simply-supported edge, the appropriate column of the matrix $\boldsymbol{G}^{-1}$ (where $\boldsymbol{G} = \boldsymbol{L}^e\boldsymbol{X}\boldsymbol{C}$ in Equation 6.41) is set to zero. For example, if node 2 on an element is fictitious then the effect of α_2 is removed by setting column two in $\boldsymbol{G}^{-1}$ to zero. This is implemented in the routine where the matrix $\boldsymbol{B}^e$ is formed.

6.3.3 Fixed and symmetrical boundaries

A fixed edge has displacements and slopes fixed at zero with curvature non-zero, leading to a possible moment reaction. A symmetrical boundary in a mesh of continua elements can be modelled by fixing the translational degree-of-freedom perpendicular to the symmetry plane and allowing only rotational degrees of freedom with vectors

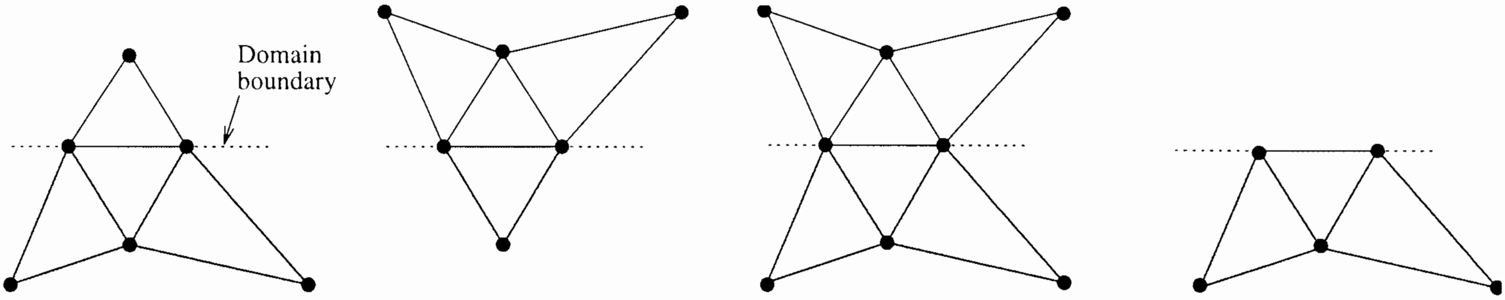

Real element Fictitious element Combined element Reduced element

Figure 6.7: **Addition & removal of fictitious element**

perpendicular to the symmetrical plane. This is simple to impose with conventional elements, providing the plane of symmetry is parallel to a global co-ordinate plane. A symmetrical boundary applies the same constraints as a fixed one but with some translational degrees of freedom released. For this reason, these two boundary conditions are modelled in the same way.

Shell elements having a centre facet edge on either a fixed or symmetrical boundary require a revised global stiffness matrix, $\boldsymbol{K}^{r}_{beg}$ to be generated. Firstly, a global stiffness matrix $\boldsymbol{K}^{c}_{beg}$ is formed, comprising the original element $\boldsymbol{K}_{beg}$ plus a global stiffness matrix $\boldsymbol{K}^{f}_{beg}$ for a fictitious element, overlapping the original element. The relationship between the original (or real) element and the fictitious element is demonstrated in Figure 6.7. Constraint equations are formed describing symmetrical displacements across the boundary. These reduce $\boldsymbol{K}^{c}_{beg}$ from 18 x 18 (for the combined, eight-noded, six-faceted element of Figure 6.8) down to a 12 x 12 matrix ($\boldsymbol{K}^{r}_{beg}$) for a six-noded element. This is further reduced, following transformation, to remove terms associated with the fictitious node on the real element in the same manner as for simply-supported and free edges.

The implementation of the procedure described above commences with the rearrangement of the original element stiffness matrix, $\boldsymbol{K}_{beg}$, determined for the real element on

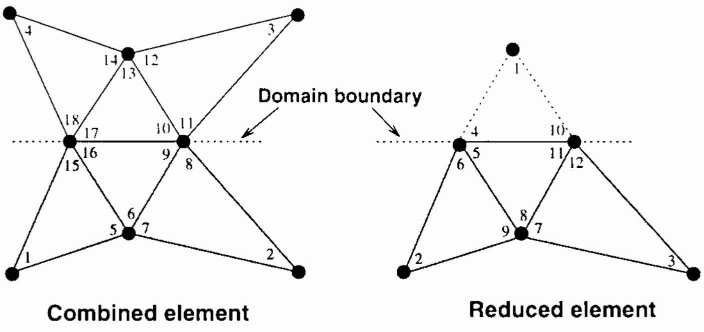

Figure 6.8: **Fixed and symmetrical boundaries, d.o.f. numbering**

the boundary, as if node 1 were the missing node. This step is to simplify coding. For elements where node nos. 2 & 3 respectively are missing, mapping vectors for local shell degrees of freedom to modify to node 1 missing are:

$$\boldsymbol{\beta}_2 = \{\, 3 \;\; 1 \;\; 2 \;\; 12 \;\; 11 \;\; 10 \;\; 6 \;\; 5 \;\; 4 \;\; 7 \;\; 8 \;\; 9 \,\}^T \tag{6.45}$$

$$\text{and, } \boldsymbol{\beta}_3 = \{\, 2 \;\; 3 \;\; 1 \;\; 9 \;\; 8 \;\; 7 \;\; 10 \;\; 11 \;\; 12 \;\; 6 \;\; 5 \;\; 4 \,\}^T \tag{6.46}$$

Then the terms k_{kl} of the rearranged element stiffness matrix are found from the original terms, k_{ij} as,

$$k_{kl} = k_{ij}, \quad i = \beta(k);\ j = \beta(l);\ k = 1, 12;\ l = 1, 12 \tag{6.47}$$

Since the fictitious element is a reflection of the real element on the boundary, its global stiffness matrix, $\boldsymbol{K}^f_{b\epsilon g}$ is $\boldsymbol{K}_{b\epsilon g}$ rearranged. The nodal numberings for the real and fictitious elements are given in Figure 6.8(b). The two stiffness matrices are combined to give $\boldsymbol{K}^c_{b\epsilon g}$, related to the 18 global degrees of freedom on the pair of elements, overlapping the boundary.

The rotational boundary conditions are now imposed. These consist of equal deflections and forces on symmetrical nodes in the combined element. For example, in terms of deflections:

$$w^r_1 = w^r_8 = w_6 = w_{13}$$

$$w^r_2 = w_1 = w_4$$

$$\begin{aligned}
w_3^r = w_2 &= w_3 \\
w_4^r = w_5^r &= w_{16} = w_{17} \\
w_6^r = w_{15} &= w_{18} \\
w_7^r = w_7 &= w_{12} \\
w_9^r = w_5 &= w_{14} \\
w_{10}^r = w_{11}^r &= w_9 = w_{10} \\
w_{12}^r = w_8 &= w_{11}
\end{aligned} \tag{6.48}$$

where the superscript r denotes deflections on the reduced element. A similar set of equations can be written for the forces $\boldsymbol{f}_c$ at each degree of freedom. These are effectively constraint equations applied to the finite element equations for the combined elements,

$$\boldsymbol{K}_{b\epsilon g}^{c}\boldsymbol{d}_c = \boldsymbol{f}_c \tag{6.49}$$

where $\boldsymbol{d}_c$ is the vector of global displacements at the 18 degrees of freedom on the combined element. The combination of constraint equations and the combined global stiffness matrix reduces the number of degrees of freedom to those of the reduced element. Manipulation of Equations 6.48and 6.49 gives the global stiffness matrix of the reduced element,

$$\boldsymbol{K}_{b\epsilon g}^{r} = \boldsymbol{K}_{b\epsilon g} + \boldsymbol{K}_a \tag{6.50}$$

where the upper diagonal members of the symmetrical matrix, $\boldsymbol{K}_a$ are:

$$\left[\begin{array}{cccccccccccc}
0 & 0 & 0 & 0 & 0 & 0 & 0 & 0 & 0 & 0 & 0 & 0 \\
 & 0 & 0 & 0 & k_{2,4} & 0 & 0 & k_{2,1} & 0 & 0 & k_{2,10} & 0 \\
 & & 0 & 0 & k_{3,4} & 0 & 0 & k_{3,1} & 0 & 0 & k_{3,10} & 0 \\
 & & & 0 & 0 & 0 & 0 & 0 & 0 & 0 & 0 & 0 \\
 & & & & k_{4,4}+2k_{4,5} & k_{4,6} & k_{4,7} & k_{1,4}+k_{1,5}+k_{4,8} & k_{4,9} & 0 & k_{4,10}+k_{5,10}+k_{4,11} & k_{4,12} \\
 & & & & & 0 & 0 & k_{1,6} & 0 & 0 & k_{6,10} & 0 \\
 & & & & & & 0 & k_{1,7} & 0 & 0 & k_{7,10} & 0 \\
 & & & & & & & k_{1,1}+2k_{1,8} & k_{1,9} & 0 & k_{1,10}+k_{1,11}+k_{8,10} & k_{1,12} \\
 & & & & & & & & 0 & 0 & k_{9,10} & 0 \\
 & & & & & & & & & 0 & 0 & 0 \\
 & & & & & & & & & & k_{10,10}+2k_{10,11} & k_{10,12} \\
 & & & & & & & & & & & 0
\end{array}\right] \tag{6.51}$$

Finally $\boldsymbol{K}^r_{beg}$ is rearranged to reflect the actual missing node, the reverse of the process given above in Equations 6.45 and 6.46. A fixed boundary condition is imposed exactly as above but the boundary nodes have all translational degrees of freedom fixed. Since the same translational fixities are required for a simply supported edge and a fixed edge and due to the absence of rotational degrees of freedom it is necessary to define, in the input data file, the location of simply supported and fixed or symmetrical boundaries. In the implementation of this element in *OXFEM*, lists of nodes along these boundary types are given.

6.4 Stress updating for the overlapping shell element

The calculation of stress resultants for the overlapping shell element follows the conventional structure adopted in *OXFEM*. Firstly, global displacements calculated from the solution of the structure stiffness matrix are converted to local membrane and bending degrees of freedom and strains are calculated using the same $\boldsymbol{B}$ matrix as used in the formation of the element stiffness matrix. This is carried out for the bending stiffness and the membrane stiffness separately. The strain vector for the element then comprises three in-plane strains and three curvatures (from $\boldsymbol{\kappa}$).

Secondly, and again separately for the bending and membrane effects, six stress resultants, $\boldsymbol{\sigma}$, are found for each element using the $\boldsymbol{D}$ matrices for membrane and bending effects. $\boldsymbol{\sigma}$ consists of one shear and two direct membrane stresses and three moments (Equation 6.21). Finally, forces at nodes, in equilibrium with the calculated stress resultants, are calculated using,

$$\boldsymbol{f}_{b\epsilon} = \int_V \boldsymbol{B}^T \boldsymbol{\sigma} \tag{6.52}$$

and are then transformed to global co-ordinates. This stage is not strictly necessary with the shell elements as implemented here since their behaviour is linear, by virtue of the (linear elastic) material model used. It is implemented to provide a check on the behaviour and to permit future non-linear material modelling.

6.4.1 Boundary conditions

As in the stiffness matrix formation, elements adjacent to boundaries require special treatment for the bending effects. In calculating curvatures at the first stage of updating, fictional nodes beyond boundaries are again formed for elements having boundary edges. Local displacements are attributed to the local degrees of freedom associated with the fictional node in accordance with the constraint provided by the boundary. The displacements are calculated using constraint equations such as those in Equation 6.48 above. In this way, the incorporation of displacements at fictitious nodes allows all elements to be treated the same for the calculation of curvatures. The strain-displacement matrix $\boldsymbol{B}_\epsilon$ is calculated by the same procedure as adopted in the stiffness matrix formation

For the final stage of updating (i.e. Equation 6.52), fixed and symmetrical edge elements require the formation of an alternative $\boldsymbol{B}_\epsilon$ matrix to take account of the use of a fictitious element at the stiffness matrix formation stage. Each column of $\boldsymbol{B}_\epsilon$ related to a fictional degree of freedom (i.e. the three on the fictitious facet of the real element) is added to the column related to its real counterpart. Taking the reduced element in Figure 6.8 columns 5, 8, and 11 of $\boldsymbol{B}_\epsilon$ (the real degrees of freedom on the centre facet) would be supplemented by the corresponding values in columns 4, 1 and 10 (the degrees of freedom on the facet beyond the boundary), respectively. This increases the forces calculated in Equation 6.52 at the real degrees of freedom to reflect the rotational stiffness of the boundary. The procedure effectively adds the forces from the overlapping outer facet of the fictional element.

This concludes the explanation of the overlapping shell element formulation which was implemented in the analysis program *OXFEM*. Details of testing are given in 6.6 but prior to this, the proposed method of modelling volume loss is discussed with respect to the particular element formulation.

6.5 Modelling volume loss

In three-dimensions the procedure for modelling volume loss is similar to that described for two-dimensional analyses since forces are calculated which result in membrane only strain in the lining elements. Volume loss is modelled by reducing the volume enclosed by a group of shell elements which line an increment of the tunnel excavation. The input data required is the volume loss, as in two-dimensions and (unlike the two-dimensional case) the global orientation of the tunnel centreline. The centreline defines

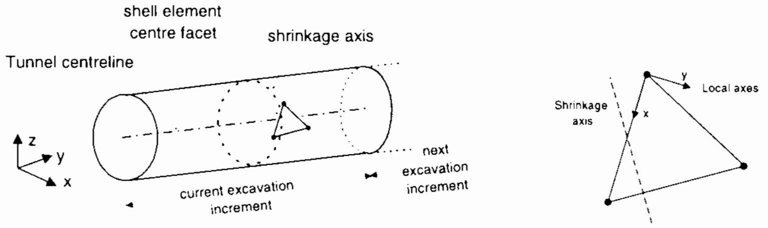

(a) (b)

Figure 6.9: **Three-dimensional volume loss modelling**

the circumferential shrinkage axis along which uniform direct strain leads to uniform volume shrinkage. Figure 6.9(a) shows the relationship between the tunnel centreline and this axis.

For each element, the nodal loads required to cause direct strain in the direction of the axis defined above are calculated and then transformed to global co-ordinates and added to the external load vector. The local nodal loads are given by

$$\boldsymbol{f}_{ax} = \int_A \boldsymbol{B}^T \boldsymbol{D} \epsilon_l \, dA \tag{6.53}$$

where $\boldsymbol{B}$ is the strain-displacement matrix and $\boldsymbol{D}$ is the material constitutive matrix, both for a constant strain triangle element of the size of the central facet. ϵ_l is the strain vector with respect to the local co-ordinate system of the facet (see Figure 6.9(b)) obtained from the single direct strain along the shrinkage axis using simple strain transformation. A is the in-plane area of the central facet.

Additional complications arise in three-dimensions with incremental excavation. Application of shrinkage loading to a group of elements will affect elements activated in previous stages if there is a connection between them, which is usually the case. This leads to over-shrinkage and an incorrect magnitude of volume loss. Figure 6.10 illustrates this problem. The first group of shell elements is activated and shrunk satisfactorily. The second group of shells is then activated and shrunk. This includes

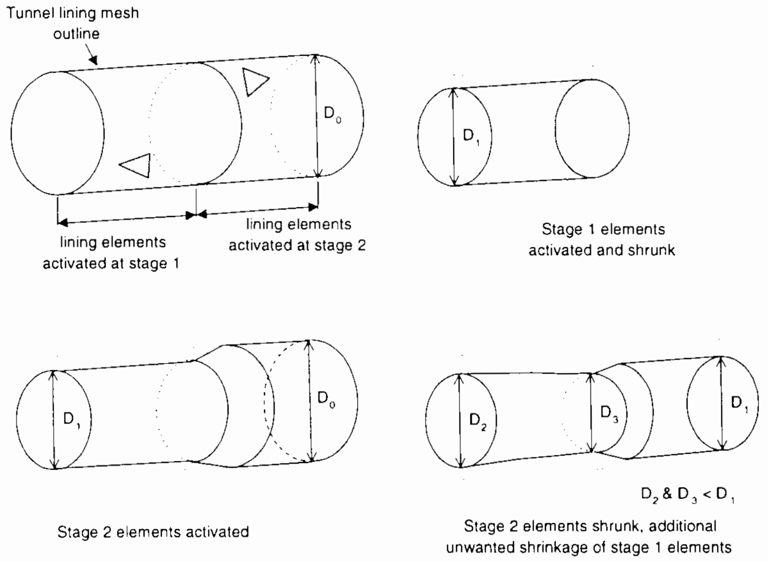

Figure 6.10: **Incremental shrinkage problem in three-dimensions**

the imposition of additional nodal loads at the junction of the groups of elements, thus leading to extra deformation in the first group of elements. To remove this problem, it is necessary to fix the nodes on the leading edge of the tunnel lining (i.e. those at the face of the current excavation) when applying the shrinkage loading. The nodes are released at the next stage of excavation and the effect of the fixing is eliminated by applying the reaction forces calculated at the fixities in reverse, also at the subsequent stage. The inclusion of these fixities is a minor additional constraint on the mesh which appears unavoidable with the three-dimensional model.

6.6 Validation and testing

The formulation of the overlapping shell element was tested with a large range of problems in Phaal and Calladine (1992b). The aim of these tests was to prove the viability of the element for analysis of complex shell problems. Difficulties arose in doing this since there are very few shell problems for which analytical solutions are known to exist. The testing of this implementation of the element in *OXFEM* did not seek to repeat Phaal & Calladine's test programme but to test in sufficient detail to ensure that the elements agreed with some of the analytical solutions available and gave results which compared well to those found from a similar, but more complex, element available in the commercial package *I-DEAS*. The elements were also tested to ensure that volume loss could be modelled as described in Section 6.5. The tests concentrated on the displacement results since the stress-resultants in the lining were of secondary interest to the main aims of the project.

Where tests were repeated in *I-DEAS* a three-noded faceted element was selected. This element is comprised of constant strain triangles overlaid with three-noded plate elements having two rotational degrees of freedom at each node and therefore is a conventional faceted formulation. The formulation of the element is described by Razzaque (1973). The drilling degree of freedom problem highlighted in Section 6.2.1 is dealt with in this element using a penalty function approach which adds a notional stiffness to the in-plane rotations at nodes without preventing rigid-body rotations. This element was the closest available in *I-DEAS* to the overlapping shell element formulation.

Four test problems are now described and results are presented. A general discussion of these results follows in Section 6.6.5.

6.6.1 Test 1 - flat square plate

The first test problem, (Figure 6.11(a)), was a flat square plate under a single central point load supported on all edges. This problem tested the flexural response of the element, i.e. the overlapping plate element component of the shell. Both fixed and simply-supported plates were analysed. Two structured mesh geometries were used, symmetric and skewed, for each boundary condition. For each mesh geometry, four

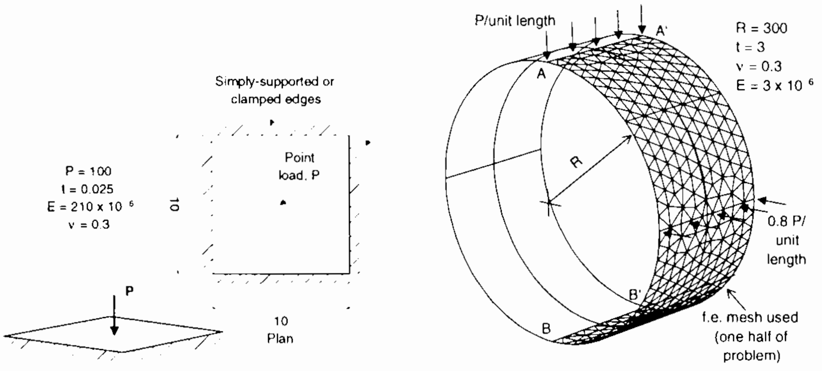

(a) Test 1 (b) Test 2

Figure 6.11: **General layouts of test problems 1 & 2**

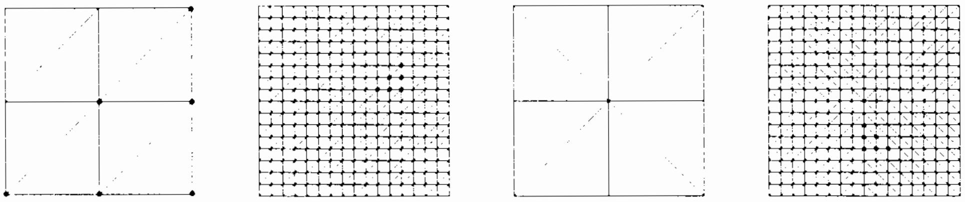

(a) coarse skew (b) fine skew (c) coarse symm. (d) fine symm.

Figure 6.12: **Plan views of meshes used in test 1**

analyses were carried out using increasingly refined meshes. Each symmetrical analysis was repeated with a quarter-size mesh and symmetrical boundary conditions to check the implementation of the latter. The coarsest and finest of the four meshes used for each geometry are shown in Figure 6.12. All analyses were repeated in *I-DEAS* for comparison. The displacements under the load predicted in the analyses are plotted in Figures 6.13(a) and 6.13(b). All results are normalised with respect to the analytical solutions (for each boundary condition) given in Pilkey (1994).

The results show slow convergence to the analytical solutions for displacements for the overlapping elements, especially for symmetrical meshes. That the element formulation is sensitive to element topology is alluded to in the original description of this formulation (Phaal and Calladine, 1992b) although the expectation would probably be

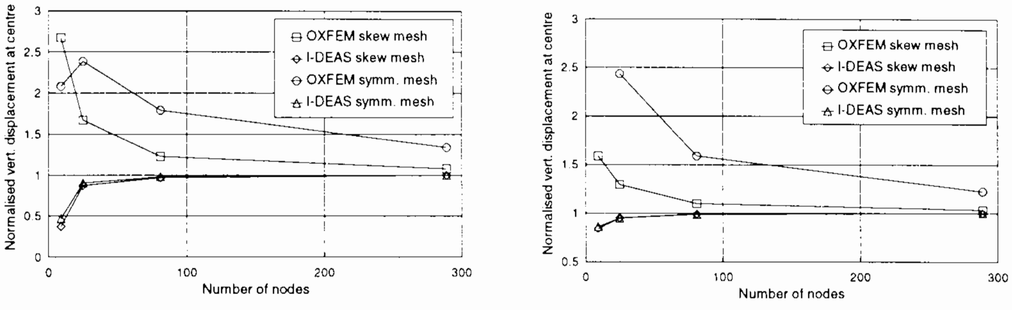

(a) Simple supports (b) Fixed supports

Figure 6.13: **Test 1 results**

that the symmetrical mesh would perform better, rather than worse, than the skew mesh. The *I-DEAS* analyses give much better convergence to the analytical solutions and do not exhibit marked differences between mesh topologies.

6.6.2 Test 2 - Three-dimensional ring under line loads and shrinkage

This test comprised the analysis of a thin circular cylinder (shown in Figure 6.11(b)) subjected to three loadings. The first loading comprised a vertical line load at the cylinder crown and a smaller horizontal line load at its springing level. The purpose of this test was to compare results with *I-DEAS* analyses for a simple arrangement of loads similar to that expected of a flexible tunnel in soft ground. The load at the springing level was 0.8 times the crown load to model a value of earth pressure at rest (K_0) of below 1, as might be expected in a normally consolidated clay. Clearly, the loading arrangement was highly simplistic but enabled checking of the combined bending and membrane behaviour of the shells, since it was unsymmetrical.

Stage 2 of this test involved removal of the line loads and imposition of a uniform membrane shrinkage load as required to model volume loss. The line loads were reap-

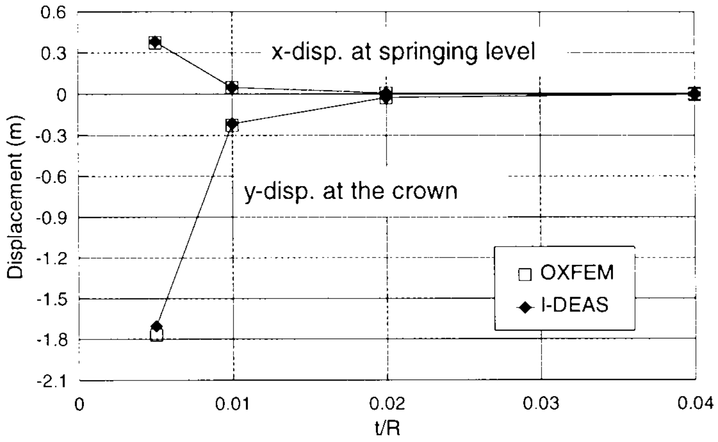

Figure 6.14: **Test 2: displacement results**

plied in a final stage to check that the response was fully elastic by comparison of the combined effect with the sum of the two loadings applied individually. The second and final stages of loading could not be compared with an *I-DEAS* analysis because no facilities existed, in that program, to model shrinkage loads. The mesh used in the analyses covered one-half of the full cylinder due to symmetry and contained 520 overlapping shell elements and 298 nodes. The boundary conditions imposed on the mesh were symmetrical along AA' and clamped along BB' (see Figure 6.11(b)).

The displacements predicted by *OXFEM* under each of the line loads for the first stage of loading are compared with results from *I-DEAS* analyses in Figure 6.14. There is strong agreement between the two programs which is encouraging. Due to the lack of rotational degrees of freedom in the overlapping shell element formulation, the *OXFEM* mesh has one-half the number of degrees of freedom showing that a more economical solution is available, with this particular loading arrangement, using the overlapping shell elements.

The deformed shapes of the mesh, predicted using *OXFEM*, are shown (as end elevations) in Figure 6.15 for each stage of loading. The deformations are uniform with respect to the axial co-ordinate (Y) as expected. Table 6.1 gives the displacements at

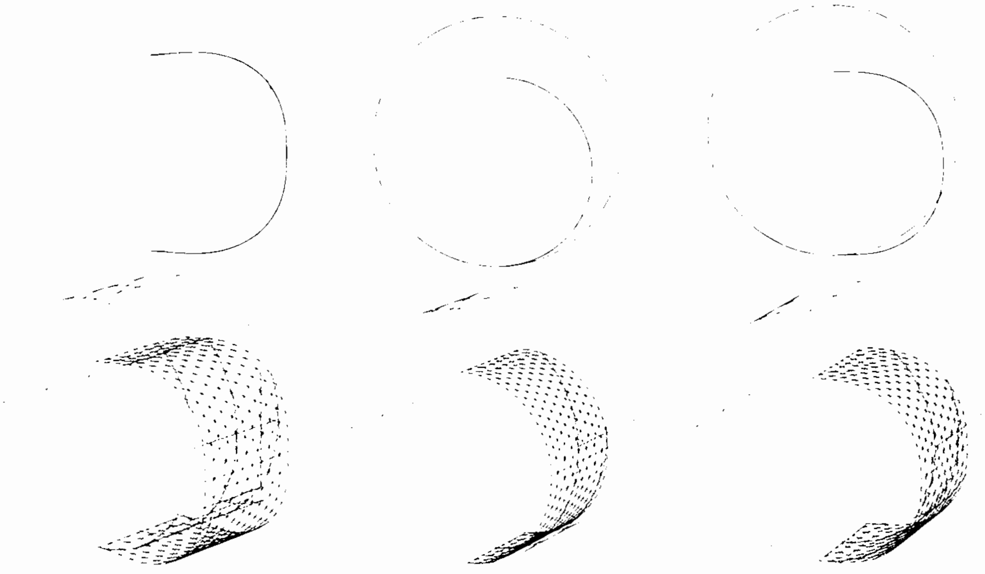

(a) stage 1 (b) stage 2 (c) stage 3

Figure 6.15: **Test 2: deformed meshes for load stages**

Table 6.1: **Test 2** *OXFEM* **results.**

	Displacement at crown			*Displacement at springing*		
Load Case	X	Y	Z	X	Y	Z
1: Line loads only	0.0	0.195×10^{-3}	−1.7682	0.3738	0.3534×10^{-3}	−0.87476
2: Shrinkage only	0.0	-0.1490×10^{-3}	−3.0226	−1.5072	-0.303×10^{-4}	−1.51032
3: Combined	0.0	-0.4530×10^{-4}	−4.7910	−1.1333	-0.3245×10^{-3}	−2.3850

crown and springing level for all three load arrangements demonstrating that stage 1 and stage 2 results sum to stage 3 results.

6.6.3 Test 3 - Lined elastic tunnel

The third test problem involved analysis of meshes containing shell and continuum elements and as such, was close to the tunnelling problem. The situation modelled is that of the excavation of a tunnel at depth through an initially prestressed but weightless linear elastic medium. The tunnel is coincidentally lined with a linear elastic thin shell. An analytical solution exists for this problem in Einstein and Schwartz (1979) (cited in Section 2.2.1) where complex curved shell theory (Flügge, 1966) is used.

A tunnel of radius, $R = 2.5$m was modelled in a cube of ground with 60m sides. The mesh consisted of 1691 nodes, 965 ten-noded tetrahedral elements to model the ground and 360 overlapping shell elements for the lining. One quarter of the whole problem was modelled, as shown in Figure 6.16 to take advantage of symmetry. Boundary conditions consisted of freedom of movement in the plane of each boundary face, i.e. no normal displacments. Shell symmetric boundaries were specified along all edges of the lining element mesh. Initial compressive stress was applied to the complete ground mesh without the lining element; in each case the vertical stress was 1000kN/m^2. The tunnel elements were then excavated coincidentally with activation of the lining elements.

While the main aim of this test was to check the performance of the shell elements under similar conditions (e.g. material properties) to those likely to occur in a tunnelling analysis, the opportunity was taken to widen the bounds of the test to examine the performance of the elements with a wider range of material properties and initial conditions. Three groups of analyses were carried out, with different values for K_0 (the ratio of horizontal to vertical initial stress) and Poisson's ratio for the ground ν_{ground} as follows,

1. $K_0 = 0.5, \nu_{ground} = 0.25$
2. $K_0 = 0.8, \nu_{ground} = 0.25$

Table 6.2: Details of analyses undertaken for test problem 3

No.	E/E_l	t/R	ν_{ground}	K_0	*No.*	E/E_l	t/R	ν_{ground}	K_0	*No.*	E/E_l	t/R	ν_{ground}	K_0
T1A	0.0005	0.05	0.25	0.5	T4A	0.0005	0.05	0.25	0.8	T7A	0.0005	0.05	0.49	0.8
T1B	0.005	0.05	0.25	0.5	T4B	0.005	0.05	0.25	0.8	T7B	0.005	0.05	0.49	0.8
T1C	0.05	0.05	0.25	0.5	T4C	0.05	0.05	0.25	0.8	T7C	0.05	0.05	0.49	0.8
T1D	0.5	0.05	0.25	0.5	T4D	0.5	0.05	0.25	0.8	T7D	0.5	0.05	0.49	0.8
T2A	0.0005	0.075	0.25	0.5	T5A	0.0005	0.075	0.25	0.8	T8A	0.0005	0.075	0.49	0.8
T2B	0.005	0.075	0.25	0.5	T5B	0.005	0.075	0.25	0.8	T8B	0.005	0.075	0.49	0.8
T2C	0.05	0.075	0.25	0.5	T5C	0.05	0.075	0.25	0.8	T8C	0.05	0.075	0.49	0.8
T2D	0.5	0.075	0.25	0.5	T5D	0.5	0.075	0.25	0.8	T8D	0.5	0.075	0.49	0.8
T3A	0.0005	0.1	0.25	0.5	T6A	0.0005	0.1	0.25	0.8	T9A	0.0005	0.1	0.49	0.8
T3B	0.005	0.1	0.25	0.5	T6B	0.005	0.1	0.25	0.8	T9B	0.005	0.1	0.49	0.8
T3C	0.05	0.1	0.25	0.5	T6C	0.05	0.1	0.25	0.8	T9C	0.05	0.1	0.49	0.8
T3D	0.5	0.1	0.25	0.5	T6D	0.5	0.1	0.25	0.8	T9D	0.5	0.1	0.49	0.8

3. $K_0 = 0.8, \nu_{ground} = 0.49$

The last of these groups most closely modelled the situation present in the tunnelling analyses. Within these groups, the ratio of the stiffnesses of the ground and support, measured by the ratio E/E_l, was varied. E was the Young's modulus associated with the ground and E_l that associated with the lining. Throughout, $E = 5 \times 10^{-4}\mathrm{kN/m^2}$ was used and analyses were undertaken for three lining thickness t between 125mm and 250mm. Details of all 36 analyses carried out of this problem are given in Table 6.2.

Single results from each of the analyses, the horizontal displacement of a node lying on the tunnel springing line at the centre of the mesh, are presented here in Figure 6.18. For each combination of t/R, K_0 & ν_{ground}, the results from each of four analyses, varying E/E_l, are plotted against the analytical solutions of Einstein and Schwartz (1979). A positive value of this displacement indicates movement away from the tunnel centreline. Some general trends are visible,

- At high values of E/E_l, movement is inwards since the tunnel lining is providing very little support and the excavation is deforming as if it were virtually unlined.

- At low values of E/E_l, the movement is outwards since the lining stiffness is significant. The greater vertical stress causes the lining to distort into a flat ellipse.

- At very low values of E/E_l, the movement reduces as the lining approaches the fully rigid state where no distortion is possible.

Aside from these general trends, which are also discussed by Einstein and Schwartz (1979), it is noticeable that as K_0 increases, the resistance to outward movement increases and at low values of E/E_l the outward movement becomes very small without a well-defined peak. The overlapping shells give a stiffer response (approximately twice as stiff) than predicted by the analytical solution in all cases but equally, follow the trends of the latter. The switch from inward to outward displacements occurs at approximately the same value of E/E_l. Agreement is also improved for the second and third group of analyses which approach the conditions found in a typical tunnelling analysis.

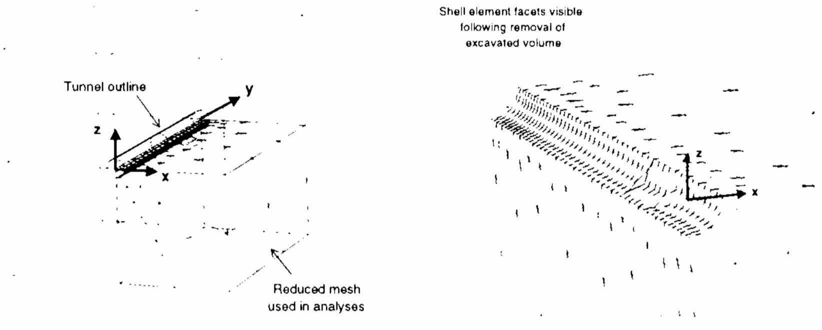

(a) Mesh used in test 3 (b) Close up around tunnel

Figure 6.16: **Mesh used for test 3**

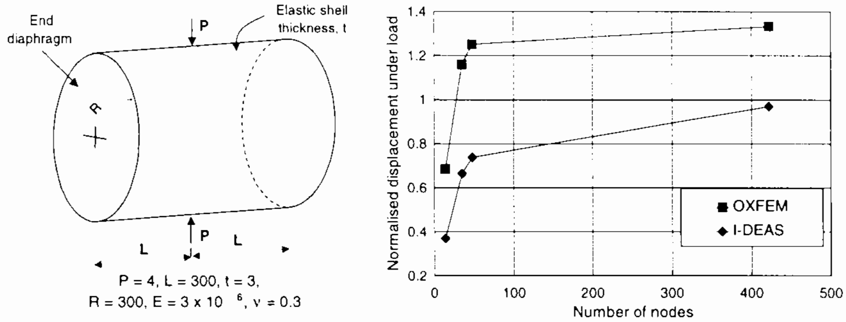

(a) General arrangement (b) Displacement results

Figure 6.17: **Test 4: Pinched cylinder problem**

6.6.4 Test 4 - Pinched cylinder

The final test problem was a repeat of a test undertaken by Phaal and Calladine (1992b). A thin-walled cylinder was subjected to two opposite point loads across a diameter at midspan. The cylinder was supported at each end by diaphragms permitting rotation and axial movement but preventing radial movement. The dimensions of the problem and the material properties used are shown in Figure 6.17(a). Phaal and Calladine (1992b) state that this problem is a severe test of the coupling between membrane and bending action in the shell elements.

Taking into account the symmetry of the problem, four meshes of one-eighth of the cylinder were analysed, in *OXFEM* and *I-DEAS*. The displacements predicted under the load from these eight analyses are plotted in Figure 6.17(b) normalised with the analytical solution ($= 0.18248 \times 10^{-4}$, quoted from Phaal and Calladine (1992b)).

The predictions using the overlapping shell elements, implemented in *OXFEM*, are very poor; convergence is apparent but towards a value approximately one-third greater than the analytical solution. It seems unlikely that the convergence is non-monotonic since the final mesh is fine and is equivalent to roughly 3150 elements in a mesh of the entire cylinder. The *I-DEAS* predictions are much better although they also appear to converge to a value slightly greater than the analytical solution.

6.6.5 Discussion of test results

The preceding sections show varied levels of success in obtaining accurate displacement results using the overlapping shell elements. This can be attributed partly to the dominance of bending or membrane actions in the problems. In problems dominated by one or other (such as bending in test 1 and stretching in test 2), the results are generally good. In test 4, where the loading is unsymmetric (leading to bending) and the boundary conditions effectively force membrane action, the results are very poor. The displacement response in a situation close to tunnelling (test 3) is between two and three times stiffer than predicted by analytical methods. This problem is likely to be membrane dominated and inaccuracies arise from modelling with constant strain elements. It can be concluded that the overlapping shell elements appear to be inadequate where there is a mixture of flexural and membrane effects, i.e. highly coupled shell problems such as test 4.

In their testing of this element, Phaal and Calladine (1992b) achieve much better results for various problems, including the pinched cylinder of test 4. On further examination it becomes apparent that this is only achieved when the analysis is carried out with two overlaid meshes of overlapping shell elements. The element facets on the two meshes are non-coincident and this may improve the overall response since, as shown in test 1, mesh topology has a marked effect on the convergence characteristics. This approach removes many of the advantages that these elements offer over conventional ones in that more complex procedures are necessary to generate the non-coincident meshes and more elements are required which leads to greater run times.

In Section 5.2.2.4, analyses using the overlapping beam elements, from which the formulation for the shell elements has been developed, were described and results for displacements were seen to converge from above (i.e. an over-flexible response for coarse discretisation). In the tests of the overlapping shell element, convergence from both sides has occurred, depending on the problem. In test 1, convergence agrees with that seen in the beam element test problems since both involve activation of the flexural response of the elements only. In test 4, convergence is from below, matching that of the *I-DEAS* shell element. This is to be expected where the membrane action of the shell is dominating convergence since this part of the shell formulation is based on standard finite elements.

In terms of the original requirement for a lining element to use in the tunnelling model the overlapping shell elements appear to be satisfactory for their intended purpose although giving a stiffer response. The results from test 3 indicate that the elements may be joined to continuum elements with no adverse effects. Test 2 shows that uniform shrinkage is feasible as required for modelling volume loss.

6.7 Summary

The choice for the three-dimensional lining element was difficult because of the wide variety of formulations available and the scarcity of impartial assessments of the quality of the formulations. A novel overlapping element was chosen for its simplicity and its lack of rotational degrees of freedom. The implementation of the element is complicated by the need to deal with certain boundary conditions at element stiffness matrix formation. Experience with the two-dimensional overlapping beam element help to explain the final procedures adopted.

The implementation was tested to check its performance agreed with the results of Phaal and Calladine (1992b) and to ascertain its suitability for the tunnelling model. The formulation is economical due to its lack of rotational degrees of freedom. This aspect of the formulation is probably also an advantage because the shell elements are connected to continuum elements in the tunnelling model although it is not clear as to the severity of problems connecting elements with and without rotational degrees of freedom.

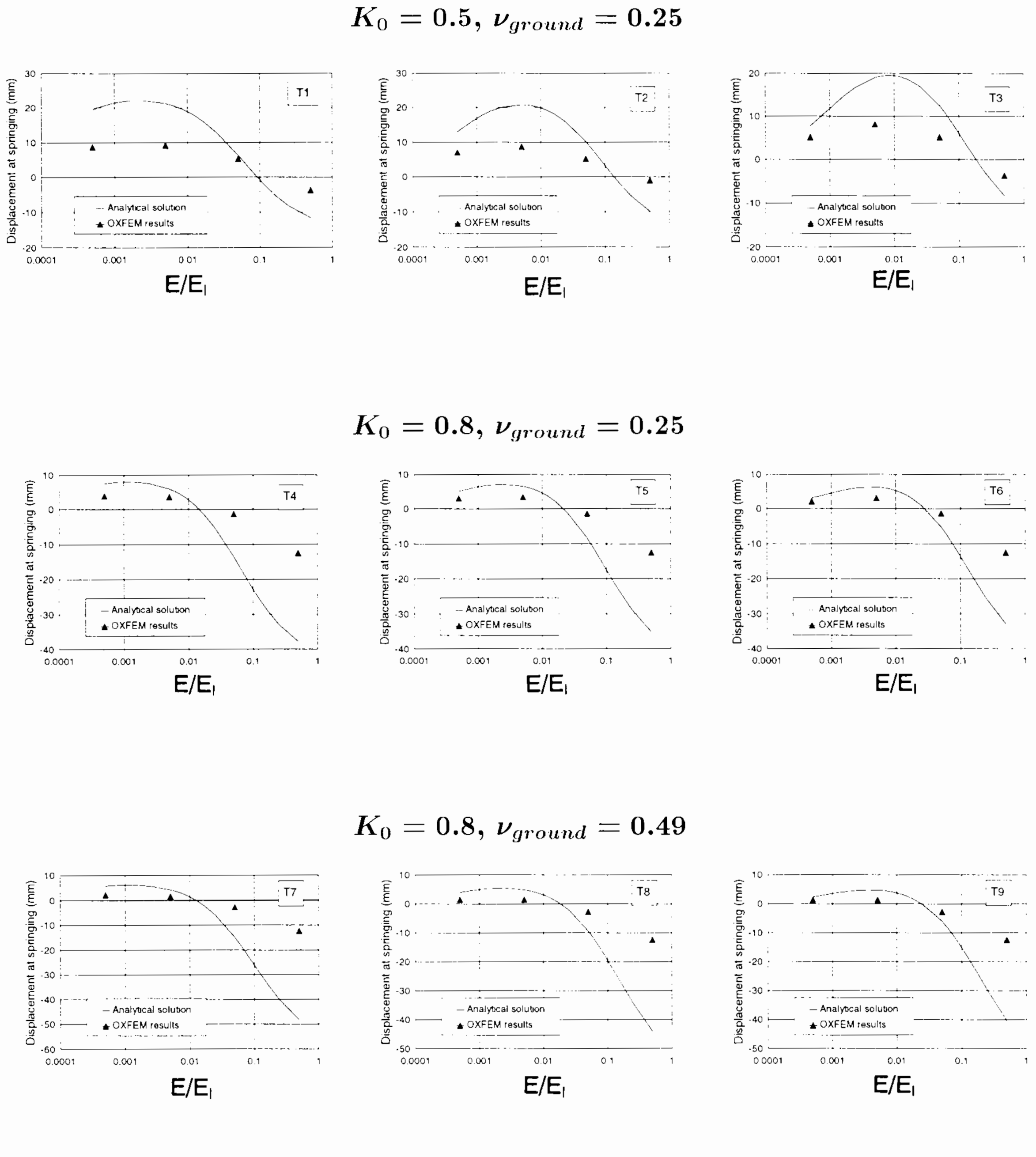

$K_0 = 0.5$, $\nu_{ground} = 0.25$

$K_0 = 0.8$, $\nu_{ground} = 0.25$

$K_0 = 0.8$, $\nu_{ground} = 0.49$

Figure 6.18: Displacement results for test 3

CHAPTER SEVEN

ANALYSIS PROCEDURE

7.1 Introduction

The preceding chapters of this thesis describe the theoretical basis for the numerical model and the validation of its individual parts. To use the model to make predictions of damage resulting from a particular tunnel construction, a three-stage procedure is required. Firstly, pre-processing is necessary to convert the geometry and specified material properties to input data. Secondly the numerical analysis is carried out. Finally, the output data must be processed and interpreted. These tasks are made more difficult by the three-dimensional nature of the model. Input data for a three-dimensional analysis is both harder to generate and to check than for a two-dimensional analysis. Three-dimensional analyses also usually produce a considerable quantity of output data. This chapter is devoted to the discussion of this three stage analysis procedure.

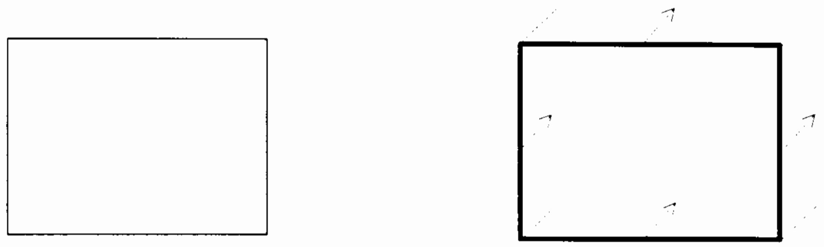

1. Rectangular wireframe

2. Extrude wireframe to create 3d block

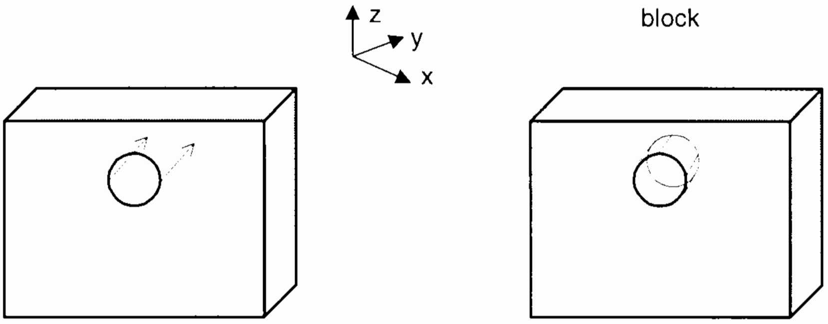

3. Draw circle wireframe on face of 3d block

4. Extrude circle wireframe through block and partition volume

Figure 7.1: **Steps in solid modelling a tunnel**

7.2 Pre-processing

7.2.1 Solid Modelling

The initial data comprises the tunnel and building dimensions and the material properties for the ground, tunnel lining and building. The overall size of the finite element mesh must be large enough to minimise any boundary effects. Previous plane strain analyses of unlined tunnels of similar dimensions (Chow, 1994) demonstrate these effects to be insignificant for a mesh with distance to a boundary of $12D$ (apart from one modelling symmetry). Other, more complex, plane strain analyses (Stallebrass et al., 1996) have used a distance of $6D$. Considering that three-dimensional boundary effects may be more complex, the former value has been adopted in all the analyses described in Chapter 8.

In order to proceed with the generation of the mesh, the domain is modelled as a solid model in the commercial program *I-DEAS*. As an example of this procedure consider a cube domain with a straight tunnel, as shown in Figure 7.1. Solid modelling begins with creation of a rectangular wireframe which is then extruded to form a cube block wireframe. To create the tunnel, a circle is drawn onto one face of the cube and extruded the full length of the block. The extrusion must also partition the block volume into two; a volume inside the tunnel and a volume outside. This is necessary for later meshing of the tunnel. At this stage, if the excavation is to be carried out in more than one increment, the tunnel volume must be further partitioned.

The building mesh is created separately using another package, developed in-house (*OXMESH*). In order to connect the building mesh to the mesh used to model the soil, it is necessary to ensure that an arrangement of nodes, that match exactly those at the base of the building, are generated at the appropriate position on the soil surface. To achieve this, surfaces are created by extruding upwards lines drawn onto the upper face of the three-dimensional domain which represent the building facades. This constrains the mesh generator to produce nodes along the building "footprint". It would be straightforward to generate meshes of two-dimensional elements on these surfaces in *I-DEAS* and export their details in the same way that the ground mesh details are exported, rather than use a separate package for mesh generation. The above procedure results from the particular development history of this project where work concerned with the building has been undertaken in isolation.

Output data at nodes are often required at other specific locations on the surface e.g. at a transverse section, halfway along the tunnel axis. Further surfaces are therefore created to produce nodes in lines at the required locations.

7.2.2 Mesh Generation

A discussion of mesh refinement in *I-DEAS* is given in Section 3.5. The determination of suitable meshing parameters for the domain in Figure 7.1 is largely a matter of trial and error. Particular difficulties arise with this type of domain since two centres of refinement are required; around the tunnel and beneath the building. This leads to excessive numbers of elements unless many local refinement parameters are specified. The most economical meshes for this form of domain are generated when the tunnel volumes (i.e. the space enclosed by the tunnel perimeter) are meshed first. These volumes are small compared to the overall size of the model and so meshing is rapid. The second step is to mesh the building facades with two-dimensional elements. This mesh of the building is not used in the analysis but this process leads to the generation of nodes at the required spacing on the building "footprint". The final step is to mesh the remaining volume (i.e. that which is not to be excavated during the analysis). The nodes generated on the outer surface of the tunnel volume and on the building "footprint" are included in elements generated for the final volume.

During meshing, *I-DEAS* echoes the numbers of nodes and elements it is generating so that the process can be halted if required. This is often necessary as it is impossible to predict accurately the number of elements that a set of meshing parameters will generate on a given domain. Because of the complexity of the model, it is necessary to limit the number of elements within the mesh in order to ensure that run times are reasonable. The maximum feasible size of the mesh is based on knowledge of solution times for previously analysed meshes. During the course of this project, there have been major improvements of the computer hardware which has increased the maximum feasible size of mesh.

Named groups are created of elements and nodes related to volumes, surfaces and edges in the domain. These are used in the input data file and in post-processing. The elements which are to be excavated are grouped according to the tunnel volume in which they are located. The nodes on the top surface of the mesh are put into a group which is then used to define intermediate results output.

Once a mesh is formed, various checks are necessary before proceeding to the analysis. Two-dimensional meshes are relatively easy to check; a visual inspection of a plot of the mesh is usually sufficient to ensure there are no unwanted voids, overlapping elements or coincident nodes. It is also easy to assess subjectively the level of distortion of the elements. Three-dimensional meshes require automated procedures to perform the same checks. *I-DEAS* provides the means to make these checks following mesh generation.

It is important to detect any excessively flat elements (often called "slivers") since their inclusion in the mesh can cause ill-conditioning in the structure stiffness matrix. Two measures of tetrahedral element shape are commonly used to detect slivers, *stretch* and *distortion*. Stretch is defined as,

$$\text{stretch} = \frac{(\text{radius of inscribed sphere})}{(\text{longest dimension between corner nodes})} \tag{7.1}$$

and is a measure of how close the element is to the ideal tetrahedral element, which has equilateral triangular faces. The stretch obtained from Equation 7.1 is normalised using the reciprocal of the stretch for the ideal element ($= \sqrt{24}$).
Distortion is defined as,

$$\text{parent element volume} \times \frac{\det J}{\text{element volume}} \tag{7.2}$$

The Jacobian, J has the same meaning as defined in Section 4.2 that is, a transformation matrix for the element from its parent element coordinates. Distortion is calculated using the minimum value of J for the Gaussian integration points in the element. A negative value of distortion means that the element is concave. For the meshes generated here, values of stretch and distortion have been kept greater than 0.05 as recommended by the *I-DEAS* online manuals. If flat elements are found they can usually be corrected by moving nodes, although this may adversely affect other elements.

The need to optimise the order in which elements are processed in the frontal solver has been discussed in Section 3.2. *I-DEAS* includes an optimisation facility based on the algorithm in Sloan and Randolph (1983). Alternatively, in-house software (*OXOPT*) is available which adds an optimal element order list, based on the same algorithm, to the end of an input data file to *OXFEM* which is followed in the frontal solver. During development of the numerical model, meshes were optimised in *I-DEAS* and checked by running *OXOPT* with the resulting input data file. Surprisingly, the two optimisers gave different results although there was insufficient time available to investigate the reasons for this or to make comparisons. Therefore the optimal order specified by *OXOPT* is used because there is confidence that the optimisation algorithm is implemented correctly. In contrast, it is not possible to examine the implementation in *I-DEAS*.

Once the meshing is complete, boundary conditions are applied and the mesh data are exported from *I-DEAS* in the format used by the *ABAQUS* commercial analysis package. This is chosen because it is an ASCII format, and hence editable, file of similar structure to the input data files required by *OXFEM*. A conversion program *CONVERT*, written as part of this research, reads the *ABAQUS* format file and writes it in *OXFEM* format, adding some further data (e.g. material properties) specified by the user.

The groups of elements to be excavated at each tunnelling increment are formed by partitioning the tunnel volume in *I-DEAS* as indicated above. These groups are checked during conversion of data from *ABAQUS* to *OXFEM* format. The checking procedure is as follows:

- The unit vector $\boldsymbol{r}$ along the tunnel centreline is first calculated from the start and end coordinates provided by the user. The coordinates of the centroid of each element in the mesh are then calculated from the mean of the element nodal coordinates. This is not exact for elements having curved sides but is accurate enough considering the low level of distortion specified in the mesh.

- The distance s along the tunnel centreline to the point where the perpendicular to the element centroid crosses is.

$$s = r_x(x_1 - x_0) + r_y(y_1 - y_0) + r_z(z_1 - z_0) \tag{7.3}$$

where.

$$r_x\boldsymbol{i} + r_y\boldsymbol{j} + r_z\boldsymbol{k} = \text{the unit vector along the tunnel centreline.} \tag{7.4}$$

$$(x_1, y_1, z_1) = \text{the coordinates of the centroid.} \tag{7.5}$$

$$(x_0, y_0, z_0) = \text{the coordinates of the start of the tunnel centreline} \tag{7.6}$$

- The length of the perpendicular. $\boldsymbol{r}_c$ is.

$$\|\boldsymbol{r}_c\| = \sqrt{((x_1 - x_0)^2 + (y_1 - y_0)^2 + (z_1 - z_0)^2 - s^2)}. \tag{7.7}$$

- If $\|\boldsymbol{r}_c\|$ is less than the tunnel radius. the element is deemed to lie within the tunnel excavation. The entire group of elements is sub-divided for incremental excavation using s for each element along the tunnel axis and these sub-groups are checked against those derived from *I-DEAS*.

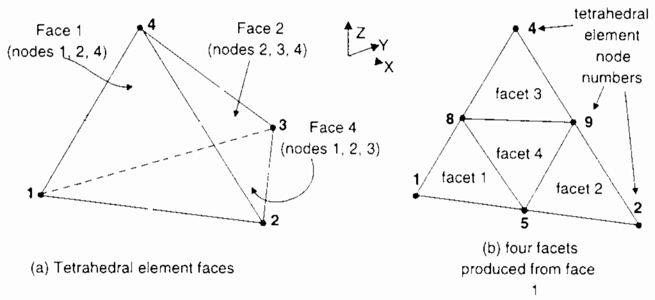

Figure 7.2: **Lining element central facet generation**

If partitioning of the tunnel volume is not carried out prior to meshing then this procedure provides the groups of elements directly. However, there is no control over the smoothness of the tunnel face and circumference at each incremental stage of excavation, which is possible with volume partitioning. Since smooth faces are required in the analyses carried out in this research, volumes were partitioned and the above procedure used only for checking.

7.2.3 Generation of lining elements

The lining elements described in Chapter 6 are defined in the *OXFEM* input data file by the three nodes around their central facet. Generation of these elements uses another program written as part of this research and is undertaken once the input data are converted to *OXFEM* format but prior to analysis. The element nodes are determined from the groups of elements to be removed at each stage of excavation and the special boundary conditions specified for nodes attached to shell elements. The procedure is as follows:

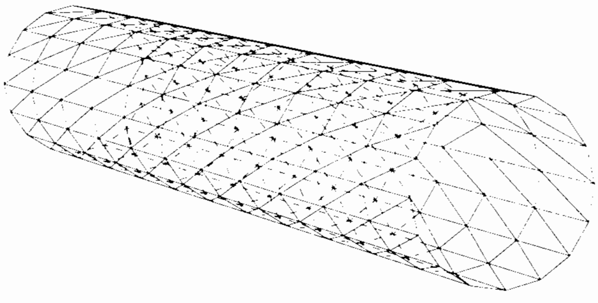

Figure 7.3: **A lining mesh**

- Assemble a list of all the faces on solid elements to be excavated which are not also shared by another excavated element. Each tetrahedral element has four faces, each of which is defined by three corner nodes (see Figure 7.2(a)). Any faces which are recorded twice are removed from the list since they are internal to the tunnel volume. The list then comprises faces on the outer surface of the tunnel volume.
- Remove faces from the list which are either
  - at the back or front tunnel faces, by calculating the angle between the normal to the face and the tunnel centreline, or
  - having all three defining nodes on a boundary.
- Split the face into four, three-noded facets using the midside nodes of the original tetrahedral element (see Figure 7.2(b)). These are the lining elements' centre facets.

The resulting mesh of lining elements given by this procedure is checked by writing the new element data to a file in a format which can be read by *I-DEAS*. The mesh can then be viewed and visually checked. An example of a lining mesh is shown in Figure 7.3. The remaining three nodes, which define the overlapping facets of each lining element, are found by a subroutine inside the *OXFEM* program using a procedure which is described in Section 7.3.2.

7.3 Analysis

Some aspects of the analysis program *OXFEM* are described earlier in this thesis, particularly the frontal solution method (Section 3.2). This section gives details of other significant steps in the execution of the analysis program that are specific to the tunnelling problems modelled.

7.3.1 General

Solution time is strongly influenced by the memory requirements of the program. Once the storage needed exceeds the available RAM , the speed of execution reduces significantly. This occurs because indirect memory (i.e. hard disk) is used and the access times, compared to that with the RAM, are much higher. Therefore it is important that the executable program used is compiled to use minimum memory. All arrays in the program must therefore be dimensioned to the minimum size to run the particular problem. Important arrays in *OXFEM* are dimensioned using maxima recognised throughout the program code. This is achieved, not by the use of Fortran COMMON blocks, but using a single file, in which the values of all the maxima are given. This file is read (or *included*) in subroutines where one or more of the maxima are referenced. Recompilation for a revised set of maxima then only requires amendment of the single "include" file. The process of recompilation of the source code for each analysis is only worthwhile when the problem is large since the time required is then insignificant to the total run time. Thirty-seven maxima are defined in the current version of *OXFEM*. Determination of the minimum size required for each of the maxima is obvious, in some cases, by reference to the input data file (e.g. maximum number of load stages, maximum number of elements in the mesh). Other maxima cannot be determined in this way, notably the maximum size of the front matrix and coefficient buffer used in the solver. These are currently determined from past experience of similar sized analyses and by a certain amount of trial and error running. There is scope for additional pre-processing where the input data file is read and these maxima are determined from running the solver without forming element stiffness matrices or attempting solution. The need to define array dimensions could be significantly reduced and perhaps eliminated if the source code were to be rewritten in Fortran 90 (rather than Fortran 77 as at present) where runtime allocation of arrays is possible.

It is possible that in the long period that the analysis program is executing there may be problems or failures of the hardware. To minimise the loss of data, should the system crash, all globally accessed variable values may be written to an unformatted file (termed a "stopfile") at the end of specified load steps or loading stages. This file can be read in conjunction with a modified version of the original input file and analysis restarted from the point where the data were recorded. In the three-dimensional analyses of Chapter 8, these stopfiles were written every 20 steps, corresponding to approximately one-day's execution time for the largest models on the fastest hardware(e.g. SUN Sparc 10 or SUN Ultra 2 processor-based machines).

Throughout the analysis, various data are echoed to a file which can be read to check progress. The major part of this file is an echoed version of the input data file and is written at the start of the analysis. Of more interest to the user is the information written at each load stage and incremental step. The volumes excavated are calculated and given for checking against the overall tunnel volume as discussed in Section 7.2.2. The maximum value of the residual out-of-balance force at all degrees of freedom in the mesh is given at the end of each incremental step. This allows the accuracy of the analysis to be assessed albeit subjectively. Large values of the residual indicates that it may be necessary to restart the analysis with a greater number of steps. In the analyses of Chapter 8, the acceptable residual level was taken as $0.01\gamma D^2$ where γ was the unit weight of the soil and D the tunnel diameter.

7.3.2 Completion of lining elements

As indicated in Section 7.2.3, the lining elements are defined in the input data file by their central facet nodes and a program (*LINING_GEN*) has been written as part of this research, to generate a list of these nodes from the list of elements to be excavated. Complete lining elements generally have six nodes, but those adjacent to boundaries have four or five nodes (as explained in Section 6.3.1). The remaining one to three nodes defining the element are generated inside the analysis program, once the input data file has been read.

In the program code, the element nodes are held in an array called *ELEM*. Initially the centre facet nodes are read from the input data file into locations 4,5 and 6 in *ELEM*. Locations 7,8 & 9 of *ELEM* are filled with integers defining for the current element, either

- the number of elements which overlap each outer facet of the current element or,
- the nature of the boundary along each edge of the centre facet of the current element

The first of the above is required when assembling the element stiffness matrix membrane terms; the stiffness matrix for a three-noded constant strain triangle element overlaying each facet is included for each element. Therefore, the stiffness terms must be factored to account for the overlapping nature of the six-noded shell elements. The second of the above is needed to detect boundaries during formation of the element stiffness matrix. The entries are determined by examining each shell element in turn and identifying the element number of each neighbouring element, or if the element is adjacent to a boundary, the nature of the boundary. Boundaries are defined by negative single integers (e.g. -4 is a simply-supported edge, -5 a clamped edge). A second loop over the elements converts the positive entries to number of overlaps and reorders $ELEM(i), i = 1,6$ so that, regardless of the total number of nodes on the element, the node numbers appear in sequence, with no gaps. This operation removes the need for the solver code to be amended to skip over empty entries in $ELEM$ which would otherwise occur with boundary elements.

7.3.3 Initial stresses

For analyses of greenfield sites, the initial stresses in the ground are specified directly in the input data file by the unit weight of the soil and the value of K_0 (coefficient of earth pressure at rest) adopted. A routine in the analysis program calculates the equivalent nodal loads to these stresses and compares these to the calculation of nodal loads using the specified unit weight. Any discrepancies between the two lead to warnings in the file of echoed input data.

The objective of this project is the determination of damage to buildings due to tunnelling, rather than from settlement caused by the self-weight of a building. It is important however, to acknowledge that the building will be subject to stresses generated by its own weight prior to tunnelling. These initial stresses will have a significant influence on the effects of the tunnel-induced settlements. The masonry material model used in the building is non-linear so that self-weight loads, calculated using Equation 4.2 (see Chapter 4), must be applied incrementally. This is carried out in the analyses as a pre-loading stage, prior to the excavation and lining of the tunnel. The loads arising from self-weight are applied to the building over 20 steps in the analyses described in Chapter 8. Ten subsequent steps are then applied to reduce the residual out-of-balance forces further, but small residuals remain which are applied in reverse with the loading for the first stage of the main analysis (as for any residual, see Section 3.2). At the end of this stage all deflections at nodes, and element strains in the building and the ground are reset to zero. Stresses remain unaltered. Displacements and strains that develop during the subsequent analysis are therefore due entirely to the installation of the tunnel. Cracks caused by the self-weight loading are closed up to model a situation where crack damage has been repaired but not increased the original strength of the material in the cracked region.

In summary, at the start of tunnelling the building is already damaged by the interaction of its weight with the ground on which it is founded. A complex field of stress is also present in the ground following imposition of the building weight. For the non-linear soil model, the changes in stress during this initial loading period will have altered its state and stiffness. Neither the damage to the building nor the stresses in the ground prior to tunnelling are examined in the analyses presented in this thesis. While this omission is unsatisfactory in that the damage arising from tunnelling may depend on the initial state of the building, the inclusion of this stage of loading goes some way to modelling the real situation.

7.4 Post-processing

The three-dimensional numerical models demonstrated in Chapter 8 produce large quantities of data which must be processed automatically. It is usual to display this data on two-dimensional media (i.e. paper or computer screen) in a two-dimensional format, e.g. line graphs and plots of contours on a plane. With suitable graphics facilities, three-dimensional data can be displayed in forms which make interpretation easier. Typical examples are the use of perspective plots of three-dimensional meshes, employed throughout this thesis. The graphics facilities of *I-DEAS* are used to display some of the results from the demonstration analyses in Chapter 8. To do this, output data from the analysis program is processed into a format acceptable to *I-DEAS* using a program written especially for the purpose. The data are read into *I-DEAS* and added to the information held for the mesh originally generated for the analysis. This ensures that the node and element numbering given in the data file corresponds to that in the mesh on which the results are subsequently displayed. Contouring of displacement results is also carried out using the program *2CAN* (developed by Professor G.T. Houlsby).

One set of results which requires additional processing relates to the cracking in the masonry building. It is useful to have a plot which shows both the magnitude and the direction of cracking in the mesh of a building facade since it gives an immediate visual indication of the effects of the tunnel construction on the building. The program *2CAN* has been adapted, as part of this research (but not by the author) to produce such a display. At the numerical integration (Gauss) points on each element in the building, the material is either uncracked or cracked. In the latter case there is also a value of tensile strain associated with the crack. A tolerance is set on the tensile strain by the user below which cracks will not be displayed. For each cracked Gauss point above this tolerance, short lines (all the same length) are plotted at each cracked Gauss point above this tolerance level, inclined along the predicted crack direction. The number of (parallel) lines indicates the magnitude of the tensile strain. This produces a good visual representation of the cracking data which may be used to indicate the mode of

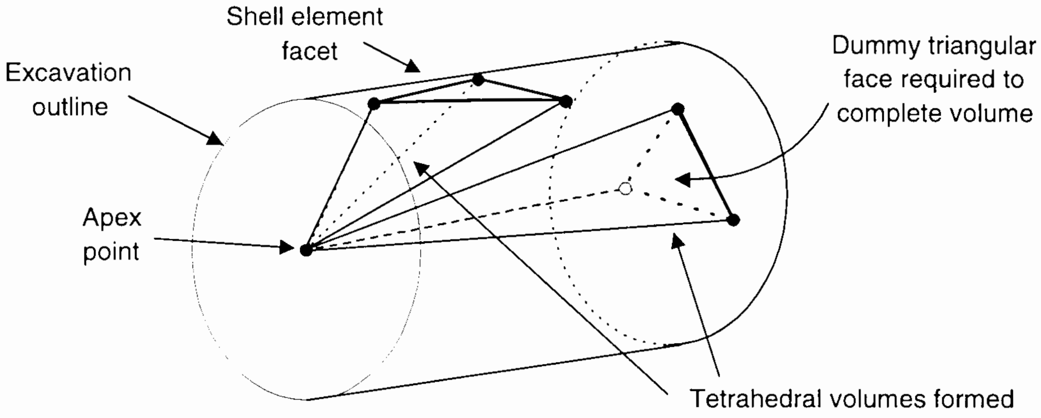

Figure 7.4: **Calculation of tunnel volumes using shell element facets**

cracking (i.e. bending or shear) and areas of significant damage.

7.4.1 Checking volume loss

The shrinking of lining elements to produce a given volume loss at the tunnel is described in Chapters 5 and 6. Following an analysis, it is important to check the value of volume loss actually occurring, which may differ slightly from that specified. The displacements of nodes around the tunnel, for each load stage, are processed to calculate the change in volume of the tunnel.

For a two-dimensional analysis, the procedure consists of splitting the tunnel volume up into triangular areas with the invert node as the apex of each. Areas are then calculated before and after imposition of the displacements from the analysis to give the change in area and hence the volume loss. A similar process is adopted in three-dimensions. Tetrahedra are formed, using as an apex a point located at the start of the tunnel centreline. The remaining three points required to complete the tetrahedron are taken from the shell element centre facets, now lining the inside of the tunnel. To complete the volume, a set of dummy triangular faces must be generated across the face of the tunnel and used to form tetrahedra in the same way. This procedure is illustrated in Figure 7.4.

A problem with calculating volumes in this way is that faces must be classified into *internal* and *external* faces with respect to the apex point chosen to form tetrahedra. Once classified, the total volume is calculated as, the sum of the tetrahedral volumes formed using internal faces **less** the sum of the tetrahedral volumes formed using the external faces (Schaer and Stone, 1991). To understand the difference between the two classes of face it is easier to consider the problem in two-dimensions as shown in Figure 7.5(a). Points B and C lie on the edge of an initially rectangular domain and are subject to displacements as shown in Figures 7.5(b) and 7.5(c). If the area of the distorted domain is calculated taking point A as the apex point then the contributions from segment BC are the shaded areas shown. In the first case (Figure 7.5(b)), the contributory area is inside the area of the deformed domain and BC is an *internal* segment for the purposes of area calculation. In the second case (Figure 7.5(c)), the hatched part of the shaded contributory area is outside the deformed domain of the shape. Therefore, inclusion of this area would give an error in the domain area calculation. In this case, BC is an *external* face. The definition of internal face, in this example, is one whose unit normal vector $\underline{n}$ makes an acute angle with any line from the apex to the segment. It will be clear, from this example that the problem can also affect two-dimensional area calculations.

Unfortunately the determination of the nature of a face with respect to an apex node is a difficult topological problem since it depends on the location of the apex node, the face normal (and hence the sequence of face node numbering) as well as the relative displacements of the nodes and as such the solution is beyond the scope of this project. Therefore it is assumed that the displacements of the nodes on the tunnel periphery

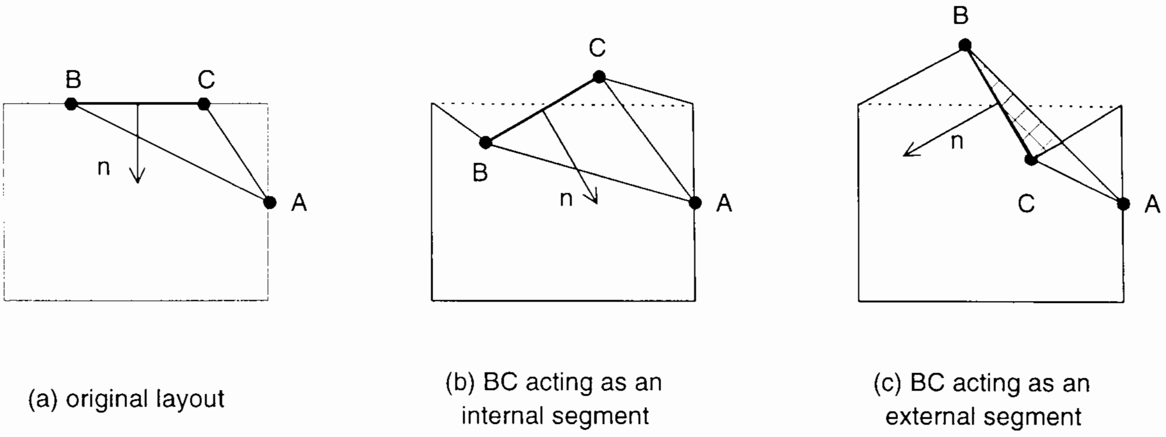

(a) original layout

(b) BC acting as an internal segment

(c) BC acting as an external segment

Figure 7.5: **Internal and external face definitions**

are small relative to the tunnel diameter such that all shell element facets can be taken as internal faces. The apex node is taken as the start of the tunnel centreline. On this basis, a straightforward program has been written to take displacement output from an analysis and, with the nodal coordinates, calculate volume loss.

7.4.2 Checking for undrained behaviour

The formulations of both soil models used in the analyses described in this thesis incorporate undrained behaviour, i.e. incompressibility. To check this aspect of the formulations the volume loss calculated at the tunnel, as described above, can be compared with the volume of the surface settlement trough (Figure 7.6). If the soil is incompressible then the volumes should be equal. The trough volumes are calculated with an adaptation of the trapezoid rule for numerical integration where settlement is assumed to vary linearly between sampling points. In two-dimensions, the area between the settlement curve and the original datum is approximated as the sum of trapezoids of uneven width (following the nodal spacing on the mesh surface). In three-dimensions the volume is approximated by the sum of volumes of triangular prisms, again of varying sizes according to the mesh surface nodal spacing. A simple

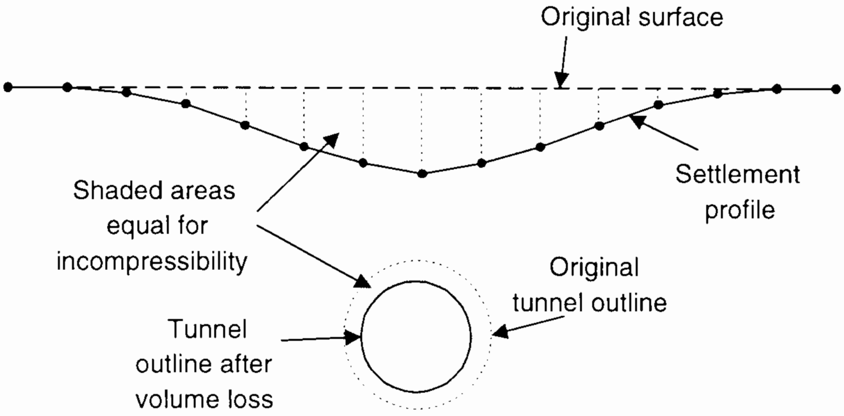

Figure 7.6: **Comparison of volumes for incompressibility check**

spreadsheet program is used for the two-dimensional calculation while a facility in the in-house program *2CAN* is used for three-dimensions. Greater accuracy could be obtained by using higher order interpolation of settlement between nodes, using cubic splines for example, but the above procedure appears sufficient given that the assumed displacement field in the elements at the surface is quadratic (Cook, 1981).

CHAPTER EIGHT

EXAMPLE ANALYSES

8.1 Introduction

The previous five chapters of this thesis describe the component parts of the numerical model of tunnelling. The purpose of this chapter is to illustrate the use of the model for the simulation of tunnel construction in soft ground with examples of two- and three-dimensional analyses. As stated in Chapter 1, the main aim of this thesis is the description of the numerical model and therefore, the analyses do not constitute a parametric study of the tunnelling problem. Such a study, using the completed model, is the next step in the research project, as discussed in the proposals for future research in Chapter 10. Having said that, conclusions are still drawn, from these results, of

- the damaging effects of tunnelling on buildings,
- the effects of the presence on a building of the surface settlement profile from tunnel construction

as well as of the performance of the numerical model. This is carried out in Chapter 9 where the results are also presented. The current chapter is devoted to descriptions of the analyses and explanation of the particular parameters chosen.

8.2 General features of the analyses

The features common to all example analyses are now explained and justified. Details are also given of some practical aspects of the analyses and the presentation of the results is explained. A major motivation for the project originally came from the increase in UK tunnelling activity, particularly on the Jubilee Line Extension Project (JLEP) in London. Many decisions were therefore made with the tunnelling conditions prevalent for the JLEP in mind.

8.2.1 Tunnel layout

The diameter and depth of tunnels vary considerably, according to their final use, so that it was difficult to decide upon a suitable layout that would be representative of real construction and give substantial surface settlements to display any trends clearly. Considering the JLEP, Potts and Addenbrooke (1996), state that typical dimensions for London Underground (LU) tunnels are tunnel diameter, D of 4m and depth Z to tunnel axis of 20 to 34m. Similar dimensions are given for earlier LU tunnels in Mair et al. (1993). However, at some locations of the JLEP, tunnels were constructed with as little as 9m of cover to structures (e.g. beneath the RAC club swimming pool). The tunnel constructed under the Mansion House (whose effects were discussed in Section 2.3.2) was both smaller and shallower than the typical LU tunnel, at 3.05m diameter and $Z = 15\text{m}$ (Frischmann et al., 1994).

In contrast, previous numerical and laboratory studies of tunnelling settlements have tended to analyse layouts with shallower tunnels. For example, the centrifuge tests and numerical modelling of Stallebrass et al. (1996) used $D = 5.0\text{m}, Z = 15\text{m}$; Lee and Rowe (1989) studied tunnels with $D = 4.5\text{m}, Z = 9.75\text{m}$ and Gunn (1993) studied tunnels with $D = 5$m and $Z = 10$m to 20m. In the light of the above, and recognising that this exercise was not a parametric study of tunnelling, the chosen dimensions were,

$$D = 5\text{m}, \quad Z = 10\text{m} \tag{8.1}$$

which is shallower than the majority of JLEP tunnels but very close to the examples of previous numerical modelling.

The tunnel was assumed to be lined with precast concrete segments (as used extensively on the JLEP) although no account was taken of its segmental nature in modelling the lining. The thickness, t chosen was

$$t = 225\text{mm} \tag{8.2}$$

which is representative of this type of lining. The ratio of lining thickness to tunnel radius R then was

$$\frac{t}{R} = 0.09 \tag{8.3}$$

The magnitude of volume loss, V_l for tunnelling in clay is usually in the range 1% to 3%. Recent confirmation that this is reasonable comes from measurements taken for tunnels constructed on the JLEP in London Clay. At St. James's Park, a true greenfield site, Standing et al. (1996) measured immediate volume losses of 2.9% and 3.3% for each of the two JLEP running tunnels. Higgins et al. (1996) give volume losses of 2-2.5% for the tunnels constructed adjacent to Westminster Station. An earlier reference, also relating to tunnelling in London (Mair et al., 1993), gives volume losses of 1.3-1.4%. Volume losses between 1% and 2.5% were therefore used in the two-dimensional example analyses. The need to limit the number of three-dimensional analyses, because of the extensive computer resources required, necessitated using just one value of volume loss, of 2%, in the middle of the range.

Table 8.1: **Computer hardware specifications**

Ref.	*Network name*	*Processor*	RAM	*Clock speed*
1	callisto	Sparc ELC	28Mb	33MHz
2	sinope	Sparc ELC	28Mb	33MHz
3	saturn	Sparc 10	128Mb	150MHz
4	mizar	UltraSparc	256Mb	200MHz

8.2.2 Computer Hardware

A variety of computer hardware configurations (all by *SUN microsystems*) were used to run the analyses. The specifications are given in Table 8.1. Processor speeds do not indicate the actual speed at which a given set of operations would be completed by the machine and are included only to fully specify the processor. A full discussion of the relative merits of these platforms, using suitable benchmarking tests, is beyond the scope of this thesis.

The two-dimensional analyses were generally run using configurations 1 and 2, while the three-dimensional analyses used configurations 3 and 4. As stated in Section 7.2.2, improvements to the hardware were made during this research and the specifications given are those at the time of writing. Most importantly, configuration 4 became available in Spring 1996 and was a significant improvement on configuration 3 for running large three-dimensional analyses. The computer resources used in some of the analyses are given with the results, in Chapter 9, where they are also discussed.

8.2.3 Presentation of results

All results are presented in Chapter 9 to accompany the discussion. The majority are of displacements (vertical and horizontal at the surface and in the tunnel lining) since settlements are the prime concern of this research. Contour plots were produced using the program *2CAN* and the graphics capabilities of *I-DEAS*. Plots of cracks induced in the masonry material of the building are given which use the post-processing described in Section 7.4.

8.3 Material properties

8.3.1 Ground

Two material models were used in the analyses. The first was linear elastic with increasing stiffness with depth. The second was a non-linear, elasto-plastic model using kinematic hardening with stiffness and strength increasing with depth. The models are described in general terms, in Section 3.4. They are referred to as materials E and N respectively in the description of the individual analyses later in this thesis.

8.3.1.1 Properties for elastic material (E)

The material properties required for the first model were:

G_0	shear modulus at the surface,
ω	rate of increase of shear modulus with depth,
ν	Poisson's ratio,
γ	saturated unit weight

The assumption of undrained behaviour was achieved by setting $\nu = 0.49$. True incompressible material behaviour occurs with $\nu = 0.5$ but the adoption of such a value leads to numerical difficulties and the use of the former value is commonplace (e.g. Gunn (1993), Bell et al. (1993)). The initial stresses in the soil were determined by taking the bulk unit weight of the soil as 20kN/m^3 and assuming the water table to lie at the surface. The ratio of horizontal to vertical effective stresses, K_0 was calculated assuming an effective friction angle $\phi' = 20°$ in the expression

$$K_0 = 1 - \sin\phi' \tag{8.4}$$

giving

$$K_0 = 0.66 \tag{8.5}$$

The ratio of horizontal to vertical total stresses was then determined as 0.83.

The model was purely elastic and so had an infinite undrained strength s_u. However, to calculate the stiffness parameters, a finite s_u was postulated assuming the Critical State Soil Mechanics (CSSM) model for undrained behaviour. The ratio of shear modulus to undrained strength G/s_u was assumed to be constant with depth and taken as 250. This was thought to be a reasonable value for a normally consolidated clay (Ng et al., 1995; Kim, 1996). The shear modulus at the surface G_0 was taken to be zero. The water table was assumed to lie at the soil surface giving the vertical effective stress $\sigma'_v = 10z$ KPa, where z was the depth from the surface. From CSSM, the undrained strength of the soil is given as

$$s_u \approx \frac{1}{4}\sigma'_v \tag{8.6}$$

therefore, in this case

$$\begin{aligned} s_u &= 2.5z\text{KPa} && (8.7)\\ \text{and} \qquad G &= 625z\text{KPa} && (8.8)\\ \text{i.e.} \qquad \omega &= 625\text{KPa/m} && (8.9) \end{aligned}$$

The properties chosen for material E are summarised in Table 8.2

Table 8.2: **Material property values for ground: 1. Elastic model (material E)**

G_0	ω	ν	γ
0.0kPa	625.0kPa/m	0.49	20kN/m^3

8.3.1.2 Properties for elasto-plastic material (N)

This model was intended to behave closer to an overconsolidated clay, such as London Clay, although the formulation was still essentially that of a normally consolidated soil. Apart from the modelling of small-strain changes in stiffness, the material was stiffer than material E and had finite stiffness at the surface to permit attachment of a structure without numerical difficulties. The model is described in Section 3.4.

The properties required for material N were:

G_0	shear modulus at the surface of the mesh for behaviour inside the first of the nested yield surfaces, i.e. at very low strain,
ω	rate of increase of shear modulus G with depth
ν	Poisson's ratio (constant throughout)
s_{u0}	undrained shear strength (triaxial compression) at surface
μ	rate of increase of undrained shear strength with depth
n_{nest}	number of nested yield surfaces
h'_α	hardening parameters
c'_α	intermediate yield strengths
γ	saturated unit weight

As with material E, Poisson's ratio ν was taken as 0.49, to model undrained conditions. A value for K_0 of unity was adopted for this material model. The ratio of shear modulus to undrained strength s_u was taken as 500 (constant with depth). The reason for using a relatively high value of this parameter was its adoption in parallel unlined tunnel analyses undertaken by Liu (1997). Previous numerical studies by Liu (1997) of a similar unlined tunnel revealed possible instability with a parameter value of 250 (as used in material E) and hence prompted the use of a relatively high value in those analyses. The same value was used here to permit comparisons to be made.

The undrained strength profile of the soil was taken from data for London Clay given in St. John et al. (1993) as

$$s_u = 60 + 6z \,\mathrm{kPa} \tag{8.10}$$

$$\text{i.e.}\, s_{u0} = 60\mathrm{kPa}, \qquad \mu = 6\mathrm{kPa/m} \tag{8.11}$$

This resulted in the following stiffness parameters,

$$G_0 = 30000\mathrm{kPa} \quad \text{and} \quad \omega = 3000\mathrm{kPa/m} \tag{8.12}$$

The implementation of the material model in *OXFEM* used the bulk modulus K (as indicated in Section 3.4) derived, using elasticity theory, from ν and the value of shear modulus at the point of interest. h'_α and c'_α, the yield surface parameters, are defined in the description of the nested yield surface model in Section 3.4. Houlsby (1996) gives values of these parameters for a model with ten surfaces (nine nested and one outer surface) which produce a good fit to the shape of the shear modulus against strain relationship for many natural clays. A plot of the variation of shear modulus with strain amplitude using these yield surface parameters is given in Figure 8.1. These parameters are adopted for material N.

Table 8.3 summarises the values selected for the properties for material N.

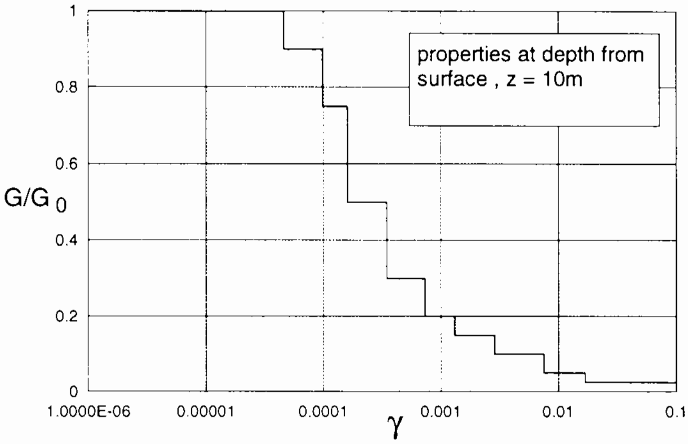

Figure 8.1: **Variation of shear modulus for material N**

Table 8.3: **Material property values for ground: 2. Nested yield model (material N)**

G_0	ω	ν	s_{u0}	μ	n_{nest}	γ
3.0×10^4kPa	3.0×10^3kPa/m	0.49	60kPa	6kPa/m	9	20kN/m^3

Yield surface	1	2	3	4	5	6	7	8	9
h'_α	0.90	0.75	0.50	0.30	0.20	0.15	0.10	0.05	0.025
c'_α	0.02	0.04	0.06	0.10	0.15	0.20	0.30	0.50	0.70

8.3.2 Lining

The material properties adopted for the lining were consistent with those normally adopted for reinforced concrete, although with infinite strength. A Young's modulus of 30kN/m^2 and Poisson's ratio of 0.2 were used throughout. The membrane and flexural properties for the lining (EA and EI for the beam (see Section 5.2.1.2), D for the shell element (see Section 6.3) were derived from these properties and the thickness, t given in Section 8.2.1.

It is useful to examine the relative flexibilities of the lining adopted with the material models for the ground. A non-dimensional measure of the ratio of the shear stiffness of the ground to the flexural stiffness of the lining, for a circular tunnel in elastic ground, is given in Einstein and Schwartz (1979)

$$\text{Flexibility Ratio, } F_R = \frac{E_g R^3 (1-\nu_l^2)}{E_l I (1-\nu_g^2)} \tag{8.13}$$

where E_g, ν_g and E_l, ν_l are the Young's moduli and Poisson's ratios of the ground and lining respectively, R is the tunnel radius and I is the second moment of area of the lining per metre run of tunnel. Considering a point at the tunnel springing level (Z = 10m) for the calculation of ground moduli, F_R was 13 for the elastic material E. Considering material N and using a value of E_g in Equation 8.13 obtained from the shear modulus inside the first yield surface at tunnel springing level, F_R is 124. These values of flexibility ratio lie within the range of 5-300 given by Kim (1996) as representative of tunnels constructed in soft ground. The ratios of Young's moduli E_g/E_s were 6.25×10^{-4} and 6×10^{-3} for materials E and N respectively which lie at the low end of the range of tests carried out in Chapter 6 (test 3, see Figure 6.17 in Chapter 6).

8.3.3 Building

Building layouts are given in the descriptions of three-dimensional analyses below. The material model for masonry, described in Section 3.7 and in detail in Liu (1997), was used throughout the buildings except immediately above openings. In these regions, collapse under self-weight would occur as a consequence of the low tensile strength of the material. Therefore, lintels of linear elastic material were modelled, spanning each opening, supporting the masonry material above.

The material properties required for the masonry model were:

E_m	Young's modulus in compression
E_t	Young's modulus in tension
ν_m	Poisson's ratio
σ_{lt}	maximum tensile stress in a singly cracked region
ϵ_{lt}	threshold tensile strain for change in stiffness
γ	unit weight
t_m	wall thickness

Table 8.4: **Material property values for building: 1. Masonry model**

E_m	E_t	ν_m	σ_{lt}	ϵ_{lt}	γ	t_m
1.0×10^7kN/m^2	0.01kN/m^2	0.2	10.0kN/m^2	4.0×10^{-6}	20kN/m^3	1.0(m)

The values chosen are summarised in Table 8.4 and were representative of old masonry constructed from stonework or strong brickwork, with narrow and brittle mortar joints. A large thickness was chosen to be representative of older mass masonry construction and to give, with the unit weight, a reasonable level of precompression as would be found in a large building. The choice of these parameters and the formulation of the model were the work of another member of the research team and are described in detail elsewhere (Liu, 1997).

The material properties required for the linear elastic lintel material were:

G	shear modulus (constant)
ν	Poisson's ratio
γ	bulk unit weight

and the values used are summarised in Table 8.5. Once again these were representative of masonry but with equal tensile and compressive stiffness and infinite strength. The same thickness and unit weight were given to the lintels as to the rest of the building material.

Table 8.5: **Material property values for building: 2. Material for lintels**

G	ν_m	γ
0.417×10^7kN/m^2	0.2	25kN/m^3

8.4 Detailed descriptions of analyses

Details of each example analysis are given in this section. Each is referenced with a code to allow ease of interpretation of the results presented in the next Chapter. The specifications are tabulated in Tables 8.6 and 8.7 to make it easy to follow the results in Chapter 9.

8.4.1 Two-dimensional analyses

The two-dimensional model of tunnelling is more than just a necessary stage in the development of the three-dimensional model. It can provide predictions of greenfield site settlements for comparison with the semi-empirical approach described in Section 1.2. The numerical predictions can also be compared to those from three-dimensional analyses of greenfield sites to investigate the differences between incremental excavation, possible with the latter, against the single stage tunnel construction of a two-dimensional model.

A building was not included in the two-dimensional analyses because it is not possible to model a three-dimensional structure with a two-dimensional finite element analysis. Studies such as Potts and Addenbrooke (1996), where a beam element was placed on the surface of the ground mesh, provide useful insights into the stiffening effect of a structure at the surface but do not provide any indication of the effects within the building itself. In addition, the overlying structure is usually short relative to

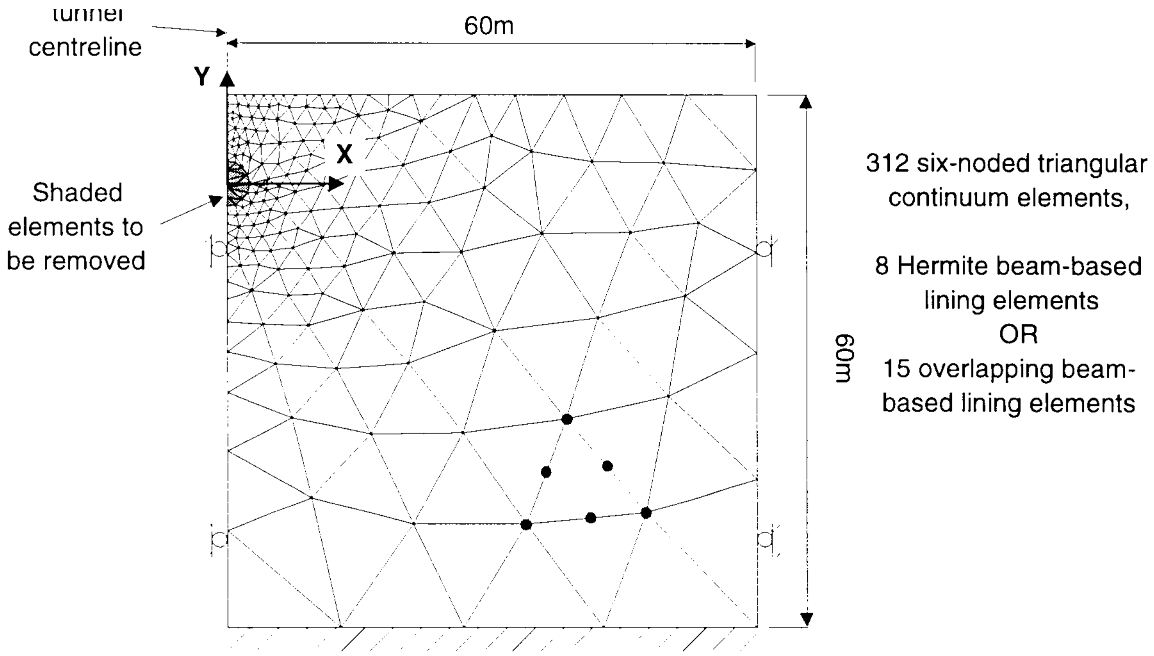

Figure 8.2: **Mesh used in two-dimensional example analyses**

the tunnel beneath and therefore the assumption of plane strain conditions, which is reasonable for the tunnel, is unreasonable for the structure. The two-dimensional study was therefore restricted to greenfield sites.

Unlined and lined analyses, using both of the two-dimensional lining elements developed in Chapter 5, were carried out and five values of volume loss, between 1% and 2.5%, were modelled. The mesh used in the analyses is shown in Figure 8.2. The mesh

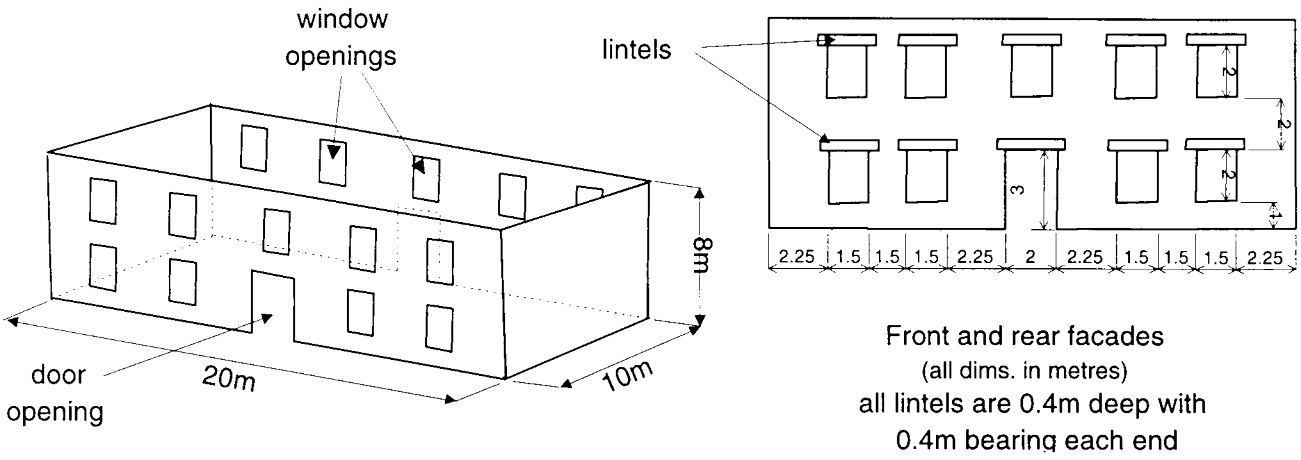

Figure 8.3: **Building layout**

has 681 nodes and 312 solid elements. There were slight differences in the locations of nodes on the tunnel periphery depending on the type of lining element. Where the lining element based on the Hermitian beam element was used, the continuum element edges bordering the tunnel had to be straight. With the overlapping beam elements, all nodes on the tunnel periphery were placed on a circular curve. The locations of the nodes were calculated, in each case, so that the tunnel area was the same as a circular area of radius $R = 2.5$m. Symmetry of the problem was exploited for all the two-dimensional analyses, as is obvious from the Figure 8.2.

The individual specifications for each test are given in Table 8.7.

8.4.2 Three-dimensional analyses

Due to the extensive computer resources needed to run realistic three-dimensional models, only ten analyses were carried out. Of these, two groups of three satisfied the final goal of this research, namely three-dimensional numerical models of tunnelling including excavation, lining, volume loss and a surface structure. For two building layouts, one symmetrical and one unsymmetrical, three separate analyses were carried out to investigate fully the effects of tunnelling on the building. Firstly, a greenfield site analysis was carried out. Secondly, the analysis was repeated with a building on the surface. Finally, the settlements predicted by the first analysis, along the outline of the building on the surface, were applied to the building. By this procedure it was hoped to be able to judge the stiffening effect of the building on the settlement profile and demonstrate the errors inherent in determining damage from the application of greenfield settlements to the building.

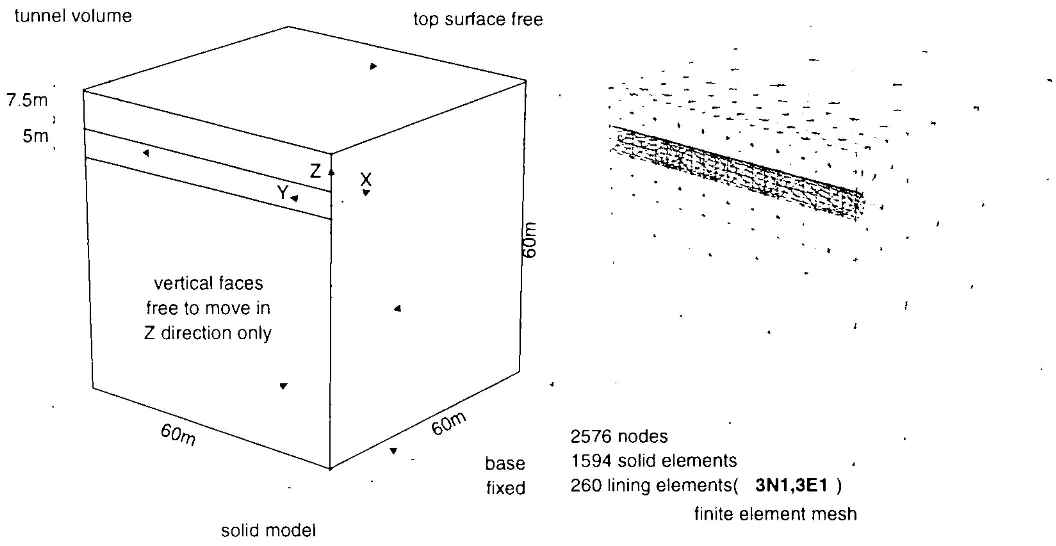

Figure 8.4: **Mesh used in analyses 3EU, 3E1, 3NU, 3N1**

8.4.2.1 Building layout

One building was used in the three-dimensional analyses consisting of four facades joined at their vertical edges (Figure 8.3). The model represented some of the main structural features of a simple two-storey masonry building. The model neglected the effects of foundations, which would supply tensile resistance to the base of the building, and also internal bracing, which would be present through transverse support members. While the dimensions of the building in analyses were the same their orientations were different as described in the specifications below. The meshes were also considerably different since it was necessary to reduce the number of elements in the mesh for the unsymmetrical layout, in the ground as well as the building, to give a reasonable run-time. The individual specifications for each test are given in Table 8.7.

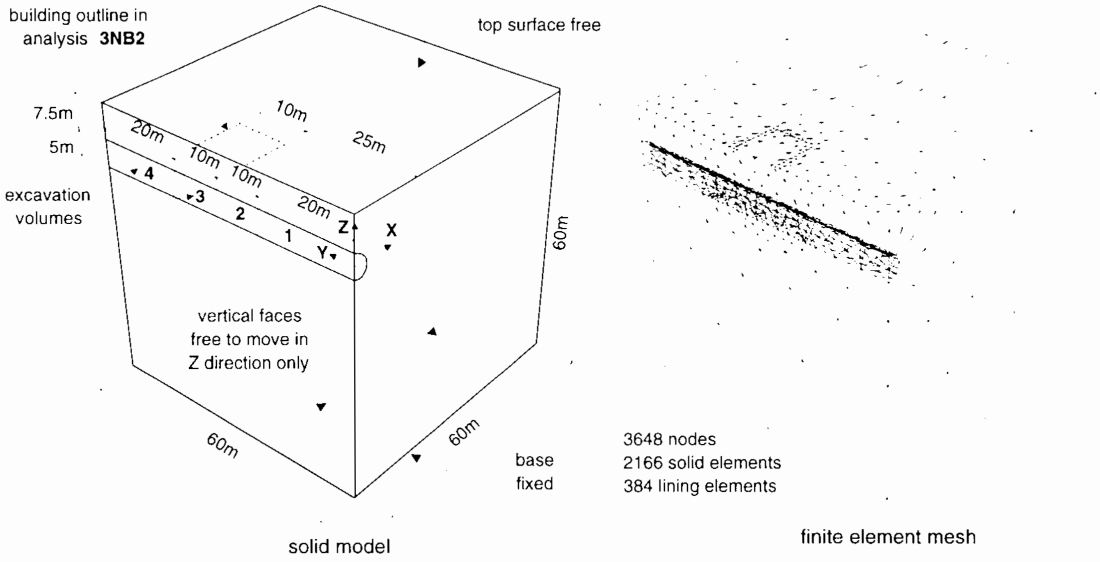

Figure 8.5: **Ground mesh used in analyses 3N2, 3NB2**

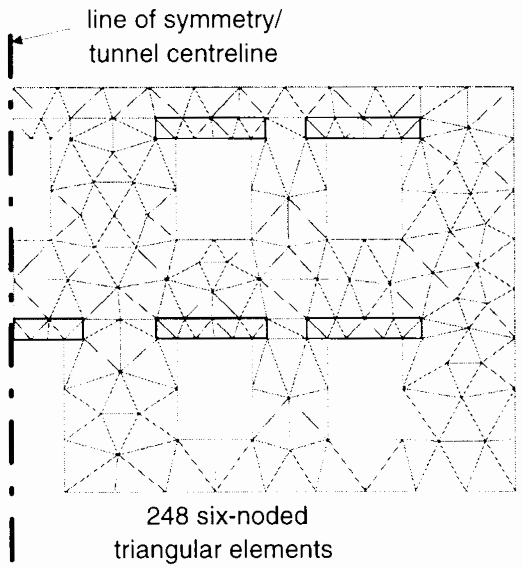

Note: this view is of the front facade from a point on the surface above the tunnel start. The rear facade mesh is the same. The side facade mesh (not shown) is comprised of 169 elements.

Figure 8.6: **Building mesh used in analyses 3NB2, 3BB2**

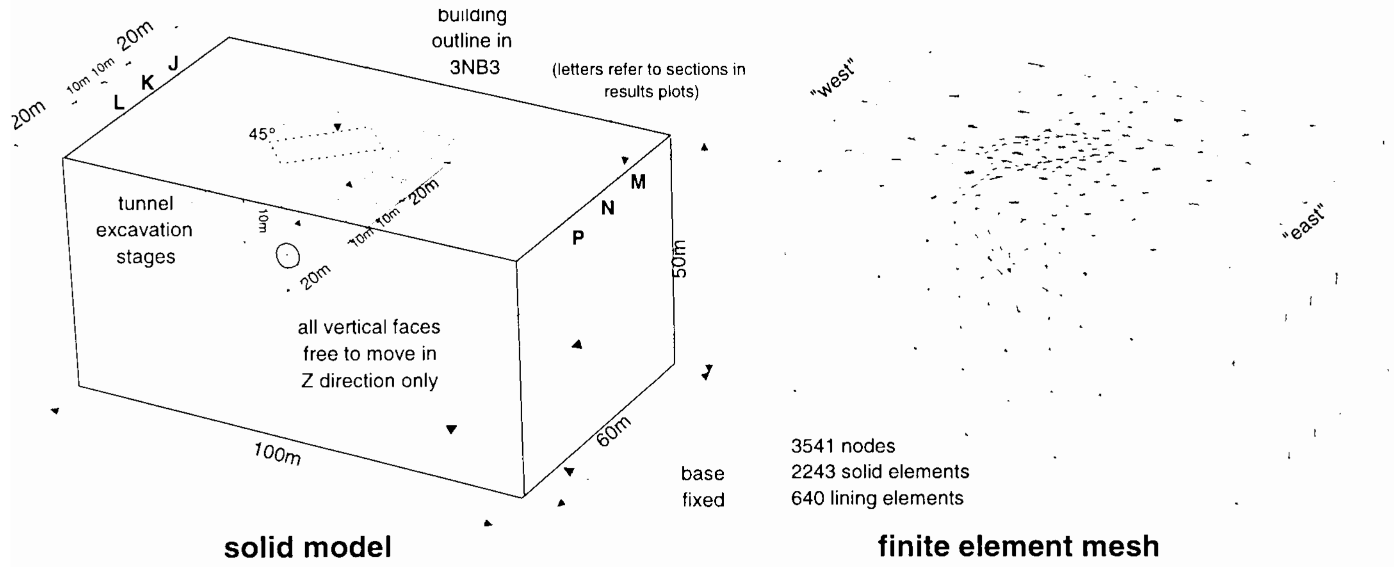

Figure 8.7: **Ground mesh used in analyses 3N3, 3NB3**

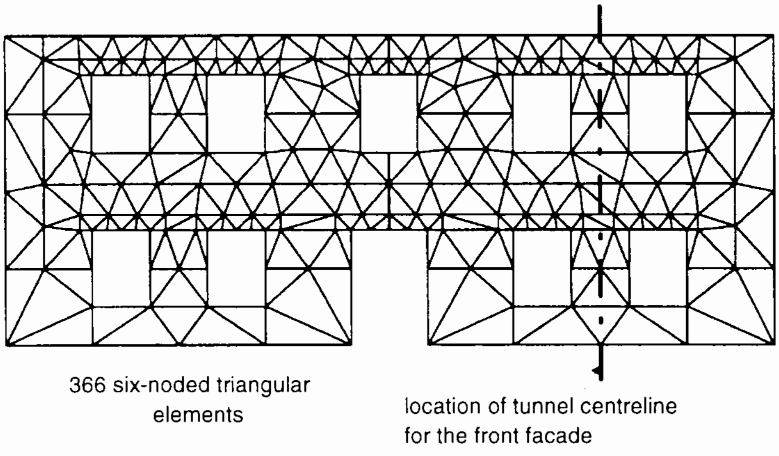

Note: front and rear facade meshes are the same. Side facade meshes (not shown) are comprised of 35 elements each.

Figure 8.8: **Building mesh used in analyses 3NB3, 3BB3**

Table 8.6: **Two-dimensional analyses**

Ref.	Material	Lined/ unlined	V_l (%)	Lining type
2E1	E	lined	1.0	Herm.
2E2	E	lined	1.5	Herm.
2E3	E	lined	2.0	Herm.
2E4	E	lined	2.5	Herm.
2E6	E	lined	1.0	over.
2E7	E	lined	1.5	over.
2E8	E	lined	2.0	over.
2E9	E	lined	2.5	over.
2EU	E	unlined	uncontrolled	none
2N1	N	lined	1.0	Herm.
2N2	N	lined	1.5	Herm.
2N3	N	lined	2.0	Herm.
2N4	N	lined	2.5	Herm.
2N6	N	lined	1.0	over.
2N7	N	lined	1.5	over.
2N8	N	lined	2.0	over.
2N9	N	lined	2.5	over.
2NU	N	unlined	uncontrolled	none

Notes:

- All analyses are greenfield.
- Material types are those referred to in Section 8.3.
- Lining type is either based on Hermite (*herm.*) beam elements (Section 5.2.1) or overlapping (*over.*) beam elements (Section 5.2.2).

Table 8.7: **Three-dimensional analyses**

Ref.	Material	Lined/ unlined	Greenfield/ building	V_l (%)	Mesh (Fig.)	Excavation stages	Remarks
3EU	E	unlined	greenfield	uncontrolled	8.4	10	
3E1	E	lined	greenfield	1.0	8.4	10	
3NU	N	unlined	greenfield	uncontrolled	8.4	10	
3N1	N	lined	greenfield	1.0	8.4	10	
3N2	N	lined	greenfield	2.0	8.5	4	see note 2
3NB2	N	lined	building	2.0	8.5,8.6	4	see notes 2,3,5
3BB2	N	n/a	building	2.0	8.6	4	see note 6
3N3	N	lined	greenfield	2.0	8.7	4	see note 2
3NB3	N	lined	building	2.0	8.7, 8.8	4	see notes 2,4,5
3BB3	N	n/a	building	2.0	8.8	4	see note 6

Notes:

1. Material types are those referred to in Section 8.3.
2. Excavation stages 1 and 4 are 20m long, stages 2 and 3 are 10m long.
3. Symmetrical building layout: the front facade of the building is situated above a point on the tunnel centreline, 25m from the start of the tunnel.
4. Unsymmetrical building layout: see Figure 8.7.
5. Six analysis load stages as follows:

Load stage	*No. of steps*	*description*
1	20	Apply loads equivalent to building self-weight (see Section 7.3.3)
2	10	Reduce residual out-of-balance forces in building
3	40	Excavate and line tunnel from $Y = 0$ to $Y = 20$
4	40	Excavate and line tunnel from $Y = 20$ to $Y = 30$
5	40	Excavate and line tunnel from $Y = 30$ to $Y = 40$
6	40	Excavate and line tunnel from $Y = 40$ to $Y = 60$

6. Building facades only analysed.

CHAPTER NINE

INTERPRETATION OF NUMERICAL RESULTS

9.1 Introduction

The results of the example analyses outlined in Chapter 8 are presented and discussed in this chapter. Firstly, volume loss control and undrained soil response are checked for each analysis. Comparisons of model results to predictions of settlement and damage from traditional approaches then follow, under three main headings:

- prediction of greenfield surface settlement profiles due to tunnelling,
- prediction of surface settlements with a building present,
- prediction of damage to structures.

Within these headings differences between two- and three-dimensional analyses, lined and unlined analyses and greenfield sites and sites with a building are highlighted and explained. The performance of the model is discussed and conclusions are stated at the end of each sub-section. All plots are placed at the end of the chapter.

9.2 Model checks

Before any conclusions can be drawn from the model results about settlement and damage prediction it is important to check that the model gives the specified volume losses and the soil behaves as close to undrained as possible.

9.2.1 Control of volume loss

Tables 9.1 to 9.3 give V_L^t, the volume loss calculated at the tunnel by the method of Section 7.4.1, for each example analysis. The volume loss specified for each analysis (from Tables 8.6 and 8.7 of Chapter 8) is also indicated. In all unlined analyses, V_L^t at the final stage of the analysis exceeds that of any similar lined analysis. Lined analyses therefore model realistic volume losses for the particular material properties and avoid the unrealistic situation of a lining pulling the ground beyond the point where deformation would cease, were the lining absent.

Final volume losses, V_L^t, are greater than the specified values for all analyses except **3E1** where V_L^t at the final stage is slightly less than the specified value. The maximum departures from specified volume loss are 0.03% for two-dimensional analyses and 0.141% for three-dimensional analyses. The presence of ground loading explains why final volume losses tend to be greater than that specified; the lining experiences loading from the ground in addition to the applied shrinkage forces. Two-dimensional analyses show greater discrepancy between specified and measured volume loss when the former is low (e.g. 1%). This is explained by the greater significance that ground forces must assume when applied shrinkage loading on the lining is low. Differences are also greater with the non-linear soil model probably due to the higher value of K_0 than in the elastic soil model.

Early stages of the three-dimensional analyses show V_L^t less than specified. For example, in analysis **3N3** V_L^t is calculated as 0.141% less than the specified value of 2% at stage 1. As the analysis proceeds V_L^t becomes closer to specified volume loss to finish with V_L^t greater than specified, as described above. This is due to the fixing of leading edge nodes between stages (as described in Section 6.5 and Figure 6.10, Chapter 6) which prevents the lining from shrinking fully at the end adjacent to the excavation face. As the analysis proceeds, this effect becomes less important since the lined tunnel volume affected by ground loading grows much larger than the region affected by the node-fixing.

Analysis **3E1** shows slightly different behaviour to the other (non-linear soil) three-dimensional analyses. While V_L^t at stage 1 is similar to that found in the equivalent non-linear soil analysis **3N1**, V_L^t does not rise as rapidly in subsequent stages and does not (quite) exceed specified volume loss at analysis completion. The explanation lies partly in the smaller ground forces present with this material model (from K_0) and in stiffness reduction ahead of the tunnel face which occurs with the non-linear soil model. Another factor not related to the model is the error in calculating volume loss at the tunnel. The volume of the deformed tunnel lining is always underestimated as the roughly cylindrical surface is approximated by flat facets (see Section 7.4.1). Therefore values of V_L^t are lower bound estimates on the true volume loss at the tunnel. This error explains why **3E1** finishes with V_L^t slightly below that specified.

While there are differences between specified and measured volume losses during the analyses, the final values are small and can be explained by the interaction between the lining and the ground which is not accounted for in the calculation of shrinkage forces. This study demonstrates that it is possible to control volume loss accurately in the model.

Table 9.1: **Volume changes for two-dimensional analyses**

Analysis	Specified V_L (%)	Volume loss measured at tunnel, V_L^t (%)	$V_{tun}(m^3)$	V_s (m^3)	ΔV (m^3)
2d unlined analyses					
2EU	N/A	2.950	0.290	0.290	0.000
2NU	N/A	2.653	0.260	0.260	0.000
2d elastic analyses using Hermitian elements					
2E1	1	1.026	0.101	0.090	0.011
2E2	1.5	1.502	0.148	0.137	0.010
2E3	2	2.001	0.196	0.186	0.010
2E4	2.5	2.501	0.246	0.236	0.010
2d nonlinear analyses using Hermitian elements					
2N1	1	1.034	0.102	0.101	0.001
2N2	1.5	1.508	0.148	0.148	0.000
2N3	2	2.005	0.197	0.197	0.000
2N4	2.5	2.503	0.246	0.247	-0.001
2d elastic analyses using overlapping elements					
2E6	1	1.034	0.102	0.093	0.009
2E7	1.5	1.508	0.148	0.141	0.007
2E8	2	2.004	0.197	0.192	0.005
2E9	2.5	2.503	0.246	0.242	0.004
2d non-linear analyses using overlapping elements					
2N6	1	1.034	0.102	0.101	0.000
2N7	1.5	1.508	0.148	0.148	0.000
2N8	2	2.005	0.197	0.197	0.000
2N9	2.5	2.503	0.246	0.247	-0.001

9.2.2 Undrained soil response

The accuracy with which the soil models represent undrained behaviour can be assessed by comparing the volume change at the tunnel with the volume of the surface settlement trough. Tables 9.1 to 9.3 contain these data for all analyses as V_{tun} and V_s respectively. The first is calculated using the method of Section 7.4.1 (used in Section 9.2.1 to derive V_L^t) and the second as described in Section 7.4.2. Also tabulated is volume difference,

Table 9.2: **Volume changes in three-dimensional analyses**

Analysis	**3EU (uncontrolled volume loss)**				**3E1 (1% volume loss)**			
Stage No.	$V_L^t(\%)$	V_{tun} (m^3)	V_s (m^3)	ΔV (m^3)	$V_L^t(\%)$	V_{tun} (m^3)	V_s (m^3)	ΔV (m^3)
1	1.914	1.127	1.156	-0.028	0.865	0.510	0.516	-0.007
2	2.156	2.540	2.601	-0.061	0.888	1.046	1.062	-0.016
3	2.300	4.064	4.155	-0.090	0.915	1.618	1.624	-0.006
4	2.390	5.631	5.704	-0.073	0.965	2.274	2.240	0.034
5	2.382	7.016	7.134	-0.118	0.949	2.796	2.790	0.005
6	2.415	8.535	8.669	-0.134	0.976	3.450	3.406	0.044
7	2.415	9.958	10.148	-0.190	0.972	4.008	3.982	0.026
8	2.116	9.971	11.683	-1.711	0.969	4.566	4.514	0.052
9	2.437	12.920	13.152	-0.232	0.971	5.149	5.092	0.057
10	2.526	14.879	15.137	-0.258	0.999	5.886	5.780	0.105
Mean				-0.290				0.029
Analysis	**3NU (uncontrolled volume loss)**				**3N1 (1% volume loss)**			
Stage No.	$V_L^t(\%)$	V_{tun} (m^3)	V_s (m^3)	ΔV (m^3)	$V_L^t(\%)$	V_{tun} (m^3)	V_s (m^3)	ΔV (m^3)
1	1.369	0.806	0.914	-0.108	0.862	0.508	0.560	-0.053
2	1.688	1.989	2.161	-0.173	0.909	1.071	1.157	-0.086
3	1.902	3.361	3.632	-0.271	0.949	1.677	1.780	-0.103
4	2.000	4.712	5.034	-0.322	1.006	2.370	2.445	-0.075
5	2.033	5.988	6.395	-0.407	0.993	2.925	3.067	-0.142
6	2.067	7.305	7.773	-0.468	1.024	3.619	3.731	-0.112
7	2.077	8.564	9.130	-0.566	1.021	4.210	4.374	-0.164
8	2.112	9.953	10.586	-0.633	1.033	4.868	5.018	-0.150
9	2.119	11.234	11.959	-0.725	1.022	5.418	5.599	-0.180
10	2.246	13.230	13.979	-0.749	1.052	6.197	6.329	-0.132
Mean				-0.442				-0.120

ΔV, equal to $V_{tun} - V_s$, which is zero for perfectly incompressible behaviour. A positive value of ΔV indicates that more volume is *lost* at the tunnel than at the surface so there is volumetric expansion during the analysis. It should be noted that the volume of the surface settlement trough, V_s is calculated less accurately in three-dimensional analyses than in two-dimensional analyses since the mesh used for the latter possesses a higher density of sampling points (i.e. nodes with displacement data). In the two-dimensional mesh used in this thesis there are 41 surface nodes giving an average density of 1 node

Table 9.3: **Volume changes in three-dimensional analyses**

Analysis	**3N2(2% volume loss)**				**3NB2(2% volume loss)**			
Stage No.	$V_L^t(\%)$	V_{tun} (m^3)	V_s (m^3)	ΔV (m^3)	$V_L^t(\%)$	V_{tun} (m^3)	V_s (m^3)	ΔV (m^3)
1	1.868	3.668	3.806	-0.138	1.868	3.668	3.814	-0.146
2	1.941	5.717	5.899	-0.183	1.941	5.717	5.919	-0.202
3	1.966	7.720	7.970	-0.250	1.965	7.717	7.995	-0.278
4	2.013	11.858	12.122	-0.264	2.027	11.940	12.149	-0.209
Mean				-0.209				-0.209

Analysis	**3N3(2% volume loss)**				**3NB3(2% volume loss)**			
Stage No.	$V_L^t(\%)$	V_{tun} (m^3)	V_s (m^3)	ΔV (m^3)	$V_L^t(\%)$	V_{tun} (m^3)	V_s (m^3)	ΔV (m^3)
1	1.859	7.300	7.833	-0.533	1.904	7.477	7.998	-0.521
2	1.941	11.433	12.138	-0.705	2.006	11.816	12.581	-0.765
3	1.965	15.433	16.028	-0.595	2.028	15.928	16.621	-0.693
4	2.027	23.880	24.956	-1.076	2.090	24.622	25.787	-1.165
Mean				-0.727				-0.786

per 1.46m^2 whereas in a typical three-dimensional mesh (**3E1**) there are 847 surface nodes giving a density of 1 node per 4.25m^2. While errors in the three-dimensional calculation have not been assessed in detail, they are not thought to be significant to the following discussion.

The most important feature of the volume differences is that, for all analyses, they are small with respect to the volume change measured at the tunnel showing that the soil response is nearly incompressible. Two-dimensional analyses show volume differences as a proportion of volume change at the tunnel varying from negligible, with non-linear soil, up to 9% for elastic analyses. In three-dimensional analyses, volume differences represent between 1.5% and 6% of the volume change at the tunnel. Some difference is to be expected from the use of a Poisson's ratio of 0.49 in both soil models (see Section 8.3.1.1). In two-dimensional analyses with the elastic soil model (**2E1 - 2E9**), volume difference is positive, being greater for low values of specified volume loss (see Table 9.1). The largest volume difference (0.01m^3) occurs in analysis **2E1** i.e. the volume *lost* at the surface is 0.01m^3 less than that calculated at the tunnel, so the mesh expands by this amount during the analysis. To assess the significance of this volume difference, the pressure necessary to produce an equivalent volumetric strain in the mesh is calculated,

$$\text{equivalent volumetric strain, } \epsilon_v = \frac{\text{volume difference}}{\text{total mesh volume}} \tag{9.1}$$

$$= \frac{0.01}{60^2} = 2.78 \times 10^{-6} \tag{9.2}$$

Taking the mean shear modulus for the mesh, $G = 18750$kPa (see Table 8.2, Chapter 8) and using Equation 3.3 gives a bulk modulus of 9.31×10^5kPa. Then pressure, Δp to produce ϵ_v is

$$\Delta p = K\epsilon_v = 2.59\text{kPa} \tag{9.3}$$

Since the unit weight of the soil is 20kN/m^3 this pressure represents only 0.6% of the weight of the tunnel volume and therefore the volume difference can be considered insignificant. This calculation uses the worst case for all two-dimensional analyses; the majority have volume differences considerably lower. Two-dimensional analyses using the non-linear soil model (**2N1-2N9**) have negligible volume differences which can be explained by the difference in formulation of the material models. Changes in stiffness in the non-linear soil are modelled using nested yield surfaces and volumetric behaviour is purely elastic (Chow, 1994). When the state of stress activates one or more of the nested surfaces the subsequent strains are purely deviatoric, following the von Mises flow rule, although the stresses are below failure. The behaviour therefore more closely approaches incompressibility than the elastic model.

The sign of the volume difference also requires explanation. In the two-dimensional elastic analyses the volume difference is positive and the mesh expands. In the three-dimensional non-linear analyses, the reverse happens and the mesh contracts. As will be seen in Section 9.3, elastic analyses with low specified volume losses exhibit surface heaves rather than settlements indicating that the heave due to unloading of the soil dominates over the deformation induced by liner shrinkage. This may explain the difference in sign of volume differences: elastic analyses are affected by unloading (leading to expansion) more than the non-linear analyses because of the greater, and variable, stiffness of the latter. The three-dimensional elastic analysis (**3E1**) shows the same pattern of volume difference seen in two-dimensions. Volume difference after stage 3 is positive indicating expansion. At stage 10, the volume difference is 0.105m^3 which, divided by the mesh volume as in Equation 9.1 above, gives a volumetric strain of 0.49×10^{-6}, a lower value to the worst two-dimensional case making volume difference similarly insignificant.

In conclusion, the data show soil behaviour reasonably close to incompressible given the value of Poisson's ratio, the errors inherent in volume calculations and the approximation of the finite element method.

9.3 Prediction of greenfield surface settlements

The ability of the model to predict surface settlement profiles for tunnelling at greenfield sites is examined in this section. All two-dimensional example analyses and the majority of three-dimensional analyses provide suitable results for this purpose. Three-dimensional analyses **3NB2, 3NB3, 3BB2, 3BB3** include a building and are not considered until later sections.

Firstly, the predicted settlement trough parameters, S_{max} and i are calculated for the tunnel configuration used in all example analyses i.e.

$$\text{depth to tunnel axis,} \quad Z = 10\text{m} \tag{9.4}$$

$$\text{tunnel diameter,} \quad D = 5\text{m} \tag{9.5}$$

Using Equation 1.2 to determine the trough width parameter, i (for a clay soil) gives

$$i = 0.5Z = 5\text{m} \tag{9.6}$$

and from Equation 1.5,

$$S_{max} \approx \frac{V_L D^2}{319i} \tag{9.7}$$

Inserting i and D for the tunnel configuration used gives

$$S_{max} = 15.67 V_L \tag{9.8}$$

where S_{max} is in millimetres and V_L is the percentage volume loss. The maximum settlement over the tunnel, S_{max} can therefore be calculated for the range of volume losses measured in the example analyses, to compare with the settlements obtained from the numerical model. Some values are given in Table 9.4.

Table 9.4: **Maximum settlement using the semi-empirical approach for values of volume loss**

V_L (%)	1.0	1.5	2.0	2.5	3.0	3.5
S_{max} (mm)	15.7	23.5	31.3	39.2	47.0	54.8

Values of S_{max} obtained with the numerical model, for each of the example analyses (including those with a building present), are given in Table 9.5. These are accompanied by the predicted values from Equation 9.8 using the volume loss measured at the tunnel, V_L^t. The final column of this table gives the model value as a percentage of the traditional prediction. In every case, the numerical model underpredicts the maximum settlement and in some cases heave (upwards movement), rather than settlement, is predicted by the numerical model.

9.3.1 Two-dimensional analyses

Transverse surface settlement plots from two-dimensional analyses are shown in Figures 9.4 to 9.7. The first two figures of this group show the results from analyses using lining elements based on the Hermitian beam formulation while Figures 9.6 and 9.7 are for the overlapping beam-based elements. The results show smooth settlement profiles which correspond reasonably well with the expected shapes where volume loss is high, especially using the non-linear soil model (N). Visual estimates of the trough width parameter, i, for these analyses are between 8m and 10m for both soil models, wider than the 5m predicted in Equation 9.6 above. This, together with the incompressibility of the material models, leads to the low values of S_{max}. The elastic soil model gives a heaving response over the tunnel at low volume losses and surface settlement in the far field for all volume losses. These features are seen particularly in analyses **2E1** and **2E6** and correspond with the findings of previous research (as described in Section 2.3.1).

For the elastic soil, the best prediction of S_{max} is 38% of the semi-empirical value occurring in the unlined analysis **2EU**. At low values of volume loss in elastic analyses, the heave due to unloading appears to dominate and is transmitted to the surface across the excavated tunnel by the (relatively rigid) lining. Improved values, of between 54% and 67% of the traditional predictions, are obtained with the non-linear soil model. However, this is disappointing considering the complexity of the material formulation. It was anticipated that there would be greater localisation of strain, and hence narrow troughs, given that the changes of stiffness at small strains are modelled (see Section 2.3.1). Despite this, there is evidence of greater strain localisation by the relatively minor far field settlements in the non-linear analyses.

The settlement profiles for the two different lining elements (e.g. Figures 9.4 and 9.6) for both the elastic and non-linear soil models are very similar confirming that the use of the unusual overlapping lining element has no deleterious effect on model behaviour. Where there are minor differences in S_{max}, with analyses **2E1** and **2E6** for example, these can be attributed to the slightly different mesh geometry required for the two types of lining element (see Section 8.4.1).

9.3.2 Three-dimensional analyses

Figure 9.8 shows transverse and longitudinal plots of surface settlements for unlined three-dimensional analyses **3EU** and **3NU**. The transverse plots are taken halfway (i.e. 30m) along the tunnel excavation, (hence the notation **CS30**). The most obvious difference from the two-dimensional plots is the irregularity of the profiles which is due to the coarser mesh necessary for three-dimensional analyses. Similarly located plots for lined analyses **3E1** and **3N1** are given in Figure 9.9 and show even more marked irregularity indicating that the presence of the lining, or its shrinkage, affects the quality of the results.

Figures 9.8 and 9.9 show similar trough width parameters to the equivalent two-dimensional results but smaller values of S_{max}. Confirmation can be found in Table 9.5 where the three-dimensional model settlements are clearly smaller percentages of the traditional predictions than seen in the two-dimensional analyses. The coarse discretisation mentioned above may also explain this difference in maximum settlement between two- and three-dimensional analyses. A mesh comprised of larger, on average, elements will be stiffer and hence lead to reduced deformation under load.

Figures 9.17 and 9.18 show contour plots of surface settlements for unlined analyses with the elastic and non-linear soil models respectively (analyses **3EU** and **3NU**). In

Table 9.5: **Comparisons of maximum settlements from traditional approach and numerical analyses**

Analysis	V_L^t(%)	Predicted S_{max} (Equation 9.8) (mm)	S_{max} from numerical model (mm)	Model S_{max} as percentage of predicted
2d unlined analyses				
2EU	2.95	46.2	17.4	37.7
2NU	2.65	41.6	27.9	67.2
2d elastic analyses using Hermitian elements				
2E1	1.03	16.1	-0.8	-4.7
2E2	1.50	23.5	2.1	9.1
2E3	2.00	31.3	5.1	16.4
2E4	2.50	39.2	8.2	20.9
2d elastic analyses using overlapping elements				
2E6	1.03	16.2	-0.7	-4.4
2E7	1.51	23.6	2.2	9.4
2E8	2.00	31.4	5.3	16.9
2E9	2.50	39.2	8.4	21.4
2d nonlinear analyses using Hermitian elements				
2N1	1.03	16.2	8.7	53.9
2N2	1.51	23.6	13.3	56.4
2N3	2.00	31.4	18.2	57.8
2N4	2.50	39.2	23.1	58.9
2d non-linear analyses using overlapping elements				
2N6	1.03	16.2	8.7	53.8
2N7	1.51	23.6	13.3	56.3
2N8	2.00	31.4	18.1	57.8
2N9	2.50	39.2	23.1	58.8
3d unlined analyses				
3EU	2.53	39.6	12.5	31.6
3NU	2.25	35.2	17.1	48.6
3d elastic lined analysis				
3E1	1.10	17.3	1.6	9.2
3d non-linear lined analyses				
3N1	1.05	16.5	6.9	41.9
3N2	2.01	31.5	15.3	48.5
3NB2	2.03	31.8	16.9	53.2
3N3	2.03	31.8	13.7	43.1
3NB3	2.09	32.7	20.5	62.6

Notes: S_{max} for 3d analyses taken as final vertical displacement at centre of mesh surface.

common with all contour plots presented in this thesis, excavation proceeds from the base of the plot upwards. Contours for similar lined analyses, **3E1** and **3N1** are shown in Figures 9.19 and 9.20 and show more clearly the irregularity in settlement profile obtained with lined analyses. These plots also show occasional sharp localised departures from the general settlement pattern (referred to as *hotspots*). The phenomenon is not seen in the two-dimensional results (e.g. Figure 9.4).

Analyses **3E1** and **3N1** both have specified volume losses of 1% and give low model values of S_{max}, particularly the elastic soil analysis where S_{max} is only 9.2% of the traditional prediction. This follows the findings of the two-dimensional analyses where low volume loss analyses show particularly poor S_{max} prediction. Interestingly, the final transverse profile in analysis **3E1** does not show a net heave over the tunnel like the equivalent two-dimensional analysis, **2E1** (in terms of volume loss and soil type). The contour plots for this analysis show that each stage of excavation and lining produce settlement immediately over the lining and small heaves ahead, as also seen in the unlined analysis **3EU**. This implies that the excavation unloading which led to heave at the surface in the two-dimensional analysis **2E1** is of less significance in three-dimensions, although it certainly reduces values of S_{max}. This is expected because the full length of the tunnel is excavated in one step in the two-dimensional analysis as compared to 6m lengths in each stage of the three-dimensional analysis. Soil ahead of the tunnel face is not subject to the same unloading and its presence adds restraint to the soil surrounding the excavated length of tunnel.

The appearance in the transverse settlement profile for analysis **3E1** of a *hinge* point at approximately 12m from the centreline, where a sharp change in settlement is apparent, is a symptom of the coarse mesh and not an error in applying mesh constraints. After stage 6 the general profile remains the same shape (since subsequent excavation and unloading take place ahead of the section) except immediately over the tunnel where small reductions in settlement are visible at late stages in the analysis. These are also present in the transverse settlement plots for unlined three-dimensional greenfield analyses and therefore cannot be due entirely to the presence of the liner but instead arises from unloading due to excavation of the tunnel volume. The effect is more pronounced in the elastic lined analysis (**3E1**) because the material is more flexible below the tunnel, and so greater heaves are induced. The presence of the lining also helps to transmit the heave at the tunnel to the surface further enhancing the effect over that seen in unlined analyses e.g. **3EU**. The continuity of the liner between stages also transmits heaves at later stages to earlier ones, hence further explaining the reductions in settlement at the centre of the mesh over the tunnel towards the end of analysis **3E1**.

Apart from the effect of coarser discretisation, direct comparison of two- and three-dimensional analyses is difficult in all cases since volume losses vary and the loads applied to the mesh to shrink linings are different. Two- and three-dimensional analyses using the non-linear soil are even more difficult to compare since the results are also affected by the number of stages and intermediate steps taken for completion. All two-dimensional analyses were undertaken using more load steps than any comparable three-dimensional analysis. The complexity of the models makes it difficult to assess whether a reduced number of steps leads to an under or over prediction of settlements. However, a larger number of solution steps will lead to a smaller error in the final out-of-balance forces in the mesh.

The greenfield analyses, **3N2** and **3N3**, which are used to assess the effect of a building in Section 9.4, show the same features of irregular settlement profiles and presence of *hotspots*. Settlement plots for these analyses are given in Figures 9.10 and 9.13 and contour plots in Figures 9.21 and 9.23. The localised deviations from generally expected patterns of settlement (*hotspots*) visible in contour plots of lined three-dimensional analyses (particularly in Figure 9.23) generally lie above areas immediately behind the current tunnel face. Figure 9.3 shows the deformed shape of the lining elements alone at intermediate and final stages of analysis **3N3**. Uniform shrinkage of the liner is clearly obtained, as required, with later stages of shrinkage not affecting earlier ones (as discussed in Section 6.5). The same uniform shrinkage is seen in all lined analyses, although deformation plots are not included here for brevity. Reference to Figure 6.10 (of Chapter 6) shows that the method of volume loss control leads to non-uniform distortion of a band of elements at the end of each stage unlike those earlier in the stage. These elements span between uniformly distorted elements and the nodes at the face which are fixed for that stage. Since this band of elements is attached to the ground, elements in the ground adjacent to the lining will experience a significantly different distortion pattern to those adjacent to linings earlier in the stage. It is possible that these elements are subjected to sufficiently large distortional strains to reduce the stiffness locally by a large degree. If these elements are relatively large, as is the case in these relatively coarse meshes, this would lead to large localised displacements at the surface and hence explain the *hotspots*.

Perhaps of greater significance are the coarse meshes and long excavation lengths used in these particular three-dimensional analyses. The reasons for using coarse meshes were linked to limitations in computer resources and achievement of practical run times as discussed in Section 7.2.2. Additionally, the non-linear soil analyses were carried out in four stages of tunnel construction with relatively few intermediate loading steps to account for the non-linearity of the ground model. Again, this was to limit run times. As a consequence of these two constraints, it would appear that, certainly in analysis **3N3**, the response is affected. The mesh for **3N3** is particularly visibly coarse over the centreline about 16m from the start of the tunnel. This is both the location of a settlement *hotspot* and just behind the face of stage 1.

9.3.3 Summary - greenfield settlement prediction

To summarise, for greenfield analyses:

- Settlement troughs predicted by the model are wider and flatter than expected and are relatively poor predictions of greenfield settlement profiles.
- The non-linear soil model performs significantly better than the elastic soil model for the ground but results are still disappointing.
- Mesh discretisation has a major effect on the smoothness of settlement results.
- The limitations imposed in the three-dimensional analyses on fineness of discretisation and numbers of loading steps have a deleterious effect on the performance of the lining elements.
- The way that volume loss is modelled (using linings) leads to greater irregularity in the settlement profiles and the presence of *hotspots* above the ends of excavation stages.

9.4 Prediction of surface settlements with a building present

The discussion above has dealt with greenfield site predictions. In many respects, the performance of the model with a building present at the surface is of prime importance considering the goal of the research project. There are no standard procedures for determining settlement profiles where a structure is present (see Section 1.4) although recently, Potts and Addenbrooke (1996) have used settlement profiles from two-dimensional analyses with buildings to modify the damage assessment procedure, as discussed in Section 2.3.2. Their method will be used in Section 9.5.

The pairs of analyses **3N2/3NB2** and **3N3/3NB3** use the same ground mesh and tunnel excavation with and without a building present at the surface and can be used to assess the effect of a surface structure on settlement profiles. Figures 9.10 and 9.11 show settlement plots for the first pair of analyses and contour plots are shown in Figures 9.21 and 9.22. The structure lies square to the tunnel axis in these analyses so that the configuration resembles the two-dimensional model of Potts and Addenbrooke (1996) and other two-dimensional analyses. In the second pair of analyses, **3N3/3NB3** the building is skewed in plan and the situation bears less relation to the standard two-dimensional model. Settlement plots for these analyses are given in Figures 9.13 and 9.14 and contour plots follow in Figures 9.23 and 9.24. Reference is made to the east and west portions of the skewed building in the following discussion. These are to the right and left, respectively, of the tunnel centreline, as indicated in Figure 8.7.

9.4.1 Building square to tunnel centreline

Transverse settlements along the base of the building (e.g. at CS25) are strongly affected by the presence of the building as indicated by comparison of the plots in Figures 9.10 and 9.11. The building facade stiffens up the response of the ground, flattening the profile. The presence of the door opening adjacent to the tunnel centreline at the surface is evident from Figure 9.11. In this location, the settlement reduces from a uniform level found where the building is attached to the ground (i.e. up to 10m horizontally from the tunnel axis). Comparison of plots with and without the building

(Figures 9.10 and 9.11) show that maximum settlements increase slightly in the former case. This is particularly clear in the plots taken along the front facade (at CS25) where S_{max} at completion rises from 15mm in the greenfield case to 17.5mm with the building. While the flattening of the profile agrees with expectations, these results also indicate the weight of the building to have a significant effect.

The effect of the building is localised as shown by comparison of transverse settlements at the centre of the square building (i.e. at CS30). The settlements over the tunnel at each analysis stage are the same for both greenfield (Figure 9.10) and building analyses (Figure 9.11). Moving away from the tunnel, settlement is seen to increase sharply from a point approximately 4m from the side facade. Maximum settlements, in excess of those found in greenfield analyses, occur directly beneath the side facade. The contour plots (Figures 9.21 and 9.22) further demonstrate this effect of the building on the surface settlements. Concentrated settlement is shown along the building outline which returns to the greenfield settlement pattern over a short distance. This leads to sharp gradients of settlement either side of the building which could have implications for adjacent, more flexible, structures. Longitudinal plots for the square building have similar shapes to the greenfield plots although values of maximum settlement are not in agreement, due to the effect of building weight.

9.4.2 Building skewed to tunnel centreline

Examination of results for the skewed building analyses (**3N3/3NB3**) lead to the same general conclusions as for the square building although the flattening out of the profile is far less severe. This can be ascribed to the less severe stiffening offered by the building as it is neither square to the tunnel nor located centrally. Figures 9.13 and 9.14 show that maximum settlements again increase with the building present. For example at CS30, over the tunnel, S_{max} increases from 13mm to 18mm. The presence of the building is evident in the transverse plots at CS20 where the western (i.e. left-hand) portion of the trough is deepened in analysis **3NB3**. This is to be expected since this is the side containing a longer stretch of building. Figure 9.15 shows plots of settlements along the front and rear of the skewed building (or building outline for the greenfield case) once again demonstrating that settlements increase with the presence of the building. Particularly in the front facade, the settlement profiles are flatter. Each facade also appears to rotate about its west end (i.e. that furthest from the tunnel axis). This is, however, an effect which is visible in the greenfield results indicating that overall rotation is not due to the presence of the building.

The contour plots for the skewed building analysis (Figures 9.23 and 9.24) show some concentration of settlements around the building base but this is confined to the east end of the building. Other parts of the building appear not to affect the pattern of settlements greatly. Interestingly, the settlement *hotspots* discussed in Section 9.3.2 appear to reduce in magnitude with the presence of the building. For evidence of this, compare contour plots in Figures 9.23 and 9.24 at stage 3. The *hotspot* above the tunnel axis, at approximately 16m from its start appears at stage 1 with the same magnitude in both analyses. At subsequent stages of the greenfield analysis, its magnitude increases while in the building analysis its magnitude remains roughly the same over subsequent stages. This may be due to the additional stiffness of the building or increased stability provided by its weight ahead of the tunnel at stage 1.

Longitudinal plots (see Figures 9.13 and 9.14) for the skewed building analysis show major differences in shape to the greenfield analysis, especially at intermediate stages 2 and 3. This is to be expected since the facades are now rotated only 45° in plan from the tunnel centreline (which coincides with the longitudinal settlement plot line. The in-plane stiffness of the facades will therefore have a greater influence in this analysis than in the square building analysis, where the front and rear facades are normal to the longitudinal plot line. These settlements also occur along a line close to the join between the front and east side facades where one might expect a large combined stiffening effect

9.4.3 Summary - effect of a building on settlements

To summarise, the results indicate that :

- The presence of a building both flattens out the settlement profile and increases the maximum settlement. The severity of the flattening depends strongly upon the geometrical arrangement of the building with respect to the tunnel axis.
- The relative lengths of building and settlement trough and how they are configured with respect to each other has an important bearing on the effect of the building. It is postulated that, for the square building analysis the flattening effect is severe partly because the building spans over both points of inflection of the greenfield settlement trough. This serves to restrain the ends of the building and thereby stiffen it across the sagging section of the trough. In the second case, the end of the skew building is within the sagging zone and the restraint is not present.

9.5 Building damage

Building damage resulting from tunnelling induced settlement is generally determined in practice separately from the prediction of settlement, as discussed in Section 1.3. In this section, the location and severity of building damage predicted by the model, for analyses **3NB2** and **3NB3**, is compared to the predictions using the method of Burland and Wroth (1975) modified by the recommendations in Potts and Addenbrooke (1996). This is accomplished through examination of patterns of cracking and of the displacements of the base of building facades. A detailed analysis of crack patterns and magnitudes is both beyond the scope of this thesis and inappropriate, given the small number of results. The discussion is therefore restricted to general points which are also relevant to an understanding of the model. The effects of applying greenfield settlements from the model to a separate finite element mesh of the building are discussed in Section 9.5.4. This is intended to show how the adoption of a two-stage procedure, where the presence of the building is ignored in the determination of settlements, leads to significantly different damage predictions.

Selected crack pattern plots from analyses **3NB2**, **3NB3**, **3BB2** and **3BB3** are presented in Figures 9.29 to 9.37. In each plot, the view given is from **outside** the building. As described in Section 7.4, groups of lines are plotted at each element integration point where cracking is indicated for the non-linear masonry model. The number and proximity of lines within groups indicates the size of the crack so that a high level of cracking is shown by a grey block. Lines are plotted at the inclination of the predicted cracking. For analyses of the full model (analyses **3NB2**, **3NB3**) the threshold crack strain, below which cracks are not plotted is 250 microstrain (.025%). Due to the much higher levels of cracking predicted for the facade-only analyses (**3BB2**, **3BB3**) the threshold level of crack strain is raised to 500 microstrain.

Figures 9.25 to 9.28 show contours of principal tensile strains (i.e. crack strains) in the main facades of the buildings at the ends of analyses **3NB2** and **3NB3**. These are included for comparison with the single values of maximum principal tensile strain derived in the existing method of damage prediction, see Section 9.5.1 which follows.

Isometric views of building base movements at each stage of analyses **3NB2** and **3NB3** are given in Figures 9.12 and 9.16 respectively. Arrows in these plots show the total displacement (i.e. not just vertical) to an exaggerated scale, of each node along the base of the facade. These are presented to help indicate the mechanism of deformation which leads to cracking in the building facade.

9.5.1 A traditional damage assessment

The procedure outlined in Mair et al. (1996) (which summarises the procedure originally devised by Burland & Wroth) is now used to predict the critical tensile strain in each building (square and skew) when subjected to settlement. Figure 9.1 shows the layout of each building in relation to the greenfield settlement trough derived from the procedure in Section 9.3 for the volume loss specified in the analyses (2%). In the case of the skew building, the profile is applied to a projection of the building front facade. Only vertical settlements are considered in this assessment since

- predicted horizontal displacement, calculated using the assumptions in Mair et al. (1996), will only be a maximum of 31% of S_{max},
- results of the numerical analyses show that horizontal movements along the facade bases are relatively small (see Figures 9.12 and 9.16) and,
- excluding horizontal displacement simplifies the assessment.

The location of the point of inflection of the settlement curve divides each building into regions affected by sagging and hogging. Maximum deflection (Δ) is not necessarily at the centre of each region and is calculated using trial and error. For each case,

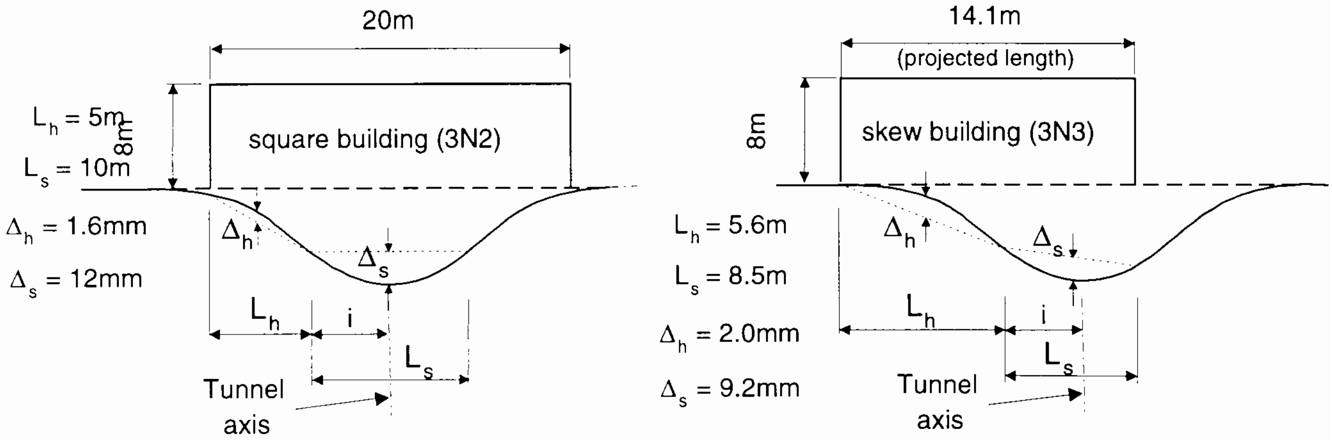

Figure 9.1: **Layouts assumed for traditional damage analyses**

the maximum tensile strains, for bending (ϵ_b) or shear deformation (ϵ_d), are calculated using locations of neutral axes following the recommendations in Mair et al. (1996). The results from this unmodified analysis are given in rows two and three of Table 9.6. These results indicate both buildings to be most susceptible to bending deformation cracking in the sagging region above the tunnel axis. The category of damage, according to the classification used in Mair et al. (1996), is *moderate* for the square building and *slight* for the skew building.

To take account of the building, the method in Potts and Addenbrooke (1996) is now used. Factors to modify the deflection ratios (Δ/L) for hogging and sagging deformation are obtained using a measure of relative bending stiffness ρ^* where

$$\rho^* = \frac{EI}{E_s H^4} \tag{9.9}$$

E and E_s are the Young's moduli of the building and ground respectively, I is the second moment of area of a beam representing the building and H is one-half of the length of the building. From the material properties given in Chapter 8, E_s is taken as 108.0×10^3kPa, being 80% of the Young's modulus of material N at a depth of $Z/2$. E is taken as 1.0×10^6kN/m^2, which is 10% of the compressive Young's modulus for the masonry material. This is to account for the negligible strength in tension. The value

Table 9.6: **Maximum tensile strains (microstrain) according to a traditional damage analysis**

Building layout	ϵ_b (sagging)	ϵ_d (sagging)	ϵ_b (hogging)	ϵ_d (hogging)
Square	1750	860	190	800
Skew	1390	850	190	350
Revised values including the effect of the building, (Potts and Addenbrooke, 1996)				
Square	790	390	40	160
Skew	620	380	40	70

of I depends on the mode of bending (i.e. hogging or sagging). The following relative bending stiffnesses are then obtained,

$$\rho^*(\text{sagging}) = 4.0 \times 10^{-2}\text{m}^{-1}, \qquad \rho^*(\text{hogging}) = 1.6 \times 10^{-1}\text{m}^{-1} \tag{9.10}$$

The modification factors corresponding to these values of ρ^* (from Figure 4 in Potts and Addenbrooke (1996)) are,

$$M^{DR_{sag}} = 0.45, \qquad M^{DR_{hog}} = 0.2 \tag{9.11}$$

Applying these to the deflection ratios used to calculate the maximum tensile strains in rows two and three of Table 9.6 gives the revised maximum tensile strains (also in Table 9.6). The predicted damage categories both reduce by one class; the square building to *slight* damage and the skew building to *very slight* damage.

9.5.2 Prediction of damage from the numerical model - square building layout, analysis 3NB2

Figure 9.25 indicates the maximum final crack strain in the front facade to be under 1000 microstrain which is closer to the worst value of the modified damage analysis (790 microstrain) than that of the original damage analysis. In contrast, the rear facade contour plot in Figure 9.26 indicates a much higher maximum crack strain (between

2500 and 3000 microstrain). However, in general the contours show crack strains to be roughly at the level of the modified analysis although it is clearly difficult to compare a single result, from a traditional analysis, to the comprehensive data from the numerical model.

Figures 9.29 to 9.31 show the predicted crack patterns for each stage of analysis **3NB2**. The first observation is of the apparently small amount of damage sustained by this facade due to tunnelling settlements. This can be explained partly by the conclusions of Section 9.3.2 for greenfield sites. It is likely that the model also underestimates settlements in analyses with buildings, leading on to lower damage predictions. Another general observation is that each facade appears to be affected, in some cases substantially, by its neighbour. Side facade patterns are generally confined to areas at the base corners i.e. where the side facade meets the front or rear facade and the ground.

The base of the facades (Figure 9.12) displace roughly as might be expected by the passage of a tunnel excavation except at stage 1 where the front facade slopes away from the tunnel. This can only be explained by mesh coarseness (in the ground) leading to an irregular pattern of displacement. Stages 2 to 4 show the front facade tilting towards the tunnel centreline followed by the rear facade as the tunnel passes beneath.

The front facade is only slightly damaged by the passage of the tunnel (Figure 9.29), cracking mainly occurring adjacent to the doorway. At this location, there is an area of vertical cracking which stabilises by stage 2, in agreement with the facade's location close to the tunnel face of stage 1 and with the displacement of the facade base. The facade appears to experience an overall horizontal displacement between stages 2 and 3 with the only new cracking occurring at the join with the side facade. At stage 4, new cracks appear between the ground floor windows due to a small sag induced along the base by the reduction in settlement at the join with the side facade. It is noticeable that the crack patterns do not always follow from the facade base displacements. For example, in stage 1, a small hogging curvature is visible approximately one-third along the facade base which is not matched by any visible cracking in Figure 9.11(a). It is possible that areas of the facade are on the verge of cracking induced by this base deformation but this is not shown in this form of plot. It is also likely that the mechanism of deformation leading to cracking is not linked simply to the facade base deformation but to interaction between facades, above the base.

The rear facade shows a large area of vertical cracking, passing down from the top to the base of the ground floor windows at stage 1. This is also visible at stage 2 but by stage 3, when the tunnel face is directly beneath, these cracks close up (i.e. they disappear from the plot). The final pattern for the rear facade is heavy vertical cracking between ground floor windows and between doorway and the adjacent window. The early stages of rear facade cracking appear to be due to interaction between facades rather than as a result of tunnelling settlements, which are negligible for this facade in stages 1 and 2. This assertion is backed up by the base displacement plot (Figure 9.12) which shows the facade to sink uniformly in stages 1 and 2. At stage 3, the tunnelling induced settlements produce a sagging curvature along the base which increases at stage 4. This deformation serves to close up the cracks at the top of the facade and induce new cracking between the ground floor windows.

The side facade shows most severe cracking at the joints with the other facades. Interaction between facades appears to dominate cracking response of this facade since the base displacements do not always lead to the expected cracking effect, as discussed above for the front facade. At stage 1, the base displacements show an overall hogging curvature which might be expected to lead to cracking at the top of the facade but this does not appear in Figure 9.30. Instead, there is an area of vertical cracking stretching from the base to the centre of the facade located slightly off-centre. Conversely, at stage 4, the general sagging curvature visible along the facade base leads to the re-emergence of cracking near to the base of the facade centre, as might be expected. Explanation of this behaviour is difficult without more detailed investigation but one aspect which has been ignored is the imposition of self-weight before tunnelling is modelled, discussed in Section 7.3.3, which will have two effects

- to add (compressive) prestress to some areas of the facade and hence greater apparent resistance to cracking once tunnelling starts,
- to weaken other areas of the building making it more susceptible to cracking.

The results of this analysis clearly show how facades which are located at different points above the tunnel centreline are damaged to differing degrees. A two-dimensional analysis would predict identical damage for the front and rear facades in this analysis. While there are clear shortcomings in this model, as shown earlier in its ability to predict greenfield settlements, it does however provide useful data on damage at intermediate stages of the analysis as the tunnel passes beneath the building. Such damage does not match the final crack pattern and could not be predicted by a conventional two-dimensional analysis.

9.5.3 Prediction of damage from the numerical model - skew building layout, analysis 3NB3

In this analysis, while the whole building is modelled only damage relating to the front and rear facades is discussed for brevity. Figure 9.2 shows the numbering scheme used in the following discussion for the windows in the skew building, as viewed from the **outside** of each facade.

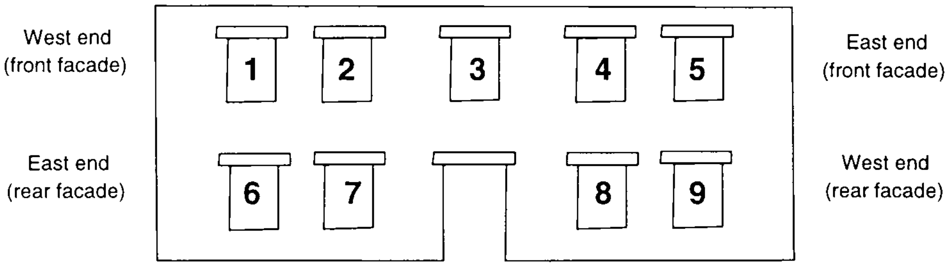

Figure 9.2: **Numbering scheme for windows in skew building analyses**

The traditional analysis predicts equal or lower levels of damage for this building as compared to the square building (see Table 9.6). A similar conclusion may be drawn from the model results but for the front facade only. Crack strain levels, shown contoured in Figure 9.27, are less than 750 microstrain and, as in the square building analysis, are generally in agreement with the modified analysis results. The rear facade crack strains, which are contoured in Figure 9.28, are generally higher than the traditional predictions with a maximum strain of between 3000 and 3500 microstrain. An explanation for this behaviour is in the locations of the two facades with respect to the tunnelling direction and in damage sustained by interaction between facades.

Figures 9.32 and 9.33 show the cracking patterns predicted for the front and rear facades of the building at each stage of the analysis. In a similar pattern to the square building analysis, the front facade is least affected, the rear facade heavily affected. This reiterates the importance of facade location, with respect to the tunnelling direction, and also implies that interaction with neighbours may be a significant factor for damage prediction.

The displacements of the base of the building at each stage are shown in Figure 9.16. The skewed and offset layout of this building to the tunnelling direction leads to different base movements to the square building. These movements appear to follow expectations, although they are more uneven. At stage 1, the west corner of the front facade has settled differentially to the rest of the building which has only slightly sunk.

At stage 2, the tunnel face lies beneath the building and the front facade has uniformly settled. The east corner of the rear facade settles in stages 3 and 4 as the tunnel clears the building and excavation is completed.

In the front facade (Figure 9.32), cracking commences at stage 1 and is heaviest around window 7. There is also some vertical soffit cracking between windows 3 and 4 indicating hogging bending. The base displacements follow these crack patterns reasonably well with a sagging curvature portion visible at the west end of the facade agreeing with the presence of cracking between the ground floor windows. At stage 2, the crack pattern changes completely: extensive, generally vertical cracking extends from the east base corner upwards towards the centre of window 5 and the earlier cracks close up. The latter can be explained by the uniform profile adopted by the base shown in Figure 9.16. The cracking at the east end indicates dominant shear effects under sagging deformation as modelled in the traditional analysis. Evidence for this lies in the angled trend followed by this area of cracking. The base displacement plot indicates this area of cracking to arise from interaction with the side facade. Further explanation of the behaviour at stages 1 and 2 may be found in the contour plot of Figure 9.24. At stage 1, settlements are affecting only the western corner of the front facade and cracking is confined to this area. At stage 2, settlements are uniform at the western end while steep gradients exist at the eastern end. This is another explanation of the major change in crack pattern between these stages. At stage 3 of the analysis, cracking reduces to a stable layout which is also seen at stage 4, again confined to the eastern end of the facade. This is in agreement with the base displacements which change little between stages 3 and 4.

Behaviour of the rear facade is characterised by sudden widespread hogging bending failure. Stages 1 and 2 show no cracking. Stage 3 shows the start of vertical soffit cracking at the west end between windows 3, 4 and 5. This agrees with slight hogging deformation seen in the transverse plot for **3NB3** (Figure 9.14) between −10m and −20m from the tunnel axis. At stage 4, major cracking is evident indicating overall hogging bending failure. Examination of the plot of rear facade base settlement for this and the previous stage (in Figure 9.15) does indicate a noticeable increase in hogging curvature, backing up the postulated mechanism. The isometric plot of building base displacement, Figure 9.16, is in agreement with the above except that hogging cracking might be expected at stage 3, rather than 4. However, there is a noticeable increase in hogging curvature between stages 3 and 4 on the base displacement plot and, as stated above, the crack plots do not show areas of the facade on the verge of cracking.

The cracking and base displacements seen in the front and rear facades suggest that, at stage 1 of the analysis the front facade is affected by tunnelling settlements. Stages 2 and 3 result in a stabilisation of the front facade crack pattern. At stage 4, the combined effects of the additional tunnelling settlements, as the tunnel face passes the east end of the rear facade, and weakening from earlier interactions through the side facades, leads to major cracking. Once again, an important conclusion to draw from these results is that the location of a building facade with respect to the tunnelling direction is important if it is connected to other facades which are affected earlier. It appears that such facades are subjected to interaction effects which may lead to weakening followed by tunnelling settlements which cause more damage.

9.5.4 Comparison with predictions of damage from the application of greenfield settlements

The final two analyses to be discussed here, (**3BB2** and **3BB3**), involve the application of greenfield settlements from the model to separate meshes of the building facades.

This exercise matches, in a limited sense, the traditional two-stage approach to tunnelling damage prediction which ignores the presence of the building in the calculation of settlements. While greenfield settlements are underpredicted by the model and there are irregularities in the pattern of settlement, as demonstrated in Section 9.3.2, these analyses demonstrate the very different damage predictions which are obtained by a two-stage numerical approach as compared to analyses which correctly include the building.

The displacements from the equivalent greenfield analyses (i.e. **3N2** and **3N3**) were applied to the nodes along the building bases in analyses **3BB2** and **3BB3** respectively. Selected cracking plots for these analyses are given in Figures 9.34 to 9.37. All plots have a threshold crack strain of 500 microstrain (.05%) i.e. double the threshold for the analyses of Sections 9.5.2 and 9.5.3. This point of presentation highlights the main observation from these results - the application of greenfield settlements leads to larger and more severe areas of cracking.

Figure 9.10 shows the transverse settlement profiles (i.e. the vertical components of the applied displacements) applied to the building base in analysis **3BB2**. The cracking pattern plots show the front and rear facades to react in similar ways although separated by one stage of excavation. Since the trough width parameter i of the applied profiles is $8-10$m, the facades lie almost entirely inside a sagging region and this behaviour clearly dominates the cracking response. Cracking is most severe adjacent to the doorway and appears to arise from shearing deformation particularly between the windows. This is at odds with the traditional approach predictions for the sagging region. The patterns are distinctly different to those seen in the combined analysis of the square building **3NB2**, see Figures 9.29 and 9.31. In particular, the large hogging effect seen in stage 2 of the combined analysis is not evident here. Since the front and rear facades react in the same way it can be concluded that the tunnelling settlements applied to the facades are dominating the response rather than any interaction effect between facades. This seems likely because of the high settlement gradients in the region of the building in the greenfield analysis results.

The analysis with the skew building arrangement, **3BB3** predicts little agreement in crack patterns between front and rear facades. This is to be expected since they are located at different distances from the tunnel axis and would therefore experience significantly different settlement profiles, assuming a simple traditional approach trough. The greenfield settlements along the front facade base (plotted in Figure 9.15) show, for stages 2 - 4, four sagging curves joined together. The steepest gradients are at the east end for stage 2 and cracking is correspondingly widespread in this location at this stage. After stage 2, extensive heavy cracking is shown in the areas below the ground floor lintels. Most heavily cracked areas coincide with the individual sag curves of the greenfield profiles. The only similarity between these results and those from the combined analysis is the appearance of cracking above ground floor level at the east end which closes up at the next stage. Once again, this may be explained by the relatively steep gradients imposed at this stage in the analysis.

Cracking in the rear facade (Figure 9.37) is also generally confined to a region below the ground floor lintels except at stage 4 where major cracking appears at the west end. It is unclear from where this originates although some interaction with the side facade appears the probable explanation. Stage 1 shows extensive horizontal cracking beneath windows 6 and 7 which must result from an interaction with the side facade since the greenfield plot in Figure 9.15 is virtually flat. The affected area shifts eastwards at stages 2 and 3 in accordance with the small sagging depressions in the profile.

9.5.5 Summary - building damage

From this discussion it is concluded that:

- Damage predictions from the model vary in their agreement with those of the traditional approaches. Front facades, i.e. those which the tunnel passes under first, appear to be damaged roughly in line with predictions. Rear facades sustain much higher levels of damage. These three-dimensional analyses therefore show that the location of facades which are connected is important in the prediction of building damage.
- The comparison between model results and the traditional approach is difficult since the model has already been shown to underpredict greenfield settlements in Section 9.3.2 and single results (strains) from traditional analyses must be compared to patterns of strains and cracking from the model.
- Cracking can appear during the passage of a tunnel which then closes up on completion of excavation. In practice, it is unlikely that cracks would disappear completely but there may be concern that this behaviour would both weaken the structure and lead to the assumption (from the results of an inspection) of lesser damage than has occurred during the tunnel construction.
- The application of greenfield displacements, predicted by the model, to the building alone leads to considerably greater damage than predicted from analyses where the building and ground are together in the model. In these analyses, facades show much less interaction with each other and more direct reaction to the pattern of base settlement.

Table 9.7: **Computer resources used in analyses**

Ref.	Real time (hms)	CPU time (s)	MAXBUF	MAXFRN	Platform
3EU	01:09:15	4147	2861992	528	3
3E1	01:06:12	3938	3214522	582	3
3NU	35:36:10	127885	2861992	528	3
3N1	41:01:37	147588	3214522	528	3
3N2	100:38:03	361931	7483519	1020	4
3NB2	184:23:08	661520	10036893	1101	4
3BB2	06:11:10	22200	788070	341	3
3N3	107:38:23	387178	8497342	1035	4
3NB3	215:31:15	772585	11401020	1296	4
3BB3	44:55:47	1022080	1201798	370	3

9.6 Other performance issues

This section gives further details of computer resources used for the example analyses. Problems with computer resources are confined to three-dimensional analyses and therefore data are not provided for the two-dimensional analyses. Some difficulties met in execution are highlighted here which lead to recommendations for future work, given in the final chapter of this thesis.

For each analysis, Table 9.7 gives the following information:

- real time for execution,
- CPU time for execution,
- MAXBUF, the maximum size of the array required to store stiffness matrix coefficients, and MAXFRN, the maximum size of the frontal matrix $\mathbf{M}_f$ during the analysis (see Section 3.2),
- the hardware platform used (see Table 8.1, Chapter 8).

It is clear from Table 9.7 that three-dimensional analyses require considerable run times even using very fast processors and high RAM configurations. The three-dimensional analyses, particularly **3NB3** have also been subjected to considerable pre-processing work to reduce the complexity of the mesh in order to achieve these run times. There is, therefore, little scope for decreasing resources in three-dimensional analyses by simplifying meshes.

A significant problem, met in using the three-dimensional model, was the behaviour of the lining elements when used with the non-linear material model (material N). Specification of realistic values of bending stiffness for the lining elements in analyses with large values of volume loss (above 1.5%) led to instabilities in the analysis. Large out-of-balance forces were predicted at nodes on ground elements attached to lining elements. Although the problem was remedied by adopting higher bending stiffnesses, the cause was not determined and its presence means that it is difficult to use the model to draw conclusions concerning liner stress resultants (although this is not in the remit of the research project). Possible explanations could be:

- a complex interaction between the unconventional lining element formulation and the non-linear material model adopted in attached ground elements.
- reduced flexural stiffness of the lining leading to large rotations of lining elements and hence reduced stiffness of the non-linear ground model due to large strains. Out-of-balance forces would be generated at nodes which would be amplified at the next load step and hence lead to instability.

The second of these speculations is harder to believe since increasing the number of steps, to reduce intermediate out-of-balance forces, appeared not to remove the problem. Scope for doing this in the three-dimensional analyses was limited, due to the resource problems highlighted above so the problem may disappear with the use of many load steps. The results of the two-dimensional analyses, where two different elements were used further confuse the issue since different responses were found with the elastic material model for the ground. The first suggestion would be resolved only by further mathematical analysis of the overlapping formulation with suitable parametric studies.

9.7 Summary

The purpose of this chapter is to demonstrate the numerical model. Conclusions have been drawn during the chapter on its performance with respect to the traditional methods of settlement and damage prediction.

1. The model predicts greenfield settlement troughs which are wider and shallower than the traditional method. Some difficulties are evident in the simulation of volume loss in that it appears to lead to localised deviations from otherwise smooth settlement contour patterns. It is clear that the coarse meshes required to keep computer resources to a reasonable level have a detrimental effect both to the accuracy of results and of the performance of the lining elements and hence the simulation of volume loss.
2. Conclusions as to the effects of a building on settlements and damage from the model should take into account this poor performance of the model in predicting greenfield settlement profiles.
3. The novel overlapping beam elements used in two-dimensional analyses for tunnel linings behave satisfactorily in the numerical model.

4. Results of analyses including a building agree with previous research in that settlement profiles are seen to flatten out under the building. The results also indicate that inclusion of the weight of the building increases maximum settlements.

5. In the assessment of the effect of a building on the settlement profile, the flattening of the trough is significantly affected by the alignment of the building facades to the tunnel axis. The degree to which the building spans the sagging portion of a greenfield trough and continues across its points of inflection also affects the stiffening effect of the building. In the analyses carried out here, the square building appears to act like a stiff beam and thus matches some of the previous two-dimensional research. However, this assumption does not follow for the skew building. The prediction of the effect of a non-square building appears to require three-dimensional analysis.

6. The results show that the direction of tunnelling is critical; the rear facades (i.e. those which the tunnel passes under last) of the buildings analysed show much greater damage. A possible mechanism is interaction between facades leading to weakening of "later" facades from interaction with facades directly experiencing tunnelling settlements. The "later" facades are then subject to tunnelling settlements as the tunnel face passes beneath. These settlements then have a greater effect on the now-damaged facade. This is a three-dimensional phenomenon which requires a three-dimensional model and cannot be modelled in two-dimensions alone.

7. The computer resources required for the three-dimensional model make its use in the field impractical except for a particularly prestigious structure where such an analysis may be justified to demonstrate better the effect of a new tunnel.

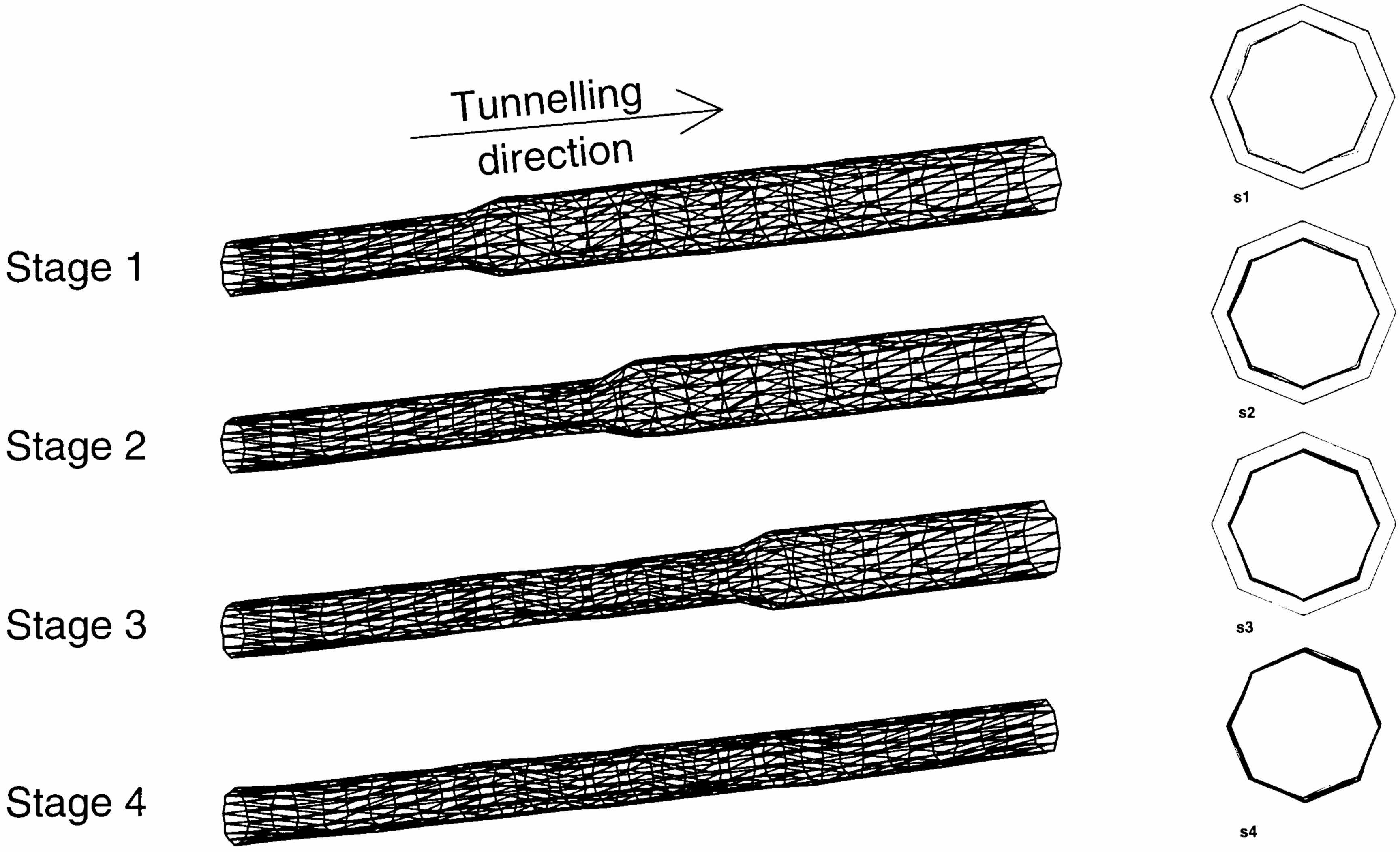

(a) Perspective views

(b) End views

Figure 9.3: **Deformed shape of lining only for analysis 3N3**

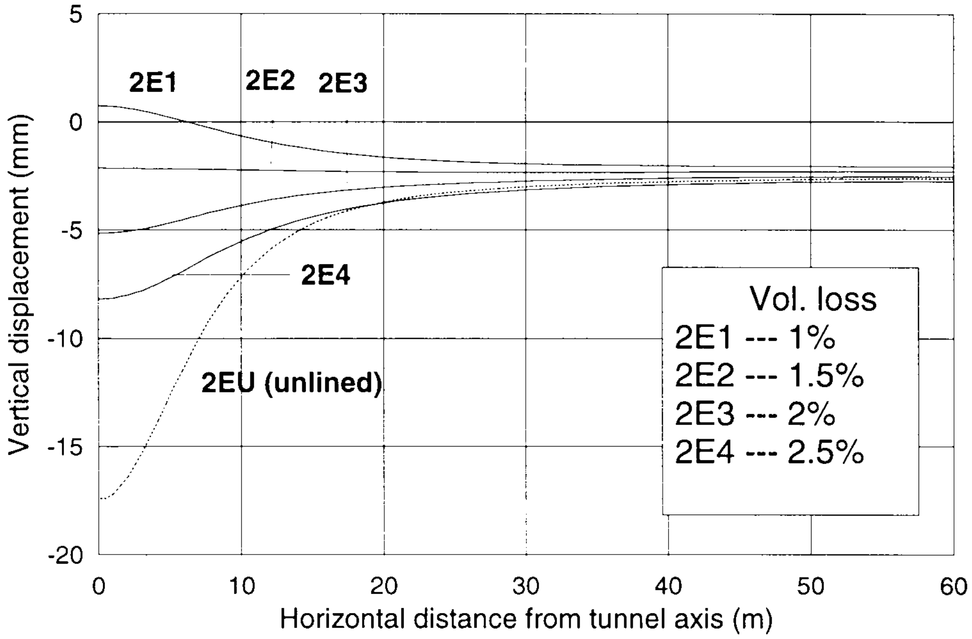

Figure 9.4: **Two-dimensional analyses, elastic ground, Hermitian beam linings**

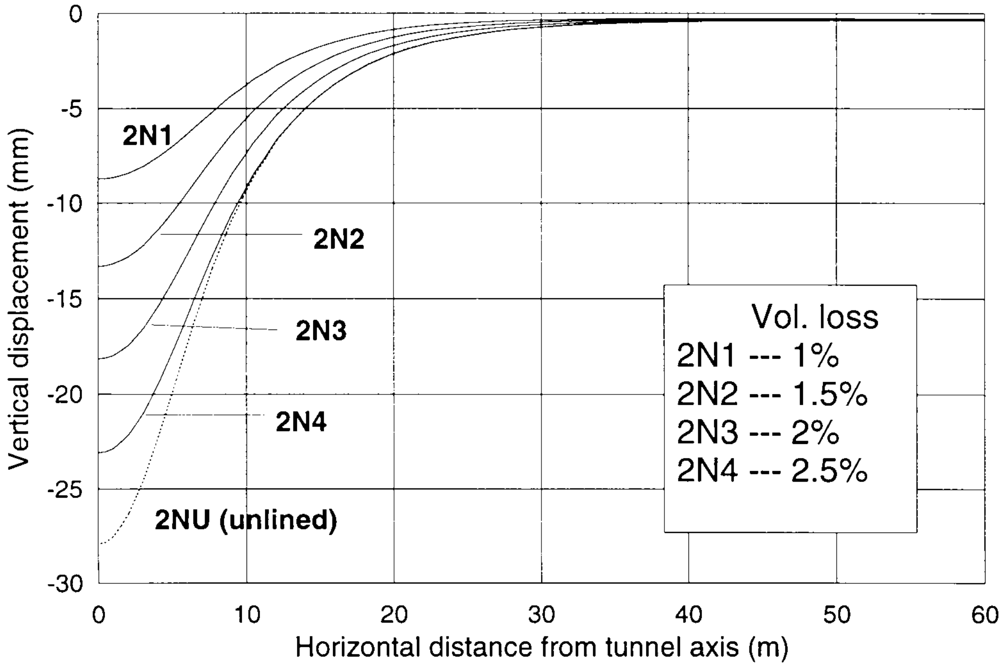

Figure 9.5: **Two-dimensional analyses, non-linear ground, Hermitian beam linings**

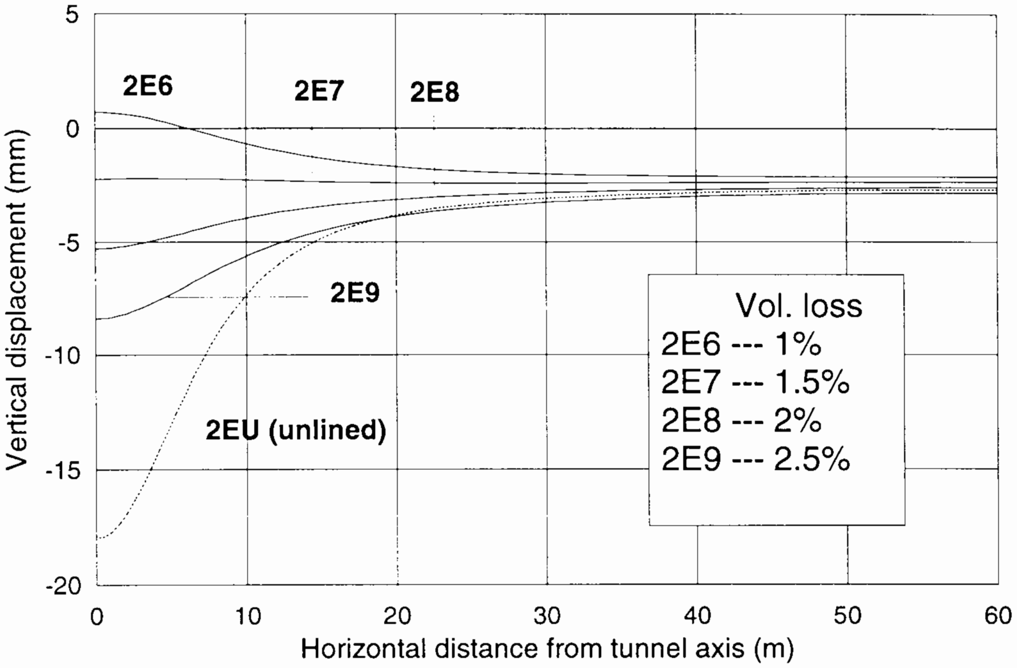

Figure 9.6: **Two-dimensional analyses, elastic ground, overlapping beam linings**

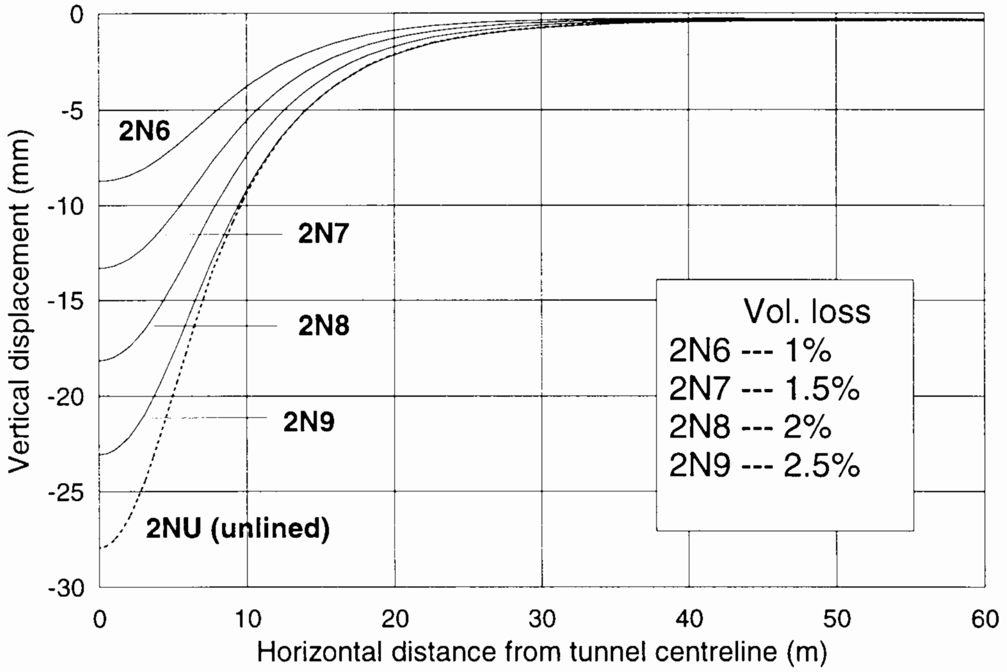

Figure 9.7: **Two-dimensional analyses, non-linear ground, overlapping beam linings**

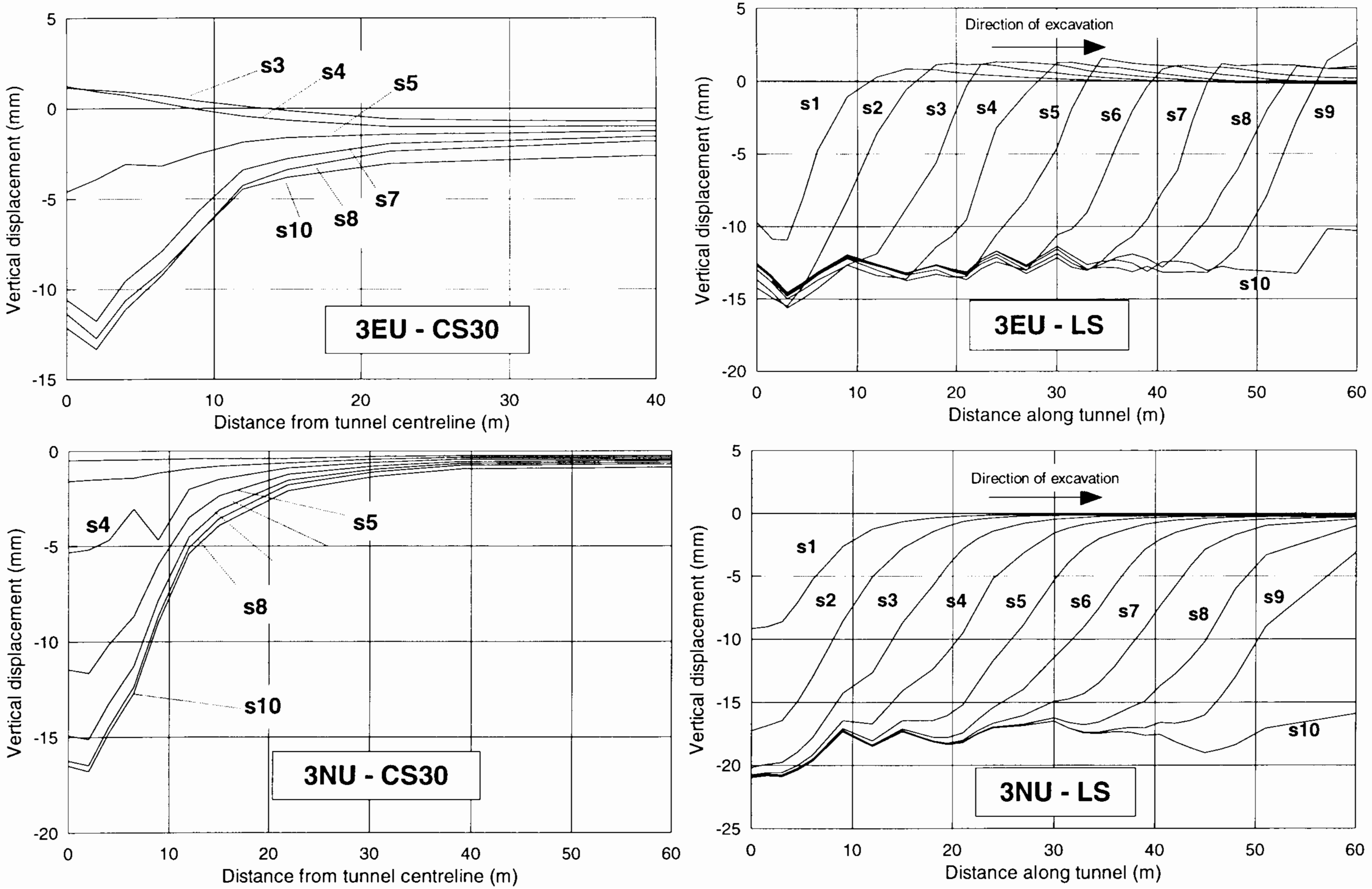

Figure 9.8: **Settlement plots for unlined three-dimensional analyses (low volume loss)**

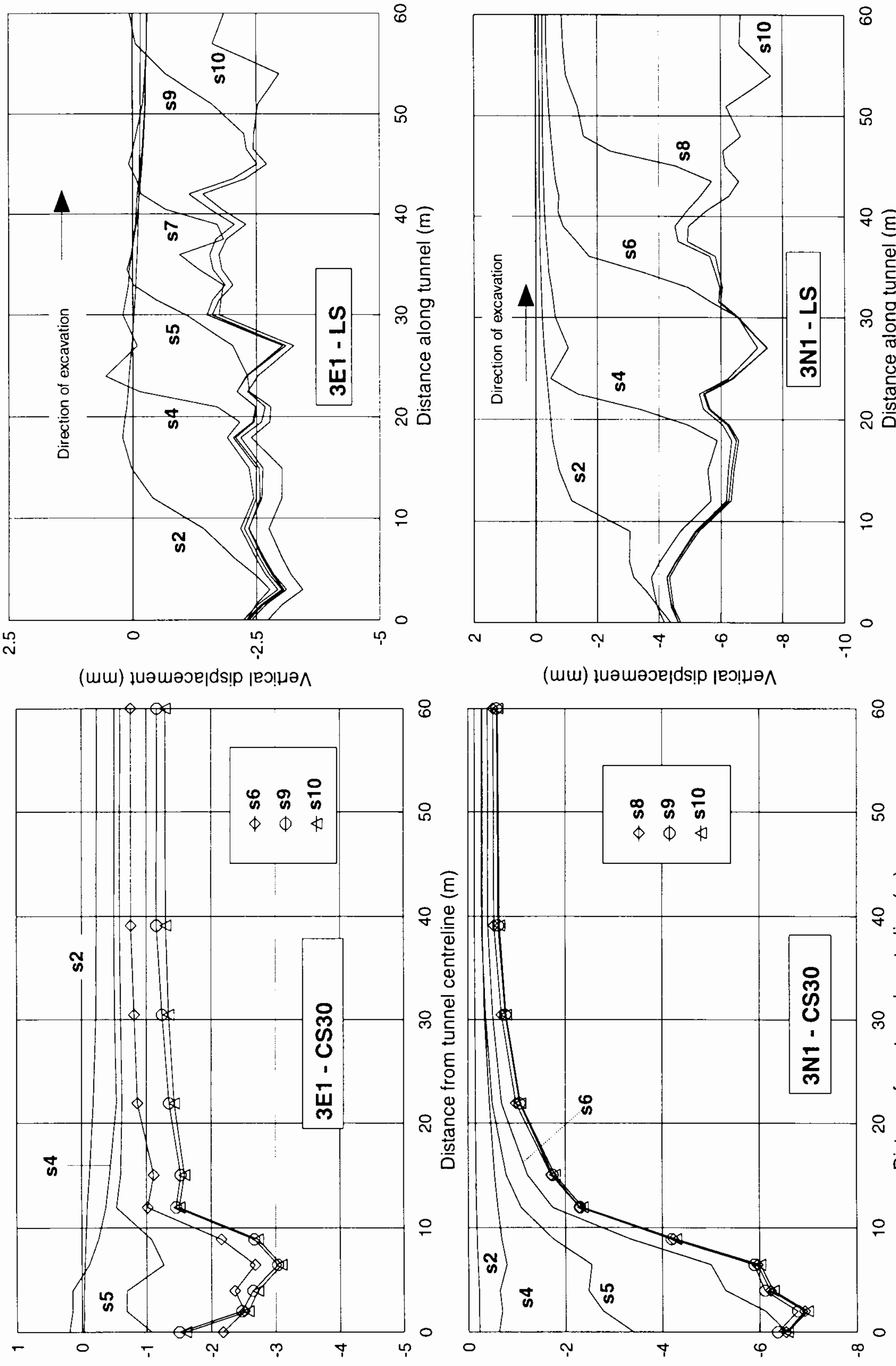

Figure 9.9: Settlement plots for lined three-dimensional analyses (low volume loss)

Figure 9.10: **Greenfield site, lined three-dimensional analysis 3N2**

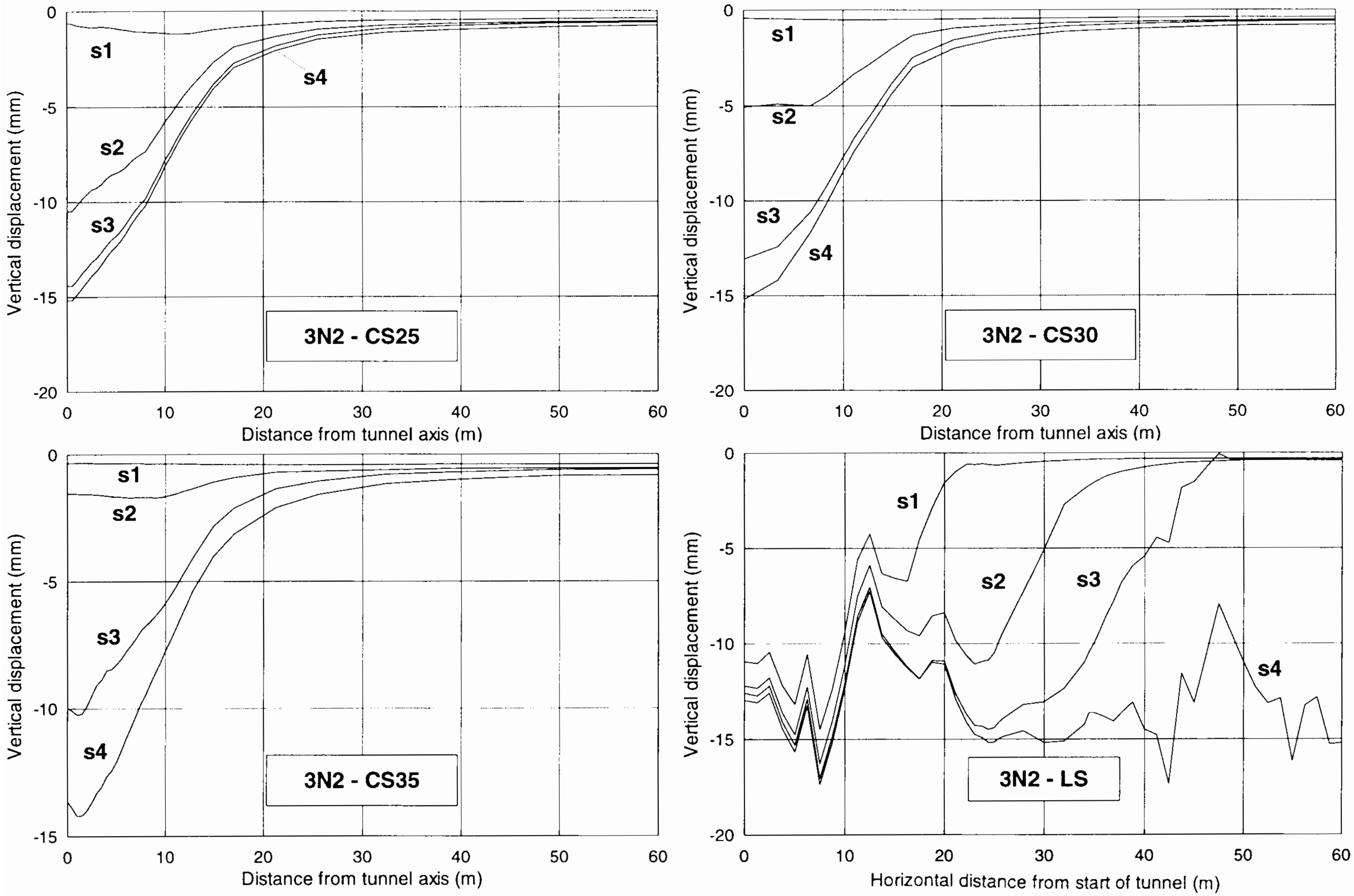

Figure 9.11: **Site with square building, lined three-dimensional analysis 3NB2**

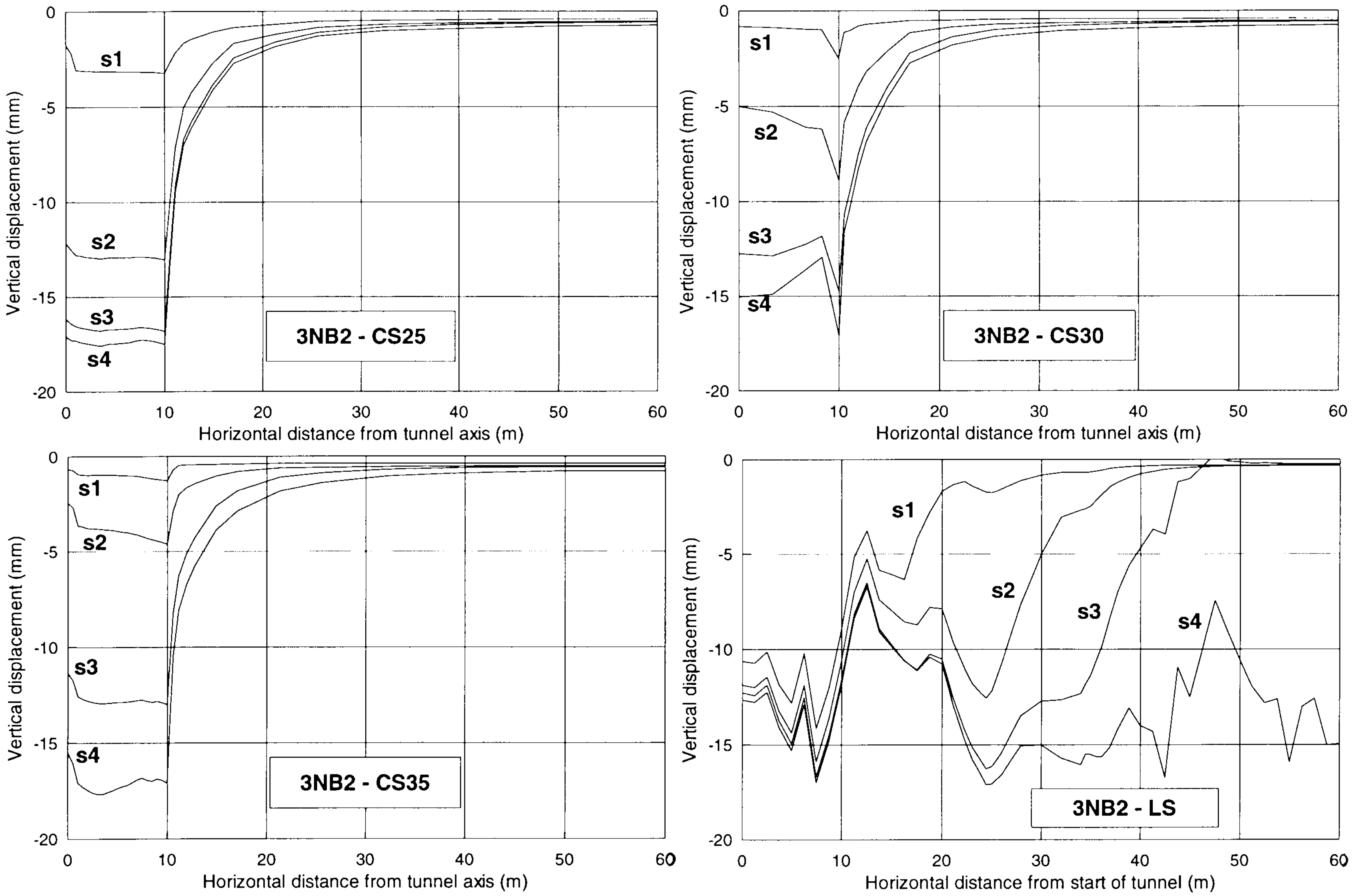

Figure 9.12: **Site with square building, base displacements, analysis 3NB2**

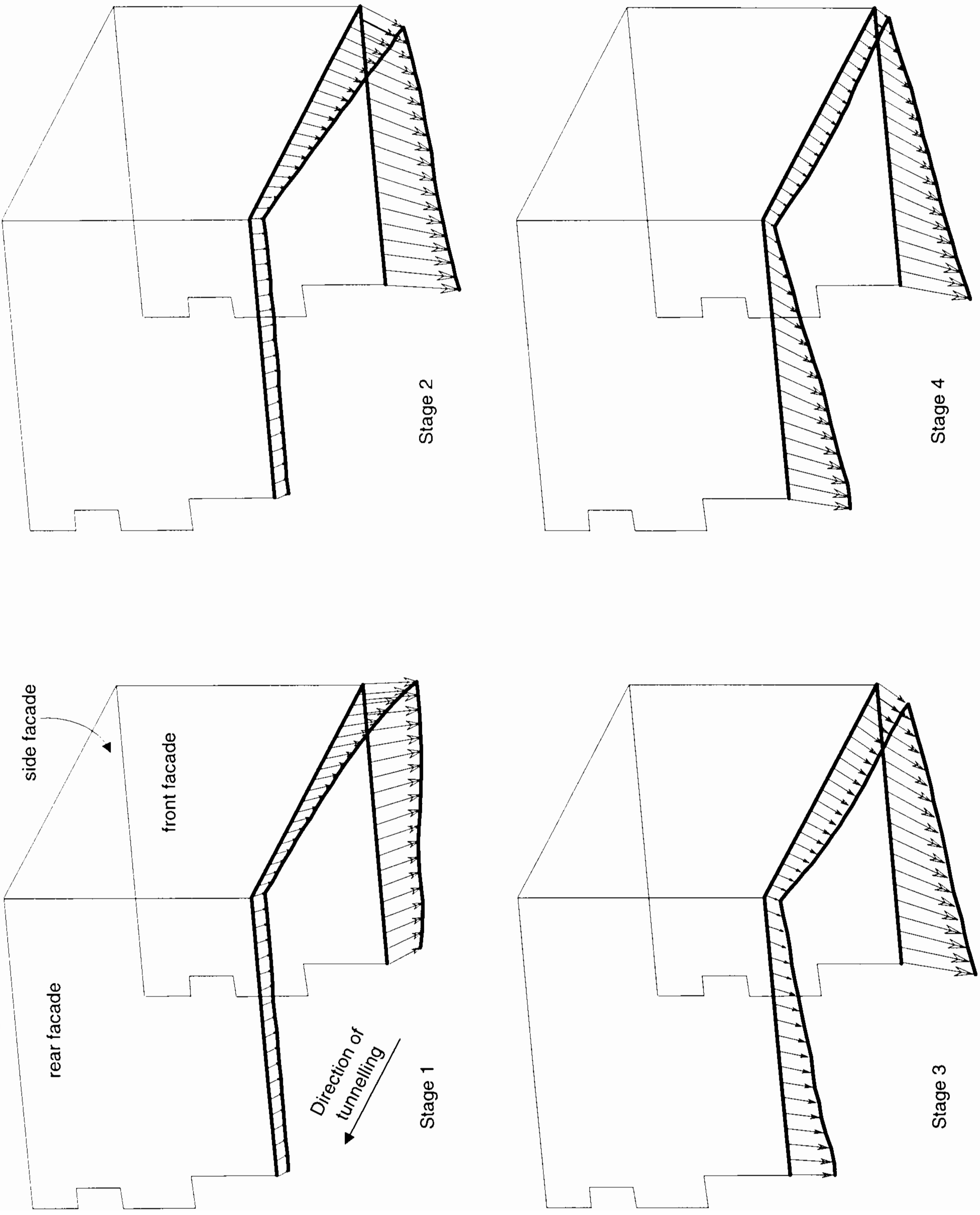

Figure 9.13: **Greenfield site, lined three-dimensional analysis 3N3**

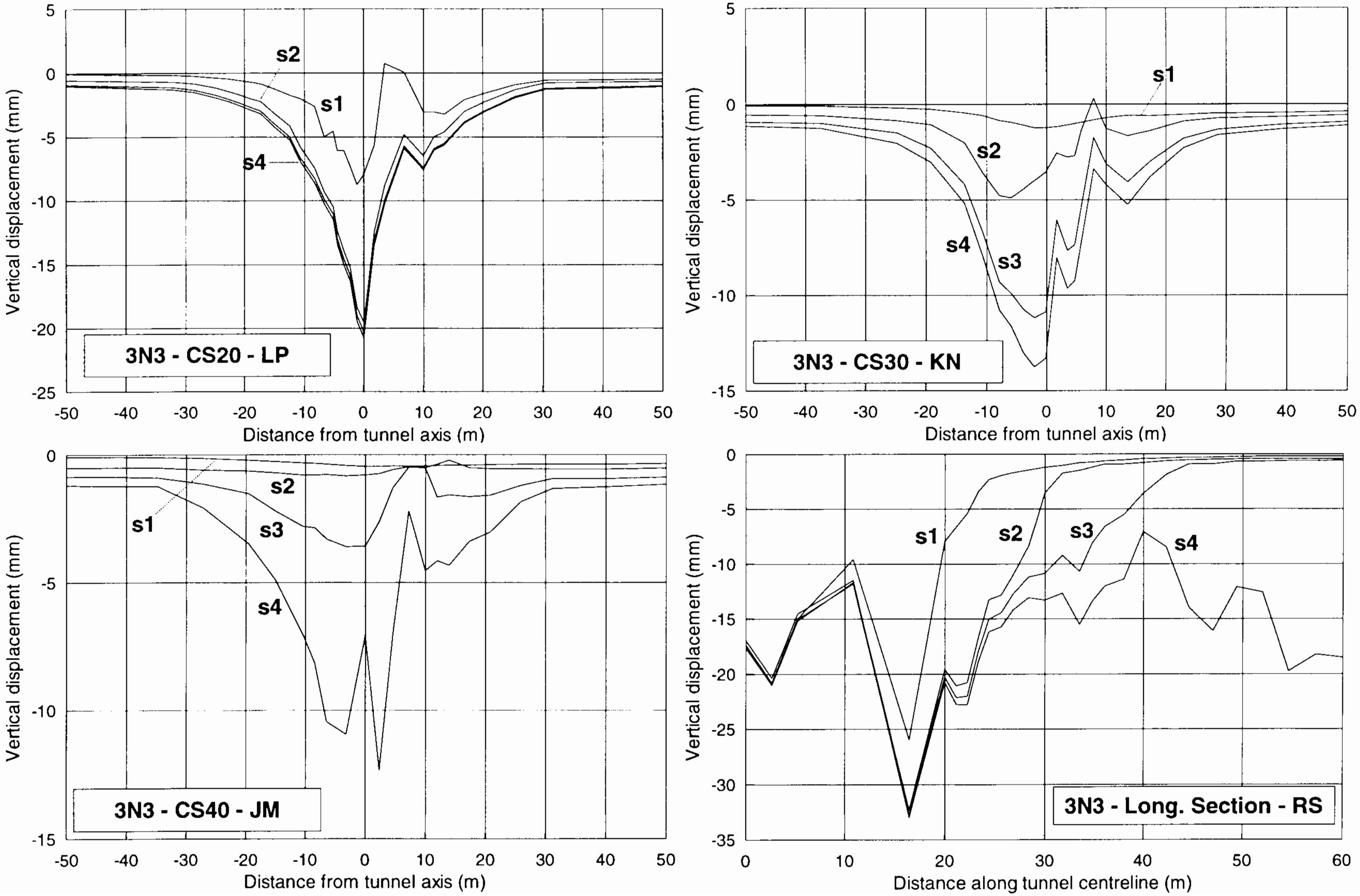

Figure 9.14: **Site with skewed building, lined three-dimensional analysis 3NB3**

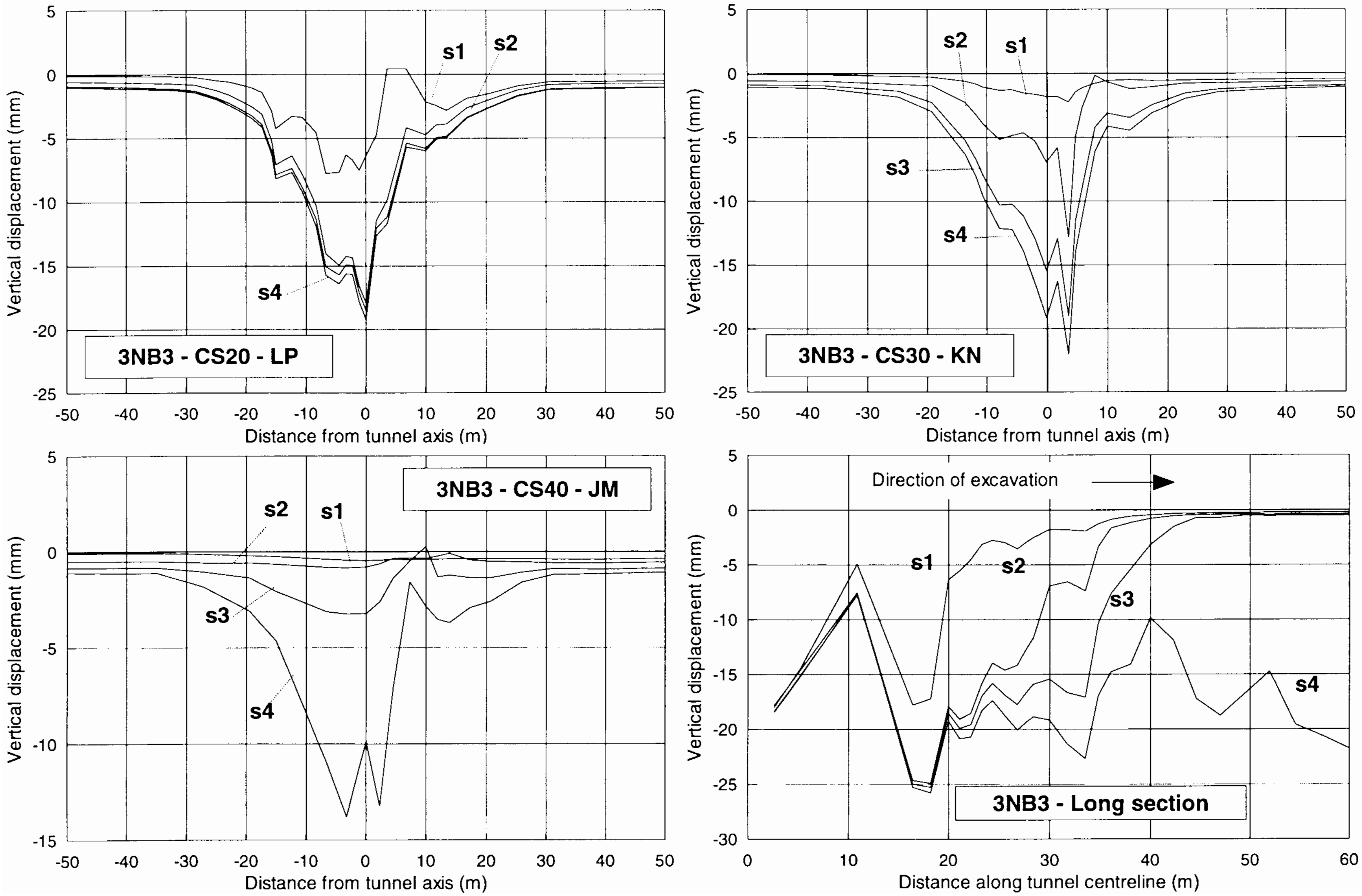

Figure 9.15: **Settlements along base of facades, analyses 3N33NB3**

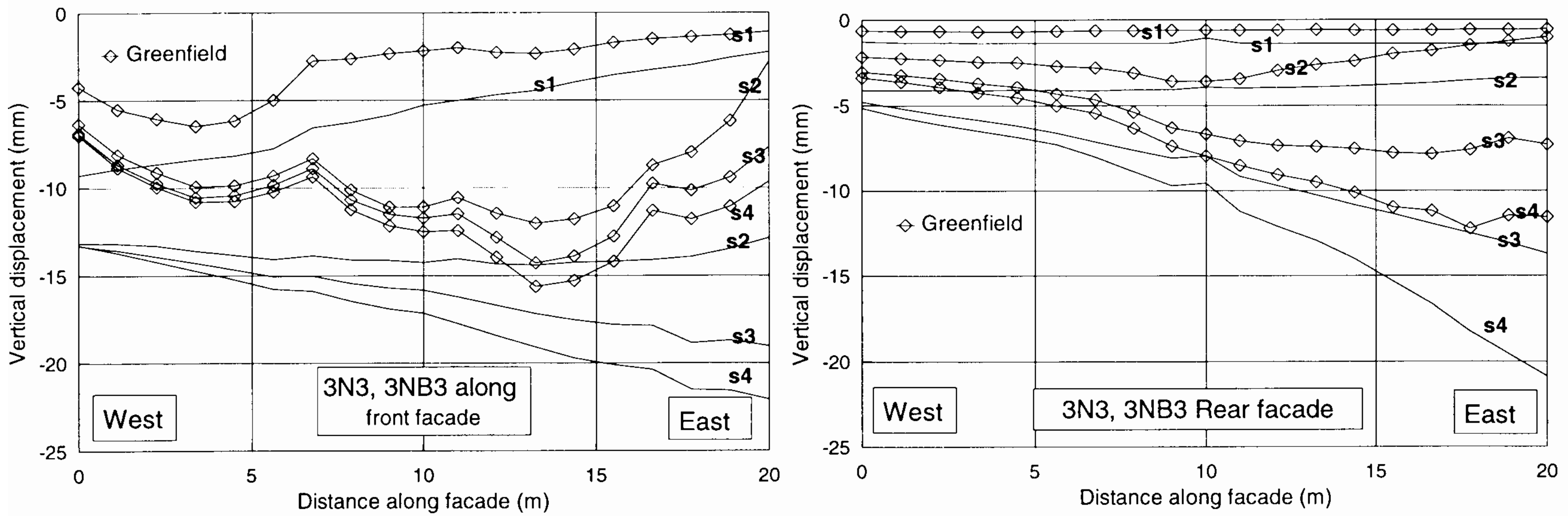

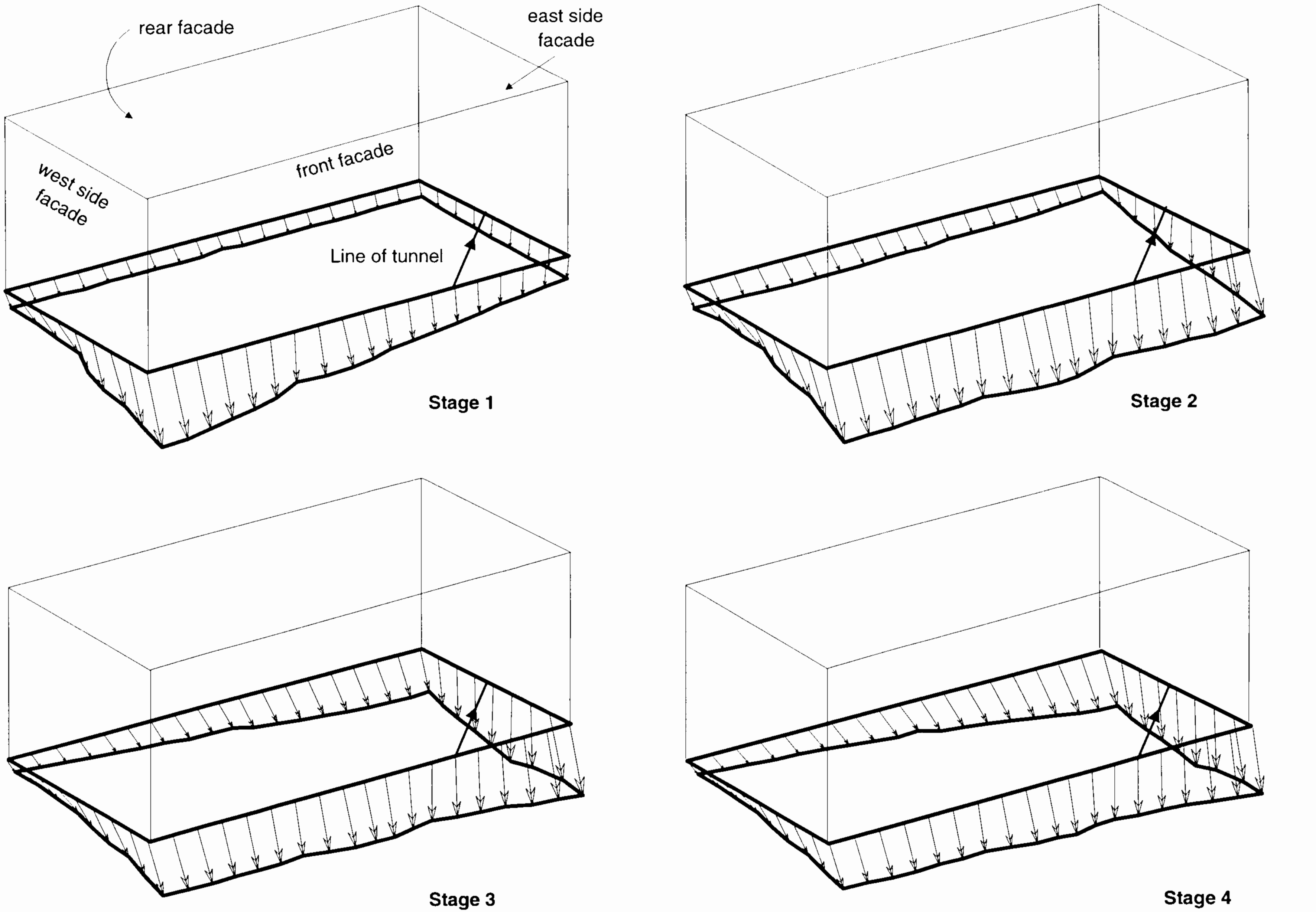

Figure 9.16: **Site with skewed building, base displacements, analysis 3NB3**

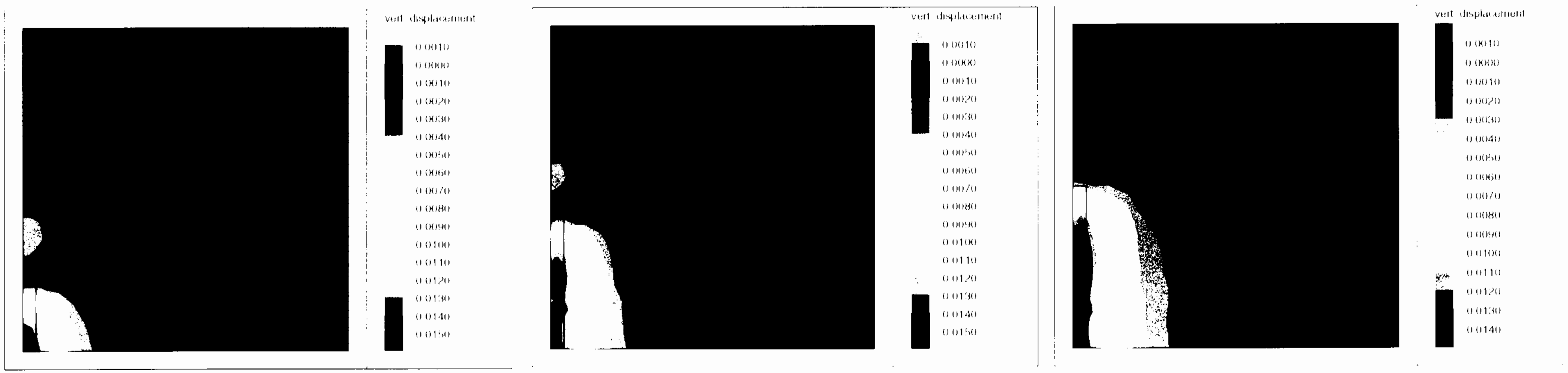

(a) s2

(b) s1

(c) s5

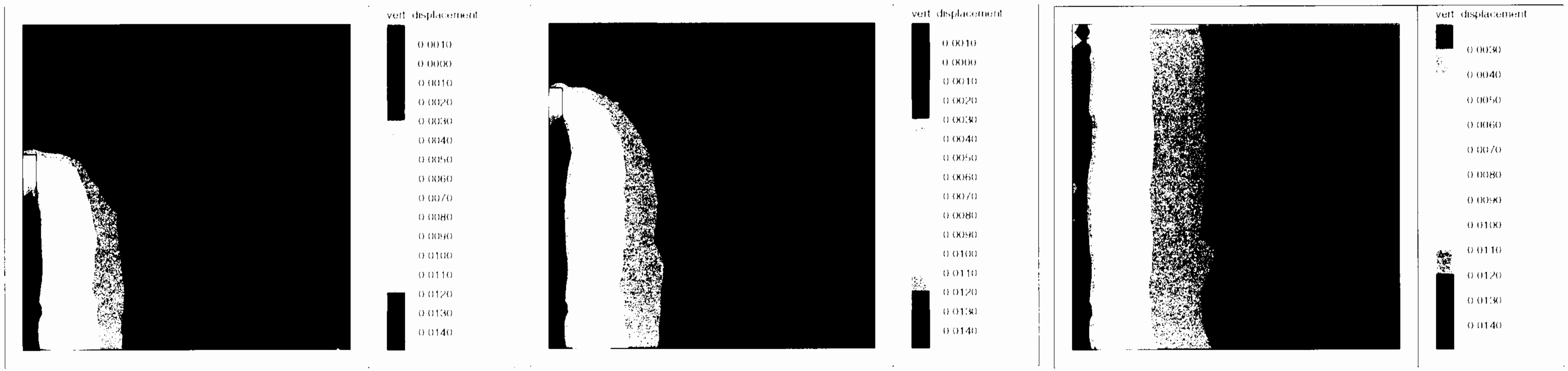

(d) s6

(e) s8

(f) s10

Figure 9.17: Contour plots for analysis **3EU** (displacements in metres)

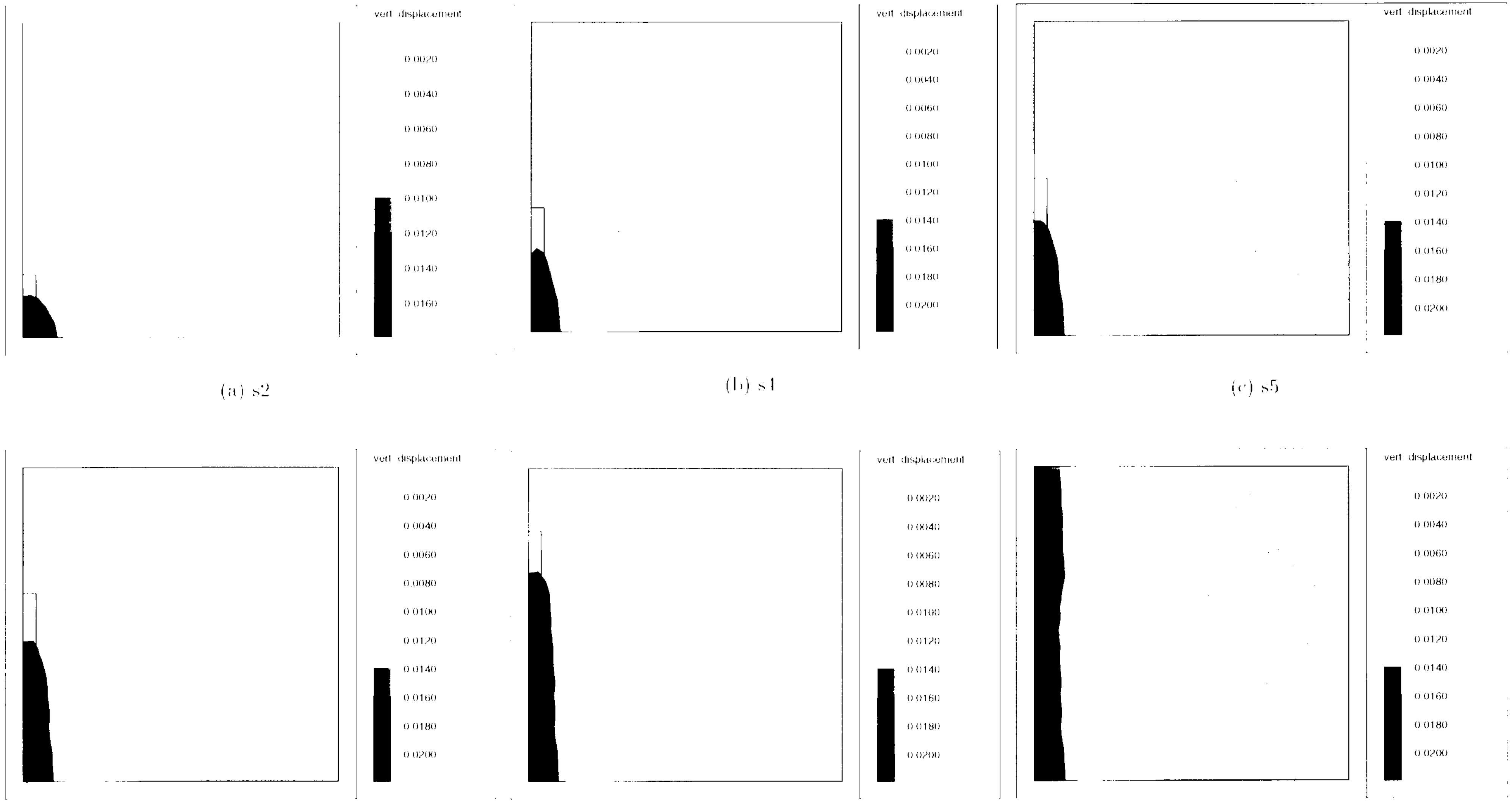

(a) s2

(b) s1

(c) s5

(d) s6

(e) s8

(f) s10

Figure 9.18: Contour plots for analysis 3NU (displacements in metres)

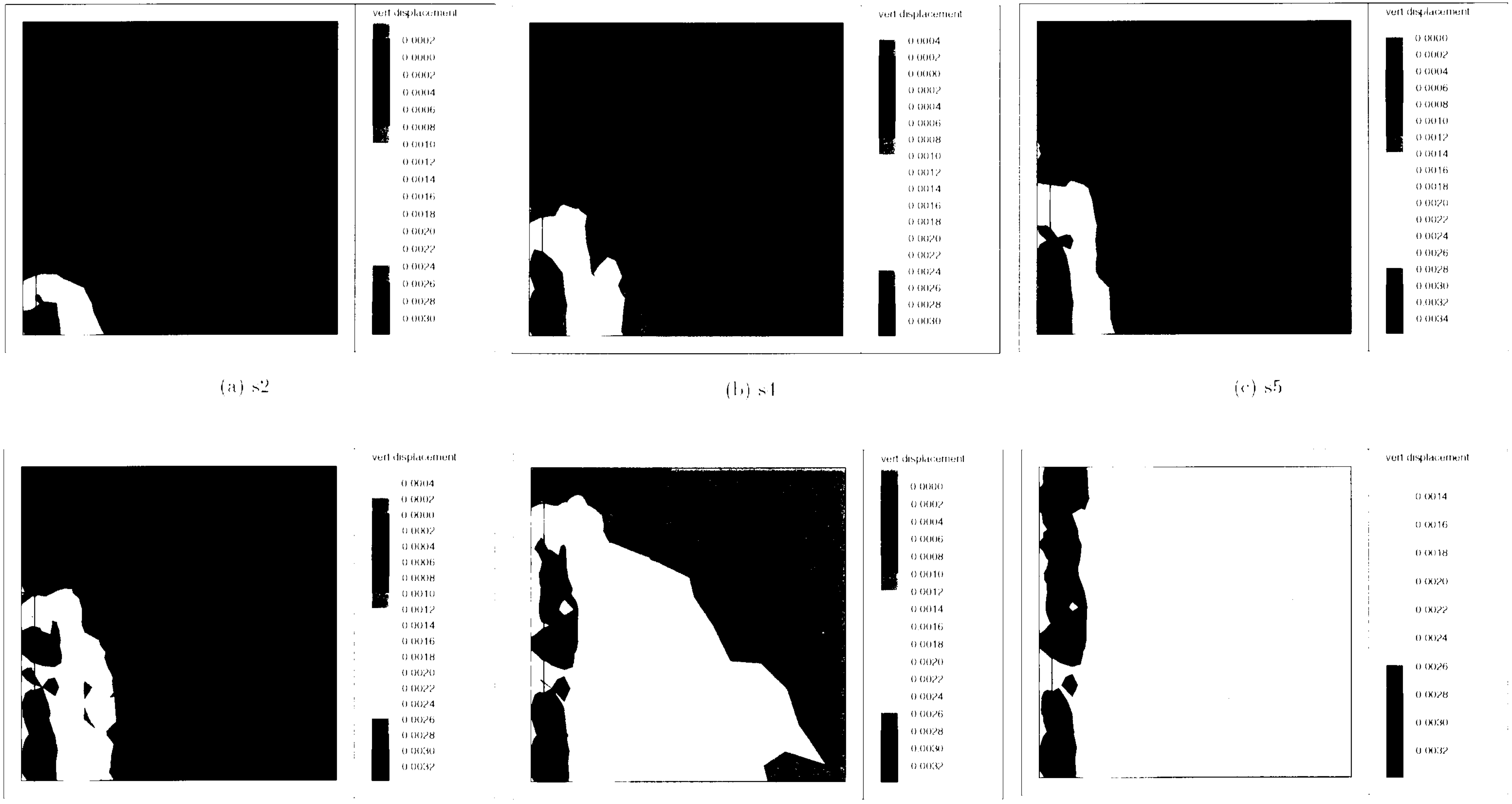

(a) s2

(b) s1

(c) s5

(d) s6

(e) s8

(f) s10

Figure 9.19: Contour plots for analysis **3E1** (displacements in metres)

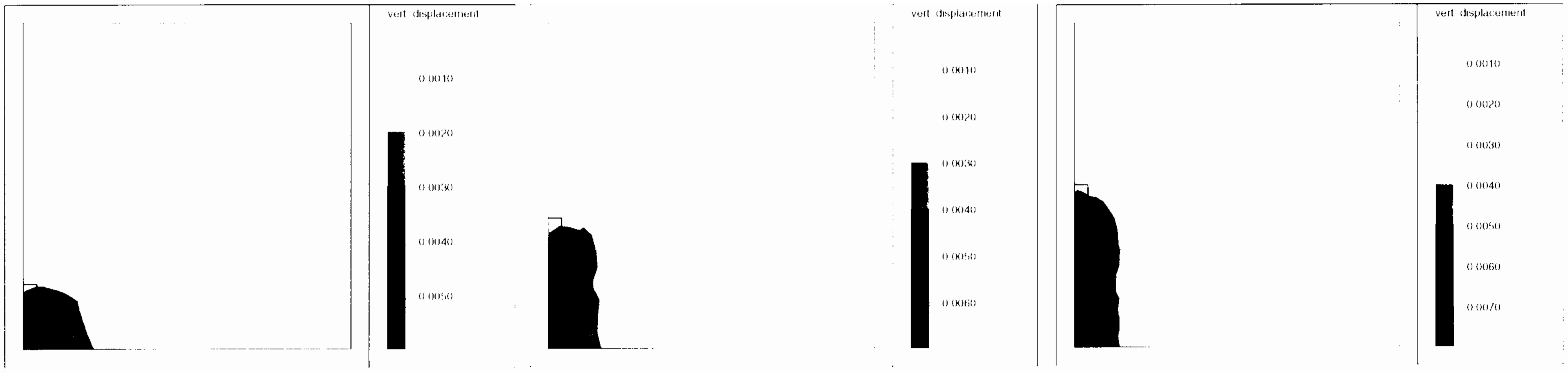

(a) s2 (b) s4 (c) s5

(d) s6 (e) s8 (f) s10

Figure 9.20: Contour plots for analysis 3N1 (displacements in metres)

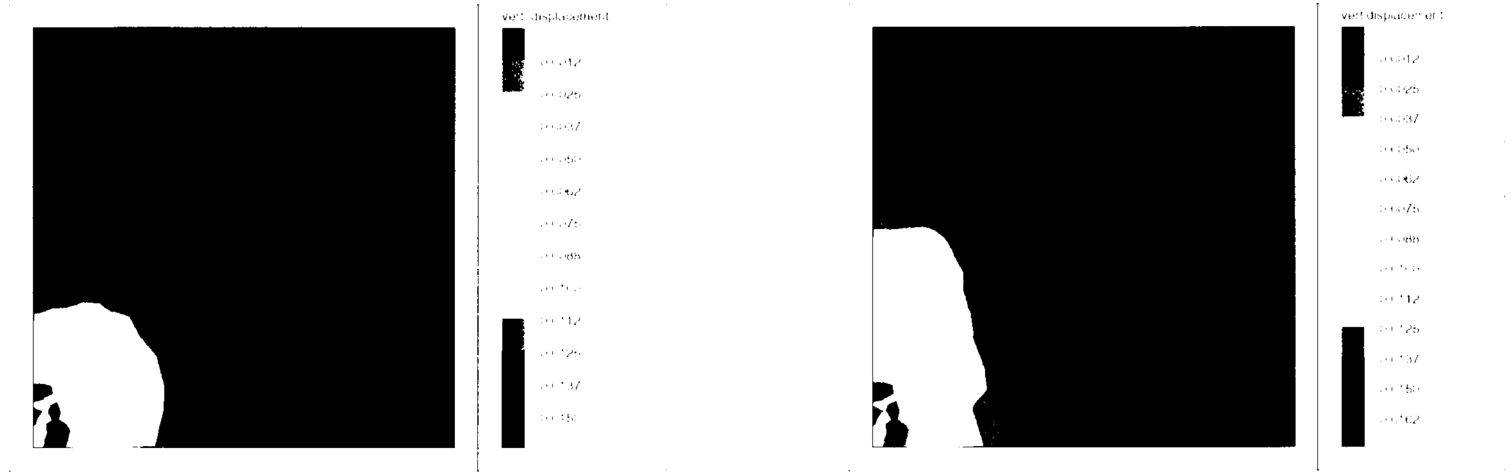

(a) s1 (b) s2

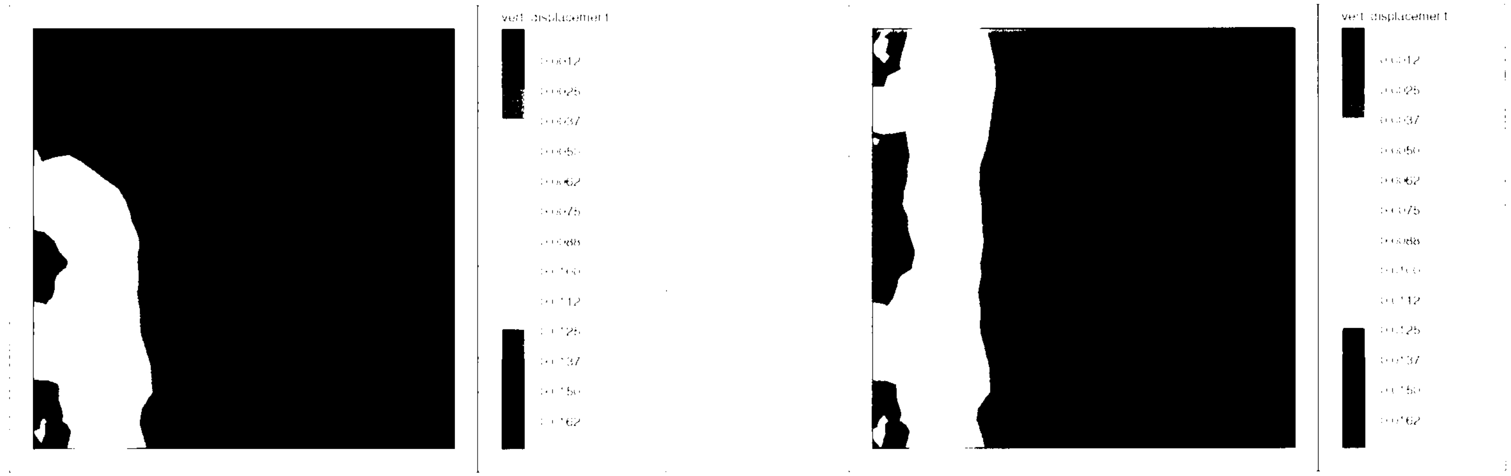

(c) s3 (d) s1

Figure 9.21: Contour plots for analysis 3N2 (displacements in metres)

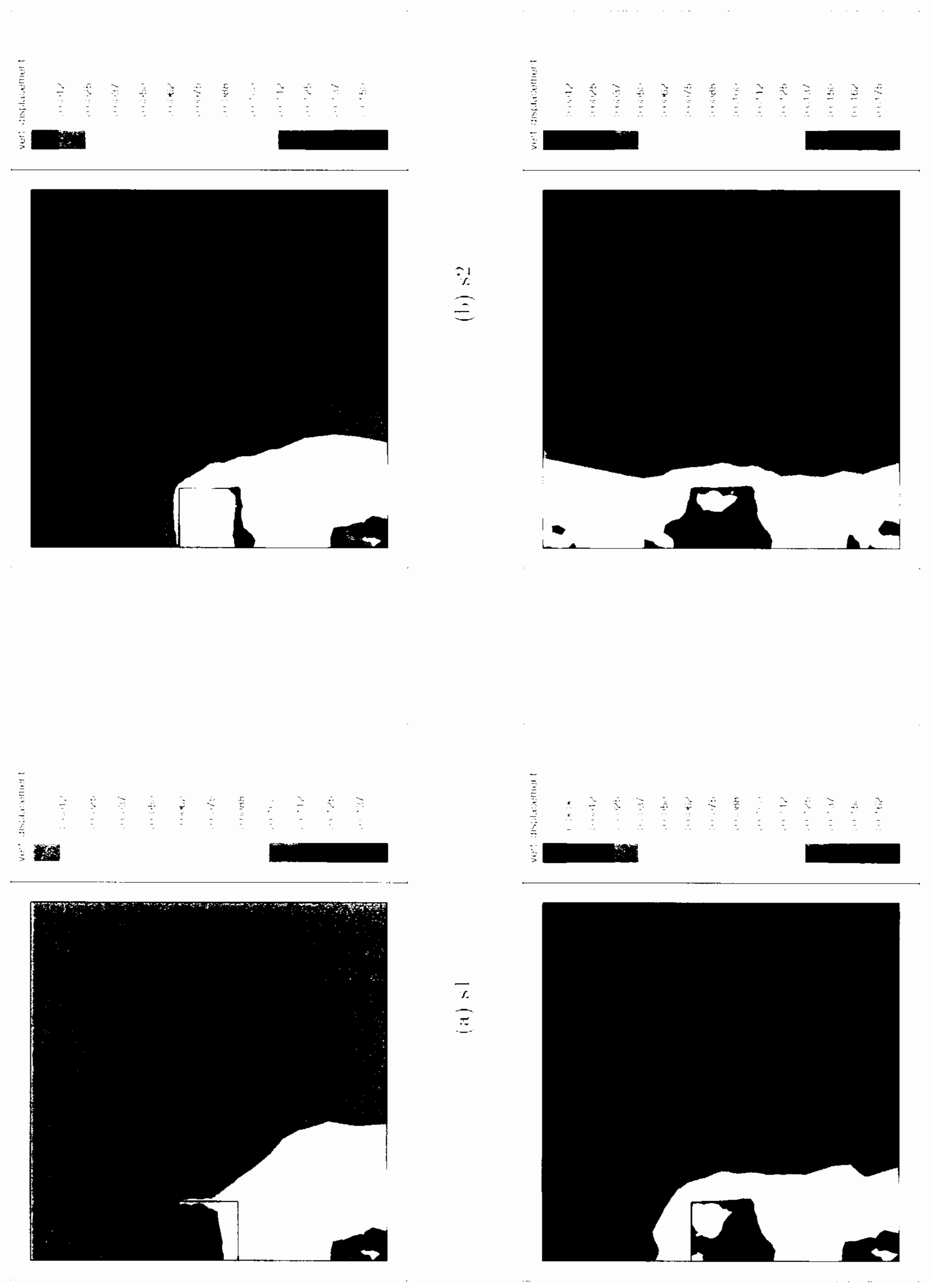

(a) s1

(b) s2

(c) s3

(d) s1

Figure 9.22: Contour plots for analysis 3NB2 (displacements in metres)

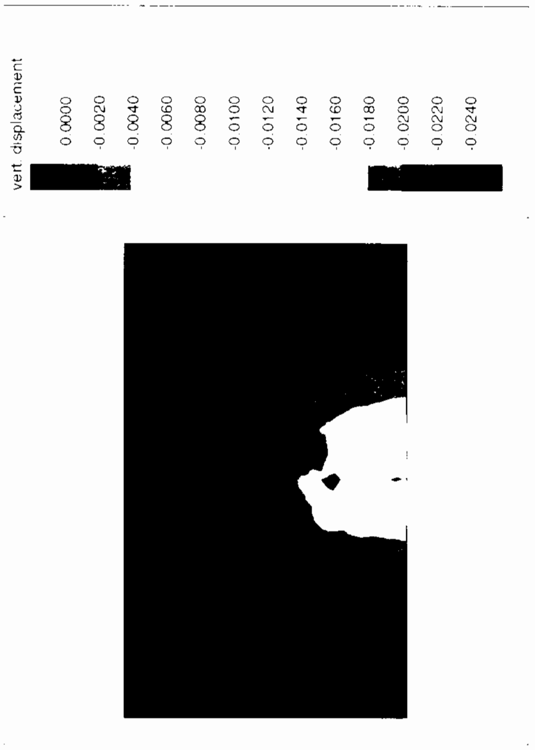

(a) s1

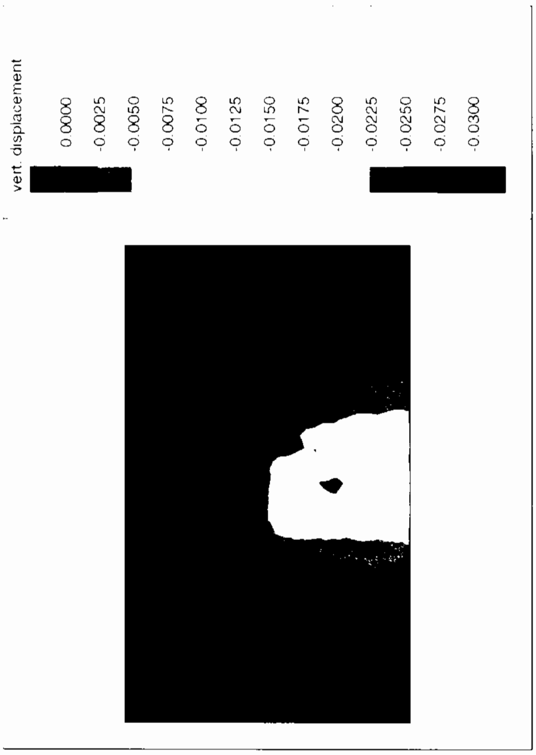

(b) s2

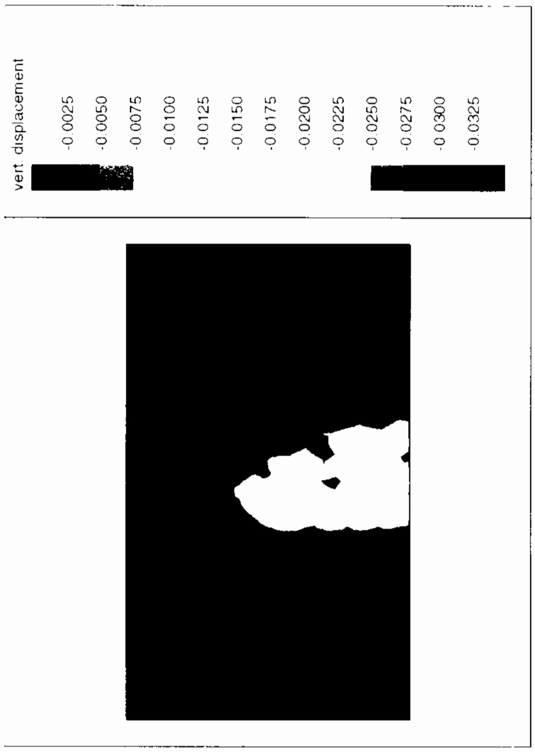

(c) s3

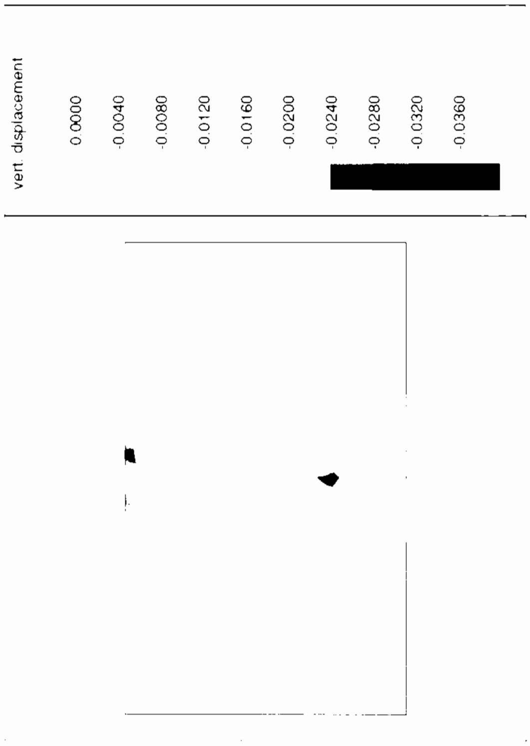

(d) s1

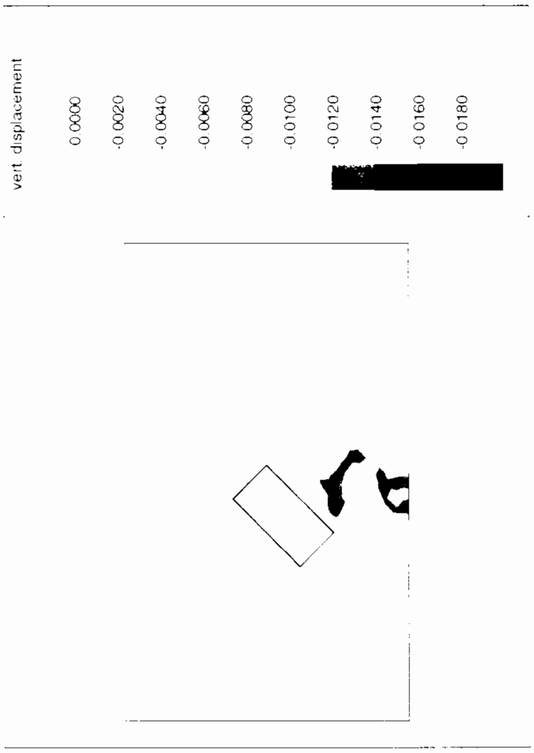

(a) s1

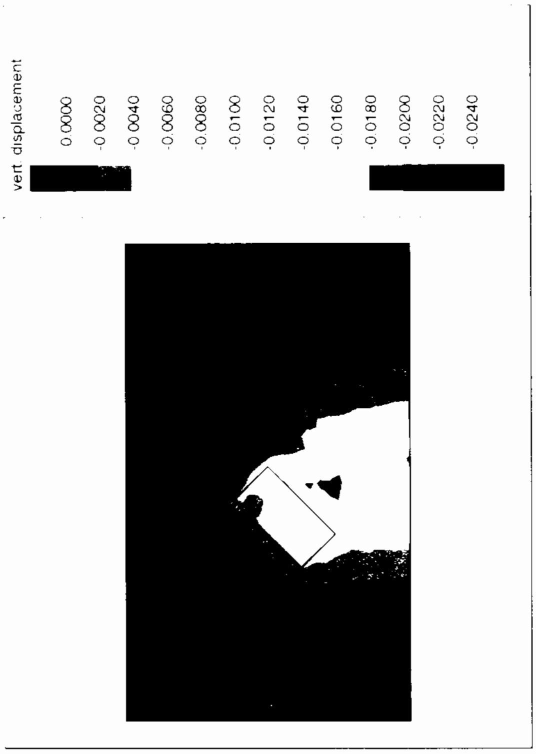

(b) s2

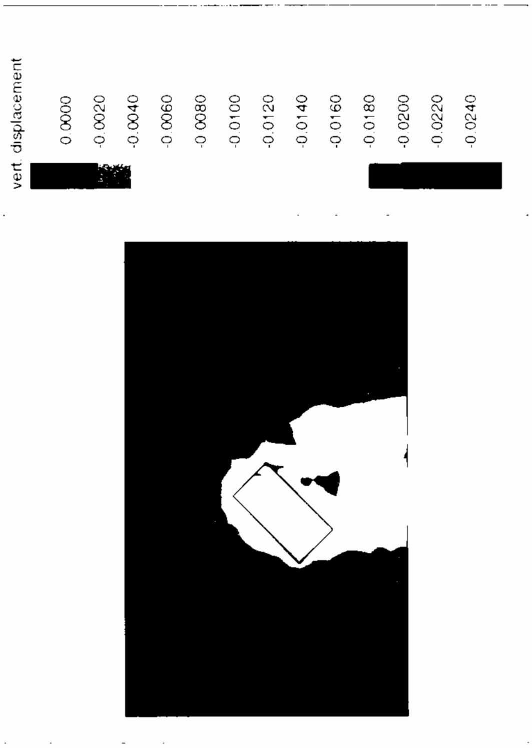

(c) s3

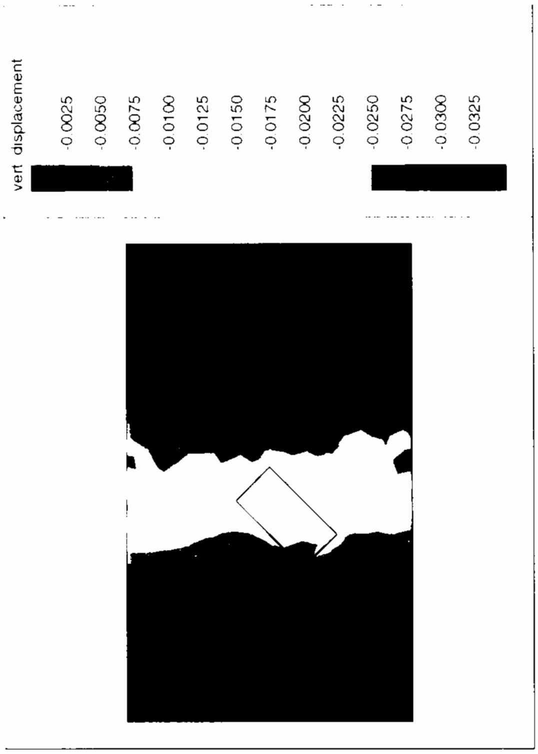

(d) s1

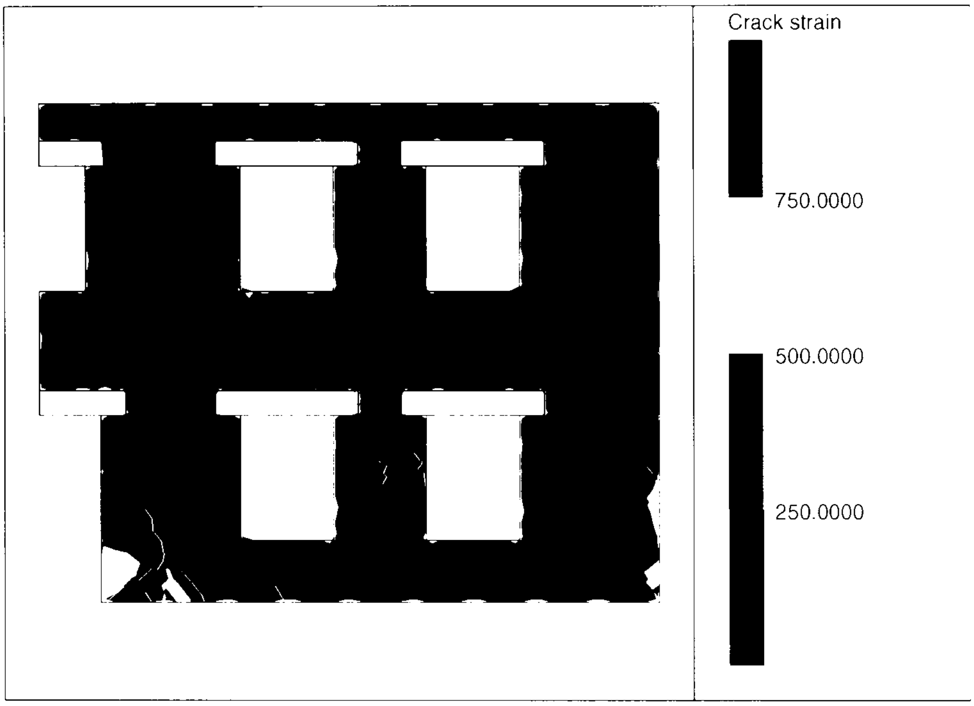

Figure 9.25: Crack strains at end of analysis 3NB2, front facade (microstrain)

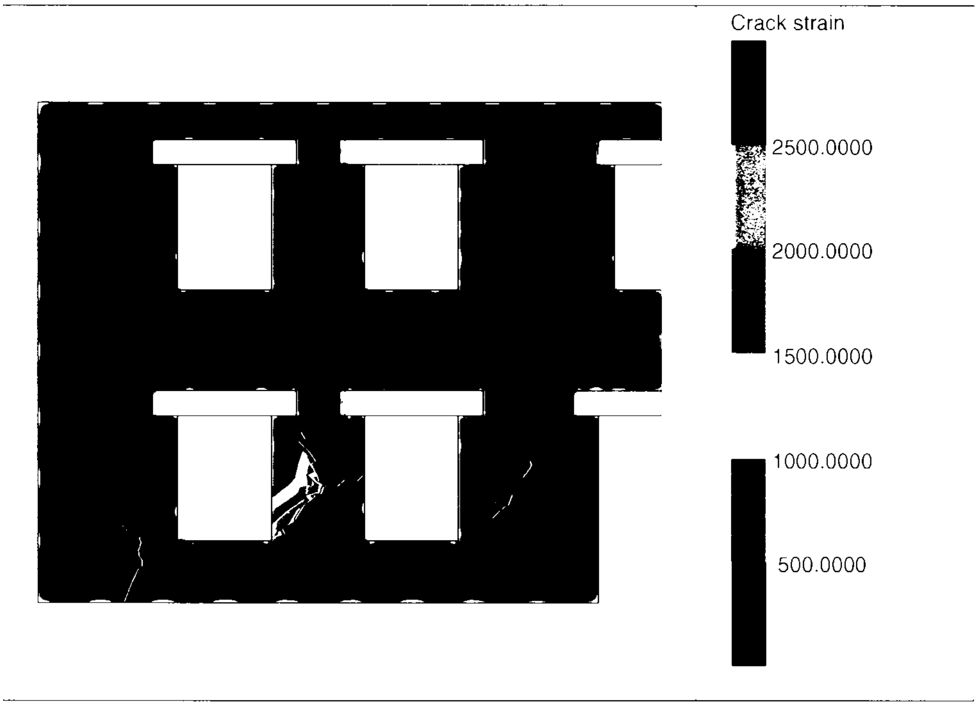

Figure 9.26: Crack strains at end of analysis 3NB2, rear facade (microstrain)

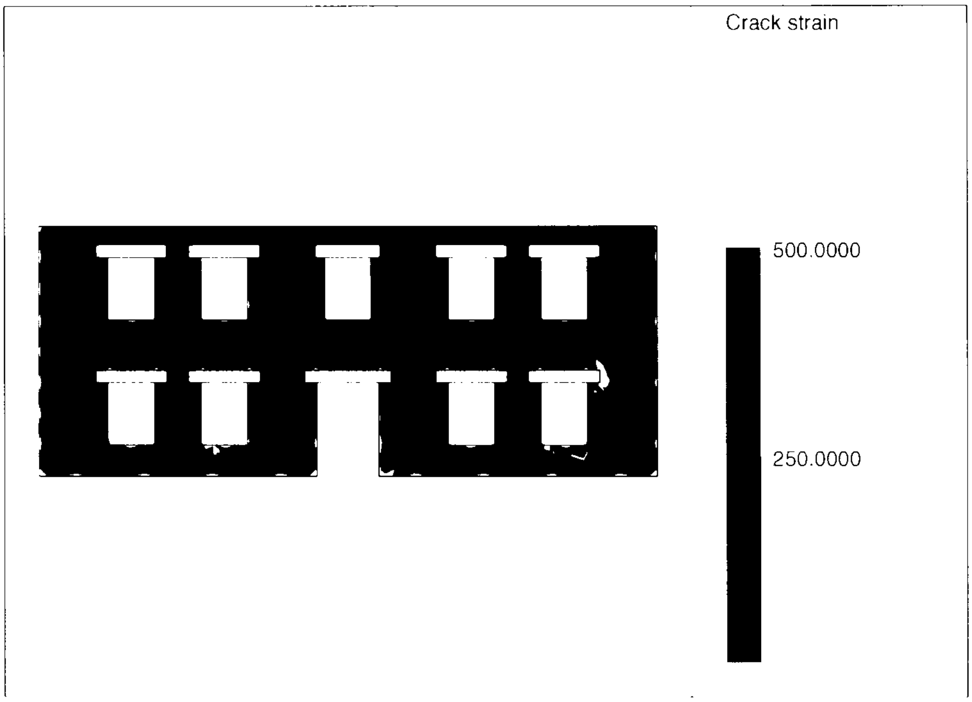

Figure 9.27: Crack strains at end of analysis 3NB3, front facade (microstrain)

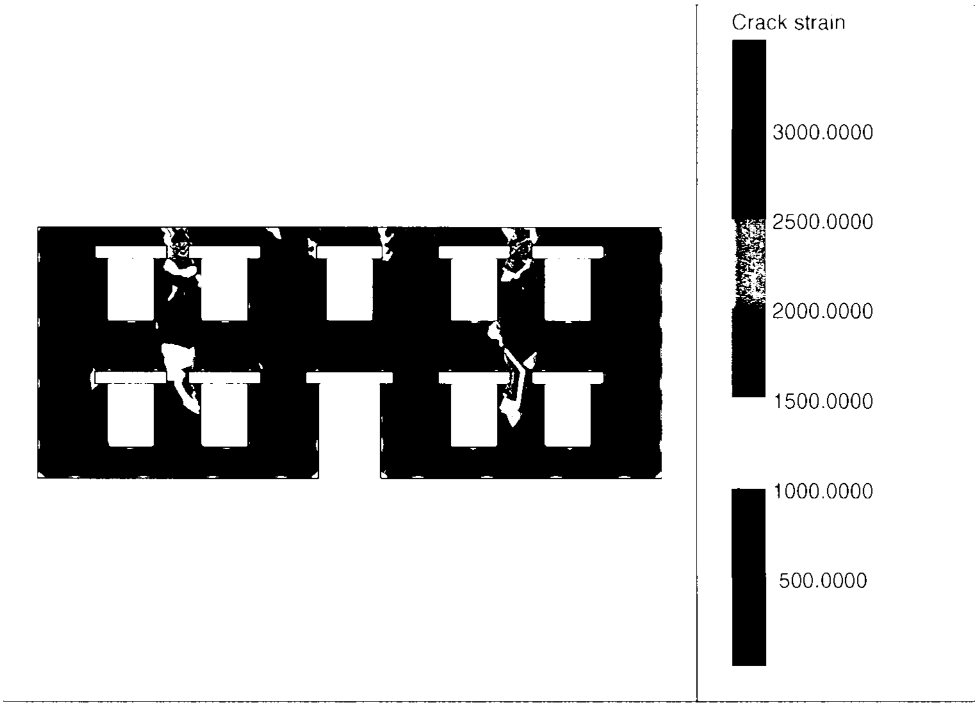

Figure 9.28: Crack strains at end of analysis 3NB3, rear facade (microstrain)

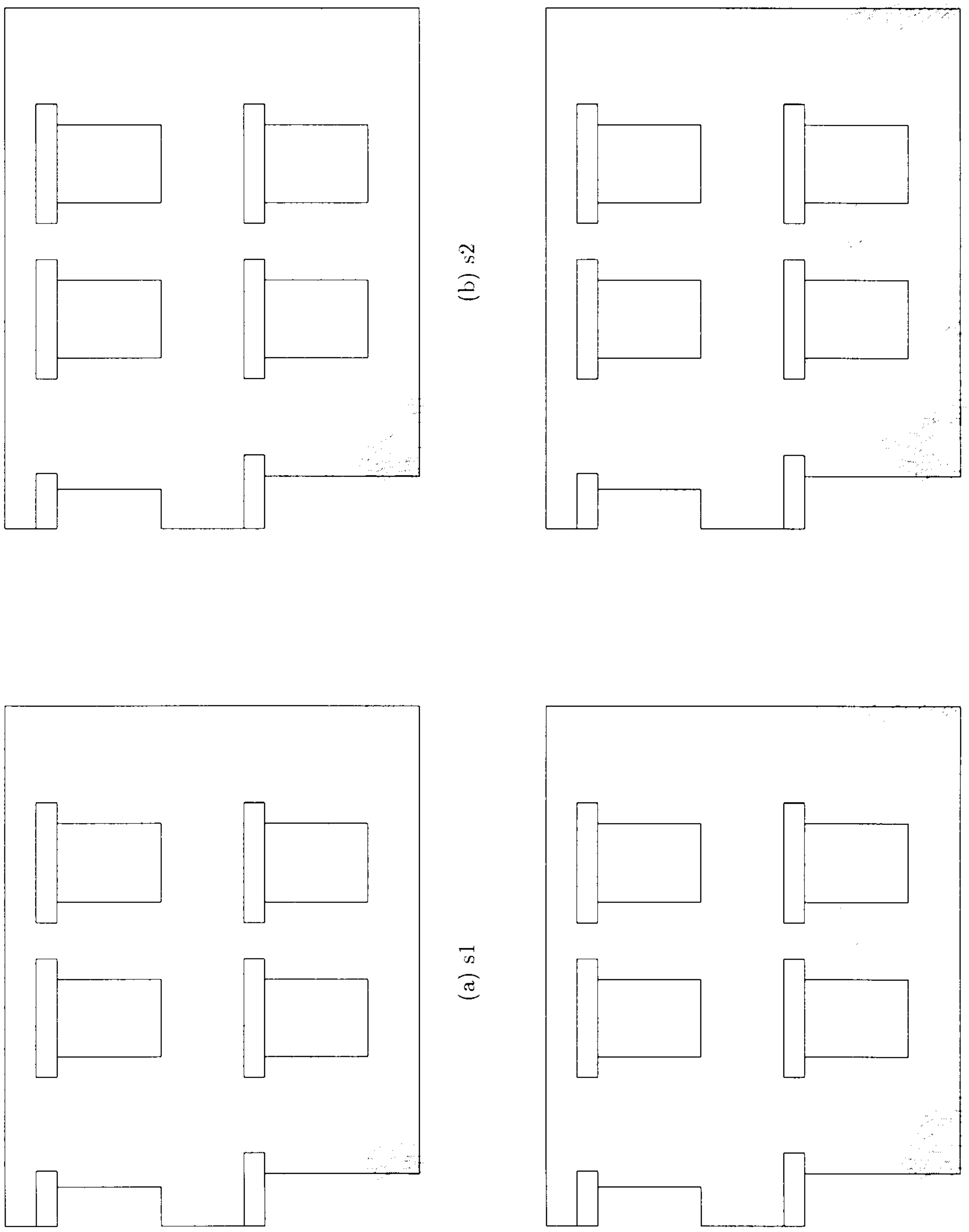

(a) s1

(b) s2

(c) s3

(d) s4

Figure 9.29: **Cracking plots for front facade in analyses 3NB2**

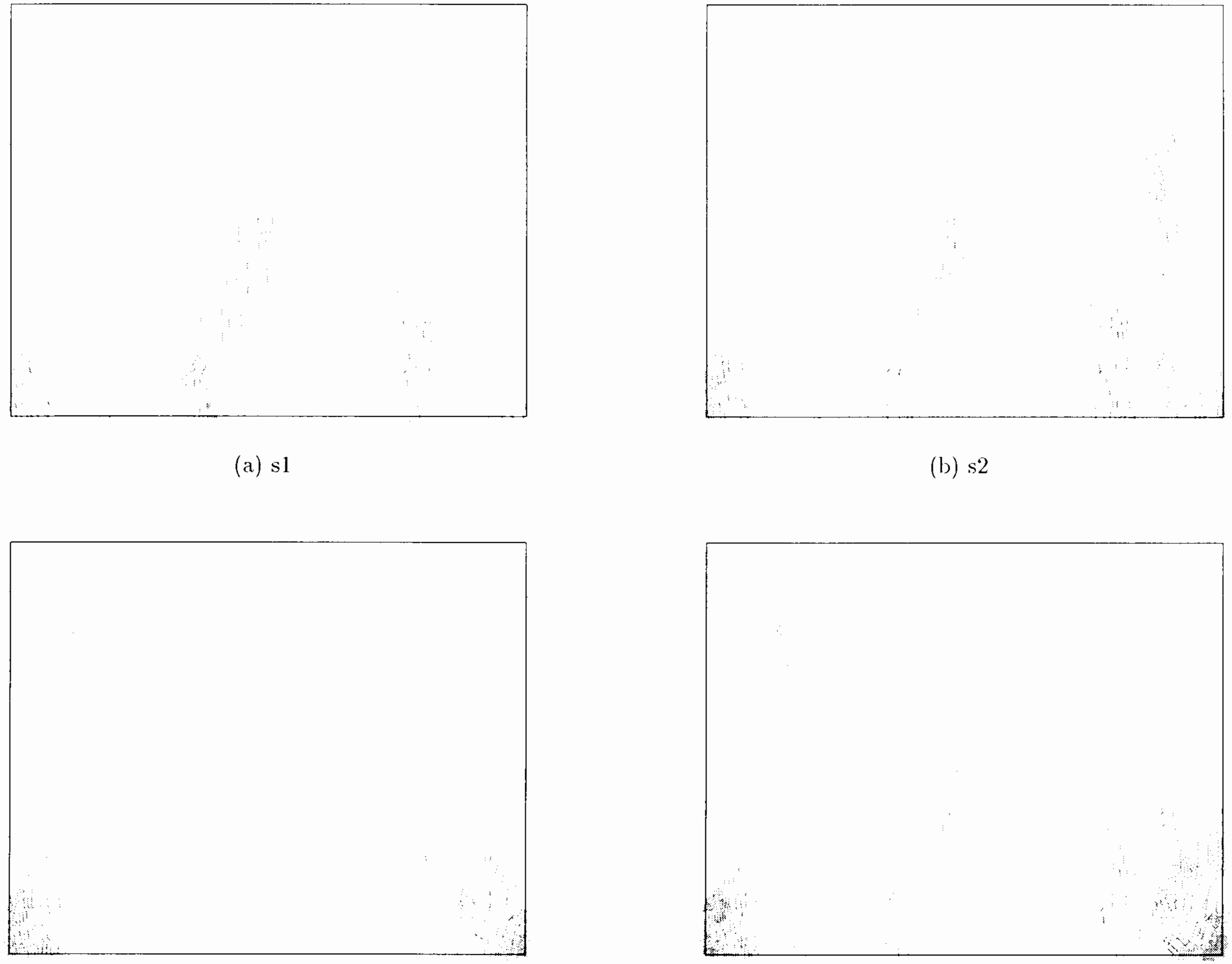

(a) s1

(b) s2

(c) s3

(d) s4

Figure 9.30: **Cracking plots for side facade in analyses 3NB2**

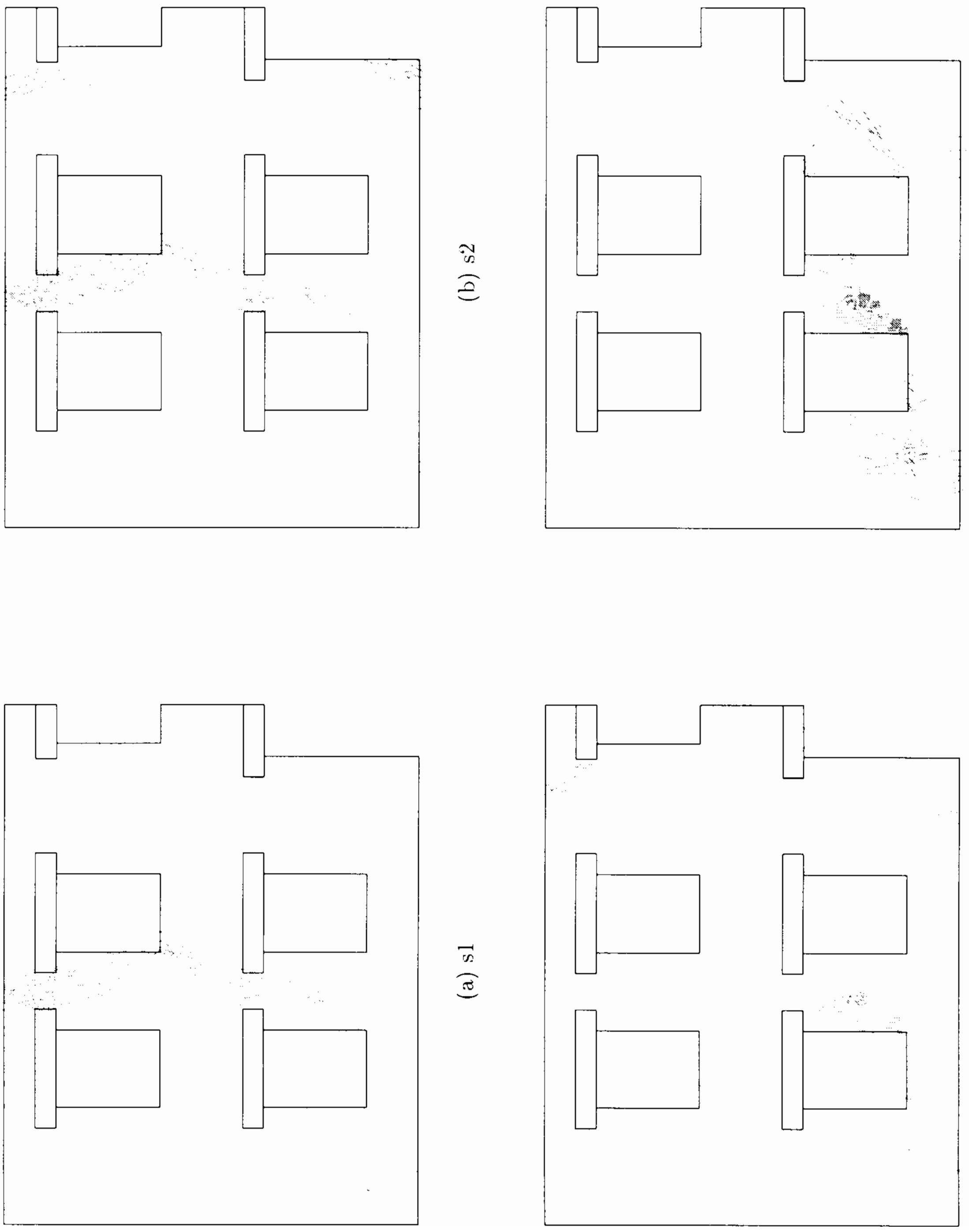

(a) s1 (b) s2

(c) s3 (d) s4

Figure 9.31: **Cracking plots for rear facade in analyses 3NB2**

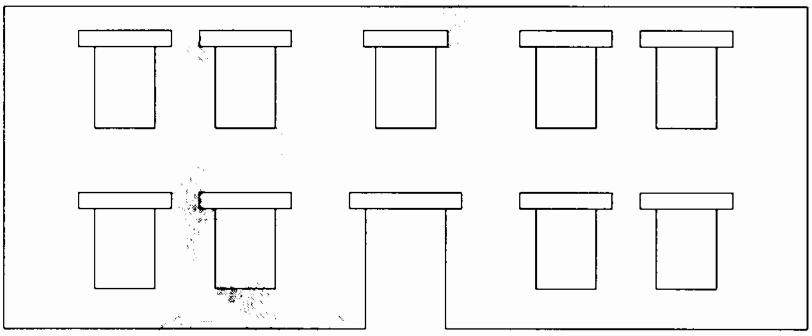

(a) s1

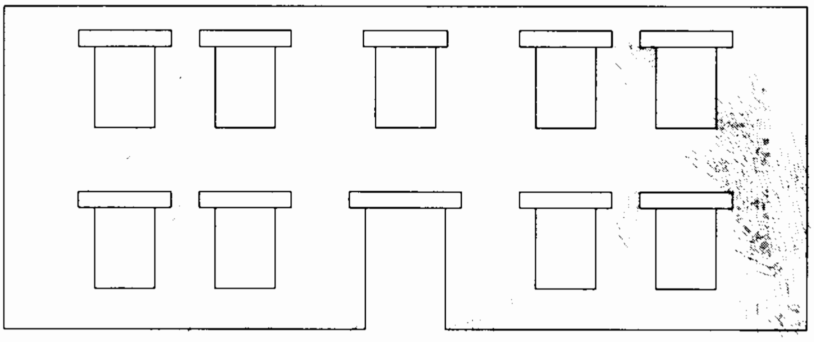

(b) s2

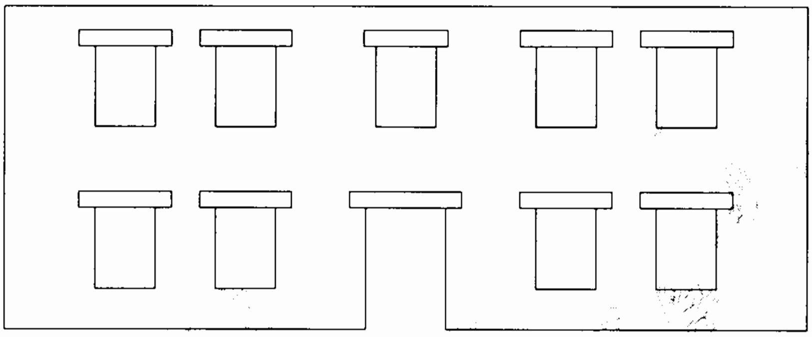

(c) s3

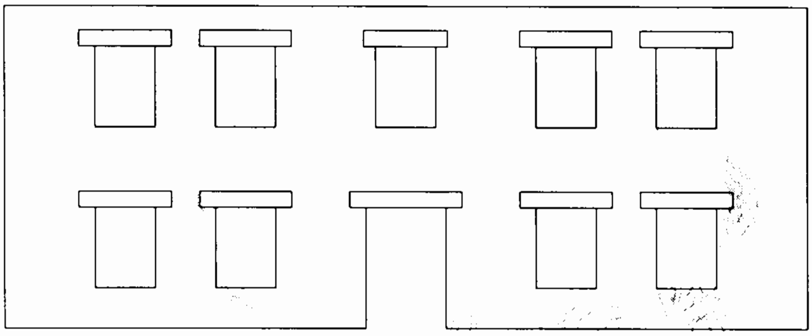

(d) s4

Figure 9.32: **Cracking plots for front facade in analyses 3NB3**

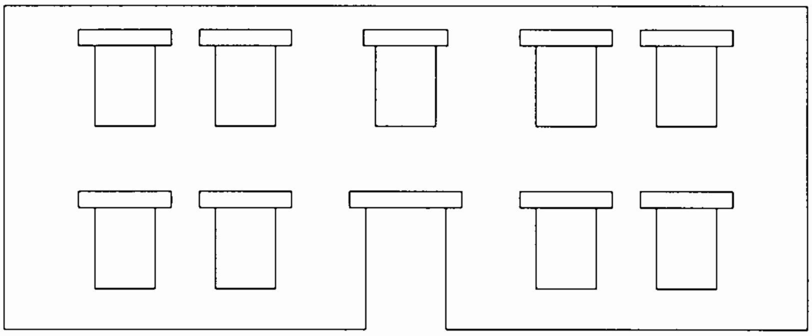

(a) s1

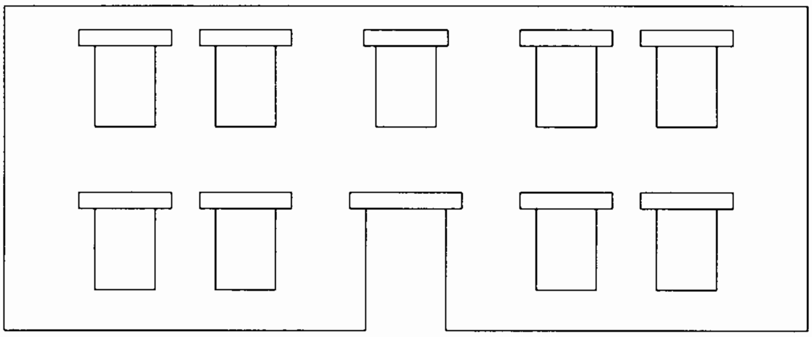

(b) s2

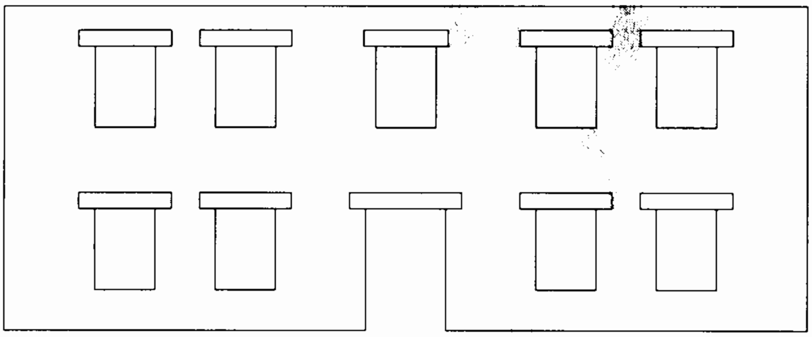

(c) s3

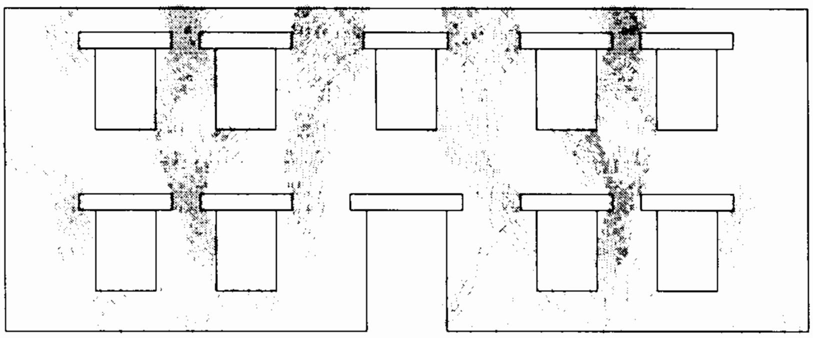

(d) s4

Figure 9.33: **Cracking plots for rear facade in analyses 3NB3**

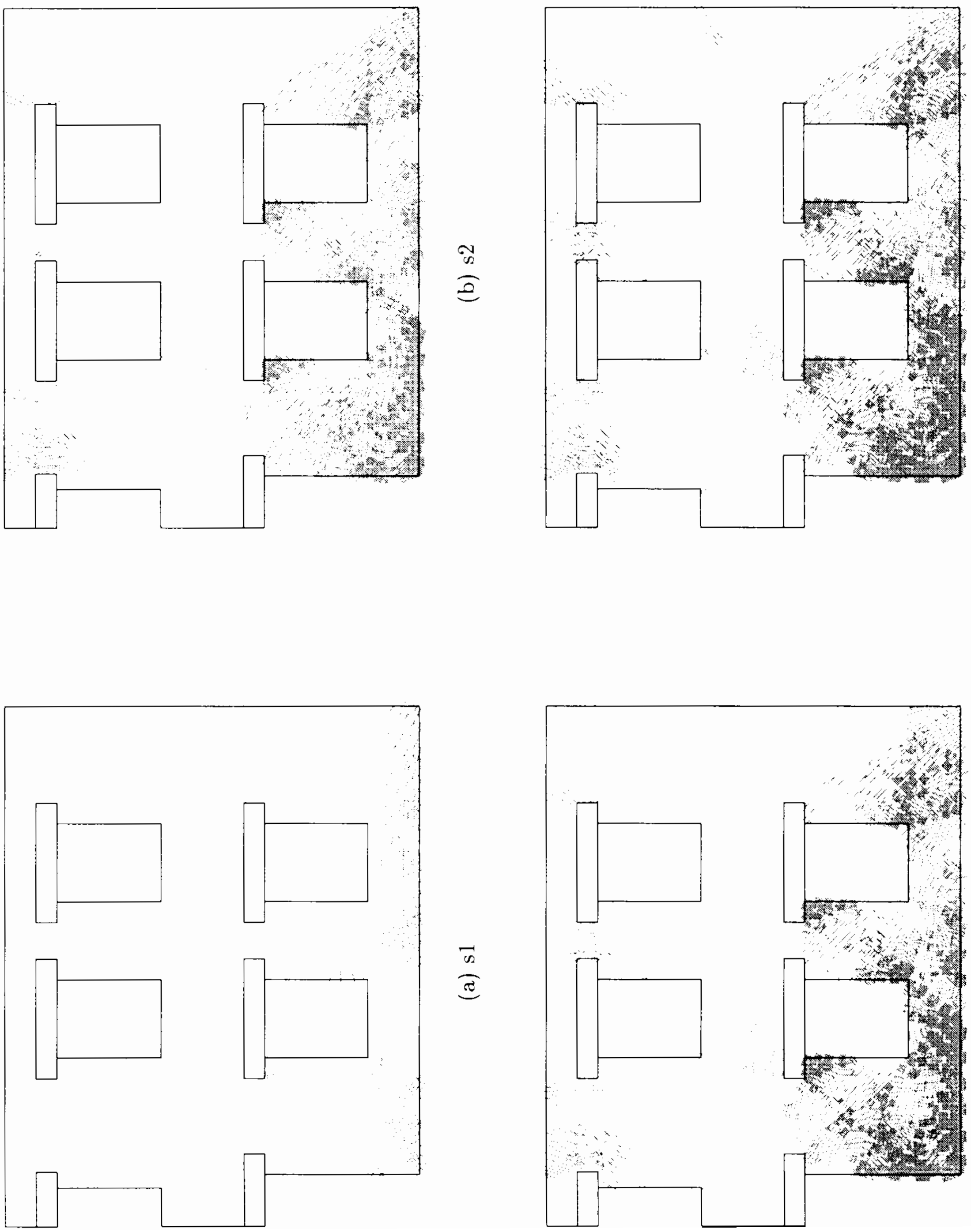

(a) s1

(b) s2

(c) s3

(d) s4

Figure 9.34: **Cracking plots for front facade in analyses 3BB2**

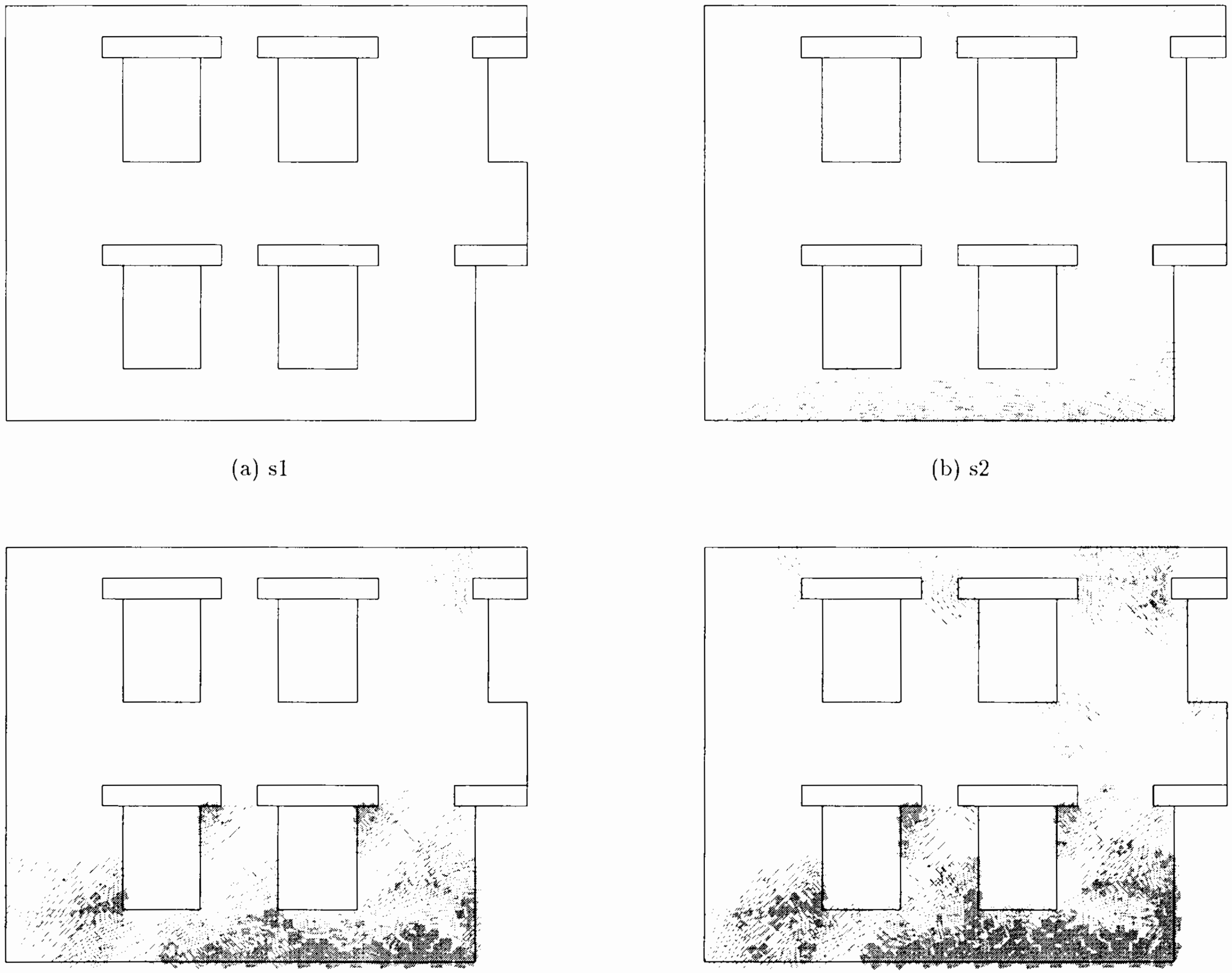

(a) s1

(b) s2

(c) s3

(d) s4

Figure 9.35: **Cracking plots for rear facade in analyses 3BB2**

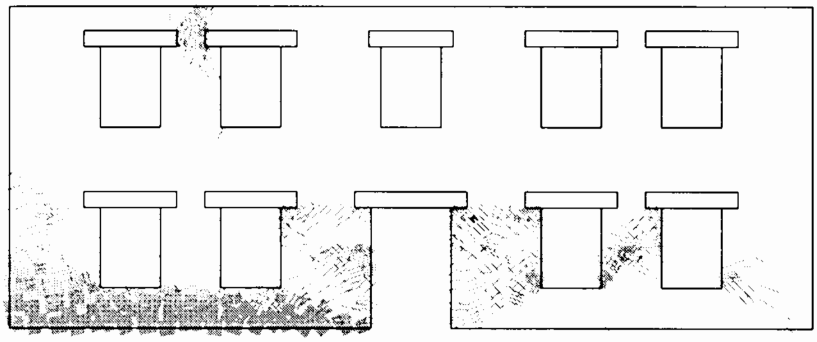

(a) s1

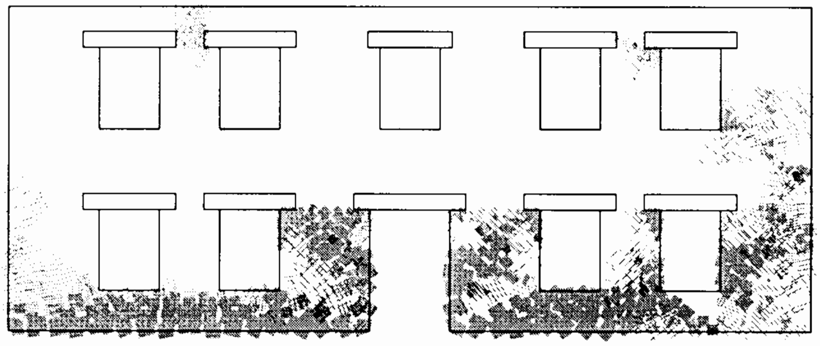

(b) s2

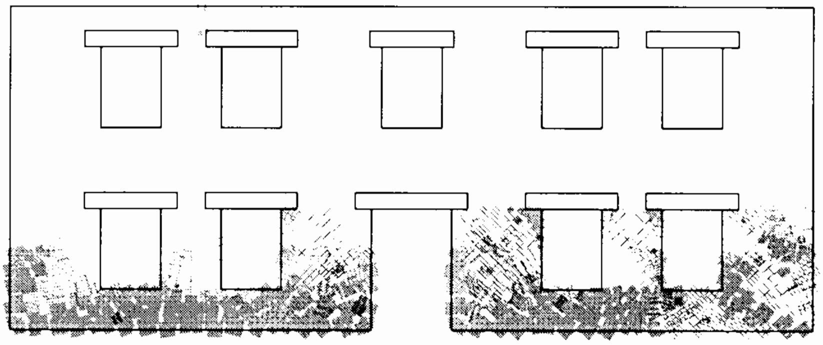

(c) s3

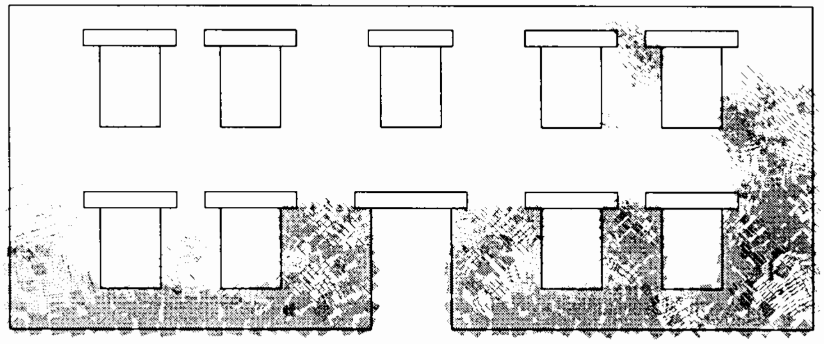

(d) s4

Figure 9.36: **Cracking plots for front facade in analyses 3BB3**

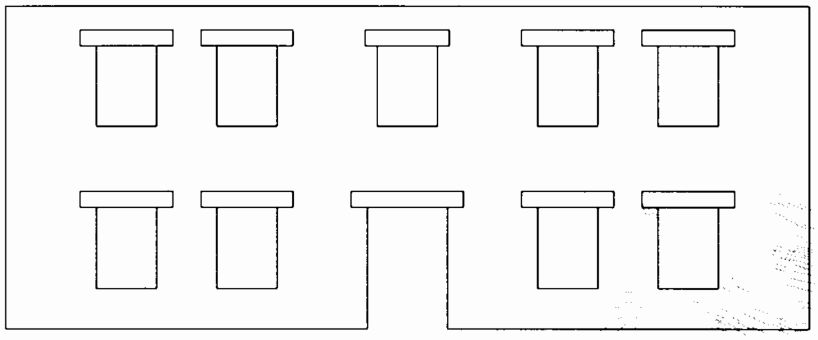

(a) s1

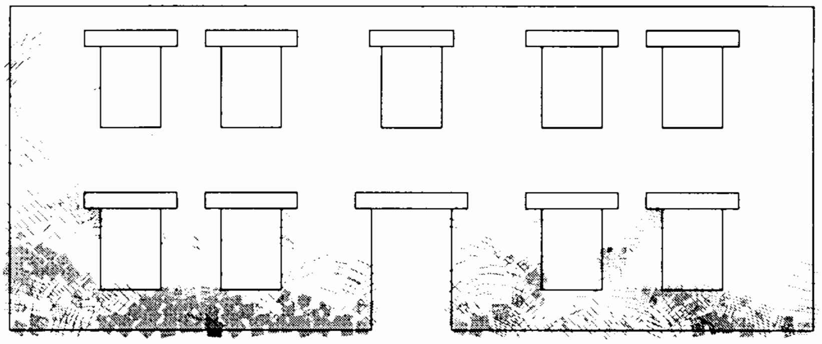

(b) s2

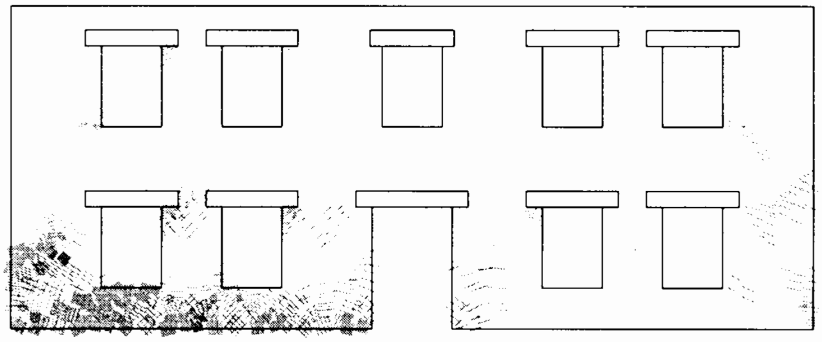

(c) s3

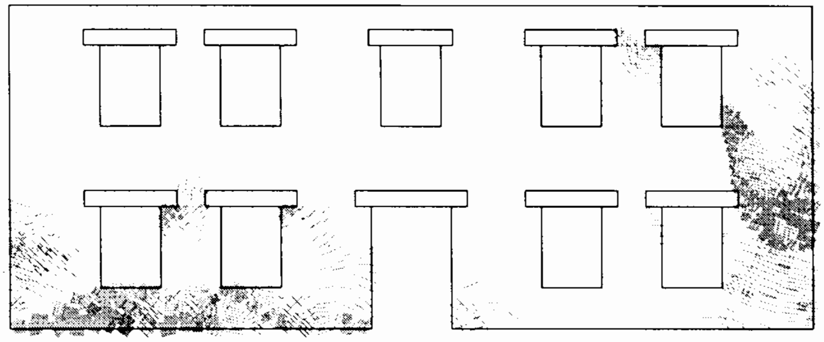

(d) s4

Figure 9.37: **Cracking plots for rear facade in analyses 3BB3**

CHAPTER TEN

CONCLUDING REMARKS

This thesis describes the development and testing of a numerical model of tunnelling. The need for this work arises because of the lack of suitable techniques for the assessment of damage to buildings resulting from tunnelling-induced settlement. Predictions of damage in such situations are usually obtained through a two stage procedure which neglects any interaction between the building and the ground. The numerical model explicitly includes the building, thereby accounting for interaction, resulting from the building stiffness and weight.

In developing the numerical model, tunnelling processes have been identified and dealt with separately. Modelling excavation consists of the application of loads and the amendment of structure stiffness to reflect the excavation of the tunnel. The latter procedure is straightforward to implement as a stepped excavation, rather than as a continuous process. Some previous attempts, by others, at this calculation have made incorrect assumptions about the loads at nodes in the finite element mesh surrounding the tunnel. The amendment of structure stiffness is also straightforward but requires careful coding to avoid using nodes which become unattached following excavation. One suggested improvement in the procedure of excavation in the model is for the element order list, used by the frontal solver, to be revised after each stage of excavation. Optimisation would be carried out over the elements remaining in the mesh following that stage exactly as carried out in pre-processing (see Section 7.2.2). This improvement would be significant only for analyses with many more excavation stages than used in the example analyses in this thesis. While it is important to model excavation it will usually be of less significance for surface settlements (and hence building damage) than the modelling of volume loss.

Analysis of an unlined tunnel requires only the ability to model excavation. The installation of a tunnel lining leads also to generation of volume losses which dominate the surface settlements. Two-dimensional tunnel linings have been modelled using beam elements, attached to the nodes surrounding the excavation while in three-dimensions, shell elements are used. Choosing a suitable shell finite element from the many different formulations described in the literature is difficult. Most formulations are either poorly tested or have rarely been employed in the situation required for this numerical model. In an attempt to adopt a simple solution, novel formulations for overlapping beam and shell elements have been investigated and implemented for use in the numerical model. In both cases, faceted approximations have been used which are considerably simpler than true curved formulations but less accurate.

The two-dimensional overlapping elements serve both as reasonable and efficient linings and as a means of understanding the overlapping formulation in three-dimensions. In both two- and three-dimensions, the imposition of boundary conditions using the overlapping formulation requires careful consideration. because only translational degrees of freedom are used. While this reduces the number of degrees of freedom in the structure, rotational fixities must be dealt with at the element stiffness matrix formation level, rather than at assembly. Tests show the two-dimensional element to perform well, both in beam problems and in the model of tunnelling. The three-dimensional shell element appears to perform well in situations where either bending or membrane effects dominate, but poorly where there is a mixture of the two. These findings agree in general with the work of Phaal and Calladine (1992) who carried out extensive tests of the element on shell-only problems. Tests carried out here, of the shell elements in conjunction with attached elastic ground, show them to follow the expected trends but to give a stiffer response.

Volume loss is simulated in this numerical model by shrinking the lining elements attached to the ground element faces around the tunnel. Calculation of appropriate loading to give uniform shrinkages in both two- and three-dimensional cases is straightforward. In three-dimensions, volume loss is imposed stage by stage, at the same time the lining elements are activated. To avoid a subsequent stage of shrinkage adversely affecting an earlier one, a somewhat artificial situation is imposed at the tunnel face. This is one of a number of problems specific to the three-dimensional model which have required careful solution during model development.

The example analyses described in this thesis first check the performance of the model in predicting greenfield settlements, for which there is an established semi-empirical approach known to agree with field measurements. The results show the model to always underpredict the settlements due to tunnelling. Even more unrealistic results are given with elastic ground, to confirm previous findings in this area by others. Two-dimensional analyses using the non-linear soil model may, by their nature, underpredict settlements since the effects of tunnelling must be three-dimensional. Despite this, it seems clear that further development of the non-linear soil model is necessary to improve the localisation of strains around and above the tunnel.

The example analyses have also shown that model response is affected by the method of volume loss simulation and by the coarse levels of discretisation necessary in three-dimensional analyses. To deal with the first of these, it is recommended that other methods of modelling volume loss are investigated and compared to the performance of the current technique. Some suggestions are as follows:

- As some doubts are expressed over the performance of the unusual shell element used in the model instead implement a more conventional curved shell element formulation.
- Adapt the method used in the two-dimensional model of Addenbrooke and Potts (1996) to three-dimensions. Here, the lining is not activated until the ground deformations indicate a given level of volume loss so there is no component of forcing the ground to follow the disposition of the shrunk liner. It is anticipated however that implementing this method in three-dimensions would be complex.
- Alternatively, model the tunnel installation without shell elements by changing the properties of the material to be excavated. The material would change to having zero self-weight but increased stiffness to provide similar restraint to that of the shell lining. Volume loss would then be modelled by shrinking these elements through the application of a volumetric strain.

The coarse discretisation necessary in three-dimensional analyses arises from the need to limit computer resources, both time to complete an analysis and memory required during execution. If remote memory, in the form of a hard disk, rather than RAM is needed, due to the size of the problem, the speed of execution reduces dramatically. Since the computing facilities used for the largest analyses described in Chapters 8 and 9 are already high specifications with respect to the hardware generally used in research and particularly in comparison to that available to industry, their improvement appears not to provide an immediate solution. Instead a fundamental revision of the solver may reduce memory needs during execution and hence allow much larger problems, with finer meshes, to be analysed. The frontal solver, which is a direct solution technique related to Gaussian elimination, has been subjected to considerable improvement during the lifetime of the research project. It is recommended that iterative solution techniques, such as the preconditioned conjugate gradient method (Wathen, 1989; Shewchuk, 1994), be investigated. Suitability of these techniques will depend on the nature of the structure stiffness matrices formed during analysis. The behaviour of the non-linear material model for clay is therefore likely to have a significant role in this investigation.

The conclusions drawn in this thesis of the effect of a surface structure on settlement profiles and, more importantly, on building damage, have to be viewed with care since they are based upon a small number of analyses. The inability of the model to predict with accuracy greenfield settlement profiles must also affect these conclusions. However, some general patterns of behaviour have been shown to be important and further investigation using the model is recommended in the following areas:

- Results presented in Chapter 9 clearly indicate that the stiffening effect of the building is dependent upon the alignment (in plan) of the building with respect to the tunnel axis. Studies should vary both the plan angle and the location of the building with respect to the expected greenfield trough. The latter procedure will permit study of the restraining effect gained from spanning both points of inflection.
- Results presented in Chapter 9 also show that the rear facade of a building is affected to a greater degree than the front facade by a passing tunnel. This phenomenon is likely to be affected by both the distance between facades and the stiffness of the side facades which join them. It would therefore be interesting to model the same strutures with windows in the side facades.
- Varying building stiffness should lead to varying degrees of flattening out of the

settlement trough. However, the brittle nature of the masonry model should produce a stepped change in the response rather than the smooth response expected from a linear elastic masonry material.

It is clear that two-dimensional modelling cannot adequately capture the three-dimensional effects of tunnelling and its interaction with surface structures and ideally, three-dimensional modelling is needed to study this problem. Such techniques are highly complex and research is made difficult by their voracious appetite for computer time and memory. The model developed in this thesis clearly needs improvement and development but it represents a first step towards practical three-dimensional modelling of this important soil-structure interaction problem.

References

Addenbrooke, T. and Potts, D. (1996). Twin tunnel construction - ground movements and lining behaviour. *in* R. Mair and R. Taylor (eds), *Geotechnical aspects of underground construction in soft ground*, Balkema, Rotterdam, pp. 441–446.

Akagi, H. and Komiya, K. (1996). Finite element simulation of shield tunnelling processes in soft ground. *in* R. Mair and R. Taylor (eds), *Geotechnical aspects of underground construction in soft ground*, Balkema, Rotterdam, pp. 447–452.

Allman, D. (1984). A compatible triangular element including vertex rotations for plane elasticity analyses. *Computers & Structures* **19**: 1–8.

Astley, R. (1992). *Finite Elements in Solids and Structures: An Introduction*, Chapman & Hall, London.

Atkinson, J. and Mair, R. (1981). Soil mechanics aspects of soft ground tunnelling. *Ground Engineering* **14**(5): 20–26.

Atkinson, J. and Stallebrass, S. (1991). A model for recent history and non-linearity in the stress-strain behaviour of overconsolidated soil. *Proc. 7th IACMAG*, pp. 555–560.

Attewell, P. (1978). Ground movements caused by tunnelling in soil. *in* J. Geddes (ed.), *Large Ground Movements and Structures*, Pentech Press, London, pp. 812–948.

Attewell, P. (1988). An overview of site investigation and long-term tunnelling-induced settlement in soil. *Proc. 23rd conf. of the Eng. Group of the Geological society*, Geological Society, pp. 55–61.

Attewell, P. and Woodman, J. (1982). Predicting the dynamics of ground settlement and its derivatives caused by tunnelling in soil. *Ground Engineering* pp. 13–22.

Attewell, P. and Yeates, J. (1984). Tunnelling in soil, *in* P. Attewell and R. Taylor (eds), *Ground movements and their effects on structures*, Surrey University Press, pp. 132–215.

Attewell, P., Yeates, J. and Selby, A. (1986). *Soil movements induced by tunnelling and their effects on pipelines and structures*, Blackie & Son Ltd., Glasgow.

Aubry, D. and Modaressi, A. (1989). A rational approach to. the analysis of construction filling or excavation, *Proc. 3rd Int. Symp. Num. Meth. Geomech. (NUMOG III)*, Elsevier Applied Science, pp. 455–462.

Augarde, C. (1993). *Three-dimensional adaptive mesh generation*, MSc. thesis, Heriot-Watt University, Edinburgh.

Augarde, C., Burd, H. and Houlsby, G. (1995). A three-dimensional finite element model of tunnelling, *in* G. Pande and S. Pietruszczak (eds), *Numerical models in geomechanics, NUMOG 5*, Balkema, Rotterdam, pp. 457–462.

Bakker, K., van Scheldt, W. and Plekkenpol, J. (1996). Predictions and a monitoring scheme with respect to the boring of the Second Heinenoord Tunnel, *in* R. Mair and R. Taylor (eds), *Geotechnical aspects of underground construction in soft ground*, Vol. 459-464, Balkema, Rotterdam.

Barrett, N. (1993). Digging through difficult ground, *Tunnels and Tunnelling* **25**(12): 61–62.

Beer, G. (1983). Infinite domain elements in finite element analysis of underground excavations, *Int. J. Numer. Anal. Meth. Geomech.* **7**(1): 1–7.

Bell, R. (1991). *The analysis of offshore foundations subjected to combined loading*, D.Phil thesis, University of Oxford.

Bell, R., Houlsby, G. and Burd, H. (1993). Suitability of two and three dimensional finite elements for modelling material incompressibility using exact integration, *Comm. Num. Meth. Eng.* **9**(4): 313–329.

Bergen, P. and Felippa, C. (1985). A triangular membrane element with rotational degrees of freedom, *Comp. Meth. Appl. Mech. Eng.* **50**: 25–69.

Bernat, S., Cambou, B. and Dubois, P. (1996). Numerical modelling of tunnelling in soft soil, *in* R. Mair and R. Taylor (eds), *Geotechnical aspects of underground construction in soft ground*, Balkema, Rotterdam, pp. 465–470.

Borja, R., Lee, S. and Seed, R. (1989). Numerical simulation of excavation in elasto-plastic soils, *Int. J. Numer. Anal. Meth. Geomech.* **13**: 231–249.

Boscardin, M. (1980). *Building response to excavation-induced ground movements*, Ph.D thesis, University of Illinois.

Boscardin, M. and Cording, E. (1989). Building response to excavation-induced settlement, *ASCE Journal of Geotech. Eng.* **115**: 1–21.

Brown, P. and Booker, J. (1985). Finite element analysis of excavation, *Computers and Geotechnics* **1**(3): 207–220.

Burd, H. (1986). *A large displacement finite element analysis of a reinforced unpaved road*, D.Phil thesis, University of Oxford.

Burd, H., Houlsby, G., Chow, L., Augarde, C. and Liu, G. (1994). Analysis of settlement damage to masonry structures, *in* I. Smith (ed.), *Numerical methods in geotechnical engineering*, Balkema, Rotterdam, pp. 203–208.

Burland, J. and Wroth, C. (1975). Settlement of buildings and associated damage, *Building Research Establishment current paper CP 33/75*.

Burland, J., Broms, B. and de Mello, V. (1977). Behaviour of foundations and structures, *State-of-the-art volume, Proc. 9th ISSMFE*, pp. 495–546.

Chandrasekaran, V. and King, G. (1974). Simulation of excavation using finite elements, *J. Geo. Eng. Div., Proc. ASCE* **100**(GT9): 1086–9.

Chen, W. and Baldauf, S. (1994). 3-d finite element analysis of a magnet/delivery shaft for the superconducting supercollider project, *Proc. 8th IACMAG*, pp. 610–616.

Chow, L. (1994). *The prediction of surface settlements due to tunnelling in soft ground*, MSc. thesis, University of Oxford.

Clough, G., Sweeney, B. and Finno, R. (1983). Measured soil response to EPB tunnelling. *ASCE Journal of Geotech. Eng.* **109**(2): 131–149.

Comodromos, E., Hatzigogos, T. and Pitilakis, K. (1990). Finite element excavation in elastoplastic soils. *Proc. 2nd. Eur. Conf. Num. Meth. Geotech. Eng.*, pp. 573–584.

Cook, R. (1981). *Concepts and applications of finite element analysis*. John Wiley & Sons, Chichester.

Cook, R. (1991). Modified formulations for nine-d.o.f. plane triangles that include vertex rotations. *Int. J. Num. Meth. Eng.* **31**: 825–835.

Davis, E., Gunn, M., Mair, R. and Seneviratne, H. (1980). The stability of underground openings in cohesive material. *Geotechnique*.

de Moor, E. and Taylor, R. (1991). Ground response to construction of a sewer tunnel in very soft ground. *Proc. Tunnelling '91*, Elsevier, Inst. Min. Met.

Desai, C. (1977). Soil-structure interaction and simulation problems. *in* G. Gudehus (ed.), *Finite elements in geomechanics*, John Wiley, pp. 209–247.

Dulacska, E. (1992). *Soil settlement effects on buildings*, Elsevier Science Publishers, Amsterdam.

Einstein, H. and Schwartz, C. (1979). Simplified methods for tunnel design. *ASCE Journal of Geotech. Eng.* **105**(GT4): 499–518.

Eisenstein, Z. and Esseldine, O. (1992). The effect of tunnelling technology on ground control. *Tunnelling and Underground Space Technology* **7**(3): 27–31.

El-Nahhas, F., El-Kadi, F. and Ahmed, A. (1992). Interaction of tunnel linings and soft ground. *Tunnelling and Underground Space Technology* **7**(1): 33–43.

Fang, Y., Lin, S. and Lin, J. (1993). Time and settlement in EPB shield tunnelling. *Tunnels and Tunnelling* **25**: 27–28.

Farmer, I. (1978). Case histories of settlement above tunnels in clay. *in* J. Geddes (ed.), *Large Ground Movements and Structures*, Pentech Press, London, pp. 357–371.

Flint, G. and Foreman, W. (1992). Bentonite tunnelling for the Greater Cairo wastewater project, *Tunnelling and Underground Space Technology* **7**(1): 45–53.

Flügge, W. (1966). *Stresses in shells*, Springer-Verlag Inc., New York.

Frischmann, W., Hellings, J., Gittoes, G. and Snowden, C. (1994). Protection of the Mansion House against damage caused by the Docklands Light Railway extension, *Proc. I.C.E., Geotech. Eng.* **107**(2): 65–76.

Geddes, J. (1992). Discussion of session vii, *in* J. Geddes (ed.), *Proc. 4th Int. Conf. Ground movements and structures*, Pentech Press, London, pp. 825–826.

Geotechnical Consulting Group (1992). CrossRail project - prediction of ground movements and associated building damage due to bored tunnelling, *Internal document*.

Ghaboussi, J. and Pecknold, D. (1984). Incremental finite element analysis of geometrically altered structures, *Int. J. Num. Meth. Eng.* **20**: 2051–2064.

Ghaboussi, J., Hansmire, W., Parker, H. and Kim, K. (1983). Finite element simulation of tunnelling over subways, *ASCE Journal of Geotech. Eng.* **109**(3): 318–334.

Gioda, G. and De Donato, O. (1979). Elastic-plastic analysis of geotechnical problems by mathematical programming, *Int. J. Numer. Anal. Meth. Geomech.* **3**: 381–401.

Gioda, G., Sterpi, D. and Locatelli, L. (1994). Some examples of finite element analysis of tunnels, *Proc. 8th IACMAG Conf., Morgantown*, pp. 165–176.

Grabinsky, M. and Curran, J. (1993). Efficient mesh generation procedures for finite element analysis of underground structures, *Int. J. Rock Mech. Min. Sci.* **30**(6): 591–600.

Gunbel, J. (1981). Dicussion on Pender, (Geotechnique, 1980, 216-222), *Geotechnique* **31**(3): 434–438.

Gunn, M. (1993). The prediction of surface settlement profiles due to tunnelling, *Predictive Soil Mechanics (Proc. Wroth Mem. Symp.)*, Thomas Telford, London, pp. 304–317.

Harris, D., Mair, R., Love, J., Taylor, R. and Henderson, T. (1993). Observations of ground and structure movements for compensation grouting during tunnel construction at Waterloo station, *Geotechnique* **44**(4): 691–713.

Hellings, J. (1994). Limiting the damage to historic buildings due to tunnelling: experience at the Mansion House, London, *Proc. Tunnelling '94*, Elsevier, pp. 253–277.

Higgins, K., Mair, R. and Potts, D. (1996). Numerical modelling of the influence of the Westminster station excavation and tunnelling on the Big Ben clock tower, *in* R. Mair and R. Taylor (eds), *Geotechnical aspects of underground construction in soft ground*, Balkema, Rotterdam, pp. 525–530.

Hirst, C. (1994). *A study, using finite elements into building damage and ground movements due to tunnelling*, Fourth year undergraduate project, University of Oxford.

Houlsby, G. (1994). *Modelling the variable stiffness of undrained clay using multiple yield surfaces*, Report OUEL 2024/94, University of Oxford Dept. of Engineering Science.

Huang, H. (1989). *Static and dynamic analysis of plates and shells*, Springer-Verlag.

Hughes, T. (1987). *The finite element method: linear, static and dynamic finite element analysis*, Prentice Hall.

Hughes, T., Masud, A. and Harari, I. (1995). Numerical assessment of some membrane elements with drilling degrees of freedom, *Computers and Structures* **55**(2): 297–314.

Imamura, S., Nomoto, T., Mito, K., Ueno, K. and Kusakabe, O. (1996). Design and development of underground construction equipment in a centrifuge, *in* R. Mair and R. Taylor (eds), *Geotechnical aspects of underground construction in soft ground*, Balkema, Rotterdam, pp. 531–536.

Inokuma, A. and Fujimoto, A. (1996). An improvement of FEM analysis in ground settlement prediction in shield tunnelling, *in* R. Mair and R. Taylor (eds), *Geotech-*

nical aspects of underground construction in soft ground, Balkema, Rotterdam, pp. 537–542.

Institution of Structural Engineers (1989). Tunnels and underground openings, *Soil-Structure Interaction*, I.Struct. E., London.

Irons, B. and Ahmad, S. (1980). *Techniques of finite elements*, Ellis Horwood Ltd.

Ito, T. and Hisatake, M. (1982). Observed and computed settlements in a case of soft ground tunnelling, *in* Z. Eisenstein (ed.), *Proc. 4th Int. Conf. Num. Meth. Geomech., Edmonton*, Balkema, Rotterdam, pp. 551–559.

Kerisel, J. (1975). Old structures in relation to soil conditions, *Geotechnique* **25**(3): 433–483.

Kim, S. (1996). *Model testing and analysis of interactions between tunnels in clay*, D.Phil thesis, University of Oxford.

Lee, K. and Rowe, R. (1989a). Deformations caused by surface loading and tunnelling: the role of elastic anisotropy, *Geotechnique* **39**(1): 125–140.

Lee, K. and Rowe, R. (1989b). The use of supercomputers for predicting three-dimensional ground deformations due to tunnelling in soft soil, *Proc. 3rd Int. Symp. Num. Meth. Geomech. (NUMOG III)*, Elsevier Applied science, pp. 557–565.

Lee, K. and Rowe, R. (1990a). Finite element modelling of the three-dimensional ground deformations due to tunnelling in soft cohesive soils: part 1 - method of analysis, *Computers and Geotechnics* **10**: 87–109.

Lee, K. and Rowe, R. (1990b). Finite element modelling of the three-dimensional ground deformations due to tunnelling in soft cohesive soils: part 2 - results, *Computers and Geotechnics* **10**: 110–138.

Lee, K., Rowe, R. and Lo, K. (1992). Subsidence owing to tunnelling. I. estimating the gap parameter, *Canadian Geotechnical Journal* **29**: 929–940.

Litwiniszyn, J. (1994). The Gauss function and the phenomena of rock mass subsidence and displacements of granular material. *Int. J. Rock Mech. Min. Sci.* **31**(2): 143–148.

Liu, G. (1997). *Numerical modelling of settlement damage to masonry buildings caused by tunnelling*. D.Phil thesis, University of Oxford.

Mair, R. (1979). *Centrifugal modelling of tunnel construction in soft clay*. Ph.D thesis, University of Cambridge.

Mair, R. (1993). Developments in geotechnical engineering research: applications to tunnels and deep excavations. *Proc. I.C.E.* **97**(1): 27–41.

Mair, R. and Taylor, R. (1993). Prediction of clay behaviour around tunnels using plasticity solutions. *Predictive Soil Mechanics (Proc. Wroth Mem. Symp.)*, Thomas Telfor, pp. 449–463.

Mair, R., Gunn, M. and O'Reilly, M. (1981). Ground movements around shallow tunnels in soft clay. *Proc. 10th ICSMFE*, pp. 323–328.

Mair, R., Taylor, R. and Bracegirdle, A. (1993). Subsurface settlements above tunnels in clays. *Geotechnique* **43**: 315–320.

Mair, R., Taylor, R. and Burland, J. (1996). Prediction of ground movements and assessment of risk of building damage due to bored tunnelling, *in* R. Mair and R. Taylor (eds), *Geotechnical aspects of underground construction in soft ground*, Balkema, Rotterdam, pp. 713–718.

Medeiros, L., El Nahhas, F., Smith, L. and Eisenstein, Z. (1982). Modelling of the construction of an underground station. *Proc. 4th Int. Conf. Num. Meth. Geomech., Edmonton*, pp. 929–934.

Mensah-Dwumah, F. (1984). *Finite element modelling of brick masonry building behaviour in response to deformations induced by soft-ground tunnelling*. Ph.D thesis, Stanford University.

Muir Wood, A. (1975). The circular tunnel in elastic ground. *Geotechnique* **25**(1): 115–127.

Najjar, Y., Zaman, M. and Ahern, J. (1989). Prediction of surface subsidence caused by underground mining using a non-linear finite element procedure. *Proc. 3rd Int. Symp. Num. Meth. Geomech. (NUMOG III)*, Elsevier, pp. 557–565.

New, B. and Bowers, K. (1994). Ground movement model validation at the Heathrow Express trial tunnel. *Proc. Tunnelling '94*, Elsevier, pp. 301–329.

New, B. and O'Reilly, M. (1992). Tunnelling induced ground movements: predicting their magnitude and effects. *in* J. Geddes (ed.), *Proc. 4th Int. Conf. Ground Movements and Structures*, Pentech Press, London, pp. 671–697.

Ng, C., Lings, M., Simpson, B. and Nash, D. (1995). An approximate analysis of the three-dimensional effects of diaphragm wall installation. *Geotechnique* **45**(3): 497–507.

Oteo, C. and Sagaseta, C. (1982). Prediction of settlements due to underground openings. *Proc. Int. Symp. Num. Mod. Geomech. Zurich*, Balkema, pp. 653–659.

Oteo, C. and Sagaseta, C. (1996). Some Spanish experiences on measurement and evaluation of ground displacements around urban tunnels. *in* R. Mair and R. Taylor (eds), *Geotechnical aspects of underground construction in soft ground*, Balkema, Rotterdam, pp. 731–736.

Parry-Jones, M. and Cline, R. (1993). *A study, using finite element analysis into cracking in buildings caused by ground movements due to tunnelling*, fourth-year undergraduate project report, University of Oxford.

Peck, R. (1969). Deep excavations and tunnelling in soft ground. *State-of-the-art volume, 7th ICSMFE*, pp. 226–290.

Pender, M. (1980). Elastic solutions for a circular tunnel. *Geotechnique* **30**: 216–222.

Phaal, R. (1990). *A two-surface computational model for the analysis of thin shell structures*, Ph.D. thesis, University of Cambridge.

Phaal, R. and Calladine, C. (1992a). A simple class of finite elements for plate and shell problems. I: Elements for beams and thin flat plates. *Int. J. Num. Meth. Eng.* **35**: 955–977.

Phaal, R. and Calladine, C. (1992b). A simple class of finite elements for plate and shell problems. II: An element for thin shells, with only translational degrees of freedom, *Int. J. Num. Meth. Eng.* **35**: 979–996.

Pilkey, W. (1994). *Formulas for stress, strain and structural matrices*, John Wiley & Sons, New York.

Polshin, D. and Tolkar, R. (1957). Maximum allowable non-uniform settlement of structures, *Proc. 4th ICSMFE*, Vol. 1, pp. 402–405.

Potts, D. and Addenbrooke, T. (1996). The influence of an existing surface structure on on the ground movements due to tunnelling, *in* R. Mair and R. Taylor (eds), *Geotechnical aspects of underground construction in soft ground*, Balkema, Rotterdam, pp. 573–578.

Poulos, H. and Davis, E. (1980). *Elastic solutions for rock mechanics*, John Wiley & Sons, New York.

Rankin, W. (1988). Ground movements resulting from urban tunnelling: prediction and effects, *Proc. 23rd conf. of the Eng. Group of the Geological society*, London: Geological Society, pp. 79–92.

Razzaque, A. (1973). Program for triangular bending elements with derivative smoothing, *Int. J. Num. Meth. Eng.* **6**: 333–343.

Romo, M. and Resendez, D. (1982). Observed and computed settlements in a case of soft ground tunnelling, *in* Z. Eisenstein (ed.), *Proc. 4th Int. Conf. Num. Meth. Geomech., Edmonton*, Balkema, Rotterdam, pp. 597–609.

Rowe, R. and Lee, K. (1992). Subsidence due to tunnelling. II. evaluation of a prediction technique, *Canadian Geotechnical Journal* **29**: 941–954.

Sagaseta, C. (1987). Analysis of undrained soil deformation due to ground loss, *Geotechnique* **37**(3): 301–320.

Schaer, J. and Stone, M. (1991). Face traverses and a volume algorithm for polyhedra, *Lecture notes in computer science* **555**: 290–297.

Shewchuk, J. (1994). An introduction to the conjugate gradient method without the agonising pain. *Technical report*, School of Computer Science, Carnegie-Mellon University.

Simpson, B. (1994). A model of interaction between tunnelling and a masonry structure. *in* I. Smith (ed.), *Numerical methods in geotechnical engineering*, Balkema, Rotterdam, pp. 221–226.

Simpson, B., Atkinson, J. and Jovicic, V. (1996). The influence of anisotropy on calculations of ground settlements above tunnels. *in* R. Mair and R. Taylor (eds), *Geotechnical aspects of underground construction in soft ground*, Balkema, Rotterdam, pp. 591–594.

Simpson, B., O'Riordan, N. and Croft, D. (1979). A computer model for the analysis of ground movements in London Clay. *Geotechnique* **29**(2): 149–175.

Skempton, A. and MacDonald, D. (1956). Allowable settlement of buildings. *Proc. I.C.E* **5**: 727–784.

Sloan, S. and Assadi, A. (1992). Stability of tunnels in soft ground. *Predictive Soil Mechanics (Proc. Wroth Mem. Symp.)*, Thomas Telford, pp. 644–663.

Sloan, S. and Randolph, M. (1982). Numerical predictions of collapse loads using finite element methods. *Int. J. Numer. Anal. Meth. Geomech.* **6**: 47–76.

Sloan, S. and Randolph, M. (1983). Automatic element reordering for finite element analysis with frontal solution schemes. *Int. J. Num. Meth. Eng.* **19**: 1153–1181.

Spanier, J. and Oldham, K. (1987). *An atlas of functions*, Hemisphere, London.

St. John, H., Potts, D., Jardine, R. and Higgins, K. (1993). Prediction and performance of ground response due to construction of a deep basement at 60 Victoria Embankment. *Predictive Soil Mechanics (Proc. Wroth Mem. Symp.)*, Thomas Telford, pp. 581–608.

Stack, B. (1985). Update on trends in soft ground tunnelling. *Tunnels and Tunnelling* **17**(1): 21–23.

Stallebrass, S., Grant, R. and Taylor, R. (1996). A finite element study of ground movements measured in centrifuge model tests of tunnels, *in* R. Mair and R. Taylor (eds), *Geotechnical aspects of underground construction in soft ground*, Balkema, Rotterdam, pp. 595–600.

Standing, J., Nyren, R., Longworth, T. and Burland, J. (1996). The measurement of ground movements due to tunnelling at two control sites along the Jubilee Line Extension, *in* R. Mair and R. Taylor (eds), *Geotechnical aspects of underground construction in soft ground*, Balkema, Rotterdam, pp. 751–756.

Sterling, R. (1992). Developments in excavation technology: a comparison of Japan, the U.S. and Europe, *Tunnelling and Underground Space Technology* **7**(3): 221–235.

Sweet, A. and Bogdanoff, J. (1965). Stochastic model for predicting subsidence, *ASCE J. Eng. Mech.* **91**(EM2): 21–46.

Swoboda, G., Mertz, W. and Schmid, A. (1989). Three-dimensional numerical models to simulate tunnel excavation, *Proc. 3rd Int. Symp. Num. Meth. Geomech. (NUMOG III)*, Elsevier Applied science, pp. 536–548.

Timoshenko, S. (1957). *Strength of materials - part 1*, D. van Nostrand Co. Inc., London.

Timoshenko, S. and Goodier, J. (1960). *Theory of elasticity*, D. van Nostrand Co. Inc., London.

Todd, J. (1974). *Structural theory and analysis*, Macmillan.

Ward, W. and Pender, M. (1981). Tunnelling in soft ground - general report, *Proc. 10th ICSMFE*, pp. 261– 275.

Wathen, A. (1989). An analysis of some element-by element techniques, *Comp. Meth. Appl. Mech. Eng.* **74**: 271–287.

Yang, H., Saigal, S. and Liaw, D. (1990). Advances of thin shell finite elements and some applications - version 1, *Computers & Structures* **35**(4): 481–504.

Zawadzki, J. (1994). The application of a full scale trial to the prediction of tunnel induced surface settlements in London clay. *Proc. of BGS Young Geo. Eng. Symp.*, University of Cardiff.

Zienkiewicz, O. and Morgan, K. (1983). *Finite elements and approximation*. Wiley.

Zienkiewicz, O. and Taylor, R. (1989). *The finite element method*. McGraw-Hill.